Tau lepton reconstruction with energy flow and the search for R-parity violating supersymmetry at the ATLAS experiment

Dissertation
zur
Erlangung des Doktorgrades (Dr. rer. nat.)
der
Mathematisch-Naturwissenschaftlichen Fakultät
der
Rheinischen Friedrich-Wilhelms-Universität Bonn

vorgelegt von

Sebastian Fleischmann

aus

Haan

Bonn 2011

Referent:	Prof. Dr. Klaus Desch
Koreferent:	Prof. Dr. Norbert Wermes
Tag der Promotion:	17.10.2011
Erscheinungsjahr:	2012

Abstract

The ATLAS experiment at the Large Hadron Collider (LHC) is measuring proton-proton collisions at a centre-of-mass energy of $\sqrt{s} = 7\,\text{TeV}$ since 2010, an energy never reached before in collider experiments. A wide variety of measurements within and beyond the framework of the Standard Model of Particle Physics are performed. Supersymmetry (SUSY) is a widely studied extension of the Standard Model. In order to keep the parameter space of the minimal supersymmetric extension of the Standard Model (MSSM) phenomenologically manageable one often uses simplifying assumptions like minimal supergravity (mSUGRA). Additionally, almost all SUSY studies of the ATLAS collaboration assume the conservation of R-parity, which leads to a stable, weakly interacting lightest supersymmetric particle (LSP).

This thesis investigates the discovery potential of the ATLAS experiment for R-parity violating (RPV) SUSY models in the framework of mSUGRA, where the stau ($\widetilde{\tau}$) is the LSP. Hence, the LSP is charged and decays in contrast to R-parity conserving models.

Monte Carlo simulations of the detector are essential for all studies in the ATLAS experiment. The ATLAS fast track simulation FATRAS is a new approach for the Monte Carlo simulation of particles in the tracking systems. Its results are compared to first data at $\sqrt{s} = 900\,\text{GeV}$. Additionally, two generic detector simulations are compared to the full simulation of the ATLAS detector.

The reconstruction of hadronic decays of tau leptons is crucial for the reconstruction of the stau mass in the considered model, but also of general interest for many searches for new physics with ATLAS. In this thesis the reconstruction of tracks for particles from tau decays is studied. A novel method, PanTau, is presented for the tau reconstruction in ATLAS. It is fully based on results of the energy flow algorithm eflowRec. Its performance is evaluated in Monte Carlo simulations. The dependency of the identification variables on the jet energy are studied in detail. Finally, the energy flow quantities and the identification variables are compared between Monte Carlo simulations and measured QCD jet events with first ATLAS data at $\sqrt{s} = 7\,\text{TeV}$.

For the first time in the framework of this RPV model a detailed signal to background analysis is performed for a specific benchmark scenario using a full Monte Carlo simulation of the ATLAS detector. The parameter space in the neighbourhood of this benchmark scenario is investigated in a parameter scan. The discovery reach with the first data of the ATLAS experiment is estimated. Furthermore a feasibility study for an estimate of the stau LSP mass is given.

Acknowledgements

First of all I like to thank my supervisor, Klaus Desch, for giving me the opportunity to join his working group in order to prepare this thesis. With his excellent support and patience he provided the most important impetus to this work while giving me the freedom to realise my own ideas and following my interests. He also provided outstanding help beyond my thesis *e.g.* in applications for scholarships and schools. I enjoyed the atmosphere of collaboration in his group very much. Peter Wienemann I have to thank as well for supporting my work and the innumerable discussions we had during the design of PanTau and his deep insight in physical processes from which I profited much in all areas of my work.

The fruitful collaboration with my theory colleagues Herbi Dreiner and Sebastian Grab was very interesting and a pleasure for me. Both I have to thank for many discussions on R-parity violating SUSY and their important input to this thesis.

Our new tau reconstruction algorithm, PanTau, is a common effort with Robindra Prabhu, Peter Wienemann and Christian Limbach. I like to express my gratitude to them for the productive collaboration in which everybody contributed with important ideas. The development of PanTau would have been impossible without the assistance of Mark Hodgkinson. He was always only "an email away" from us, when questions concerning eflowRec came up. Stan Lai, Elzbieta Richter-Was, Ryan Reece, Philip Bechtle and Michel Janus provided their help to the tau studies and supported the development of PanTau.

The developers of TMVA I thank for their very useful toolkit. My special thanks go to Eckhard von Törne, who provided much support on TMVA and with whom I discussed many ideas on the application of machine learning.

My work on the fast track simulation FATRAS was supported by Andreas Salzburger, Simone Zimmermann, Michael Dührssen and Jörg Mechnich. Thanks to them and "Stay on track"!

My colleagues Robert Zimmermann, Carolin Zendler, Till Nattermann, Mathias Uhlenbrock, Steffen Schaepe and Adrian Vogel I wish to thank for the nice working environment and also for many smaller and larger contributions and assistance of my work.

Peter Richardson I thank for his help on Herwig. Markus Bernhardt, Jong Soo Kim and Siba Prasad Das answered many of my questions for which I thank them. I am

grateful to Vasiliki Mitsou and David Milstead for their support of the studies on R-parity violating SUSY in the ATLAS experiment.

Computing was an essential ingredient to my thesis and I therefore have to thank the team of the Bonn Analysis Facility, especially Gizo Nanava and Thomas Loddenkötter. Similarly I thank the support team of the National Analysis Facility (NAF) at DESY, in particular Wolfgang Ehrenfeld.

Sebastian Grab, Mark Hodgkinson, Tatjana Lenz, Andreas Salzburger and Marisa Sandhoff I thank for proof reading parts of the manuscript.

I am much obliged to the Bonn-Cologne graduate school of physics and astronomy (BCGS) for their financial support and many interesting lectures, workshops and events beyond the curricula. Jürgen Stutzki I thank for his support as my mentor at Cologne University.

Andrea Fürstenberg and Gisela Streich I thank for their assistance and guidance through the bureaucracy of the institute. Peter Mättig I like to thank for his patience. Many other members of the ATLAS collaboration contributed to my work with their help. Amongst them are Attilio Andreazza, Stephen Haywood, Wolfgang Liebig, Sven Menke and Jochen Schieck.

Contents

"For Klara Johanna and Christina Maria"

Preface

Since ancient times philosophers have asked the question, what are the constituents of the world around us. In modern times this philosophical question has become a matter of detailed empirical studies and the fruitful idea of laws of nature in a mathematical language grew. In parallel our understanding of the building blocks of matter and the laws determining their interactions evolved enormously in the last century.

Not only the theoretical understanding evolved, but also the experimental techniques allowed to investigate smaller and smaller constituents of matter with higher and higher precision. This development in the field of particle physics, which tries to reveal the elementary constituents, came to its latest climax with the commissioning of the Large Hadron Collider (LHC) at the European Laboratory for Particle Physics (CERN) in Geneva, Switzerland. Over more than twenty years thousands of physicists and engineers built the largest machine ever constructed by mankind.

One important aim of the LHC is the discovery of the so-called Higgs-boson, the last missing piece in our current understanding of the world on sub-atomic scales. Still the quest will not be over, even if the Higgs-boson will be found as theoretically predicted. Many theoretical questions are still open. One of the most prominent is the combination of the sub-atomic description of our world and the theory of gravity relevant for the description of the large scale structures. Our current theory of the elementary particles – the Standard Model of Particle Physics – was proven to work extremely precise in its predictions since its formulation in the 1960's and 1970's. In general such a situation is very fortunate in science, but it also means that no or only very few experimental hints exists for theories beyond the Standard Model. Still the Standard Model is known to be incomplete and "unaesthetic" in its theoretical formulation. Even though many experiments were conducted, only two new elementary particles – the top quark in 1995 and the tau neutrino in 2000 – were discovered in the last three decades, both being predicted by the Standard Model. Only very few measurements, like the anomalous magnetic moment of the muon $(g-2)_\mu$, the existence of dark matter in the universe and in a limited way the non-vanishing neutrino masses provide experimental evidence for theories beyond the Standard Model.

One theoretically appealing and well motivated extension of the Standard Model is supersymmetry (SUSY), a symmetry between bosons and fermions, which also addresses the aforementioned experimental hints. It predicts a whole set of new elementary particles, but none of those have been observed so far, even though many attempts were made at previous experiments in high energy physics. For supersymmetry to be useful

to solve some theoretical puzzles, like the so-called hierarchy problem, the mass scale of the new particles should be within the reach of the Large Hadron Collider.

In this thesis the discovery potential of the ATLAS experiment at the LHC for a special class of supersymmetric extensions of the Standard Model is investigated. This model includes R-parity violating decays which violate the conservation of lepton number. R-parity violating SUSY models are only poorly studied by the ATLAS collaboration in contrast to R-parity conserving models. This thesis tries to close this gap for R-parity violating models where the the superpartner of the tau lepton, the stau, is the lightest supersymmetric particle (LSP). The stau is a very natural LSP candidate in R-parity violating models, while it is excluded in case of conserved R-parity.

Tau leptons are of special relevance for the measurement of the stau mass in the considered models, but also more generally for the discovery and the estimate of parameters of many supersymmetric models. Those heavier versions of electrons and muons decay rapidly, such that only their decay products can be detected in the LHC experiments. In the tau decays always one or two neutrinos are produced as well, which are invisible for the detectors. From the experimental point of view it is therefore challenging to reconstruct and identify tau leptons from their visible decay products. In this thesis a new approach, fully based on energy flow algorithms, is presented for the reconstruction of tau leptons in the ATLAS experiment. This approach, named PanTau, has conceptional advantages compared to previous algorithms, because it operates more closely to the level of physical particles, than to individual detector measurements. Its performance is evaluated in Monte Carlo simulations and its observables are validated with first data measured by the ATLAS detector in 2010.

The outline of the thesis is as follows. Chapter 1 introduces the relevant aspects of the theoretical framework of R-parity violating SUSY and the differences of models with and without R-parity conservation. In Chapter 2 an overview of the LHC and the ATLAS experiment is given. The simulation of particles in the detector and its response is essential for almost all studies of the ATLAS experiment and is discussed in Chapter 3. In this Chapter the concept of the new ATLAS fast track simulation FATRAS is explained and comparisons to first measurements of the ATLAS detector are shown. Certain experimental challenges for the reconstruction of tau leptons in ATLAS are investigated in Chapter 4, which also presents the new approach, PanTau, to tau identification. Finally Chapter 5 analyses the discovery potential of the ATLAS experiment for the considered SUSY model and the prospects for the determination of the stau mass.

Chapter 1

Theoretical Background

"Zur schlüssigen Darlegung möglicher Schadensereignisse, die eine Reaktion staatlicher Stellen erzwingen könnten, genügt es insbesondere nicht, Warnungen auf ein generelles Misstrauen gegenüber physikalischen Gesetzen, also gegenüber theoretischen Aussagen der modernen Naturwissenschaft zu stützen. Praktisch vernünftige Zweifel setzen – wenigstens – die Auseinandersetzung mit Gegenbeispielen, also Widerlegungsversuchen der jeweiligen Aussagen voraus. Namentlich im Bereich der theoretisch weit fortgeschrittenen Naturwissenschaften erfordern vernünftige Zweifel zudem ein hinreichendes fachliches Argumentationsniveau."

— 2. Kammer des Zweiten Senats des Bundesverfassungsgerichts, 18th February 2010

1.1 The Standard Model of particle physics

The so-called "Standard Model" (SM) of particle physics [1–4] is based on relativistic quantum field theory (QFT) and makes use of the gauge principle to derive interactions between elementary particles [5, 6]. Gravity, however, is not included in the theory as it is orders of magnitude weaker than the other interactions described by the Standard Model at sub-atomic scales. Only at extremely high energies far beyond the reach of collider experiments gravity is expected to become important again[1]. The Standard Model has been a story of great success and up to now almost all experimental results in the fields of atomic, nuclear and sub-nuclear physics are in perfect agreement with its predictions [8]. The observation of neutrino mixing (*cf. e.g.* [9, 10]) implicates non-vanishing neutrino masses, which are by default not included in the Standard Model, but can easily be added without conceptional difficulties in the Standard Model [6]. Except for the so-called *"Higgs-boson"*, which is needed in the Standard Model for the elementary particles to acquire masses, all of its predicted particles have been observed

[1] There are extensions of the Standard Model however, like models with extra spatial dimensions [7], that predict observable effects of gravity already at the TeV scale under certain conditions.

	families			
	1	2	3	electric charge/e
leptons	$\begin{pmatrix} \nu_e \\ e \end{pmatrix}_L$	$\begin{pmatrix} \nu_\mu \\ \mu \end{pmatrix}_L$	$\begin{pmatrix} \nu_\tau \\ \tau \end{pmatrix}_L$	0
	e_R	μ_R	τ_R	-1
quarks	$\begin{pmatrix} u \\ d \end{pmatrix}_L$	$\begin{pmatrix} c \\ s \end{pmatrix}_L$	$\begin{pmatrix} t \\ b \end{pmatrix}_L$	$2/3$
				$-1/3$
	u_R	c_R	t_R	$2/3$
	d_R	s_R	b_R	$-1/3$

Table 1.1: Fermions in the Standard Model

in experiment. The anomalous magnetic moment of the muon $(g-2)_\mu$ [11, 12] is one of the only few deviations in experimental results at the 3σ-level. Still, there are good theoretical reasons to predict effects beyond the Standard Model (BSM) around the energy scale probed by the Large Hadron Collider and the ATLAS experiment. Additionally, the need for dark matter in cosmological models can give hints for the existence of still unknown particles, that may be detectable at the LHC [13].

The following sections will give a short overview of the basics of the Standard Model and its implications for the ATLAS experiment. They will also provide a short motivation, why physical effects beyond the Standard Model can be expected in the reach of the ATLAS experiment. However, the impact of the parton content of the proton on the phenomenology of particle production in hadron collisions and related effects like the hadronisation of quarks and gluons will not be discussed here, instead the reader is referred *e.g.* to reference [14].

1.1.1 Particle content and interactions

In the Standard Model the buildings blocks of matter are spin-$\frac{1}{2}$ fermions. They are split in two categories, quarks, which take part in the strong interaction and leptons, which do not. The underlying group theoretical representation is $\mathrm{SU}(3)_C \times \mathrm{SU}(2)_L \times \mathrm{U}(1)_Y$, where $\mathrm{SU}(3)_C$ refers to the strong interaction of quarks and $\mathrm{SU}(2)_L \times \mathrm{U}(1)_Y$ to the electroweak interaction, which affects all fermions. Additionally, three families of particles exist, which are heavier "copies" of each other and mix in the quark sector[2]. Table 1.1 shows the fermion content of the Standard Model.

[2]With the introduction of neutrino masses a similar mixing occurs in the lepton sector and a mixing matrix between the neutrinos, similar to the CKM-matrix, needs to be introduced [15].

The mixing in the quark sector is described by the complex CKM-matrix, which relates the eigenstates of the weak interaction to their mass eigenstates. As one has three families of quarks, the CKM-matrix is a 3×3 unitary matrix allowing for a complex phase, which can give rise to $\mathcal{CP}$-violation, where $\mathcal{C}$ denotes charge conjugation and $\mathcal{P}$ parity inversion.

$\mathrm{SU}(3)_C$ is the symmetry of the strong interaction. Connected to it is the so-called *colour charge*, carried by the quarks. Three colours (usually denoted "red", "blue", "green") and the corresponding anti-colours exist. From the gauge principle follows the existence of eight massless bosons, the gluons, each carrying one colour and another anti-colour. The gluons are the mediators of the strong interaction. Due to the large coupling constant α_s of the strong interaction and the fact that gluons interact which each other as they carry colour charge, one observes the *confinement* of quarks at low energies, *i.e.* only colour neutral objects are observed as free particles. Though, they can behave asymptotically free at high energies [16].

The charged current weak interaction itself provides maximal parity ($\mathcal{P}$) violation and couples only to the left-handed fermions. The left-handed components $\begin{pmatrix} \nu_\ell \\ \ell \end{pmatrix}_{\mathrm{L}}$ form $\mathrm{SU}(2)_{\mathrm{L}}$ doublets, separated from the ℓ_{R} singlets (with $\ell = \mathrm{e}, \mu, \tau$). Neutrinos are assumed to be massless within the Standard Model, with two important consequences. Firstly, right-handed neutrinos are not included in the Standard Model, because they would not show any interaction with other particles, except for possible Yukawa interactions. Secondly, electroweak symmetry must be broken, because the left-handed massive leptons ℓ_{L} belong to the same doublet as the massless neutrinos.

From $\mathrm{SU}(2)_{\mathrm{L}} \times \mathrm{U}(1)_Y$ one gets four massless vector bosons by gauge invariance. Two of them mix to give the W^+ and W^- bosons. The two others form the Z^0 and the photon fields. However, $\mathrm{W}^\pm$ and Z^0 bosons are observed as massive particles of 80.4 GeV and 91.2 GeV [8], respectively, requiring a mechanism of symmetry breaking.

Renormalisability of the theory requires, however, that the electroweak symmetry is only broken spontaneously or better hidden, *i.e.* the underlying Lagrangian still obeys the symmetry and only the vacuum state breaks it. In the Standard Model the electroweak symmetry breaking is explained by the Higgs mechanism [17, 18], introducing a scalar field with non-vanishing vacuum expectation value. Particle masses are generated dynamically by interactions with the scalar field.

1.2 R-parity violating supersymmetry

In the following sections, the basic properties of supersymmetric theories are summarised which are relevant for this thesis. This summary can only provide a general sketch of supersymmetric theories in particle physics and the reader is referred to the comprehensive descriptions in the review articles [19–24] and the references therein. First a short moti-

vation is given, why supersymmetry provides a theoretically appealing extension of the Standard Model. Afterwards the minimal ingredients are described, which are needed to build a supersymmetric version of the Standard Model [25, 26]. The framework of minimal supergravity (mSUGRA) is used to make simplistic assumptions on the mechanism to break supersymmetry down to the observed properties of the Standard Model and to obtain a framework to make predictions, which can be experimentally tested at the Large Hadron Collider. In the minimal supersymmetric Standard Model (MSSM) usually the conservation of the so-called R-parity is required to make the predictions consistent with the experimentally observed long life-time of the proton [8]. However, it has been shown, that other discrete symmetries can fulfil this purpose equally well [27]. The differences in the signatures of the MSSM with and without conserved R-parity will be presented briefly. Finally, the benchmark models will be described, which have been used in this thesis to investigate the discovery potential of the ATLAS experiment for certain mSUGRA models with broken R-parity.

1.2.1 Motivation

In the Standard Model the Higgs mass suffers from large quantum corrections from loop diagrams in which every fermion contributes up to the scale where the theory is valid (*cf.* Figure 1.1a). The additional contributions from a fermion with mass m_F to the bare Higgs mass can be very large as one expects radiative corrections of the order [19]

$$\Delta m_{\mathrm{H}}^2 \propto m_F^2 + \dots \tag{1.1}$$

Even if the the new fermions do not directly couple to the Higgs, but only through interactions with other particles one still gets corrections

$$\Delta m_{\mathrm{H}}^2 \propto \mathrm{const} \cdot \lambda^2 + \mathrm{const} \cdot m_F^2 \ln(\lambda / m_F) + \dots \,, \tag{1.2}$$

when renormalising the theory, where λ is the cut off up to which the Standard Model is effectively valid [19, 20]. If the Standard Model would be valid nearly up to the Planck scale $M_{\mathrm{Pl}} = \mathcal{O}(10^{19}\,\mathrm{GeV})$, where gravity becomes significant, one would get huge corrections. On the other hand, the Higgs mass should not be larger than a few hundred GeV for the Higgs mechanism to explain electroweak symmetry breaking. The bare Higgs mass and the corrections would therefore need to be two large numbers that cancel over many digits to obtain the physical Higgs mass. This is not prohibited, but contradicts the concept of "naturalness" [28] and is known as the *hierarchy problem*.

By introducing corresponding bosonic terms for each fermionic loop (Figure 1.1b) one can achieve a cancellation between the fermion and boson loops as they turn out to have opposite sign [20]. This cancellation follows automatically, if one assumes a fundamental symmetry relating fermions and bosons. Symbolically one gets

$$Q|\mathrm{Boson}\rangle = |\mathrm{Fermion}\rangle, \;\; Q|\mathrm{Fermion}\rangle = |\mathrm{Boson}\rangle \,, \tag{1.3}$$

where the operator Q, which generates the symmetry, turns out to be an anti-commuting spinor. When requiring a relativistically invariant and analytic quantum field theory the possible algebraic relations are strongly restricted by the Coleman-Mandula theorem [29] and its extension by Haag, Lopuszanski and Sohnius [30] to obey the relations of a *supersymmetry algebra* [19]:

$$\{Q, \bar{Q}\} \propto P\,, \tag{1.4}$$
$$\{Q, Q\} = \{\bar{Q}, \bar{Q}\} = 0\,, \tag{1.5}$$
$$[Q, P] = [\bar{Q}, P] = 0\,, \tag{1.6}$$

where $[,]$ and $\{,\}$ denote the commutator and anti-commutator, respectively, and P is the four-momentum generator of spacetime translations. This theorem gives another motivation why supersymmetry is theoretically appealing, because it is the only spacetime symmetry besides Lorentz invariance, which is consistent with relativistic quantum field theory. The relevance of supersymmetry in theories, which try to unify the electroweak and the strong force, the so-called grand unified theories (GUT) [31], is underlined by the fact that the three running coupling constants in the Standard Model do not obtain the same value at a high mass scale. In a minimal supersymmetric extension of the Standard Model the running is modified such that the coupling constants get equal at a GUT scale $M_X \approx 10^{16}\,\text{GeV}$, if the mass scale of supersymmetry is around the TeV scale [32]. Furthermore local supersymmetry is strongly linked to general relativity and may therefore lead to a theory including gravity. It arises naturally in string theories [33].

Certain supersymmetric extensions of the Standard Model have other desirable properties explaining other puzzles of the Standard Model as well. For example the shape of the Higgs potential may be explained by radiative electroweak symmetry breaking, *i.e.* the negative squared Higgs mass parameter at the weak scale is generated from a positive parameter at the GUT scale. In the minimal supersymmetric extension of the Standard Model one naturally obtains a light Higgs particle in accordance with electroweak precision measurements [34, 35]. Also the aforementioned discrepancy in the anomalous magnetic moment of the muon $(g-2)_\mu$ can be explained in supersymmetric models [36]. Additionally, if lepton number is violated in the SUSY model it can provide natural mechanisms to explain the observed neutrino masses [37]. Other SUSY models predict particles, which would have been pair produced in the hot phase after the big bang and may explain the observed cold dark matter content of the universe [38, 39].

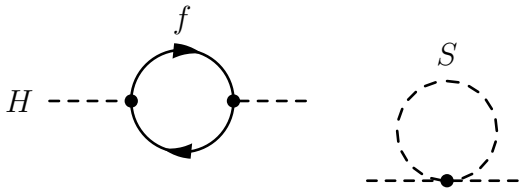

(a) Dirac fermion f **(b)** scalar S

Figure 1.1: One-loop quantum corrections to the Higgs mass

1.2.2 The MSSM

If one tries to build a supersymmetric extension of the Standard Model, one first has to incorporate the particle content of the Standard Model into the extended theory. The supersymmetric extension of the Standard Model with minimal particle content is called the minimal supersymmetric Standard Model (MSSM). In supersymmetry bosonic and fermionic states are arranged in irreducible supermultiplets, where the fermionic and bosonic states are called *superpartners* of each other. As the supersymmetry generators Q and $\bar{Q}$ commute with the generators of the gauge groups, particles in the same supermultiplet must have the same quantum numbers (electric charge, weak isospin, colour). Additionally they commute with P^2, as equation (1.6) shows, *i.e.* the masses of particles within a supermultiplet must be equal. It also follows, that the number of bosonic degrees of freedom n_B must be equal to the number of fermionic degrees of freedom n_F for each supermultiplet.

Particle Content

The first type of supermultiplets are the chiral or matter supermultiplets build from a single Weyl fermion ($n_F = 2$) and a complex scalar field ($n_B = 2$). Table 1.2a summarises the chiral supermultiplets needed to incorporate the Standard Model fermions.

The left-handed and right-handed components of quarks and leptons in the Standard Model have different gauge properties, *i.e.* each must have its own complex scalar partner. Their partners are called left- or right-handed squarks and sleptons to denote the connection to their Standard Model partners, even though they have no defined helicity.

names		spin 0	spin 1/2
sleptons, leptons	L	$(\widetilde{\nu}\ \widetilde{\mathrm{e}}_\mathrm{L})$	$(\nu\ \mathrm{e}_\mathrm{L})$
	$\bar{E}$	$\widetilde{\mathrm{e}}^*_\mathrm{R}$	$\mathrm{e}^\dagger_\mathrm{R}$
squarks, quarks	Q	$(\widetilde{\mathrm{u}}_\mathrm{L}\ \widetilde{\mathrm{d}}_\mathrm{L})$	$(\mathrm{u}_\mathrm{L}\ \mathrm{d}_\mathrm{L})$
	$\bar{U}$	$\widetilde{\mathrm{u}}^*_\mathrm{R}$	$\widetilde{\mathrm{u}}^\dagger_\mathrm{R}$
	$\bar{D}$	$\widetilde{\mathrm{d}}^*_\mathrm{R}$	$\widetilde{\mathrm{d}}^\dagger_\mathrm{R}$
Higgs, higgsinos	H_u	$(\mathrm{H}^+_\mathrm{u}\ \mathrm{H}^0_\mathrm{u})$	$(\widetilde{\mathrm{H}}^+_\mathrm{u}\ \widetilde{\mathrm{H}}^0_\mathrm{u})$
	H_d	$(\mathrm{H}^0_\mathrm{d}\ \mathrm{H}^-_\mathrm{d})$	$(\widetilde{\mathrm{H}}^0_\mathrm{d}\ \widetilde{\mathrm{H}}^-_\mathrm{d})$

(a) Chiral supermultiplets

names	spin 1/2	spin 1
gluino, gluon	$\widetilde{\mathrm{g}}$	g
winos, W bosons	$\widetilde{\mathrm{W}}^\pm\ \widetilde{\mathrm{W}}^0$	$\mathrm{W}^\pm\ \mathrm{W}^0$
bino, B boson	$\widetilde{\mathrm{B}}^0$	B^0

(b) Gauge supermultiplets

Table 1.2: Chiral and gauge supermultiplets in the MSSM. The notation has been chosen such that all spin-1/2 fields are left-handed two-component Weyl fermions and spin-0 fields are complex scalars [19].

One needs two Higgs chiral supermultiplets to give masses to the up-type quarks and to the down-type quarks, because one cannot simply add interaction terms of a single chiral supermultiplet and its conjugate to the up-type and down-type multiplets at the same time without destroying the structure of supersymmetry. Additionally a gauge anomaly would occur with only one Higgs supermultiplet due to the fermionic partner of the Higgs doublet, making the theory inconsistent [19]. This means one gets five physical Higgs particles, instead of one as in the Standard Model after electroweak symmetry breaking. Three degrees of freedom are used as longitudinal component of the W and Z bosons.

The second type of supermultiplet contains a (massless) spin-1 vector boson ($n_B = 2$) and a (massless) spin-1/2 Weyl fermion ($n_F = 2$) and is called a gauge supermultiplet. Table 1.2b summarises the gauge supermultiplets of the MSSM. The superpartners of the Standard Model bosons are denoted by adding the suffix "-ino" to the corresponding Standard Model names.

After electroweak symmetry breaking the higgsinos, bino and winos have the same quantum numbers and mix with each other[3] to form two different mass eigenstates with charge ± 1 called charginos ($\widetilde{\chi}_{\mathrm{i}}^{\pm}$, $i = 1, 2$) and four neutral mass eigenstates called neutralinos ($\widetilde{\chi}_{\mathrm{i}}^{0}$, $i = 1, \ldots, 4$).

Interactions

The interactions in the supersymmetric theory are often written down in terms of the so-called superpotential. The most general terms in the MSSM which keep the theory renormalisable and gauge invariant are the following [40]

$$
\begin{aligned}
W &= W_{\mathrm{P}_6} + W_{\Delta L=1} + W_{\Delta B=1}\,, && (1.7)\\
W_{\mathrm{P}_6} &= \epsilon_{\alpha\beta}\Big[(\mathbf{Y_E})_{ij} L_i^a H_d^b \bar{E}_j + (\mathbf{Y_D})_{ij} Q_i^{ax} H_d^b \bar{D}_{jx} \\
&\qquad + (\mathbf{Y_U})_{ij} Q_i^{ax} H_u^b \bar{U}_{jx} + \mu H_d^a H_u^b\Big]\,, && (1.8)\\
W_{\Delta L=1} &= \epsilon_{ab}\left[\frac{1}{2}\lambda_{ijk} L_i^a L_j^b \bar{E}_k + \lambda'_{ijk} L_i^a Q_j^{bx} \bar{D}_{kx}\right] + \epsilon_{ab}\kappa^i L_i^a H_u^b\,, && (1.9)\\
W_{\Delta B=1} &= \frac{1}{2}\epsilon_{xyz}\lambda''_{ijk} \bar{U}_i^x \bar{D}_j^y \bar{D}_k^z\,. && (1.10)
\end{aligned}
$$

Here $i = 1, 2, 3$ is a generation index, $x = 1, 2, 3$ is the $\mathrm{SU}(3)_C$ and $a = 1, 2$ is the $\mathrm{SU}(2)_{\mathrm{L}}$ gauge index. $\mathbf{Y_{U,D,E}}$ are 3×3 matrices of Yukawa couplings; ϵ_{ab} and ϵ_{ijk} are the totally anti-symmetric tensors. The Yukawa couplings determine the superpotential, while its structure is given by gauge invariance.

[3] If lepton number is violated by additional couplings, the higgsinos, bino and winos will also mix with the neutrinos. This can finally give masses to the neutrinos. The effect must therefore be small in order to have small neutrino masses consistent with the experimental bounds ($m_{\nu_e} < 2\,\mathrm{eV}$ [8]).

The terms in $W_{\Delta L=1}$ violate lepton number (L) and the terms in $W_{\Delta B=1}$ baryon number (B). They are proportional to the coupling constants $\lambda, \lambda', \lambda'', \kappa$ and are usually suppressed by a discrete symmetry (proton hexality, P_6) in the MSSM for the reasons summarised in Section 1.2.2. The terms that conserve the P_6 symmetry are therefore denoted W_{P_6} here. The terms proportional to λ, λ' and λ'' are trilinear couplings and always couple one SUSY sparticle to two SM particles. They are illustrated by the Feynman diagrams in Figure 1.2. The bilinear term proportional to κ^i leads to a mixing of higgsinos and neutrinos and can therefore generate neutrino masses.

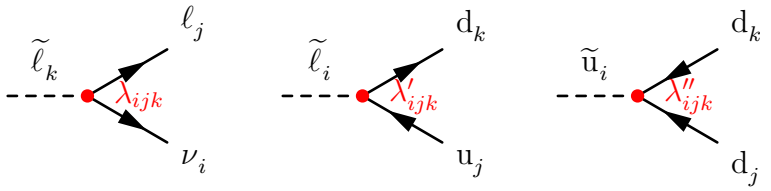

(a) λ coupling **(b)** λ' coupling **(c)** λ'' coupling

Figure 1.2: Feynman diagrams for the trilinear R-parity violating couplings

Soft supersymmetry breaking and mSUGRA

As already mentioned above, particles within the same supermultiplet must have the same masses, if supersymmetry holds. However, none of the superpartners has been observed yet, which can only be explained if they have masses above the energy scale accessible by experiments up to now. This means supersymmetry must be broken at those energy scales. The nice feature of cancellation of the divergent Higgs mass terms must be preserved in supersymmetry breaking and one therefore speaks of "soft" supersymmetry breaking.

It can be shown that the effective Lagrangian of the MSSM can be extended with terms which break supersymmetry, but contribute only logarithmically to the Higgs squared mass. However, they require at least the lightest superpartners to have masses of about 1 TeV at most, otherwise SUSY would not solve the hierarchy problem. The mechanism of supersymmetry breaking introduces the most unknowns into the MSSM, whereas the supersymmetric parts of the Lagrangian are mostly fixed by the requirement to reassemble the Standard Model. Various different models exist for supersymmetry-breaking, but only one example (minimal supergravity, mSUGRA) which is relevant for this thesis will be mentioned here.

In most cases, one simply parametrises the unknown breaking mechanism by introducing extra terms that break supersymmetry explicitly in the effective Lagrangian of

the MSSM and gives extra mass terms for the superpartners [19].

$$\begin{aligned}\mathcal{L}_{\text{soft}}^{\not{\text{P}}_6} &= -\frac{1}{2}\left(M_1\widetilde{B}\widetilde{B} + M_2\widetilde{W}\widetilde{W} + M_3\tilde{g}\tilde{g} + \text{c.c.}\right) \\ &\quad -\widetilde{\bar{U}}\mathbf{a_U}\widetilde{Q}H_u - \widetilde{\bar{D}}\mathbf{a_D}\widetilde{Q}H_d - \widetilde{\bar{E}}\mathbf{a_E}\widetilde{L}H_d + \text{c.c.} \\ &\quad -\widetilde{Q}^\dagger\mathbf{m_Q^2}\widetilde{Q} - \widetilde{L}^\dagger\mathbf{m_L^2}\widetilde{L} - \widetilde{\bar{U}}\mathbf{m_{\bar{U}}^2}\widetilde{\bar{U}}^\dagger - \widetilde{\bar{D}}\mathbf{m_{\bar{D}}^2}\widetilde{\bar{D}}^\dagger - \widetilde{\bar{E}}\mathbf{m_{\bar{E}}^2}\widetilde{\bar{E}}^\dagger \\ &\quad -m_{H_u}^2 H_u^* H_u - m_{H_d}^2 H_d^* H_d \\ &\quad -bH_uH_d + \text{c.c.} \end{aligned} \tag{1.11}$$

In total one gets the mass parameters M_1, M_2, M_3 of the bino, winos and gluinos; the parameters $\mathbf{a_U}, \mathbf{a_D}, \mathbf{a_E}$ of trilinear scalar couplings (each being a complex 3×3 matrix) and the mass squared parameters of the squarks and sleptons $\mathbf{m_Q^2}, \mathbf{m_{\bar{U}}^2}, \mathbf{m_{\bar{D}}^2}, \mathbf{m_L^2}, \mathbf{m_{\bar{E}}^2}$ (each being a 3×3 hermitian matrix) and finally the SUSY breaking contributions to the Higgs potential $(m_{H_u}^2, m_{H_d}^2, b)$. If one allows for the lepton and baryon number violating terms $W_{\Delta L=1}$ and $W_{\Delta B=1}$ in the superpotential (1.7) one also get corresponding terms $\mathcal{L}_{\text{soft}}^{\not{\text{P}}_6}$ in addition to $\mathcal{L}_{\text{soft}}^{\text{P}_6}$. Without the $\mathcal{L}_{\text{soft}}^{\not{\text{P}}_6}$ terms one gets more than 100 new free parameters in addition to the Standard Model parameters and more than 200 including these terms.

Supergravity inspired models of SUSY breaking assume a hidden sector that spontaneously breaks SUSY which is only connected with the MSSM particles through gravity. Finally this leads to the following universality assumptions of the soft SUSY breaking terms:

$$M_1 = M_2 = M_3 = M_{1/2}\,, \tag{1.12}$$

$$\mathbf{m_Q^2} = \mathbf{m_{\bar{U}}^2} = \mathbf{m_{\bar{D}}^2} = \mathbf{m_L^2} = \mathbf{m_{\bar{E}}^2} = M_0^2\mathbf{1}\,, \tag{1.13}$$

$$m_{H_u}^2 = m_{H_d}^2 = M_0^2\,, \tag{1.14}$$

$$\mathbf{a_U} = A_0\mathbf{Y_U}\,, \tag{1.15}$$

$$\mathbf{a_D} = A_0\mathbf{Y_D}\,, \tag{1.16}$$

$$\mathbf{a_E} = A_0\mathbf{Y_E}@M_{\text{GUT}}\,. \tag{1.17}$$

This simplification of the MSSM is also called minimal supergravity (mSUGRA) and leaves only the following free parameters: $M_{1/2}$ denotes the universal gaugino soft breaking mass, M_0 is the universal soft breaking scalar mass and A_0 the soft breaking universal trilinear coupling. Additionally one has as a free parameter $\tan(\beta) = \frac{v_u}{v_d}$ as the ratio of the vacuum expectation values v_u, v_d of the two Higgs doublets H_u, H_d and finally the sign of the Higgs mixing parameter $\text{sgn}(\mu)$ from equation (1.8). The assumption of diagonal mass parameters, equation (1.13), is phenomenologically appealing, because it avoids flavour changing neutral currents (FCNC). The reduction of free parameters makes the phenomenology of the theory predictable. In principle, the exact dependence of the phenomenology on the parameters is not important from the experimental point of view as long as the models in the reduced parameter space give a good representation of the signatures of all models allowed by the MSSM.

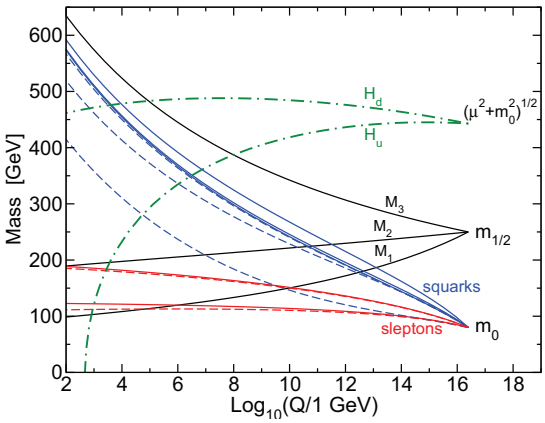

Figure 1.3: Renormalisation group evolution of sparticle masses in the MSSM with typical mSUGRA boundary conditions at the GUT scale $M_X = 2.5 \times 10^{16}\,\mathrm{GeV}$ (from [19]). mSUGRA parameters: $M_0 = 80\,\mathrm{GeV}, M_{1/2} = 250\,\mathrm{GeV}, A_0 = -500\,\mathrm{GeV}, \tan(\beta) = 10, \mathrm{sgn}\,\mu = +1$.

The mass parameters above fix the masses of the sparticles at the GUT scale $M_X \approx 10^{16}\,\mathrm{GeV}$. Using the renormalisation group equations (RGEs) of the MSSM the actual masses at the weak scale can be calculated. Figure 1.3 shows the evolution of the sparticle masses in a typical mSUGRA model. M_1 fixes the bino mass $m_{\widetilde{\mathrm{B}}^0}$ which mainly determines the mass of the lightest neutralino $\widetilde{\chi}_1^0$. In the given example in Figure 1.3 the $\widetilde{\chi}_1^0$ is the lightest supersymmetric particle (LSP). With increasing $M_{1/2}$ (or smaller M_0) one of the sleptons will be the LSP, which is mostly the scalar tau, the stau $\widetilde{\tau}_1$.

R-parity and *R*-parity violation

The terms $W_{\Delta L=1}$ and $W_{\Delta B=1}$ of the superpotential in equation (1.9) and (1.10) violate lepton and baryon number, respectively. If both lepton and baryon number violating couplings are allowed one can get processes like the one illustrated in Figure 1.4 which lead to rapid proton decay. A dimensional argument [22] gives the following estimate for the decay width of the proton

$$\Gamma(\mathrm{p} \to \mathrm{e}^+\pi^0) \approx \frac{(\lambda'_{11k})^2(\lambda''_{11k})^2}{16\pi^2\widetilde{m}_{dk}^4} m_\mathrm{p}^5\,. \tag{1.18}$$

Experimentally very strong bounds exist on the lifetime of the proton ($\tau_\mathrm{p} > 10^{32}$yr, [8]), which yield the bound [22]

$$\lambda'_{11k} \cdot \lambda''_{11k} \lesssim 2 \cdot 10^{-27} \left(\frac{\widetilde{m}_{dk}}{100\,\mathrm{GeV}}\right)^2\,. \tag{1.19}$$

Such a strong bound can only be explained naturally, if at least one of the couplings is fixed to zero. This can be achieved by a new discrete symmetry. Usually one introduces R-parity (R_p) as

$$R_p = (-1)^{3(B-L)+2s}\,, \tag{1.20}$$

where B denotes baryon number, L lepton number and s the spin of a particle [19]. For the MSSM all SM particles have $R_p = +1$ and their superpartners $R_p = -1$. Requiring R_p to be conserved, effectively suppresses all couplings which violate baryon or lepton number in the superpotential and one is left with the term W_{P_6} in equation (1.7).

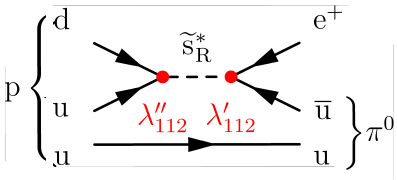

Figure 1.4: Example of a Feynman diagram for a possible process leading to proton decay ($p \to e^+\pi^0$), if both λ' ($\Delta L = 1$) and λ'' ($\Delta B = 1$) couplings are allowed.

R_p conservation has various implications on the phenomenology of the MSSM at collider experiments. SUSY particles can only be produced in pairs, because all initial states have $R_p = +1$. Additionally the lightest supersymmetric particle (LSP) has to be stable, because there is no lighter $R_p = -1$ state it could decay into. A stable LSP has some cosmological implications, because it would have been produced in pairs in thermal equilibrium during the hot phase of the big bang. Using cosmological models and assuming an annihilation cross section of the LSP one can calculate the relic density of the LSP one would expect today. It turns out, that this relic density can be quite high and therefore the LSP has to be neutral, because otherwise it would have been detected already [19]. In mSUGRA models usually only the lightest neutralino ($\widetilde{\chi}^0_1$) fulfils this requirement as an LSP. At the same time the stable $\widetilde{\chi}^0_1$ LSP can be a very promising dark matter candidate [13, 39].

For collider experiments a stable and neutral LSP means, that one always expects an LSP at the end of the decay chain of SUSY particles which escapes detection. In fact, one expects two LSPs per event, because the SUSY particles are produced in pairs. An important signature for all SUSY searches with conserved R_p at collider experiments is therefore a significant amount of missing transverse energy ($E_{\mathrm{T}}^{\mathrm{miss}}$) due to the two undetected LSPs. In case of conserved R-parity large regions of the mSUGRA parameter space are excluded, because they predict the superpartner of the tau lepton, the so-called stau $\widetilde{\tau}^{\pm}_1$, as lightest supersymmetric particle (Figure 1.5). This parameter space is re-opened in models with R-parity violation, if the $\widetilde{\tau}_1$ LSP is unstable at least on cosmological time scales.

In fact, R-parity alone does not suppress certain dimension-five operators, which may lead to proton decay, but instead a discrete symmetry named proton hexality (P_6) can be applied [27] which is derived from a gauge symmetry of a potential grand unified theory embedding the MSSM. However, other discrete symmetries exist as well, which avoid a rapid proton decay, but violate R-parity [40]. It was shown, that only baryon triality, B_3, which prohibits the λ'' couplings and lepton parity, which prohibits the λ and λ' couplings in equation (1.7), provide theoretically acceptable solutions. Baryon triality is anomaly-free in contrast to lepton parity, which makes it theoretically more appealing than the latter. This thesis concentrates on certain R-parity violating (RPV) models with conserved baryon triality, *i.e.* including lepton number violating couplings.

Various low-energy measurements constrain the lepton number violating couplings, like the anomalous magnetic moment $(g-2)_\mu$ of the muon and rare decays like $\mathrm{b} \to \mathrm{s}\gamma$

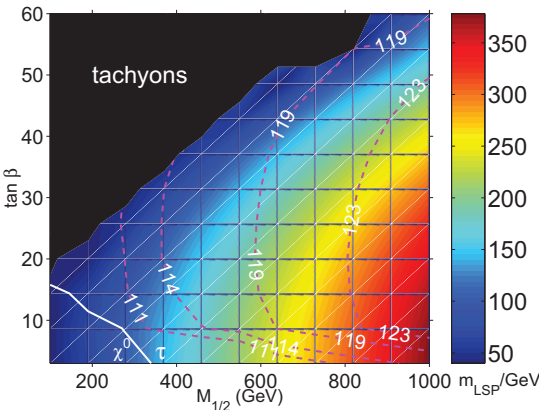

Figure 1.5: Mass and nature of the lightest supersymmetric particle in no-scale mSUGRA ($M_0 = A_0 = 0\,\text{GeV}$) versus $M_{1/2}$ and $\tan(\beta)$ in the R-parity conserving limit (from [40]). The dashed lines show contours of the mass of the lightest Higgs boson. The region with $\widetilde{\chi}_1^0$ LSP is excluded in no-scale mSUGRA, because of the Higgs mass bound determined at LEP[41, 42].

and $B_s^0 \to \mu\mu$ [40, 43]. Additional constrains can be derived from upper bounds on the sum of the neutrino masses and the absence of tachyons in the model [40, 44].

If the $\not{R}_p$ couplings are small, they have only minor influence on the production of SUSY particles at collider experiments and their decays[4]. Only the decay of the lightest supersymmetric particle is dominated by the $\not{R}_p$ coupling, because the other Yukawa couplings (W_{P_6} terms in equation (1.8)) cannot directly contribute to its decay. Especially the mass spectrum of the SUSY particles is only significantly changed compared to the corresponding R_p conserving case, if the the $\not{R}_p$ coupling gets as large as the gauge couplings. Hence, the mass spectrum can usually be calculated in the R_p conserving limit. However, in certain cases the nature of the LSP can change with increasing R_p coupling, because the masses of some SUSY particles at the low end of the mass spectrum are reduced [46].

In case of extremely small $\not{R}_p$ couplings the LSP can be meta-stable and obtain lifetimes which are large enough, that the LSP in collider experiments decays away from its production vertex or even escapes the detector without decay. Depending on the exact model parameters one can observe displaced decay vertices or even strange effects like late decays of stopped LSPs or highly ionising particle tracks of massive, charged LSPs [47]. In the following we do not consider such special signatures, but concentrate on $\not{R}_p$ models, which have prompt decays of the LSP, *i.e.* decays directly in the vicinity of the production vertex. In these models the LSP cannot be a candidate to explain dark matter. However, extensions of the MSSM exist in which the axino [48–50] or the lightest U-parity particle [51, 52] are viable dark matter candidates. Furthermore gravitino dark matter has been studied as well *e.g.* in case of bilinear RPV [53–55]. Therefore, the existence of dark matter is not an argument against R-parity violation.

1.2.3 RPV mSUGRA with stau-LSP

As discussed in the previous sections supersymmetry is a theoretically promising extension of the Standard Model and already for many years various experiments are searching

[4] In some special cases also resonant single sparticle production is possible [45], but such scenarios will not be discussed here.

for its signatures. Already the minimal supersymmetric extension of the Standard Model includes an overwhelming number of free model parameters and simplistic models including well motivated assumptions like mSUGRA are usually studied in terms of their phenomenology. However, most of those studies assume conserved R-parity with a stable and neutral lightest supersymmetric particle. This restriction yields special signatures in collider experiments and includes the risk to miss the discovery of supersymmetric particles, because of prejudiced search strategies. Figure 1.5 already showed that large regions of the parameter space of mSUGRA is excluded in the case of R-parity conservation, because one gets a charged LSP. Regions with charged LSP can get phenomenologically valid again, if R-parity violation is considered.

In recent years models which violate R-parity gained increasing attention, see *e.g.* [55–58] and references therein. Reference [43] proposed a set of example models in the framework of mSUGRA with $\not{R}_p$. In three of these models the scalar tau ($\widetilde{\tau}$) is the lightest supersymmetric particle. Their relevant properties are summarised in this section. Details on the existing bounds, which have been considered and lead to the choice of the scenarios, can be found in the referenced paper. In all of the benchmark scenarios only a single non-vanishing R-parity violating coupling is assumed at the GUT scale. This is a reasonable assumption, because the experimental bounds on products of $\not{R}_p$ couplings are much stronger than the bounds on only a single coupling [24]. Note, that additional $\not{R}_p$ couplings at the weak scale are generated by the renormalisation group equations from the single coupling at the GUT scale. The generated couplings are taken into account in the branching ratios of sparticle decays given in reference [43] and in the related Monte Carlo simulations.

	BC 1	BC 2	BC 3	BC 4
Coupling ($@M_{\mathrm{GUT}}$)	$\lambda_{121} = 0.032$	$\lambda'_{311} = 3.5 \times 10^{-7}$	$\lambda'_{331} = 0.122$	$\lambda''_{212} = 0.5$
Coupling ($@M_{\mathrm{EW}}$)	0.048	1.1×10^{-6}	0.344	
LSP and main decay mode	$\widetilde{\tau}_1^{\pm} \to \tau^{\pm}\, \ell^+\, \ell^-\, \nu$	$\widetilde{\tau}_1 \to \mathrm{ud}$	$\widetilde{\nu}_\tau \to \mathrm{bd}$	$\widetilde{\tau}_1 \to \mathrm{cds}\tau$
M_0/GeV	0	0	100	0
$M_{1/2}$/GeV	400	400	250	600
$\tan\beta$	13	13	10	30
A_0/GeV	0	0	-100	0

Table 1.3: The main parameters of the B_3 mSUGRA benchmark points from reference [43].

The main parameters of the four benchmark scenarios are summarised in Table 1.3. BC 1 with a $\widetilde{\tau}$ LSP is the scenario which is mainly investigated here. The BC 2 scenario has identical parameters, but another $\not{R}_p$ coupling, therefore leading to a different LSP decay and final state. Here the $\not{R}_p$ coupling is relatively small, such that the LSP decay vertices may be displaced with respect to the production vertex. In BC 3 the sneutrino

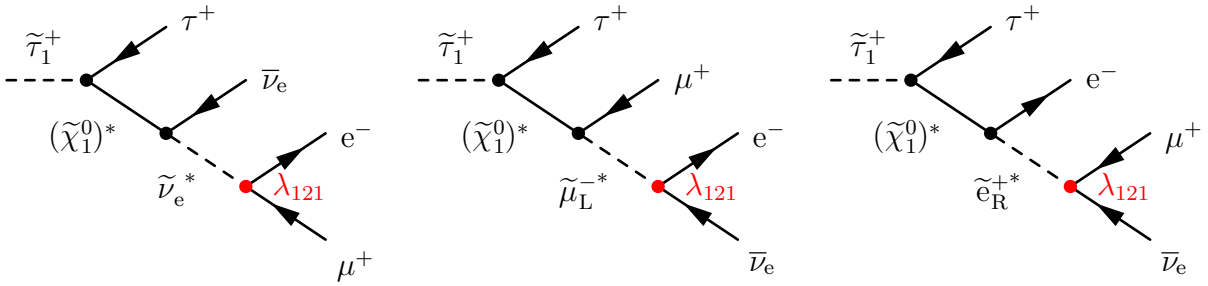

Figure 1.6: Feynman diagrams for the R-parity violating decay in the BC 1 scenario contributing to the decay $\widetilde{\tau}_1^+ \to \tau^+ \mu^+ e^- \overline{\nu}_e$.

$\widetilde{\nu}_\tau$ is the lightest supersymmetric particle. It is therefore not considered here. BC 4 on the other hand has a $\widetilde{\tau}$ LSP, which decays into light quarks and a tau lepton by means of a baryon number violating operator. Additionally the SUSY particle spectrum is heavier here making it much more difficult for early discoveries at the LHC.

BC 1 and BC 2 are especially interesting to compare. While they only differ in the $\not{R}_p$ coupling, they still cover two extreme cases in the phenomenology of R-parity violating mSUGRA with a $\widetilde{\tau}$ LSP. In BC 2 the LSP couples directly to quarks of the first generation by $\lambda'_{311} L_3 Q_1 \bar{D}_1$, which leads to the two-body decay $\widetilde{\tau}_1 \to ud$, *cf.* Figure 1.2b. In contrast, the $\widetilde{\tau}$ LSP cannot directly couple to Standard Model particles in BC 1. The $\lambda_{121} L_1 L_2 \bar{E}_1$ coupling requires (virtual) sparticles of the first or second generation in between. One therefore obtains the four-body decay $\widetilde{\tau}_1^\pm \to \tau^\pm \ell^+ \ell^- \nu$, where $\ell^\pm = e^\pm, \mu^\pm$. The (tree-level) Feynman diagrams contributing to the decay $\widetilde{\tau}_1^+ \to \tau^+ \mu^+ e^- \overline{\nu}_e$ *e.g.* are shown in Figure 1.6. The $\widetilde{\tau}_1$ decays into a tau lepton and a virtual neutralino[5] ($\widetilde{\chi}^0$), which itself converts into a (charged or neutral) lepton and a slepton. The slepton of the first or second family decays into a pair of leptons by the $\not{R}_p$ coupling. Reference [45] discusses in detail, when four-body decays dominate over two-body decays in scenarios with a $\widetilde{\tau}$ LSP and which additional $\not{R}_p$ couplings are generated by the renormalisation group equations at the weak scale, if only one non-vanishing $\not{R}_p$ coupling is assumed at the GUT scale.

In both scenarios the couplings are such that the sparticles are produced in pairs and cascade decay to the LSP. One can therefore assume the following process at the LHC,

$$\begin{array}{l} qq/gg \to \widetilde{q}\widetilde{q} \to j\widetilde{\chi}_1^0 j\widetilde{\chi}_1^0 \\ \qquad\qquad\quad \big\lfloor\!\!\longrightarrow \widetilde{\tau}_1\tau \end{array} \tag{1.21}$$

where $\widetilde{q}$ is a squark, and j denotes a jet. Note that gluino ($\widetilde{g}$) pair production instead of squark pair production will usually give two additional jets, *e.g.* via the decay $\widetilde{g} \to j\widetilde{q}$.

[5] In principle every $\widetilde{\chi}^0$ can occur as a virtual particle, but due its mass mainly the $\widetilde{\chi}_1^0$ is exchanged. Also decays with charginos are possible, but they are suppressed by their mass and due to the fact, that they are wino-like in BC 1, whereas the $\widetilde{\chi}_1^0$ is bino-like and couples therefore much stronger to the $\widetilde{\tau}_1$, which is mainly right-handed [59].

Table 1.4 summarises the $\widetilde{\tau}_1$ decays and the resulting signatures at the LHC for the different R-parity violating couplings. Only one $\not{R}_p$ coupling is assumed at a time, which is a reasonable assumption as the bounds for products of couplings are even stronger than for single $\not{R}_p$ couplings [24].

From the table one can see, that BC 1 and BC 2 are two extreme cases in the expected final states at the LHC. BC 1 with its λ_{121} coupling represents the multi-lepton signature, whereas BC 2 (λ'_{311}) is the multi-jet extreme of the lepton number violating couplings. In

coupling	$\widetilde{\tau}_1^+$ decay	LHC signature
$\lambda_{121} = -\lambda_{211}$	$\tau^+\mu^+\mathrm{e}^-\overline{\nu}_\mathrm{e}$	
	$\tau^+\mu^-\mathrm{e}^+\nu_\mathrm{e}$	
	$\tau^+\mathrm{e}^+\mathrm{e}^-\overline{\nu}_\mu$	
	$\tau^+\mathrm{e}^-\mathrm{e}^+\nu_\mu$	$2j + 4\tau + 4\ell + E_\mathrm{T}^\mathrm{miss}$
$\lambda_{122} = -\lambda_{212}$	$\tau^+\mu^+\mu^-\overline{\nu}_\mathrm{e}$	with $\ell = \mathrm{e}, \mu$
	$\tau^+\mu^-\mu^+\nu_\mathrm{e}$	
	$\tau^+\mathrm{e}^+\mu^-\overline{\nu}_\mu$	
	$\tau^+\mathrm{e}^-\mu^+\nu_\mu$	
$\lambda_{131} = -\lambda_{311}$	$\mathrm{e}^+\nu_\mathrm{e}$	
$\lambda_{132} = -\lambda_{312}$	$\mu^+\nu_\mathrm{e}$	
$\lambda_{231} = -\lambda_{321}$	$\mathrm{e}^+\nu_\mu$	$2j + 2\tau + 2\ell + E_\mathrm{T}^\mathrm{miss}$
$\lambda_{232} = -\lambda_{322}$	$\mu^+\nu_\mu$	
$\lambda_{123} = -\lambda_{213}$	$\mu^+\overline{\nu}_\mathrm{e}$	
	$\mathrm{e}^+\overline{\nu}_\mu$	
$\lambda_{133} = -\lambda_{313}$	$\mathrm{e}^+\overline{\nu}_\tau$	
	$\tau^+\overline{\nu}_\mathrm{e}$	$2j + 2\tau + 2\ell + E_\mathrm{T}^\mathrm{miss}$
	$\tau^+\nu_\mathrm{e}$	$2j + 3\tau + 1\ell + E_\mathrm{T}^\mathrm{miss}$
$\lambda_{233} = -\lambda_{323}$	$\mu^+\overline{\nu}_\tau$	$2j + 4\tau + E_\mathrm{T}^\mathrm{miss}$
	$\tau^+\overline{\nu}_\mu$	
	$\tau^+\nu_\mu$	

(a) $L_iL_j\bar{E}_k$ operator

coupling	$\widetilde{\tau}_1^+$ decay	LHC signature
λ'_{1jk}	$\tau^+\overline{\mathrm{u}}_j\mathrm{d}_k\mathrm{e}^+$	
	$\tau^+\mathrm{u}_j\overline{\mathrm{d}}_k\mathrm{e}^-$	
	$\tau^+\overline{\mathrm{d}}_j\mathrm{d}_k\overline{\nu}_\mathrm{e}$	$6j + 4\tau + \ell\ell$
	$\tau^+\mathrm{d}_j\overline{\mathrm{d}}_k\nu_\mathrm{e}$	$6j + 4\tau + \ell + E_\mathrm{T}^\mathrm{miss}$
λ'_{2jk}	$\tau^+\overline{\mathrm{u}}_j\mathrm{d}_k\mu^+$	$6j + 4\tau + E_\mathrm{T}^\mathrm{miss}$
	$\tau^+\mathrm{u}_j\overline{\mathrm{d}}_k\mu^-$	
	$\tau^+\overline{\mathrm{d}}_j\mathrm{d}_k\overline{\nu}_\mu$	
	$\tau^+\mathrm{d}_j\overline{\mathrm{d}}_k\nu_\mu$	
λ'_{3jk}	$\mathrm{u}_j\overline{\mathrm{d}}_k$	$6j + 2\tau$

(b) $L_iQ_j\bar{D}_k$ operator

coupling	$\widetilde{\tau}_1^+$ decay	LHC signature
λ''_{ijk}	$\tau^+\mathrm{u}_i\mathrm{d}_j\mathrm{d}_k$	$8j + 2\tau$
	$\tau^+\overline{\mathrm{u}}_i\overline{\mathrm{d}}_j\overline{\mathrm{d}}_k$	

(c) $\bar{U}_i\bar{D}_j\bar{D}_k$ operator

Table 1.4: Signatures and decays of scenarios with a $\widetilde{\tau}_1$ LSP assuming one non-vanishing $\not{R}_p$ operator (published in [59]). The SUSY cascade $qq/\mathrm{gg} \to \widetilde{q}\widetilde{q} \to j\widetilde{\chi}_1^0 j\widetilde{\chi}_1^0 \to jj\tau\widetilde{\tau}_1\tau\widetilde{\tau}_1$ has been assumed in the LHC signatures. Note that gluino ($\widetilde{\mathrm{g}}$) pair production instead of squark pair production will usually give two additional jets, *e.g.* via the decay $\widetilde{\mathrm{g}} \to j\widetilde{q}$.

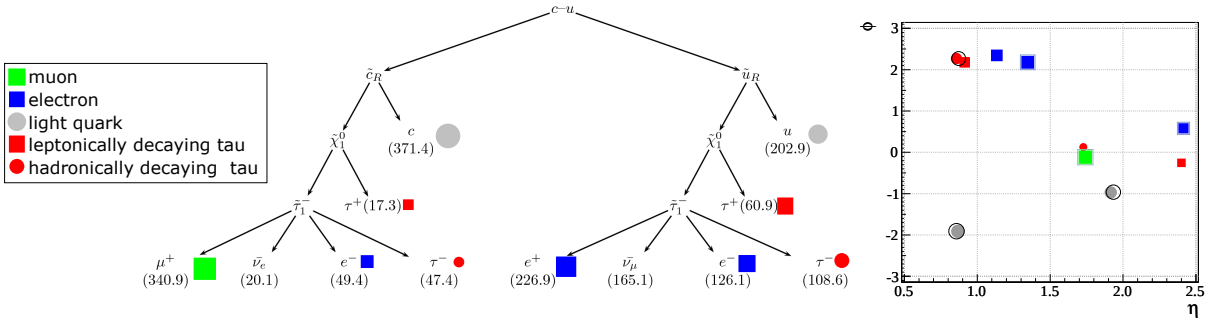

(a) SUSY cascade **(b)** Particles in η-ϕ plane

Figure 1.7: Example event of the BC 1 scenario at the LHC. (a) Graph of the SUSY cascade. The numbers in parentheses denote the transverse energy in GeV. For the τ leptons only their visible decay products are included. (b) Visualisation of the particles in the η-ϕ plane. The solid markers denote the Monte Carlo truth particles, where their size corresponds to the transverse energy. Open symbols visualise the reconstructed particles in fast detector simulation.

the list of signatures one distinguishes electrons and muons ($\ell = \mathrm{e}, \mu$) from tau leptons, which are much more difficult to identify experimentally than electrons and muons. Note, that a fraction of BC 2 events also has a di-lepton signature with two electrons or muons, due to leptonic tau decays of the tau from the $\widetilde{\chi}_1^0$ decay.

Note also the asymmetry in the number of electrons and muons between $\widetilde{\tau}_1$ decay modes in the λ_{121} versus the λ_{122} coupling, due to the flavour indices in the superpotential. The missing transverse energy $E_{\mathrm{T}}^{\mathrm{miss}}$ refers to neutrinos in the $\widetilde{\tau}_1$ decay, but additional $E_{\mathrm{T}}^{\mathrm{miss}}$ contributions can come from the τ lepton decays.

Figure 1.7 illustrates a typical BC 1 event at the LHC. Two squarks are pair produced here and each of them cascades via the $\widetilde{\chi}_1^0$ to the $\widetilde{\tau}_1$ LSP. The sketch of the η-ϕ-plane[6] (Figure 1.7b) shows the angular distribution in which the particles are emitted in this specific event. A pair of squarks is produced in the collision event, where each of them produces a jet from a light quark and a $\widetilde{\chi}_1^0$. Both neutralinos decay into a tau lepton and the $\widetilde{\tau}_1$ LSP. In this example one of the LSPs decays into an electron and a high momentum muon, the second into two high momentum electrons in addition to the tau lepton and the neutrino. The tau lepton from the $\widetilde{\chi}_1^0$ decay can be relatively soft, whereas the tau leptons from the $\widetilde{\tau}_1$ decays are usually harder. One can already see from this example that the leptons can be very collimated, which can make it difficult to identify them individually in the experiment. The kinematic properties of the particles in BC 1 events will be discussed in Chapter 5 in detail.

[6] In polar coordinates one measures the azimuthal angle ϕ in the transverse plane around the beam axis and the polar angle θ from the beam axis. The pseudo-rapidity η is defined as $\eta \equiv -\ln\tan(\theta/2)$, *cf.* Section 2.2.

Chapter 2

The ATLAS detector at the Large Hadron Collider

"Experiment is the sole source of truth. It alone can teach us something new; it alone can give us certainty."
— Henri Poincaré, "Science and Hypothesis", 1905

The experimental setup of this study is the ATLAS (A Toroidal LHC ApparatuS) detector at the Large Hadron Collider (LHC). Here, protons collide with each other at energies never reached before in collider experiments. This allows us to explore and to test the Standard Model of particle physics in new energy regimes. The LHC is therefore often called a "discovery machine", because its aim is to find the still missing Higgs boson of the Standard Model and signals of physics beyond the Standard Model (BSM). This Chapter will give a short overview of the LHC project and especially the ATLAS experiment. Detailed information about the LHC and its experiments can be found in the references [60–66]. The specifications of the LHC and the ATLAS experiment summarised in this Chapter were taken from reference [60] and [62, 67], respectively.

2.1 The Large Hadron Collider

The Large Hadron Collider (LHC) is the latest accelerator complex of the European Organization for Nuclear Research (CERN) located near Geneva, Switzerland. It has been installed between 2003 and 2008 into the tunnel of the former Large Electron Positron Collider (LEP), which constrained its circumference to be 26.7 km. First drafts even proposed to build the LHC beam pipe on top the LEP beam lines within the same tunnel [68].

In contrast to LEP the LHC accelerates protons instead of electrons and positrons. They produce much less synchrotron radiation due to their higher mass when being deflected in magnetic fields to be kept on their path through the accelerator. This allows us to accelerate protons to much higher energies than electrons while keeping the

radius of the accelerator ring constant. The main limitation of the energy per proton beam at the LHC is the bending power of its magnets, *i.e.* the strength of the magnetic field which can be achieved. Using superconducting magnets the LHC was designed to reach an energy of 7 TeV per beam corresponding to a dipole field of 8.3 T. Two beams of counter-rotating proton bunches are brought to collision at four interaction points providing a centre-of-mass energy of the collisions of $\sqrt{s} = 14\,\text{TeV}$ at design energy. However, the LHC is currently operated at a beam energy of 3.5 TeV. The design energy can only be reached after a longer maintenance period of 1–2 years as the magnets are not yet ready for the electric currents needed. It was planned to operate at a beam energy of 5 TeV in the first years, but after a severe incident in 2008 [69, 70] it was decided to keep the beam energy at 3.5 TeV at least until the end of 2011. Beam energies higher than about 4 TeV can only be achieved after the replacement of electrical connections between the superconducting magnets and the installation of further machine protection systems.

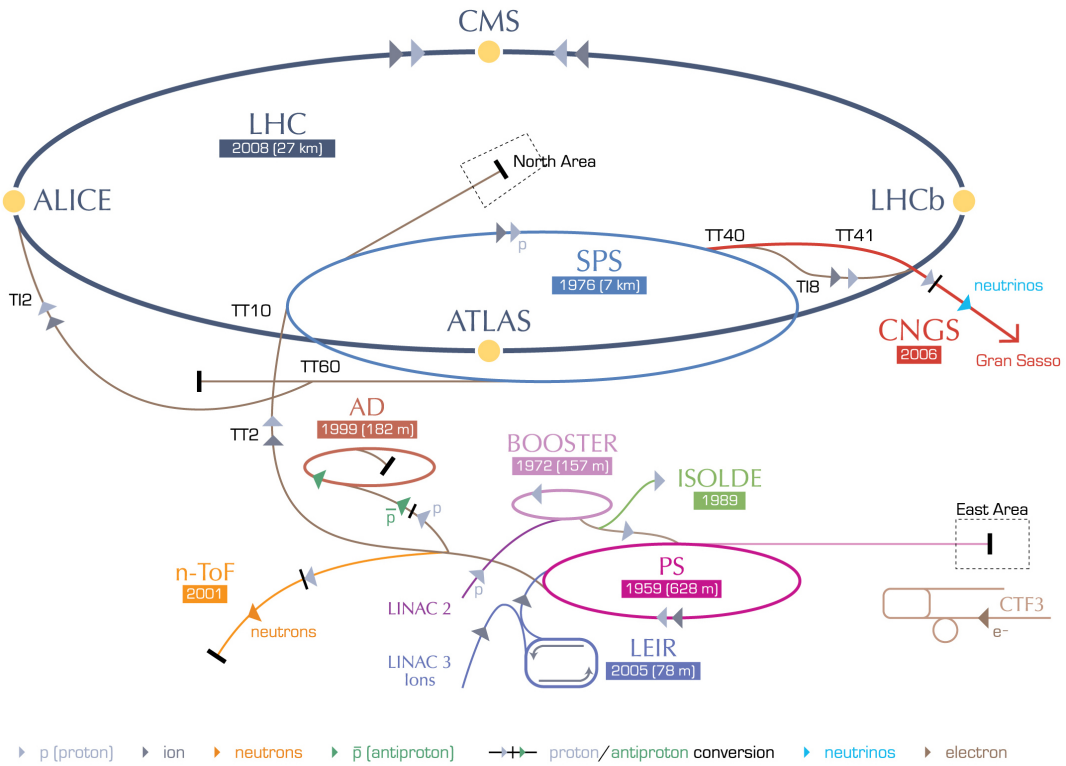

Figure 2.1: CERN accelerator complex. Protons are extracted from hydrogen gas and accelerated to an energy of 50 MeV in the LINAC 2 linear accelerator and to 1.4 GeV in the PS Booster. The Proton Synchrotron (PS) increases their energy to 25 GeV and stores bunches, *i.e.* spatially separated packets, of protons. The bunches are further accumulated in the Super Proton Synchrotron (SPS) and accelerated to 450 GeV before finally being injected into the Large Hadron Collider (LHC) by two transfer lines in opposite directions. Lead ions can be accelerated in the Low Energy Ion Ring (LEIR) before being transferred to the PS. Further experimental infrastructures can make use of the PS and SPS chain (image source: CERN-DI-0812015).

Figure 2.1 illustrates the CERN accelerator complex and shortly describes the different stages of energy until the proton bunches are injected into the LHC at an energy of 450 GeV. The staged process is not only needed to reach the final energy, but also to accumulate proton bunches. Up to 2808 bunches with about 1.1×10^{11} protons each will be stored in the LHC to reach the design luminosity of $\mathcal{L} = 10^{34}\,\mathrm{cm}^{-2}\,\mathrm{s}^{-1}$. In a simplified form, the *instantaneous luminosity* $\mathcal{L}$ can be written as [60]

$$\mathcal{L} = f\frac{n_1 n_2}{4\pi\sigma_x\sigma_y}\,, \tag{2.1}$$

where f is the frequency of head-on collisions of bunches with n_1 and n_2 protons and σ_x, σ_y the widths of the transverse bunch profiles[1].

The high luminosity increases the demands for the trigger systems of the experiments to be very restrictive. With a time of 25 ns between two bunch crossings the particles from consecutive bunch crossings will even traverse the ATLAS detector at the same time, *i.e.* new collisions take place, while particles from previous bunch crossing have not reached the outer parts of the detector, yet, even though they are travelling (nearly) at the speed of light. 25 proton-proton interactions will take place on average each bunch crossing at the design luminosity, causing *in-time pile-up*, *i.e.* interesting, but rare interactions are overlaid by a certain number of additional interactions with higher cross sections. The pile-up events usually have low momentum transfer, but still create additional tracks and energy deposits in the calorimeter, which have to be taken into account. Another kind of pile-up "noise" is created by particles like neutrons, that are created in previous bunch crossings and create a "bath" of particles in the cavern of the experiment.

In addition to the operation with protons the LHC is also capable to accelerate lead ions to an energy per nucleon of up to 2.76 $^{\mathrm{TeV}}/_{\mathrm{u}}$. Lead-lead collisions can create very high energy densities and are intended to study QCD effects at high temperature and the predicted quark-gluon-plasma. The ALICE experiment was especially designed for this purpose, but also the ATLAS experiment could provide new measurements during the first lead-lead collisions in the LHC [71]. For the present thesis, lead-lead collisions are of minor relevance and will not be discussed further.

2.2 The ATLAS Experiment

The ATLAS experiment was designed as a multi-purpose detector which allows to explore a broad physics program in proton-proton collision as well as in heavy ion collisions [62, 67, 72, 73]. Herewith it is very similar to the Compact Muon Solenoid detector (CMS), the second big experiment at the LHC. The general design is in the tradition of

[1] The LHC is operated with a small beam crossing angle of $\theta_c \leq 100\,\mu\mathrm{rad}$ to avoid unwanted "parasitic" collision points along the path, where the two beams share a common beam pipe. This modifies equation (2.1) and reduces the luminosity due to geometrical effects by about 15 % [8].

the previous large collider experiments at LEP or the Tevatron, though some components include very innovative techniques.

Its design is guided by the following requirements needed to identify interactions with interesting processes by their final state particles. Leptons – electrons, muons and in a limited fashion also taus – need to be identified according to their type and their four-momenta need to be reconstructed. Particle jets created by the hadronisation of quarks and gluons have to be reconstructed as well. Furthermore jets from b-quarks should be distinguished from jets induced by light quarks. Finally one likes to measure the missing transverse energy $E_{\mathrm{T}}^{\mathrm{miss}}$ to obtain information about weakly interacting particles like neutrinos, which escape detection. The latter is possible, because the initial colliding particles have no or only very small transverse momenta and the conservation of momentum can be used to constrain the (transverse) sum of the momenta of all outgoing particles. No detection method is able to fulfill all demands at once. Therefore, different techniques are combined to obtain a full picture of the created particles.

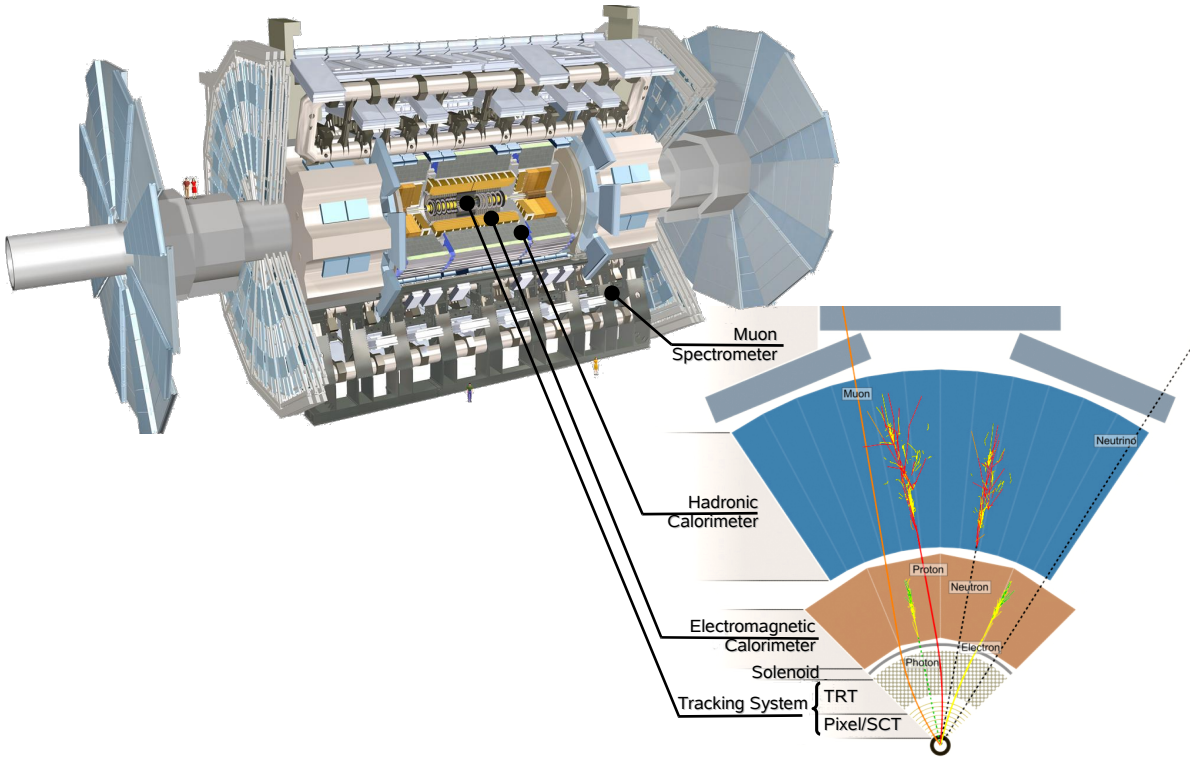

Figure 2.2: 3-dimensional view of the ATLAS detector (above) and sketch of one slice of the detector in the transverse plane visualising the functions of the detector components (below). Different types of particles (from left to right: muon, photon, proton as charged hadron, neutron as neutral hadron, electron and neutrino) produce signals in different sub-detectors allowing for particle identification.

The sub-detectors are arranged cylindrically around the interaction region, *cf.* Figure 2.2. Proton beams from both directions travel through the same beam pipe at the location of the experiment. The innermost part of ATLAS is a tracking system, the

Inner Detector, embedded in a 2 T solenoidal magnetic field used to measure the momenta of charged particles. With the known magnetic field the momenta can be derived from the bending of the particle tracks. Additionally a high spatial resolution allows us to distinguish particles from different interaction points and to reconstruct secondary particles with displaced decay points. In this way decays of particles with a lifetime down to about 10^{-13} s can be distinguished from the primary interaction as it is needed for the identification of b- and τ-jets.

The tracking system is not sensitive to neutral particles[2] and further sub-detectors are needed to measure those. In ATLAS the solenoid is surrounded by the calorimeter system. In the first part, the electromagnetic calorimeter, (mainly) electrons and photons interact with the detector material and create showers of secondary electrons and photons until the energy of the primary particle is fully absorbed. Hadrons can undergo hadronic interactions, but are usually only stopped in the hadronic calorimeter surrounding the electromagnetic calorimeter. Together both systems are designed to be hermetic, *i.e.* all particles despite muons and weakly interacting particles like neutrinos should be stopped inside the calorimeter volume and their energy be measured.

In principle, the Inner Detector and the calorimeter system would be sufficient to reconstruct the created particles. However, one can make use of the fact that muons traverse the calorimeters as minimum ionising particles (MIP) and do not get stopped there. Another tracking system, the Muon Spectrometer, surrounds the calorimeters and allows to measure the momenta of muons in a toroidal magnetic field. Muons can therefore be identified very reliable and their momenta be measured with very high precision. As muons are usually the only detectable particles reaching the Muon Spectrometer only very low detector occupancies are found there. Additionally muons are often signs of interesting processes and the Muon Spectrometer is therefore an ideal trigger system.

Table 2.1 summarises the performance goals of the ATLAS detector for its main components.

Coordinate system and related measures

ATLAS uses a Cartesian coordinate system with origin at the nominal interaction point. The z-axis is defined by the beam direction, the x-axis points towards the centre of the LHC ring and the y-axis upwards. In polar coordinates one measures the azimuthal angle ϕ in the transverse plane around the beam axis and the polar angle θ from the beam axis. The interacting partons within the protons carry only a fraction of the total proton momentum, therefore the rest frame of the hard interaction between the partons is not identical to the lab frame, but generally boosted along (or against) the z-axis. One can show that differences in the rapidity $y = \frac{1}{2} \ln \left(\frac{E+p_z}{E-p_z} \right)$ and the shape of

[2] In principle, hadronic interactions of neutral hadrons or conversions of photons in the Inner Detector material can be used to measure those particles, but both effects are not intended and regarded as negative detector effects.

detector	required resolution	η coverage	
		measurements	trigger
tracking	$\sigma_{p_\mathrm{T}}/p_\mathrm{T} = 0.05\,\% p_\mathrm{T}/\mathrm{GeV} \oplus 1\,\%$	± 2.5	
EM calorimetry	$\sigma_E/E = \frac{10\,\%}{\sqrt{E/\mathrm{GeV}}} \oplus 0.7\,\%$	± 3.2	± 2.5
Hadronic calorimetry			
barrel, end-cap	$\sigma_E/E = \frac{50\,\%}{\sqrt{E/\mathrm{GeV}}} \oplus 3\,\%$	± 3.2	± 3.2
forward	$\sigma_E/E = \frac{100\,\%}{\sqrt{E/\mathrm{GeV}}} \oplus 10\,\%$	$3.1 < \lvert\eta\rvert < 4.9$	$3.1 < \lvert\eta\rvert < 4.9$
Muon Spectrometer	$\sigma_{p_\mathrm{T}}/p_\mathrm{T} = 10\,\%$ at $p_\mathrm{T} = 1\,\mathrm{TeV}$	± 2.7	± 2.4

Table 2.1: Performance goals of the ATLAS detector [62]. $\oplus$ denotes addition in quadrature.

distributions dN/dy are invariant under such boosts. It is therefore useful to define the pseudo-rapidity η as

$$\eta \equiv -\ln\tan(\theta/2) \tag{2.2}$$

which approximates the rapidity y for $|\vec{p}| \gg m$. This means $\eta = 0$ corresponds to directions perpendicular to the beam axis and $\eta \to \pm\infty$ to the beam directions. Angular distances are usually expressed in terms of

$$\Delta R \equiv \sqrt{(\Delta\eta)^2 + (\Delta\phi)^2}. \tag{2.3}$$

Transverse quantities like the transverse momentum p_T and the transverse energy E_T are defined in the x-y-plane.

The detector components are distinguished according to their η coverage in *barrel* (small $|\eta|$) and *end-cap* (larger $|\eta|$) devices. Detectors in the barrel part are cylinders around the beam axis which are usually symmetric around it, whereas the end-cap detectors are "disks" in the transverse plane, again symmetric around the beam axis.

2.2.1 Tracking detectors

The ATLAS Inner Detector consists of two solid state (semiconductor) detectors, the Pixel detector and the Semiconductor Tracker (SCT) as well as a gaseous detector, the Transition Radiation Tracker (TRT), *cf.* Figure 2.3. Both semiconductor detectors use silicon as sensor material covering a region up to $|\eta| < 2.5$. By doping the material and applying a bias voltage of 150 V the active sensor can be fully depleted[3] and cre-

[3]During operation of the LHC the silicon structure will be damaged by the high radiation doses. This leads to a reduction of the effective charge density and higher voltages need to be applied to achieve

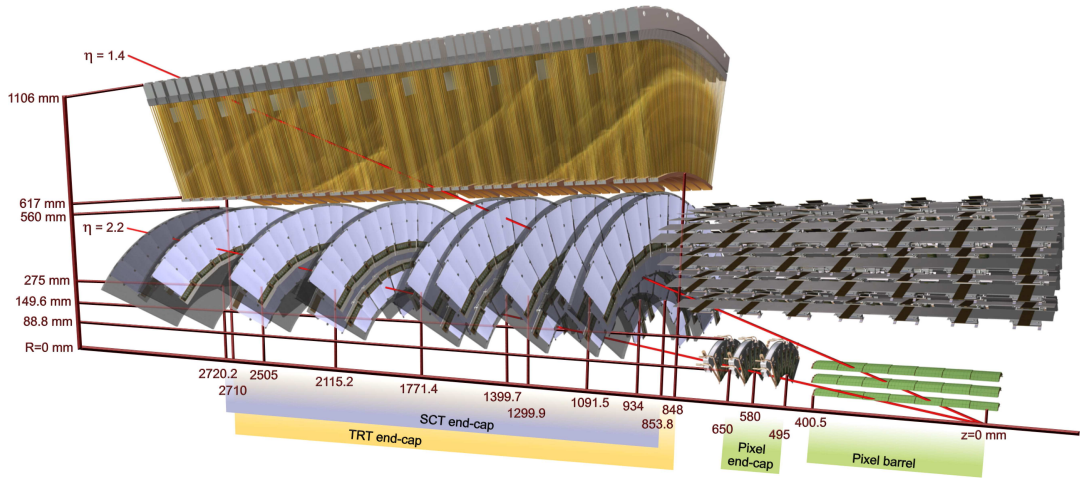

Figure 2.3: 3-dimensional drawing of the ATLAS Inner Detector modules (from [62]). On the right the three Pixel barrel layers (green) and the four layers of (double-sided) SCT modules (grey) are visible. The barrel part of the TRT is omitted here. The Pixel end-cap modules are located inside the SCT and TRT barrel volume. On the left the SCT (blue) and TRT (yellow) end-cap modules are drawn. Two lines of pseudo-rapidity ($\eta = 1.4$ and $\eta = 2.2$) starting at the nominal interaction point are shown for comparison.

ates electron-hole-pairs when charged particles pass the material, which acts as bipolar diodes. The Pixel sensors are segmented in 144 columns and 328 rows with a pitch of 400 µm × 50 µm and 600 µm × 50 µm, respectively. Each pixel is individually bump-bonded to the front-end readout electronics. The SCT uses about 6 cm long strips with a pitch of 80 µm at a sensor thickness of about 300 µm. Both Pixel and SCT allow for charge interpolation between adjacent pixels and strips. The final spatial resolution of the measurements can therefore even be below the pitch sizes.

Special demand in the design of the Pixel and SCT detectors was the radiation hardness, allowing to operate the detectors for several years in the expected particle fluxes, while keeping the material budget low to minimise multiple scattering of the particles in the detector material. Furthermore both detectors need to be cope with high track densities as one expects roughly 1000 particles every 25 ns within $|\eta| < 2.5$ [62]. The high granularity especially of the Pixel tracker are not only needed to achieve high precision measurements, but also to keep the occupancies with respect to the readout channels small. Otherwise dead-times and efficiency losses due to overlapping tracks will occur.

In the barrel part the Pixel detector consists of three layers of modules, where intrinsic accuracies of 10 µm in R–ϕ and 115 µm in the z direction are achieved. The innermost layer at a radius of 51 mm plays a crucial role for the reconstruction of secondary vertices

sufficient depletion. The initial doping is performed in a way that a type inversion occurs during irradiation, which allows to finally operate the sensors even without achieving full depletion. The Pixel will require bias voltages of up to 600 V and the SCT up to 350 V for good charge collection efficiencies after ten years of operation.

and is therefore also named b-layer, due to its relevance for the identification of b-jets. The end-cap part of the Pixel detector consists of three disks on each side (positive and negative z). In total the Pixel detector provides 80.4 million readout channels. Plans exist already to introduce a fourth layer of pixel sensors inside the existing Pixel detector [74] in the year 2013. This so-called *Insertable b-Layer* (IBL) would significantly increase the vertexing capabilities and could recover efficiency losses due to Pixel modules with radiation damages.

Double-sided modules with small stereo angles of 40 mrad are used in the SCT, leading to an intrinsic accuracy per module in the barrel part of 17 µm in R–ϕ and 580 µm in the z direction. Without the stereo angle no z information would be available in the barrel SCT. Nine disks on each side form the end-cap SCT, giving in total 6.3 million readout channels of the SCT.

At larger radii, the demands concerning occupancy and spatial resolution are more relaxed. Therefore a straw tube detector is used as the last part of the Inner Detector covering a region $|\eta| < 2.0$. The TRT tubes with a diameter of 4 mm are used as cathodes, holding a 31 µm diameter anode wire operated with a high voltage of about 1530 V. They are filled with a gas mixture of 70 % Xe, 27 % CO_2 and 3 % O_2. The straws of the barrel TRT are aligned parallel to the beam axis in a honey comb like structure. They have a length of 144 cm and their anode wires are split in the middle to obtain distinct readouts with positive and negative z coordinate to reduce the occupancy. The TRT measures the drift time of electrons from ionisation clusters in the gas to the anode wire. As the electrons drift with approximately constant speed until the vicinity of the wire, one can translate the drift time into the minimum distance the particle passed by the wire. The obtained intrinsic resolution is 130 µm perpendicular to the straw axis. Even though the resolution is much worse than those achieved in the silicon detectors the TRT improves the measurement of track momenta significantly, because of the large lever arm due to its large radius. Additionally the TRT provides a high number of measurements (30 on average) of the particle's flight path.

In addition to its tracking capabilities the TRT offers information for particle identification. Fibres and foils surround the TRT tubes and can create transition radiation, which is measured as a *high threshold* signal in the straws, because the transition radiation photons can convert and create additional ionisation in the gas. The emission of transition radiation depends on the relativistic γ factor of the particle passing the material border. Therefore electrons have a higher chance to create high threshold signals by transition radiation than pions of the same momentum due to their smaller mass. The fraction of high threshold measurements on a particle track can therefore serve as a discriminant *e.g.* between electrons and pions.

Track reconstruction

Track reconstruction in the Inner Detector starts from seeds of 3-dimensional measurements in the Pixel and SCT detectors. Pixel measurements are taken as such, whereas

SCT measurements are combined from the two sides of a module to incorporate the stereo angle. Along the seed directions additional compatible measurements are searched for and used in a track fit. Several different track fit algorithms can be used in parallel, like a global χ^2 minimisation [75] or a Kalman filter [76]. In the track fits the two sides of a SCT module are treated individually. At this stage many fitted tracks will share the same measurements and many ghost tracks are usually found. Algorithms for ambiguity solving order the candidate tracks according to quality scores and remove shared measurements until high quality tracks survive only. These are extrapolated in the TRT volume and compatible TRT measurements are added in another track fit. This inside-out sequence reconstructs most of the high momentum tracks ($p_{\mathrm{T}} \gtrsim 1\,\mathrm{GeV}$), but can be supplemented by an outside-in sequence starting from the remaining TRT measurements. In the outside-in sequence also tracks from late decays or material interactions can be reconstructed that do not leave measurements in the Pixel or SCT layers. Further specialised track fitters exist *e.g.* for high occupancies in the TRT or tracks from electrons, which can suffer from bremsstrahlung. A summary of the Inner Detector tracking can be found in reference [77].

ATLAS does not intrinsically assume helical tracks, but uses a local helix representation at given points in space. The point of closest approach of a track to a given axis is calculated. Its position along the axis gives the longitudinal impact parameter z_0 and its distance in the transverse plane the transverse impact parameter d_0. Additionally the direction of the track momentum is given in the azimuthal angle ϕ and the polar angle θ at the point of closest approach. The magnitude of the momentum is internally represented as the charge signed inverse momentum q/p.

2.2.2 Calorimetry

The whole ATLAS calorimeter system including the forward calorimeters covers a pseudo-rapidity range $|\eta| < 4.9$. Different techniques are applied, because the requirements concerning granularity and particle fluxes vary over this wide range. One important design issue is the containment of electromagnetic and hadronic showers, in order to measure the full energy of isolated particles and jets and to avoid a *punch-through* of particles other than muons into the Muon Spectrometer. For electromagnetic showers the radiation length X_0 is the characteristic amount of matter, because it is related to the mean path length for energy loss of electrons by bremsstrahlung and the mean free path for pair production of photons [8]. The electromagnetic calorimeter of ATLAS has a total thickness of more than $22X_0$ (up to $33X_0$) in its barrel part and more than $24X_0$ (up to $38X_0$) in its end-caps [62]. Similarly the nuclear interaction length λ is related to the mean energy loss by nuclear interactions of high energetic hadrons in matter. The full ATLAS calorimeter provides approximately 9.7λ of active calorimeter material in its barrel part (10λ in the end-caps), from which the hadronic tile calorimeter contributes $\approx 7.4\lambda$.

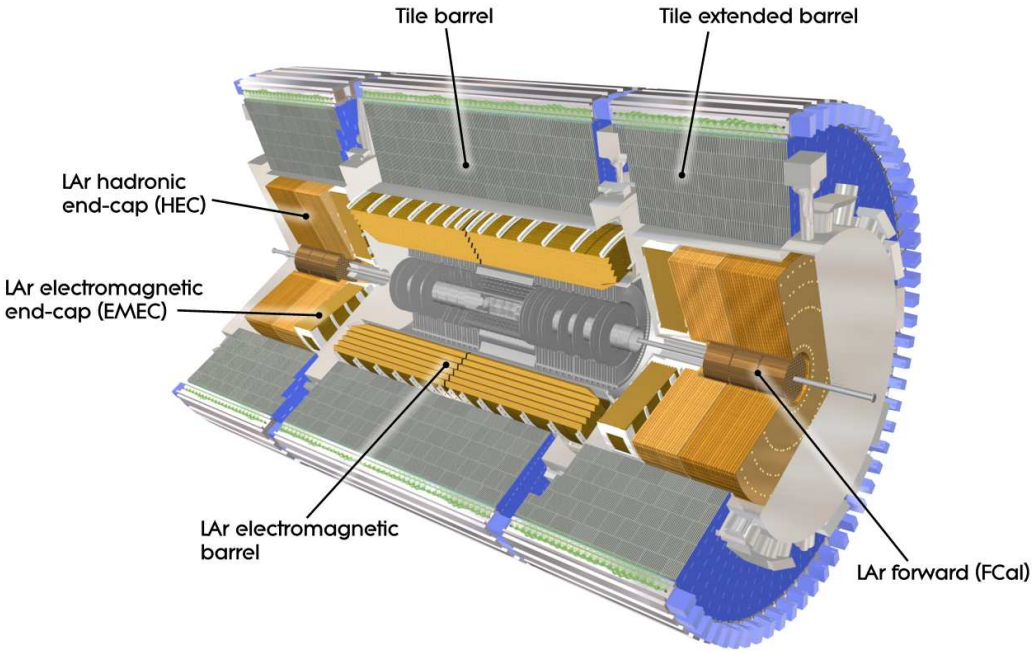

Figure 2.4: Cut-away view of the ATLAS calorimetry (from [62]).

Figure 2.4 gives a cut-away view of the different components of the ATLAS calorimeter system. The electromagnetic (EM) calorimeter is realised as a lead-liquid argon (LAr) detector with accordion-shaped electrodes and lead absorber plates. The accordion-shape structure was chosen to avoid cracks in azimuthal (ϕ) direction. The barrel part ($|\eta| < 1.475$) is split at $\eta = 0$ into two barrels and extended by two end-cap wheels ($1.375 < |\eta| < 2.5$ and $2.5 < |\eta| < 3.2$) on each side. The region between the barrel and end-cap cryostats contains services and cables for the Inner Detector and the barrel EM calorimeter. Special scintillators have been installed to partially recover the energy lost in inactive material in this region. Still the energy resolution is slightly degraded here and the detector description difficult. Electrons reconstructed in this crack region are therefore often disregarded (*cf.* Section 2.2.5).

In the region $|\eta| < 2.5$, which is most important for many processes and also covered by the tracking system of the Inner Detector, the EM calorimeter is radially segmented in three layers (layer 1 to layer 3). The middle layer has the biggest depth of $16X_0$ and a fine granularity of $\Delta\eta \times \Delta\phi = 0.025 \times 0.025$ in this region. The first layer is partially segmented as $0.025/8 \times 0.1$, *i.e.* has a very high granularity in the η direction, and is therefore sometimes also denoted as the η-strip layer. Up to $|\eta| < 1.8$ a pre-sampler is installed in front of layer 1 which also serves as pre-shower material for photons[4] and should recover energy lost in showers starting in front of the EM calorimeter. Note that the solenoid magnet is located inside the EM calorimeter in ATLAS, which has some drawbacks on the energy resolution.

[4] Photons initiate an electromagnetic shower only after they have converted into an electron-positron pair. Photon showers therefore usually start about one radiation length X_0 later than electron showers.

Liquid argon is used as active medium between the accordion-shaped lead absorbers. The electrodes are located in the middle of the spacing between the absorbers hold by honeycomb spacers. With a drift gap of 2.1 mm on each side of the electrodes one obtains a total drift time of about 450 ns at an operating voltage of 2000 V. This maximum drift time is long compared to the bunch crossing time of 25 ns at the LHC. Therefore an analog pulse shaping is applied to "squeeze" the detector signal into a main peak within 100 ns. The resulting signal is sampled with the bunch crossing frequency.

For the hadronic calorimeter scintillating tiles as well as liquid argon is used. The tile calorimeter forms the barrel part ($|\eta| < 1.0$) and the extended barrels ($0.8 < |\eta| < 1.7$) surrounding the EM barrel and end-caps, *cf.* Figure 2.4. It has a sandwich structure of steel absorbers and scintillating tiles, which are read out by photomultiplier tubes (PMT) via wave-length shifting fibres. The tile calorimeter is segmented in three layers with a granularity of $\Delta\eta \times \Delta\phi = 0.1 \times 0.1$ and 0.2×0.1, respectively.

The hadronic end-cap (HEC) and the forward calorimeter (FCal) use liquid argon as active medium again. A flat-plate design was chosen for the HEC, *i.e.* copper plates as absorber alternate with gaps filled with liquid argon. Within each gap two electrodes provide the high voltage and another electrode in the middle serves as readout structure. The FCal ($3.1 < |\eta| < 4.9$) needs to withstand high particle fluxes from underlying event and diffractive processes. Thus the LAr gaps need to be small to avoid problems with ion build-up and to obtain faster signals. In the first layer the gap is only 0.27 mm thin, giving a full drift time of only 60 ns. This is achieved by coaxial copper tubes and copper rods serving as electrodes. They are placed in holes drilled in stacks of copper plates. The first layer is optimised for electromagnetic interacting particles and the second and third layer, using tungsten absorbers, for hadronic interactions.

Note that the ATLAS calorimeters are non-compensating. This means hadronic showers need additional corrections, because they create lower signals than electromagnetic showers at the same primary particle energy. ATLAS applies different calibration schemes, which either try to correct jets with global factors or by local schemes, which reweight cell energies according to a classification into hadronic and electromagnetic clusters (*cf.* Section 2.2.5).

2.2.3 Muon Spectrometer

In contrast to the Inner Detector with its solenoid magnet, the Muon Spectrometer (MS) uses a toroidal magnetic field. It is generated by three air-core superconducting magnets (one in the barrel $|\eta| < 1.4$ and two in the end-caps $1.6 < |\eta| < 2.7$) consisting of eight coils each. The bending power $\int B\mathrm{d}l$ along a straight line through the whole spectrometer is between 1.5 and 5.5 T m in the barrel and 1 to 7.5 T m in the end-cap toroids.

In the MS different detector technologies are combined. Gaseous detectors somewhat similar to the TRT, the Monitored Drift Tubes (MDTs) are used to measure the track

coordinate in the bending plane. They are arranged in layers of three and four tubes, building one MDT chamber. The barrel MDT chambers are located cylindrically within the toroid magnet coils. The end-caps, build as wheels, are placed besides the end-cap toroids. The tubes have a diameter of $\approx 30\,\text{mm}$ and are operated with a Ar/CO_2 gas mixture at an anode voltage of 3080 V. This corresponds to a maximum drift time of 700 ns and allows to reach average spatial resolutions of 80 µm per tube.

Because of higher particle fluxes and bigger densities of muon tracks in the forward region $2.0 < |\eta| < 2.7$ of the MS, the innermost MDT layer in this region was replaced by Cathode Strip Chambers (CSCs). The CSCs are multiwire proportional chambers, *i.e.* parallel anode wires are span in the middle between two cathode plates. Both cathodes have readout patches segmented perpendicular to each other, while the anode wires have no readout. Even though the readout pitch is $\approx 5.5\,\text{mm}$ in the bending direction one can achieve a resolution of 60 µm per CSC plane by charge interpolation between neighbouring readout strips. In the perpendicular direction a courser readout leads to a resolution of approximately 5 mm.

MDTs and CSCs as precision chambers for track reconstruction are supplemented by trigger chambers with fast signals to provide track measurements within a few 10 ns. Resistive Plate Chambers (RPC) are used in the barrel region ($|\eta| < 1.05$) and Thin Gap Chambers (TGC) in the end-cap ($1.05 < |\eta| < 2.4$). They have high intrinsic time resolutions of 1.5 ns (RPC) and 4 ns (TGC) allowing for reliable identification of the bunch crossing and may also be used for time-of-flight measurements in special analyses. Both types of chambers measure the track coordinate 2-dimensionally, *i.e.* in the bending plane (η) and perpendicular (ϕ). Hence they provide the ϕ information lacking from the precision measurements of the MDT. The trigger chambers alone allow to estimate the track momenta and to distinguish high-p_T (9–35 GeV) and low-p_T muons (6–9 GeV).

The RPC is a gas detector using parallel plates as electrodes at a distance of 2 mm, allowing for very high field strengths. It can be operated in avalanche and streamer mode, where the avalanche production strongly dominates at the operating voltage of 9.8 kV. The spatial resolution is given by the granularity of the readout structures coupled capacitively with the electrodes. The layout of the TGCs is similar to the CSCs. Whereas the wire pitch is equal to the anode-cathode spacing in the CSCs, the TGCs have a gap smaller than the wire-to-wire distance, hence the name Thin Gap Chambers.

2.2.4 Trigger system

The rate of bunch crossings with 40 MHz at design parameters of the LHC is much higher than the maximum rate of 200 Hz with which the full detector information can be read out and stored on disk (about 300 MB/s). At the same time the cross section for interesting processes, like vector boson production or the production of heavy, new particles, is orders of magnitude smaller than the total proton-proton cross section.

Therefore good selection methods are needed already in the first place to store only events with potentially interesting processes.

The ATLAS trigger system consists of three stages, the Level 1 (L1) trigger based on hardware (ASICs and FPGAs) and the Level 2 (L2) and Event Filter (EF) stages, implemented in software on large computing farms. In the Level 1 trigger decisions must be taken within 2.5 µs at the bunch crossing rate. It has access to limited data from the Muon Spectrometer (RPC and TGC) and the calorimeters, where dedicated read outs are used. Calorimeter data is available at the level of trigger towers with granularity $\Delta\eta \times \Delta\phi = 0.1 \times 0.1$. Different thresholds on trigger objects like electromagnetic clusters, jets, muons, taus or missing transverse energy can be applied and combined in Level 1 trigger configurations, named L1 items. Pre-scales can be applied at each trigger stage, which let only a given fraction of the events pass, that triggered a certain item. Pre-scales are useful the obtain limited samples of processes with higher cross sections that are *e.g.* needed for calibration purposes.

In the Level 2 trigger regions-of-interest (ROI) can be investigated with a higher level of detail than available in the L1 trigger. For example calorimeter measurements with higher granularity and also measurements from the Inner Detector can be processed in the regions seeded by the L1 items. Finally the Event Filter runs after the event building step that combines the data from all detector systems. It therefore has access to the full event information and can run algorithms similar (or even identical) to the offline event reconstruction. The final output rate is limited by the data storage and computing capabilities of the offline processing.

2.2.5 Particle reconstruction and identification

The measurements in the various detector components need to be combined and evaluated by reconstruction algorithms to derive information about the particles produced in the collision events. One major step is the reconstruction of quantities like track momenta or clusters of energy deposits in the calorimeter. At a higher level these data are combined to relate them to physical objects like individual electrons, muons or jets from the hadronisation of quarks and gluons. The identification of such objects and the tagging according to their type can be ambiguous and is only possible with a certain reliability.

The ATLAS collaboration developed a special event reconstruction and analysis software, athena, based on the Gaudi software framework [78]. In this structure, physical objects are not reconstructed exclusively, *e.g.* a single reconstructed track in the Inner Detector may be assigned to a reconstructed electron and a muon at the same time. The reconstructed objects are usually also categorised in different levels of confidence in the identification. Usually higher efficiencies in the identification of an object (*i.e.* lower false-negatives) are gained at the expense of higher rates of misidentifications (*i.e.* higher false-positives). The choice of quality criteria on the objects and their order of precedence in case of ambiguities are specific to the physical process studied by an

analysis. In the following the general concepts of the reconstruction and identification algorithms for electrons, muons and jets in the ATLAS software are summarised. Tau leptons are discussed in more detail in Chapter 4.

Electron identification

Electrons are identified by their specific signatures in the electromagnetic calorimeter. Showers in the calorimeter from electrons and photons have a very regular shape and are much more collimated than jets including hadrons. Furthermore their energy is mainly contained in the EM calorimeter. Tracks are matched to the calorimeter clusters to distinguish them from photons, where the ratio between energy in the calorimeter and the track momentum is required to be $E/p < 10$. Additionally, the transition radiation measurements of the TRT can be included to improve the rejection against charged pions.

The standard identification method uses simple cuts. Three levels of identification exist with an increasing number of applied ID variables. The "loose" ID uses only basic calorimeter variables and has therefore a high efficiency, but the largest rate of false positives. The "medium" selection includes additional calorimeter variables and track quality criteria. In the "tight" ID also isolation cuts and more information from the track matching and the TRT measurements are included. Recent estimates of the performance of the electron identification can be found in reference [79].

Muon reconstruction

In principle muons can easily be identified in the ATLAS experiment as they are the only particles creating tracks in the Muon Spectrometer, except for noise effects from various sources and punch-through of hadrons, which are not stopped completely in the calorimeter. Basically one distinguishes *stand-alone muons* being reconstructed from tracks in the Muon Spectrometer only and *combined muons* reconstructed from track segments in the MS and the Inner Detector. Additionally methods exist to tag Inner Detector tracks as muons by their minimum ionising signal in the calorimeter, which may help to recover inefficiencies of the Muon Spectrometer at $\eta = 0$.

ATLAS supports two families of algorithms for muon reconstruction, Staco and Muid. The two differ in details of their implementation and in the way how the track parameters of combined muons are estimated (*cf.* reference [80]). The best momentum resolution is obtained for combined muons, where the Inner Detector mostly contributes for low-p_{T} muons and the Muon Spectrometer at high p_{T}. Note that muons as minimum ionising particles loose about 3 GeV to 4 GeV of their energy in the calorimeters. The matching of ID and MS tracks is done with the $\chi^2 = (\vec{t}_{\mathrm{MS}} - \vec{t}_{\mathrm{ID}})^T (\mathbf{C}_{\mathrm{MS}} + \mathbf{C}_{\mathrm{ID}})^{-1} (\vec{t}_{\mathrm{MS}} - \vec{t}_{\mathrm{ID}})$ where $\vec{t}_{\mathrm{MS}}$ and $\vec{t}_{\mathrm{ID}}$ are the reconstructed track parameters extrapolated to the origin of the global coordinate system from the Muon System tracks and the Inner Detector tracks, respectively. $\mathbf{C}$ denotes the corresponding covariance matrix. The track parameters of

the combined muons are obtained by a statistical combination (Staco) or a partial refit of measurements in the ID and MS (Muid).

Jet reconstruction

The reconstruction of jets in ATLAS mainly starts from *topological clusters* of calorimeter cells [81]. These clusters form spatially connected regions in the calorimeter with dynamical sizes, giving 3-dimensional representations of energy deposits. By construction they provide an intrinsic noise suppression. One needs to distinguish the cluster energy at the electromagnetic scale and the hadronic scale, because of the non-compensating calorimeter (*cf.* Section 2.2.2). Topological clusters can be classified into electromagnetic and hadronic energy deposits by means of cluster shapes and the distribution of energy densities inside the clusters. With the classification the cluster energy can be calibrated to the hadronic scale by reweighting the cell energies and including out-of-cluster and dead material effects.

In the ATLAS experiment different jet algorithms like ATLAS cone (*cf.* [82–84]), $k_\perp$ [85, 86] and anti-$k_\perp$ [87] can be applied to the topological clusters at the EM scale or the hadronic scale. In case of jets formed from EM scale clusters a global calibration scheme ("H1-style") based on the energy densities in the calorimeter cells is used to obtain the jet energy at the hadronic scale. Further scale factors of the jet energy are applied as a function of the jet energy and pseudo-rapidity η to correct for residual non-linearities of the energy response. Also in the case of jets from hadronic scale clusters additional calibrations are applied to the jet energy, *e.g.* to take into account the bending of charged particles out of the jet. Why and how the energy and angular resolution of the jet reconstruction can be improved by means of *energy flow algorithms* will be discussed in Section 4.3.

Several different methods exist to measure the missing transverse energy $E_{\mathrm{T}}^{\mathrm{miss}}$. In its simplest form only calorimeter clusters and tracks in the Muon Spectrometer are taken into account. However, the energy response of the calorimeter is slightly different for the various kinds of particles. The best resolution can be obtained by combining the fully calibrated reconstructed objects, like electrons, muons and jets and correcting for energy deposits not included in those. Reference [67] summarises the different definitions used by the ATLAS experiment and reference [88] estimates the $E_{\mathrm{T}}^{\mathrm{miss}}$ resolution in data.

Chapter 3

Detector simulation

"There is something irreversible about acquiring knowledge; and the simulation of the search for it differs in a most profound way from the reality."

— J. Robert Oppenheimer, "Physics in the Contemporary World", 1947

In the ATLAS experiment – as in nearly all current experiments in high energy physics – discoveries and measurements can usually only be done in comparison to theoretical predictions of already known processes. Even if one tries to reduce the dependency on predictions as much as possible by using so-called data-driven methods for background estimation, one still needs theoretical predictions of the background and signal processes at least to test the data-driven methods and to tune the algorithms for event reconstruction. The predictions include at least two distinct steps. Monte Carlo simulations of the interactions in the collision events are performed by *event generators*. They use various numerical methods to evaluate the matrix elements corresponding to a certain process. Additionally parton showers and the hadronisation of colored objects like quarks and gluons to jets of hadrons needs to be simulated. This process cannot be treated perturbatively and needs special shower models like the ones implemented in the two generators Herwig [89] and Pythia [90].

However, those final states cannot be directly compared to observables, because detector acceptances, reconstruction efficiencies and resolutions have to be taken into account. Modern detectors in High Energy Physics are extremely complex systems of sub-detectors of different technologies. Therefore, only Monte Carlo techniques are applicable to include detector effects in the prediction of observables from the generated event samples. To obtain reliable estimates how an event simulated by an event generator will be measured, one needs detailed simulations of the detector itself. The *detector simulation* needs to include the propagation of particles, like bending of charged particles in the magnetic field of the detector, the interaction of particles with active and passive detector material, and decays of particles inside the detector. For this purpose software packages exists like the widely used Geant 4 toolkit [91]. Finally, the response of the detector electronics to the signals of particles in active detector elements needs to be simulated in the so-called *digitisation* before the event reconstruction can be run on the

simulated data as it is done for measured data [92] as well. Hence, Monte Carlo simulation of the detector response is an essential part of any kind of analysis of contemporary high energy physics experimental data.

At the LHC these simulated data sets are needed with large statistics and a high level of precision, which makes their production a CPU-intensive task. For example the simulation of a single $t\bar{t}$ event in the full ATLAS simulation takes about 30 kSI2Kminutes [92], corresponding to about 15 min on recent CPUs. Some processes need the simulation of millions of events which can easily add up to decades of CPU-years even on most recent machines. Therefore, several fast detector simulations exist in addition to the fully-fledged Geant 4-based simulation of the ATLAS detector.

Section 3.1 presents the new fast track simulation engine FATRAS which implements a detailed Monte Carlo simulation based on the modules and the geometry of the standard ATLAS track reconstruction application. The basic concepts of the fast track simulation are explained and the performance with respect to first data taken with the ATLAS detector at a centre-of-mass energy of $\sqrt{s} = 900\,\text{GeV}$ is shown[1].

Besides the official simulations of the ATLAS detector also generic detector simulations have been developed outside the ATLAS collaboration. Delphes [94] and PGS [95] are two examples of such, which are applicable for ATLAS and the LHC with corresponding parametrisations of its resolution. In Section 3.2 some comparisons of the fast and generic detector simulations to the full ATLAS simulation are shown on selected physics processes, which are relevant for the studies on R-parity violating SUSY presented in Chapter 5.

3.1 The ATLAS fast track simulation FATRAS

Due to the high computing demands of the full simulation, the ATLAS collaboration decided to adopt a three-fold way in its detector simulation. In addition to the full Geant 4-based simulation the fast simulation ATLFAST-I exists, which uses a parametric approach. It directly includes all effects on momentum and energy resolution and reconstruction efficiencies in the parametrisation. High-level objects used in the physics analyses are directly produced from the output of the Monte Carlo event generator. In recent times this has been complemented by ATLFAST-II, which uses a simplified detector model, but still allows to run the full reconstruction chain of the ATLAS software. Hence it is more detailed for example in the simulation of correlations between objects and additional fake tracks. As another advantage no parametrisation has to be modified in case of changes in the reconstruction software.

[1] The comparisons to first data have already been published in reference [93].

3.1.1 Basic principle

The ATLAS fast track simulation FATRAS [96] is part of ATLFAST-IIF and simulates tracks of charged particles in the ATLAS Inner Detector and the Muon Spectrometer. It uses the extrapolation engine of the ATLAS reconstruction software [97], while including all important material interactions like multiple scattering, energy loss, bremsstrahlung, photon conversions and hadronic interactions. Measurements are simulated along the path of charged particles using an own implementation of the digitisation. This has been achieved by reusing certain modules of the reconstruction software or replacing them with Monte Carlo versions. For example the module to estimate the energy loss of particles penetrating detector layers was supplemented by a version that simulates the energy loss according to the Bethe-Bloch formula and radiation loss according to the Bethe-Heitler formula.

The whole simulation process in FATRAS is based on the so-called Tracking Geometry [98], which is also used during track reconstruction. The Tracking Geometry is a simplified detector description, that is derived from the detailed geometry model of the ATLAS detector implemented for the Geant 4 simulation. Spatially extended parts of the detector are subsumed in material layers. Especially for the rather thin Pixel and silicon strip modules of the ATLAS detector the layer-based description is a very good approximation. Active detector layers in the tracking system are identical between the full simulation and FATRAS.

Figure 3.1 illustrates the basic steps of the track simulation. A particle stack is filled with all relevant final state particles. By default the primary vertex position of those

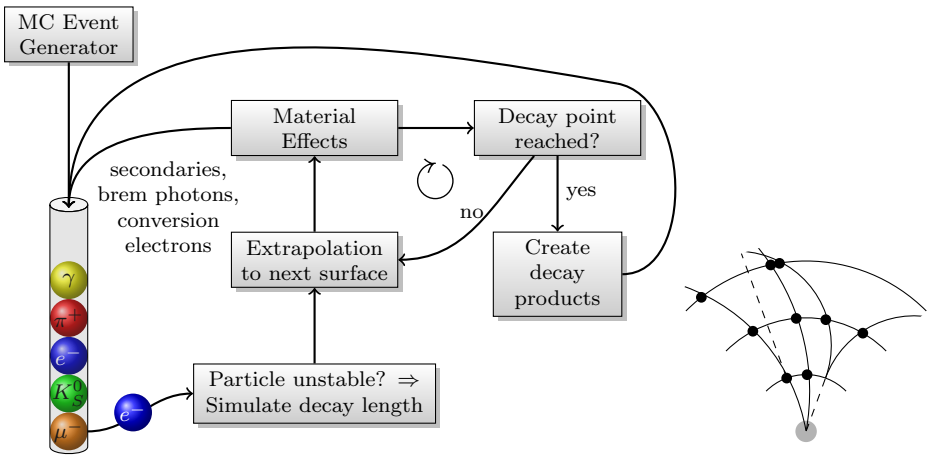

Figure 3.1: Sketch of the most important steps of the track simulation in FATRAS. Input particles from the generator are put on a stack and processed one after another. The extrapolation and the simulation of material effects are done layer-wise until a particle decayed or left the detector. Secondary particles from interactions with the material are put on the stack. The inlay on the right sketches the layer-based simplification of the detector.

particles is shifted to the beam spot position as provided by the detector conditions data base and smeared according to its resolution. Arbitrary vertex positions can be simulated as well. Next, all particles of the stack are processed in sequence. For unstable particles the path length up to the decay is simulated. Charged and neutral particles are extrapolated through the detector stepwise from one material layer to the next. In each of these steps detector material effects are simulated.

Simulated material effects include bremsstrahlung for electrons, conversion to e^+e^--pairs for photons, multiple scattering and energy loss. All of the above effects can be estimated from "first principles" like the Bethe-Bloch formula. However, hadronic interactions cannot be simulated that way. FATRAS uses a parametrisation obtained from simulated Geant 4 events instead. Figure 3.2 shows an example of a single electron event in the ATLAS Inner Detector simulated with FATRAS. The effects of interactions with the detector material are clearly visible here. Secondary particles from interactions are put on FATRAS' particle stack to be further propagated through the detector, until they fall below a certain threshold in their transverse momentum. Particle decays inside the detector are simulated via direct use of the corresponding Geant 4 module to obtain the types and 4-momenta of the decay products. Therefore all decay modes implemented in Geant 4 are available in FATRAS as well.

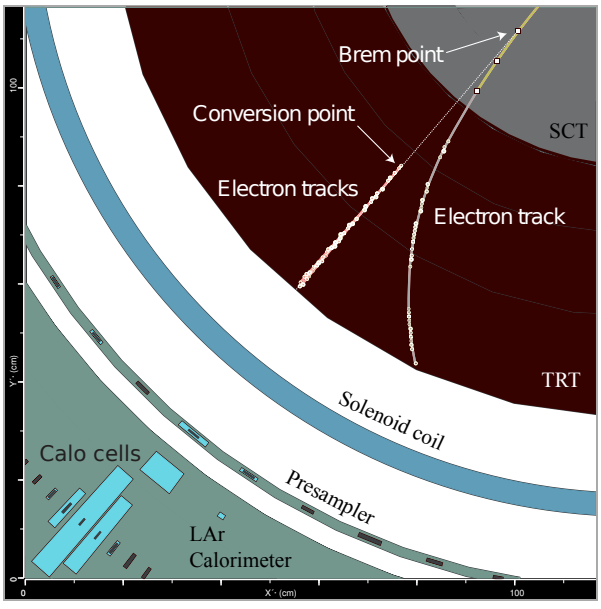

Figure 3.2: Event display of a single electron event simulated with FATRAS for the Inner Detector and the fast calorimeter simulation `FastCaloSim` for the calorimeter response. The electron creates a photon by bremsstrahlung in the ATLAS silicon tracker (SCT), which itself converts into an e^+e^--pair inside the Transition Radiation Tracker (TRT).

After the whole particle stack has been processed in the Inner Detector, all final particles are extrapolated to the entrance surface of the calorimeter. They are picked up by the subsequent calorimeter simulation. For this purpose the ATLAS collaboration developed the fast calorimeter simulation `FastCaloSim` (see [99] and references herein). In Figure 3.2 it can be seen how the secondary (or even tertiary) particles created by FATRAS are used for the calorimeter simulation. Muons crossing the calorimeters can afterwards be handed back to the Muon System part of FATRAS.

In a final post-processing step measurements are extracted from the simulated tracks. Noise measurements can be added at the level of individual pixels or strips in the silicon detectors. Overlapping clusters are merged, so that FATRAS can provide rather precise predictions of two-track resolutions. In the TRT noise hits will mask measurements from particles.

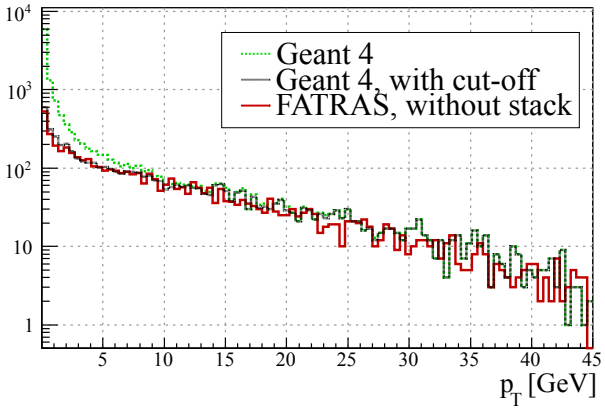

Figure 3.3: Transverse momentum distribution of simulated electrons in single photon events. The green, dashed histogram shows all electrons created by Geant 4 inside the Inner Detector volume and the black, dotted histogram only electrons stemming from a conversion directly of the initial photon. The red, solid line corresponds to the distribution by FATRAS before introducing the particle stack.

Various validations of the FATRAS simulation have been done in comparison to the full Geant 4 simulation to make both agree as good as possible. In Figure 3.3 one can see for example one problem which has been identified in a previous version of FATRAS. The figure compares the transverse momentum distribution of electrons in single photon events, *i.e.* all electrons stem from the conversion of photons inside the Inner Detector. It is clearly visible that the number of very low momentum photons is underestimated in this version FATRAS, which did not use a particle stack yet, but instead a fixed number of iterations in the processing of secondary particles. With the fixed number of iterations no electrons produced in photon conversions of bremsstrahlung photons which themselves stem from conversion electrons are produced. The distributions agree well, when the tree of interactions in Geant 4 is cut at the same place, where FATRAS stopped in the older version. This problem has been fixed with the introduction of the particle stack, where secondary, tertiary, etc. particles are processed until they fall below a certain momentum threshold.

The typical time to simulate a $t\bar{t}$ event in the whole ATLAS detector reduces from about 2000 kSI2Kseconds for full Geant 4 to ≈100 kSI2Kseconds when using the fast calorimeter simulation `FastCaloSim`, but keeping Geant 4 for Inner Detector and Muon System. One gains another factor of more than 10, when using FATRAS for the track simulation (≈7 kSI2Kseconds) [92]. The simulation time of the Inner Detector reduces from ≈ 146 kSI2Kseconds (simulation) + 4.3 kSI2Kseconds (digitisation) for Geant 4 to ≈ 2.8 kSI2Kseconds (total) for FATRAS compared to about 0.02 kSI2Kseconds for the parametrisation based simulation ATLfast-I [96]. A further speed-up of FATRAS would not improve the overall timing as the FATRAS simulation takes already about the same amount of CPU-time as the Inner Detector reconstruction chain.

3.1.2 Comparison to first ATLAS data

Besides validating FATRAS with the full ATLAS simulation the final check needs to be done with measured data. The first proton-proton collisions in the LHC were recorded by the ATLAS experiment at a centre-of-mass energy of $\sqrt{s} = 900\,\text{GeV}$ as minimum bias events. Minimum bias refers to the trigger used to record those events. The minimum bias trigger tries to introduce a minimum selection bias by using only very basic trigger modules, like the beam crossing monitor and very forward scintillation detectors. Ideally all events originating from proton-proton collisions with inelastic interactions are recorded. They allowed us to confront the fast track simulation for the first time with data from collisions [93].

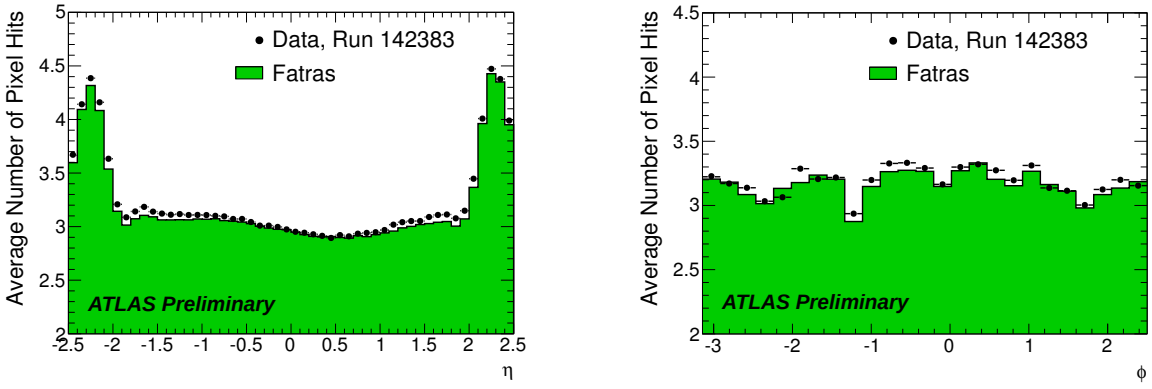

(a) As a function of η

(b) As a function of ϕ

Figure 3.4: Average number of pixel hits per selected track as a function of pseudo-rapidity η and azimuthal angle ϕ of the track, respectively. Comparison of the FATRAS Monte Carlo and the data is shown. The structure is mainly determined by the inactive pixel modules that have been also masked in the digitisation process of the MC samples to reproduce the run conditions.

Figure 3.4a shows the mean number of measurements of the Pixel detector associated to reconstructed tracks versus the pseudo-rapidity η. The sinusoidal-like shape in the central part of the distribution comes from a convolution of two effects: First, two detector modules in the same layer have been inactive during the run, which means that tracks in this region hit only two instead of three modules. Secondly, the beam spot position along the beam (z-) axis was shifted a few centimeters with respect to the nominal center of the detector, which leads to a shift between the η angle at the beam spot position and the η angle of the position of the inactive detector modules. Figure 3.4b shows the same for the azimuthal angle ϕ. The good agreement between simulation and data shows, that the fast track simulation does not only describe the detector geometry correctly but also includes information about the detector conditions changing from run to run. FATRAS automatically includes conditions data like the beam spot position and size and inactive or masked detector modules.

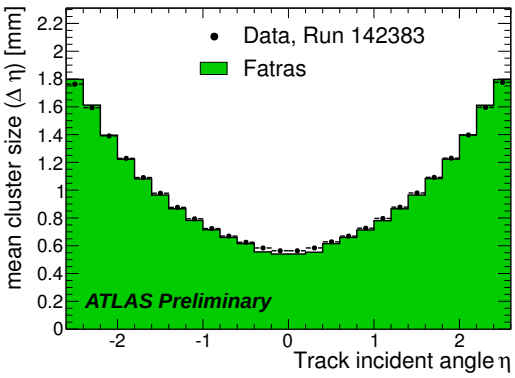

(a) Mean cluster size in the Pixel detector

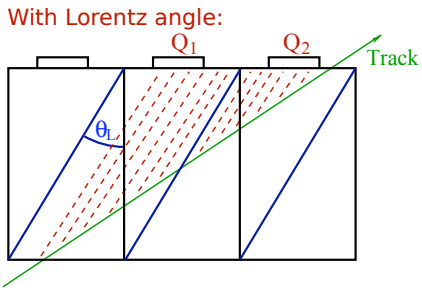

(b) Sketch of the clusterisation model in FATRAS.

Figure 3.5: Comparison of the FATRAS geometrical clusterisation model in the Pixel detector with the data. The right sketch illustrates the dependency of the cluster size on the incident angle of the track with respect to the detector module. On the left the mean cluster size in the Pixel detector versus track incident angle η for good tracks is compared in FATRAS simulation with data.

The clusterisation model of FATRAS could also be tested with the first data. As illustrated in Figure 3.5b the cluster size in the Pixel detector depends on the track incident angle on the detector module. Figure 3.5a shows the measured and simulated mean cluster size versus the track incident angle in the Pixel detector. FATRAS has not been tuned to data at this stage, but already here a reasonably good agreement could be achieved.

3.2 Comparison of generic detector simulations

In Section 5.1.2 event selection cuts for a specific model of R-parity violating SUSY will be derived. Some of the relevant kinematic distributions of jets and leptons will be shown there relying on the fully-fledged simulation of the ATLAS detector. In this Section comparisons of the simulated signal process between the generic detector simulations Delphes 1.9 [94] and PGS 4 [95] and the full ATLAS detector simulation will be performed. The generic simulations can be used *e.g.* by theorists, who do not have access to the simulations developed by the experimental collaborations. Still they allow to easily incorporate detector acceptances and effects into studies of new theoretical models and predictions.

Delphes and PGS both use strongly simplified models of the calorimeter system and simulate the energy deposition in cells of η and ϕ. Both simulate an electromagnetic and a hadronic calorimeter, where no longitudinal segmentation is simulated. The bending of charged particles in the magnetic field of the tracking devices is taken into account in Delphes to estimate the impact points of tracks in the calorimeter system. Constant

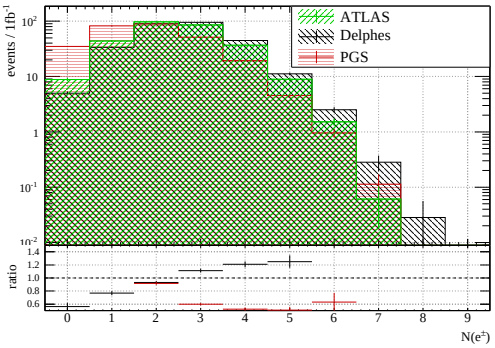

(a) Number of electrons

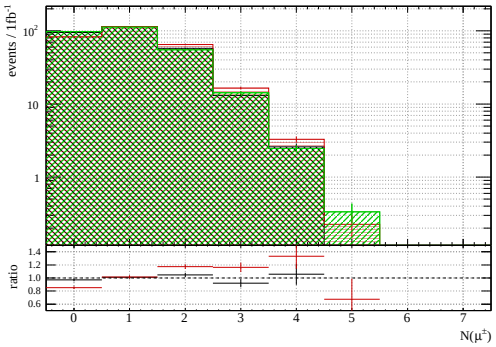

(b) Number of muons

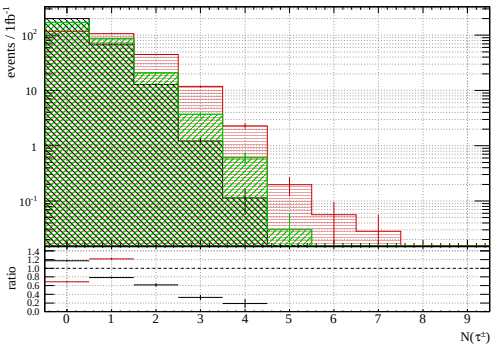

(c) Number of taus

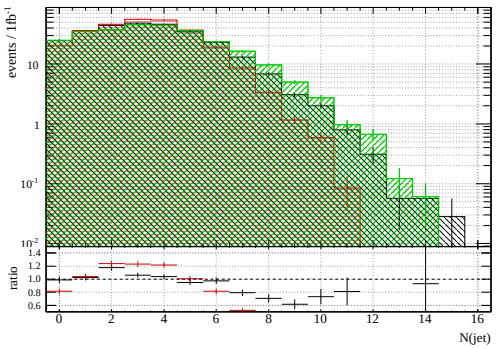

(d) Number of jets

Figure 3.6: Number of reconstructed and identified objects in BC 1 SUSY events for the full simulation of the ATLAS detector and two generic simulations. The quality requirements for the electrons, muons and (hadronically decayed) taus considered here are described in the text. Additionally the mentioned overlap removal procedure between reconstructed objects was performed. No event selection cuts, despite the pre-selection explained in the text, were applied.

track reconstruction efficiencies are assumed for charged particles. The energy deposits in the calorimeter cells of individual particles are smeared according to parametrised energy resolutions with stochastic, noise and constant terms. However, an energy sharing between neighbouring calorimeter cells is not simulated. The types of particles (e/γ versus hadrons) are used to determine to which kind of calorimeter (EM, hadronic) the energy is accounted for.

Jets are reconstructed by running jet algorithms on the simulated energy accumulation of the calorimeter cells. The cell energies are also taken to calculate the expected missing transverse energy $E_{\mathrm{T}}^{\mathrm{miss}}$. For the simulation of electrons, muons and photons simply the corresponding final state particles from the event generator are used, where the energy resolution of the calorimeter may be taken into account for electrons and photons. This means no false-positives (fakes) are simulated for these particles. Tau leptons are more difficult to simulate and are both in Delphes and PGS based on the combination of tracking and calorimeter variables. Only hadronic tau decays with a single charged pion are considered.

We will not go into the details how the generic detector simulations may be further tuned to the ATLAS results, but only show that the parameters used in this analysis yield sufficient agreement at least for Delphes with the ATLAS full simulation in the distributions and the cut flow relevant for the SUSY analysis in Chapter 5. The tau identification in Delphes *e.g.* can be improved by using multivariate techniques instead of simple cuts and may be tuned to different working points of the identification efficiency as it was shown in the bachelor thesis, reference [100].

In order to get sensible comparisons the internal overlap removal within PGS has been disabled. Instead the same procedure for overlap removal between reconstructed electrons, muons, taus and jets has been applied following the definitions summarised in Section 5.1.1. Also the object identification in case of the full simulation was done as mentioned there. Both for the full simulation and Delphes an anti-$k_\perp$ jet algorithm [87] was applied with parameter $R = 0.4$. PGS does not provide the anti-$k_\perp$ jet algorithm itself, instead the $k_\perp$-algorithm [85, 86] was used. The same comparison was also done using a cone algorithm for all three simulations, but it will not be shown here, because the results are very similar. The "crack region" of the ATLAS calorimeter (*cf.* Section 2.2.2 and 2.2.5) is especially difficult to simulate and usually electrons within this region are disregarded. We do the same here and reject events with identified electrons in this region ($1.37 < |\eta| < 1.52$). An identical sample of generated events has been used for Delphes and PGS, whereas a statistically independent sample was used as input for the full ATLAS simulation. However, the same version of Herwig implemented in the ATLAS software framework was used, such that no systematic differences in the input of all detector simulations occur.

Figure 3.6 shows the number of selected objects after overlap removal for the three detector simulations. One can see immediately that the ATLAS tune of Delphes matches the full ATLAS simulation much better than PGS with its LHC tune. This is not surprising as Delphes uses a more detailed simulation of the calorimeter granularity and was developed with the LHC experiments in mind, whereas PGS was mainly developed for the Tevatron experiments. Good agreement can be achieved for the reconstructed muons, which is also visible in the p_T spectra of the p_T-leading and sub-leading muons in Figure 3.7e and 3.7f. The p_T spectra of electrons (Figure 3.7a – 3.7d) fit reasonably well for Delphes, even though the number of electrons per event (Figure 3.6a) shows that too many electrons are simulated. As a result the scalar sum of the transverse lepton momenta $\sum_\mathrm{lep} p_\mathrm{T}$ shows large deviations for PGS (Figure 3.8). We do not want to discuss details of the electron simulation in Delphes here, but instead show that the discrepancies can be largely reduced by simply applying an additional efficiency factor of 95 % to 98 % (*cf.* Figure B.2 in Appendix B) for electrons.

Tau leptons are badly described in PGS as well as in Delphes. Both simulate too many tau leptons (Figure 3.6c) and do not correctly reproduce their transverse momentum spectra (Figure 3.7g and 3.7h). This lead to the aforementioned bachelor thesis [100] in which a more detailed tau identification procedure was tested. For the purposes Delphes is applied in this thesis, the tau leptons are not essential and no further corrections and tunings are performed. PGS provides a smaller number of jets (Fig-

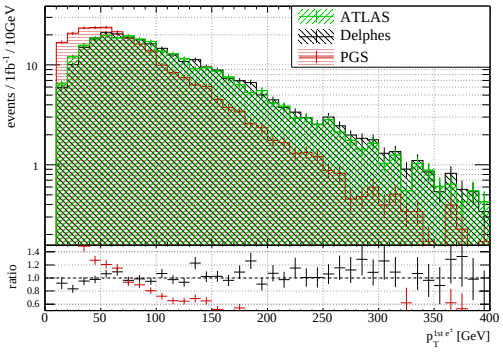

(a) Leading electron

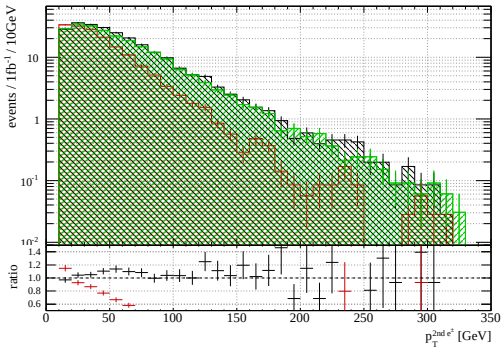

(b) 2nd electron

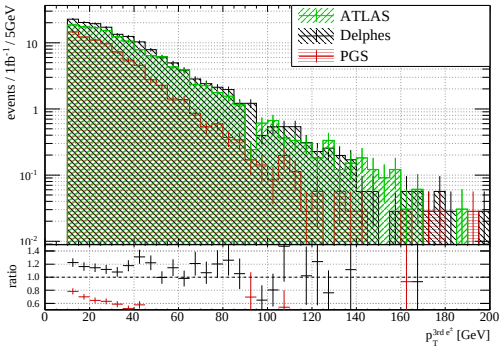

(c) 3rd electron

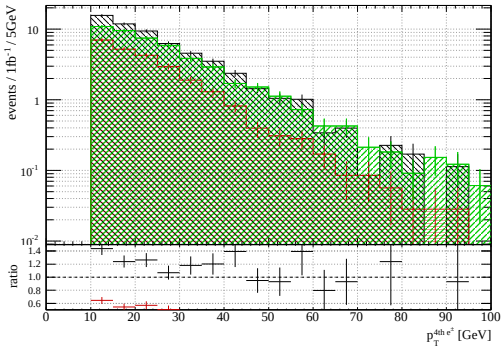

(d) 4th electron

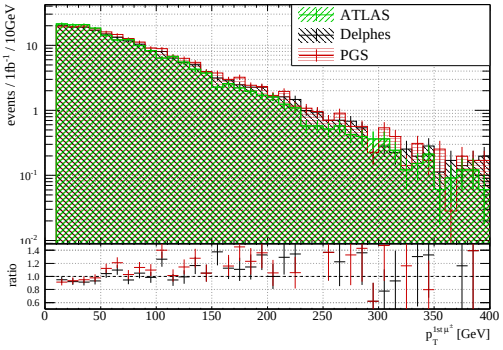

(e) Leading muon

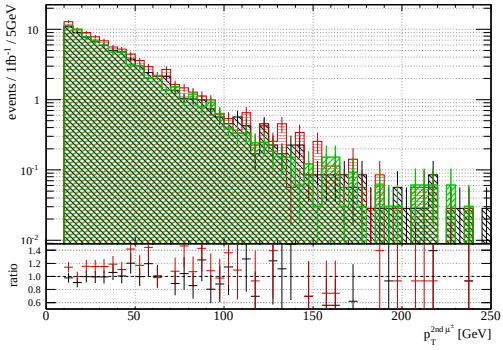

(f) 2nd muon

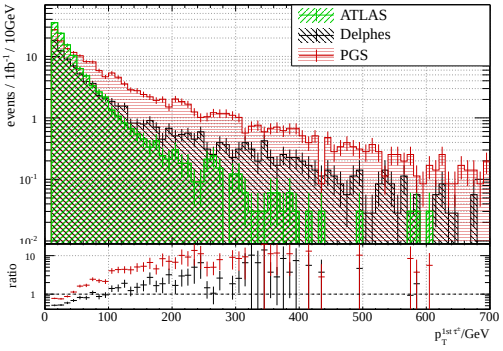

(g) Leading tau

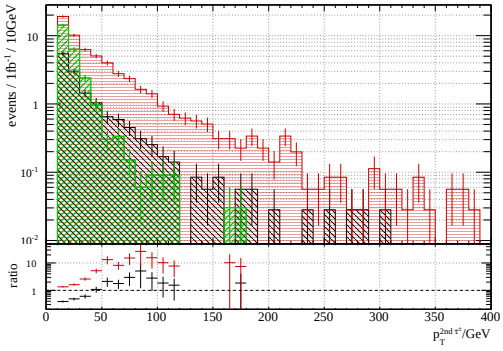

(h) 2nd tau

Figure 3.7: Transverse momentum p_T of the leading and the 2nd reconstructed and identified lepton in each event for the BC 1 signal and Standard Model background. The quality requirements for the electrons, muons and (hadronically decayed) taus considered here are described in the text. Additionally the mentioned overlap removal procedure between reconstructed objects was performed. No event selection cuts, despite the cleaning cuts explained in the text, were applied.

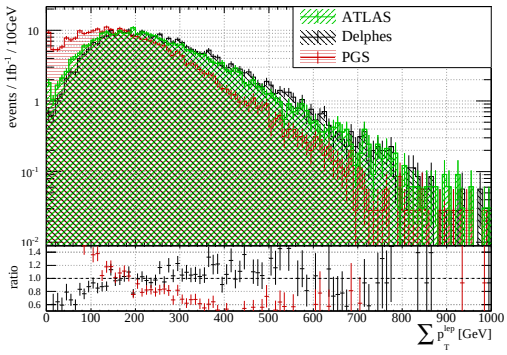

Figure 3.8: $\sum_{\text{lep}} p_{\text{T}}$ in BC 1 signal in different detector simulations. No event selection cuts, despite the cleaning cuts explained in the text, were applied.

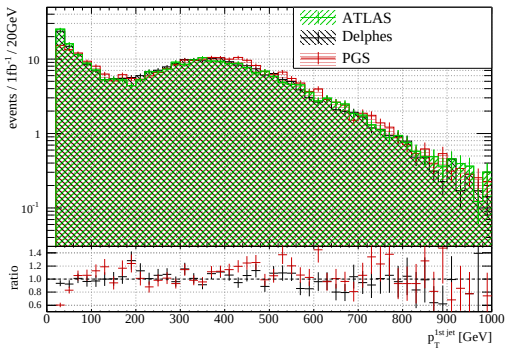

(a) Leading jet

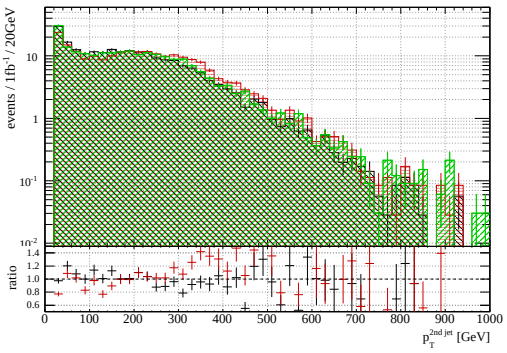

(b) 2nd jet

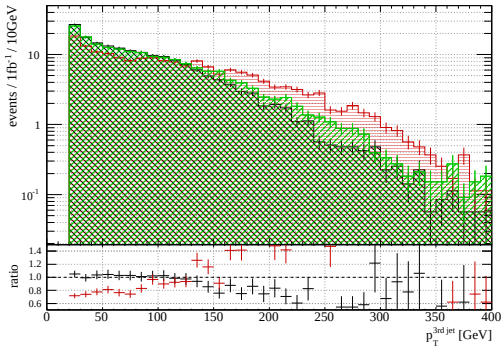

(c) 3rd jet

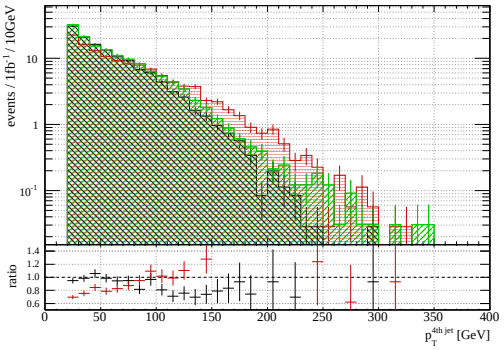

(d) 4th jet

Figure 3.9: Transverse momentum p_{T} of the four hardest jets in each event for the BC 1 signal. Additionally the mentioned overlap removal procedure between reconstructed objects was performed. No event selection cuts, despite the cleaning cuts explained in the text, were applied.

ure 3.6d) with higher momenta as the full ATLAS simulation (Figure 3.9), which may partly be accounted for the fact that not the identical jet algorithm was used. Though, also comparisons using a cone algorithm for both detector simulations showed larger discrepancies. The description of jets by Delphes is reasonably good, even though the jet energy scale is slightly off. Comparisons with the jet energy scale increased by 5 % and 10 %, respectively (*cf.* Figure B.1), in addition to a reduced electron efficiency of $\epsilon'_{\text{e}\pm} = 95\,\%$ show a better agreement. Consequently the scalar sum of the transverse

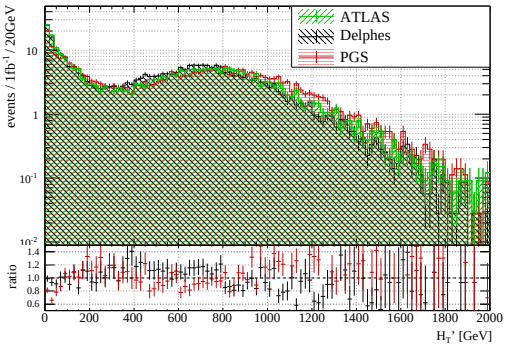

(a) H'_{T}

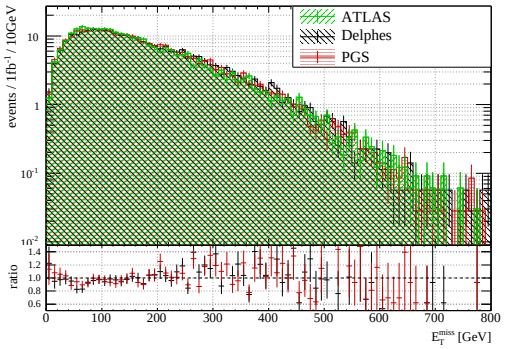

(b) $E_{\mathrm{T}}^{\mathrm{miss}}$

Figure 3.10: H'_{T} and $E_{\mathrm{T}}^{\mathrm{miss}}$ in BC 1 signal for different simulations of the ATLAS detector. No event selection cuts, despite the cleaning cuts explained in the text, were applied.

cut	ATLAS	Delphes	Delphes $\epsilon_{\mathrm{e}} = 95\,\%$	$\epsilon_{\mathrm{e}} = 95\,\%$, JES+5 %	$\epsilon_{\mathrm{e}} = 95\,\%$, JES+10 %
before cuts	341.4 ± 3.5	341.4 ± 1.9	341.4 ± 1.9	341.4 ± 1.9	341.4 ± 1.9
no electrons in crack region	306.7 ± 3.4	304.7 ± 1.8	306.5 ± 1.8	306.5 ± 1.8	306.5 ± 1.8
$p_{\mathrm{T}}(1\mathrm{st}\ \mu^{\pm}) > 30\,\mathrm{GeV}$	156.9 ± 2.4	158.5 ± 1.3	159.4 ± 1.3	159.4 ± 1.3	159.4 ± 1.3
$p_{\mathrm{T}}(1\mathrm{st}\ \mathrm{e}^{\pm}) > 30\,\mathrm{GeV}$	135.7 ± 2.2	138.7 ± 1.2	136.0 ± 1.2	136.0 ± 1.2	136.0 ± 1.2
$p_{\mathrm{T}}(2\mathrm{nd}\ \mathrm{e}^{\pm}) > 10\,\mathrm{GeV}$	112.7 ± 2.0	117.7 ± 1.1	111.7 ± 1.1	111.7 ± 1.1	111.7 ± 1.1
$\sum_{\mathrm{lep}} p_{\mathrm{T}} > 85\,\mathrm{GeV}$	112.6 ± 2.0	117.6 ± 1.1	111.6 ± 1.1	111.6 ± 1.1	111.6 ± 1.1
$H'_{\mathrm{T}} > 100\,\mathrm{GeV}$	81.4 ± 1.9	85.9 ± 0.9	81.9 ± 0.9	82.5 ± 0.9	83.3 ± 0.9
$H'_{\mathrm{T}} > 200\,\mathrm{GeV}$	71.7 ± 1.6	75.7 ± 0.9	72.1 ± 0.9	72.7 ± 0.9	73.5 ± 0.9
$H'_{\mathrm{T}} > 300\,\mathrm{GeV}$	66.4 ± 1.6	69.5 ± 0.8	66.2 ± 0.8	66.9 ± 0.8	67.6 ± 0.8
$H'_{\mathrm{T}} > 465\,\mathrm{GeV}$	57.4 ± 1.5	57.9 ± 0.8	55.1 ± 0.8	56.8 ± 0.8	58.3 ± 0.8

Table 3.1: Cut flow comparison between the ATLAS simulation and Delphes

momenta of the four leading jets $H'_{\mathrm{T}} = \sum_{\mathrm{jet}\ 1\text{–}4} p_{\mathrm{T}}$ fits reasonably well in Figure 3.10a. The same holds for the missing transverse energy (Figure 3.10b).

Table 3.1 applies the event selection cuts which will be derived in Section 5.1.2 to events simulated with the ATLAS full simulation as well as Delphes with different corrections of the electron efficiency and the jet energy scale. It can be seen that good agreement within the statistical uncertainty of the samples used can be achieved for a correction of the electron efficiency of $\epsilon'_{\mathrm{e}^{\pm}} = 95\,\%$ and an increased jet energy scale of 5 %. This level of agreement is sufficient to apply Delphes for a parameter scan in Section 5.2.

3.3 Summary

Simulations of the detector are essential to compare predictions by Monte Carlo event generators to measured data. Event generators and detector simulations need to be tuned to give reliable predictions of Standard Model backgrounds as well as the signal processes one is interested in. The computing time is a very crucial point in the detector simulations, because the propagation of particles through the detector volume and the simulation of their interaction with the detector material can be very complicated, depending on the level of detail. For the same reason not one single detector simulation can serve all needs. In general one tries to apply a detector simulation, which matches the real detector best. For some applications this may be prohibitively slow, especially when regions of the parameter space of new theoretical models are investigated.

The ATLAS experiment provides a very detailed detector simulation based on Geant 4, but also fast simulations at different levels. FATRAS is a novel approach to simulate the tracks of charged particles in the ATLAS Inner Detector and the Muon Spectrometer. Its results can be fed into the standard event reconstruction algorithms giving it a significant advantage in comparison to detector simulations purely based on parametrisations of detector resolutions. The simulation time of the ATLAS Inner Detector can be reduced by a factor of 50 in typical $t\bar{t}$ events compared to the full Geant 4 based simulation using the FATRAS approach. Comparisons of FATRAS to the full simulation and to first collisions data showed a good agreement.

Generic detector simulations like Delphes and PGS are another option to estimate the detector response. They are much more simple than the previous solutions, but may provide already a good overall picture, what may be expected in certain models. PGS does not describe the ATLAS detector very well for models with many final state leptons. However, Delphes was adjusted to give a reasonably good agreement for the R-parity violating SUSY signal we are interested in. Hence it will be used in Section 5.2 to investigate the discovery potential for a certain class of R-parity violating SUSY models in the parameter space around the chosen benchmark scenario.

Chapter 4

Tau identification

"... die schlechten ins Kröpfchen, die guten ins Töpfchen."
— Brüder Grimm, "Aschenputtel", 1812

Tau leptons ($\tau^{\pm}$) together with the related neutrino form the third generation of leptons (Greek: $\lambda\epsilon\pi\tau o\varsigma$ =light) in the Standard Model. However, they have a mass of 1777 MeV [8], *i.e.* about 3500 times the mass of the electron and about 17 times the mass of the muon, giving them very special properties. They decay via the weak interaction, but are heavy enough to decay into leptons as well as hadrons. This allows for example to measure the strong coupling constant in tau decays, which gives indeed one of the most precise single measurements of the strong coupling constant α_s at low energies [101].

Due to their high mass, they are also interesting for the discovery of the Higgs boson in low Higgs mass ranges at the LHC, especially for charged MSSM Higgs bosons [67], because the coupling of the Higgs is proportional to the particle mass. Furthermore, the third generation plays a special role in many theories beyond the Standard Model, and often new particles are expected to decay predominantly into tau leptons. SUSY models *e.g.* in general violate universality between electrons, muons, and taus, and decays to tau leptons can be dominant [19, 67]. The kinematic properties of the tau decay products can even give hints on polarisation effects as we will shortly see in the next section. We have already seen in Section 1.2.3, that tau leptons are also interesting in the framework of R-parity violating SUSY models with a $\widetilde{\tau}$ as lightest supersymmetric particle.

The following Section 4.1 will shortly review the most important properties of tau leptons and Section 4.2 describes the experimental challenges to identify tau leptons in (hadron) collider experiments. Energy flow algorithms (Section 4.3) can help to improve the reconstruction of tau leptons and their decay products. The conventional algorithm for tau identification in ATLAS is described in Section 4.4. In Section 4.5 a new approach to tau lepton identification in the ATLAS experiment is introduced, which is based on a generic energy flow algorithm. Details of the new approach are given in Section 4.5.1 and comparisons of its performance in Monte Carlo studies and first data of the ATLAS detector are made in Section 4.5.4.

4.1 Tau lepton properties

Tau leptons have a short, but finite lifetime of $\tau_\tau = (290.6 \pm 1.0) \times 10^{-15}$s, equivalent to $c\tau_\tau = 87.11\,\mu$m [8], *i.e.* a tau lepton with an energy of $E = 10\,$GeV would have a mean flight path of 490 µm. Therefore only its decay products are directly detected in typical collider experiments.

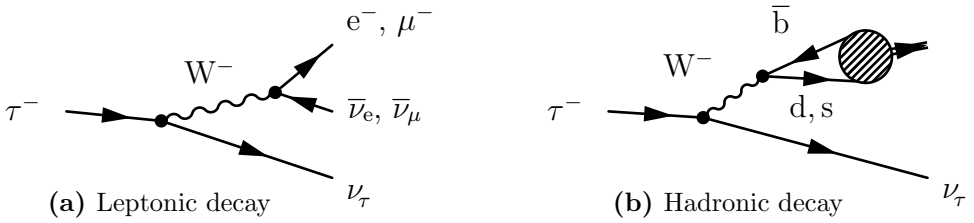

(a) Leptonic decay **(b)** Hadronic decay

Figure 4.1: Feynman diagrams for tau lepton decays.

Tau leptons decay weakly via (virtual) $\mathrm{W}^\pm$ bosons as indicated by the Feynman diagrams in Figure 4.1. They are heavy enough such that the W boson can decay into electrons or muons (Figure 4.1a) and into a pair of light quarks (Figure 4.1b). The branching ratios between leptonic ($\mathcal{B}(\tau^- \to \mathrm{e}^-\overline{\nu}_\mathrm{e}\nu_\tau) = 17.85\,\%$, $\mathcal{B}(\tau^- \to \mu^-\overline{\nu}_\mu\nu_\tau) = 17.36\,\%$) and hadronic decays follow roughly the naive expectations for three color/anti-color states and two lepton families that can occur equiprobable in the decay.

The pair of light quarks produced in the hadronic decay forms a mesonic resonance (mainly $\rho^\pm$ and $\mathrm{a}_1^\pm$ in addition to $\pi^\pm$), which itself decays into charged and neutral mesons. Most of these resonances have a large decay width compared to their mass, *i.e.* they decay nearly immediately. One classifies the hadronic decay modes according to the number of charged particles (mainly $\pi^\pm$) into 1-prong ($\mathcal{B} \approx 50\,\%$) and 3-prong ($\mathcal{B} \approx 15\,\%$) decays. Decays with five and more charged particles occur with a branching ratio of about $\mathcal{B} \approx 0.1\,\%$ [8]. Especially in the 1-prong decays one also observes a significant fraction of decays with additional neutral mesons (mainly π^0). Table 4.1 summarises the most important decay modes and their branching ratios. Neutral pions are not stable themselves but decay with a mean life time of $\tau_{\pi^0} = (8.4 \pm 0.5) \times 10^{-17}\,$s ($c\tau_{\pi^0} = 25.1\,$nm) nearly completely into two photons ($\mathcal{B}(\pi^0 \to \gamma\gamma) = 98.82\,\% \pm 0.03\,\%$) [8]. The remaining decays include electron-positron pairs.

The branching ratios of the tau decays and their properties have already been measured with high precision in previous experiments. This knowledge is used to tune the identification of tau decays at the LHC experiments. Additionally the special properties of some hadronic decay modes of the tau lepton can be used to gain insights in the polarisation states of certain processes including tau leptons. For example reference [102] makes use of tau decays to estimate the spin configuration of sparticles in SUSY decay chains. This requires not only the identification of tau decays, but also the decay

decay mode	branching ratio $\mathcal{B}$ (%)
$\tau^- \to e^- \overline{\nu}_e \nu_\tau$	17.85 ± 0.05
$\tau^- \to \mu^- \overline{\nu}_\mu \nu_\tau$	17.36 ± 0.05
$\tau^- \to h^- \nu_\tau$	11.61 ± 0.06
$\tau^- \to h^- \pi^0 \nu_\tau$	25.94 ± 0.09
$\tau^- \to h^- 2\pi^0 \nu_\tau$	9.51 ± 0.11
$\tau^- \to h^- \geq 3\pi^0 \nu_\tau$	1.34 ± 0.07
$\tau^- \to h^- h^+ h^- \nu_\tau$	9.80 ± 0.08
$\tau^- \to h^- h^+ h^- \pi^0 \nu_\tau$	4.75 ± 0.06

Table 4.1: Branching ratios of selected decay modes of tau leptons (compiled from [8]). h^- stands for π^- or K^-, even though the modes are mainly π^- dominated.

mode. Here one makes use of the conservation of angular momentum in the tau decay in combination with the helicity of the neutrino. Depending on the polarisation of the decaying tau lepton the sharing of energy between the neutrino and the hadronic decay products is different.

4.2 Experimental challenges

The identification of leptonic tau decays is usually not considered in collider experiments, because the distinction from electrons or muons which are created promptly, *i.e.* directly at the primary interaction point, is assumed to be too complicated. The only criterion for leptonic decays is the flight path of the tau lepton, which is mostly too small in the interesting energy range to be resolved. However, in the context of the mass reconstruction of certain sparticles in supersymmetric models tau decays into muons have been considered as well [103].

Hadronic decays of tau leptons can be distinguished from particle jets produced in the hadronisation of color charged objects, *i.e.* quarks and gluons, because the decay of the W boson into hadrons is much more constrained. Firstly, one observes the distinct feature of one or three charged particles as explained above. Secondly, the decay products are usually much more collimated, than a quark or gluon jet of the same energy. Thirdly, one also observes a "hierarchy" between the most energetic charged pion and the other decay products. Figure 4.2 illustrates how a tau jet may be thought of.

Consequently, the treatment of hadronically decayed tau leptons in the experiment usually consist of two steps. At first one searches for candidates of hadronic tau decays and calculates specific quantities which characterise the tau decay. Afterwards multivariate techniques, but also simple cuts, are applied to identify candidates which stem from real tau decays.

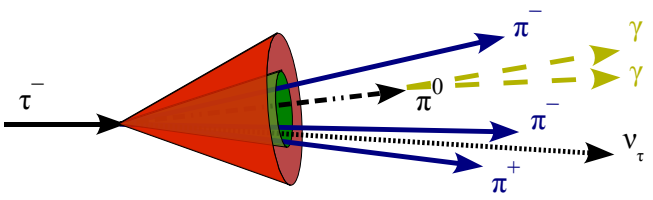

Figure 4.2: Sketch of a tau jet for a hadronic tau decay. The green cone illustrates the collimated decay products and the red cone the isolation region assumed in the tau identification.

4.2.1 Track reconstruction for charged pions from tau decays

To fully exploit the properties of the hadronic tau decays in the experiment one needs a very efficient and pure reconstruction of charged pions, as well as a high spatial and energy resolution for charged and neutral particles. In the following, some of the problems of the reconstruction of charged pions which occur in the context of tau lepton identification in the ATLAS experiment are investigated.

It turns out that two effects have the main impact on the efficiency and purity of the reconstruction of charged pions in the inner tracking system. Tracks from charged pions can be lost due to hadronic interactions of the pions with the detector material. Ideally this only happens in the hadronic calorimeter, but there is a chance for an early interaction in the innermost layers of the Inner Detector. The products of the hadronic interaction are usually not reconstructed by the tracker or at least not enough correlated with the original pion and one reconstructs less tracks than pions produced in the tau decay. Additional tracks may be reconstructed in the vicinity of the tau jet, because photons from π^0 decays can interact with the detector material and produce electron–positron pairs in photon conversions. If the interaction happens in the innermost detector layers the electrons can mimic $\pi^\pm$ from the tau decay and disturb the reconstruction of the tau decay.

Lost $\pi^\pm$ tracks cannot easily be recovered, but "fake" tracks from photon conversions or "ghost" tracks from noise measurements can be suppressed by certain track selection criteria. The requirement of tracks to originate from a region around the primary interaction vertex also helps to suppress tracks from cosmic ray muons and pile-up events. One therefore applies cuts on the transverse ($|d_0|$) and longitudinal impact parameters ($|z_0 \cdot \sin\theta|$) which are calculated with respect to the reconstructed primary vertex or to the estimated beam spot position if no primary vertex was reconstructed in the event. One also requires a certain number of measurements being used in the track fit to make sure that only well reconstructed tracks are taken into account. The SCT measurements are counted individually for each side of a detector module. Therefore 3 Pixel hits, 8 SCT hits and 30 TRT hits are expected on average for a well reconstructed track in the Barrel region of the Inner Detector[1]. Detector modules known to be inactive are taken

[1] In fact the average number of Pixel and SCT hits is even slightly higher, because the detector modules are mounted with a small overlap in each layer and tracks in this region can pass two modules in one layer.

selection criteria	PanTau qualified	TauRec leading	TauRec other
$p_{\mathrm{T}}^{\mathrm{min}}$ (GeV)	1.0	6.0	1.0
max. $\lvert d_0 \rvert$ (mm)	2.0	2.0	1.0
max. $\lvert z_0 \cdot \sin\theta \rvert$ (mm)	10.0	10.0	1.5
min. b-layer hits	0	0	1
min. Pixel hits	2	0	2
min. SCT hits	0	0	0
min. silicon hits	7	7	7
min. TRT hits	0	0	0

Table 4.2: Track selection criteria for tracks in tau jets. The transverse ($|d_0|$) and longitudinal impact parameters ($|z_0 \cdot \sin\theta|$) are calculated with respect to the reconstructed primary vertex or to the estimated beam spot position if no primary vertex was reconstructed in the event.

into account in the requirement of the minimal number of Pixel, SCT and TRT measurements, *i.e.* a track passing a region where all Pixel modules are non-operational would still pass the Pixel hits requirement. This does not apply, however, for the requirement of b-layer hits, *i.e.* tracks in a region with a dead b-layer module would never pass this cut.

Figure 4.3 shows the number of selected tracks inside tau jets in simulated $\mathrm{Z} \rightarrow \tau\tau$ events[2] for different track selection criteria. It is clearly visible in Figure 4.3a, where no track selection is applied, that more tracks are usually reconstructed than charged pions occur in the tau decay. The impact of photon conversions is also visible as the mean number of reconstructed tracks is higher in tau jets with photon conversions in the Inner Detector volume than in jets of the same decay mode without conversions.

The different track selection criteria are summarised in Table 4.2. "PanTau qualified" denotes a track selection which is used for tracks in the new PanTau approach for tau identification in ATLAS which will be described in detail in Section 4.5.1. "TauRec leading" and "TauRec other" are two selection criteria as they are used in the standard tau reconstruction software TauRec of the ATLAS experiment. The former is used to define regions of interest ("seeds") for the track-based TauRec reconstruction and the latter for further tracks to be considered by TauRec. The "PanTau qualified" selection performs better than the "TauRec other" selection in terms of the number of reconstructed tracks, because it has a slightly higher probability to select the correct number of tracks. The main reason for the better efficiency of the "PanTau qualified" selection is the drop of

[2]The study presented in this section uses `MC09` Monte Carlo samples at a centre-of-mass energy of $\sqrt{s} = 7\,\mathrm{TeV}$ which are summarised in Appendix A.1

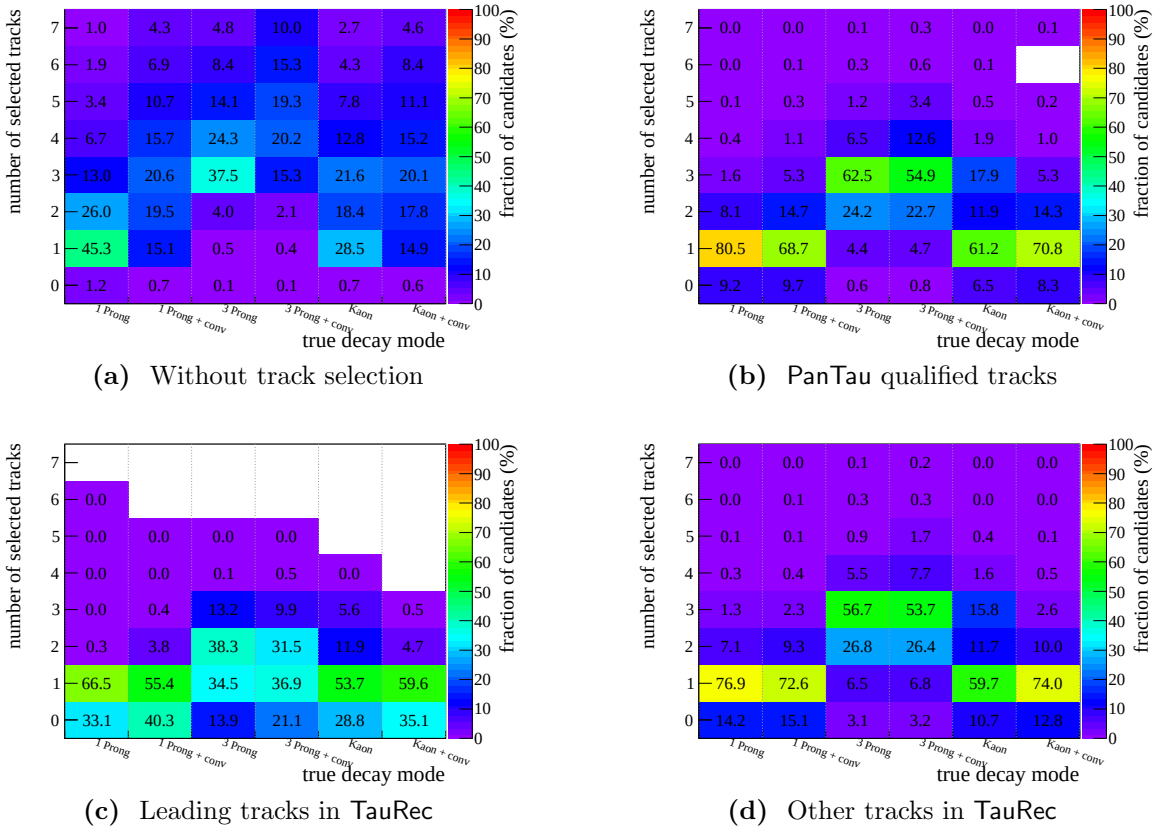

(a) Without track selection

(b) PanTau qualified tracks

(c) Leading tracks in TauRec

(d) Other tracks in TauRec

Figure 4.3: Number of selected tracks in a cone with size $\Delta R < 0.4$ around the true visible momentum $\vec{p}^{\,\mathrm{vis}}$ of tau leptons in simulated $\mathrm{Z} \rightarrow \tau\tau$ events. The diagram shows the fraction of tau jets with a certain number of tracks separately for the main decay modes. Decays with and without photon conversions (denoted "conv") in the Inner Detector volume are distinguished. The different track selection criteria are described in Table 4.2.

the requirement for a b-layer measurement. The relaxed impact parameter requirements have only minor effects.

Figure 4.4a shows the tracking efficiency after applying the "PanTau qualified" selection as a function of the transverse momentum p_{T} of the charged pion. All $\pi^{\pm}$ from hadronic tau decays in $\mathrm{Z} \rightarrow \tau\tau$ events are investigated separately for 1-prong and 3-prong decays. One observes that the track efficiency is about 1 % worse for 3-prong than for 1-prong decays. The occurrence of conversions into e^{+}-e^{-}-pairs inside the Inner Detector volume of photons from the tau decay further reduces the track efficiency by about 1 %. Both effects can be accounted for overlaps between the particle tracks and tracks sharing hits especially in the Pixel layers of the Inner Detector.

Most of the remaining inefficiencies are due to hadronic interactions of the charged pions in the Inner Detector. In those interactions showers of secondary particles are created. The track of the original particle therefore cannot be fully reconstructed. If

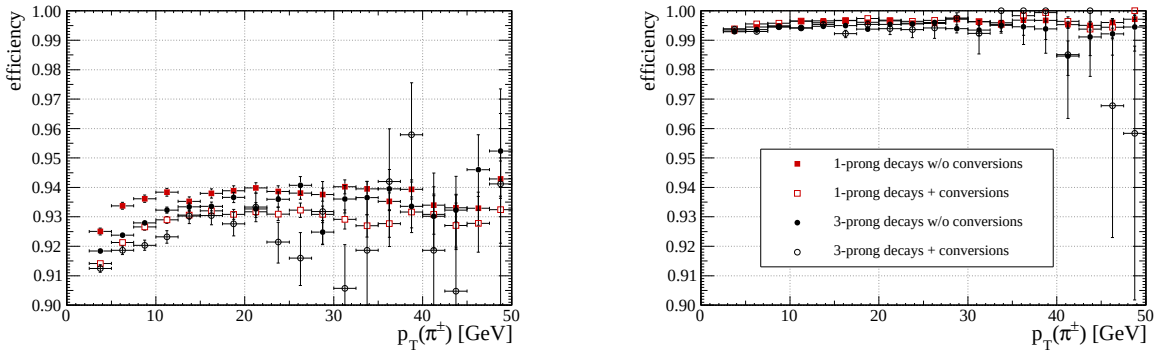

(a) All tau decays **(b)** Without hadronic interactions

Figure 4.4: Track reconstruction and selection efficiency for $\pi^{\pm}$ from hadronic tau decays in $Z \to \tau\tau$ events as a function of the transverse momentum of the $\pi^{\pm}$ (PanTau qualified tracks with $|\eta| < 1.5$). The efficiencies are given separately for 1-prong and 3-prong tau decays. Additionally one distinguishes tau decays where photons from the decay converted into e^+-e^--pairs inside the Inner Detector volume. (a) includes all tau decays, whereas (b) excludes tau decays where at least one $\pi^{\pm}$ interacted hadronically with the detector material inside the Inner Detector volume.

the interaction happens early, *i.e.* in the beam pipe or in one of the first detector layers the track may be lost. Figure 4.4b shows the same graph as Figure 4.4a, but excluding tau decays, where at least one charged pion interacted inside the Inner Detector volume. Here the efficiency for all decay types is nearly 99.5 % compared to $\approx$ 93 % before.

In addition to effects from hadronic interactions further degradations in the track reconstruction efficiency for charged pions can be observed in highly boosted tau decays. The more the tau decay products are boosted, the smaller the angular separation between tracks gets in 3-prong decays. If the pions themselves have high transverse momenta, such that they are only slightly deflected in the magnetic field, their tracks will overlap in the Inner Detector and may not be resolvable anymore at a certain point.

It is clearly visible in Figure 4.5a how the track reconstruction efficiency in 3-prong decays from highly energetic taus decreases as the angle between the pions gets smaller. However, this effect is not observed for tau leptons from $Z \to \tau\tau$ events (Figure 4.5b), which have lower momenta on average than those in Figure 4.5a. Even though the angular separation at the primary vertex can be small, no large overlap occurs, because the tracks of lower momentum are bent away from each other due to the magnetic field.

Tau leptons from the Standard Model processes with the highest tau abundance ($Z \to \tau\tau$ and $W \to \tau\nu$) do not suffer from reduced track reconstruction efficiencies due to Lorentz boosts. The tau leptons expected in the SUSY scenarios studied in this thesis have even lower mean momenta. Hence this effect is not considered further. If one is interested in tau leptons with very high momenta as they are predicted *e.g.* in the

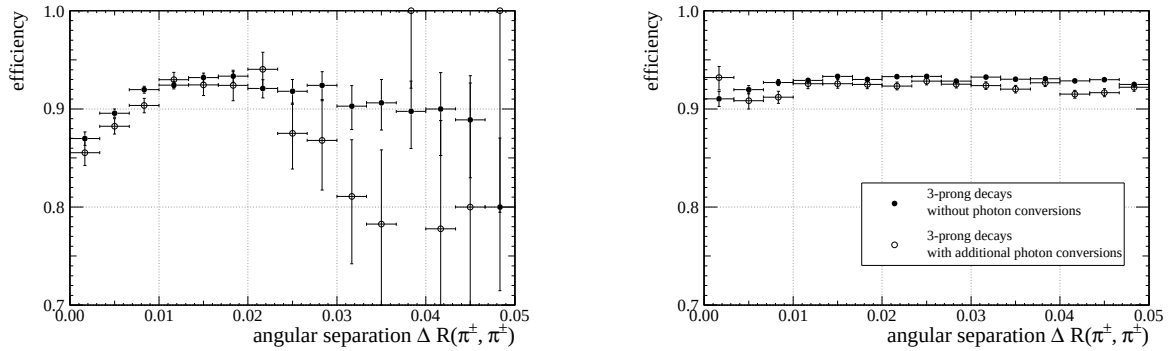

(a) $A^0(m = 500\,\text{GeV}) \to \tau\tau$ **(b)** $Z^0 \to \tau\tau$

Figure 4.5: Track reconstruction efficiency versus the minimal angular separation ΔR of charged pions from 3-prong tau decays (PanTau qualified tracks with $|\eta| < 1.0$). The minimal ΔR from Monte Carlo truth between the considered track and the two other $\pi^{\pm}$ is used for each track. The two figures compare the behaviour for very high momentum taus from $A^0 \to \tau\tau$ events with a simulated A^0 mass of $m_{A^0} = 500\,\text{GeV}$ and taus with medium momenta from $Z^0 \to \tau\tau$ events.

decay of heavy supersymmetric Higgs bosons ($A^0 \to \tau\tau$), specialised track reconstruction algorithms for dense track environments may be considered (*cf. e.g.* [104], [105]).

4.2.2 Detector misalignments

In very early data, *i.e.* in the first one to three months after the beginning of operation, but also later on, additional uncertainties in the track reconstruction arise from an imperfect alignment of the tracking devices. The knowledge about the exact positions of detector modules can be significantly increased by using particle tracks from collision events in a so-called alignment procedure. Before operation of the accelerator the alignment can only be performed by external systems and tracks from cosmic muons, which have a limited precision. However, even after considering millions of tracks from collision events in the alignment procedure still systematic uncertainties in the knowledge of the position of the detector modules remain due to so-called *weak modes*. Weak modes correspond to distortions in the detector geometry which do not contribute to the measured χ^2 of reconstructed tracks. Hence, they are only weakly constrained in the alignment procedure. The track selection criteria should therefore be robust to effects from misalignments. Prior to the start of operation the impact of misalignments of the Inner Detector on selected physics processes including tau lepton reconstruction has been studied using Monte Carlo simulations [106]. Contrary to the other studies presented in this thesis, the misalignment studies in this section use MC08 Monte Carlo samples at a centre-of-mass energy of $\sqrt{s} = 10\,\text{TeV}$, *cf.* Appendix A.

The "TauRec other" and the "TauRec leading" track selection differ, despite the momentum cut, mainly in the harder requirements on the longitudinal and transverse

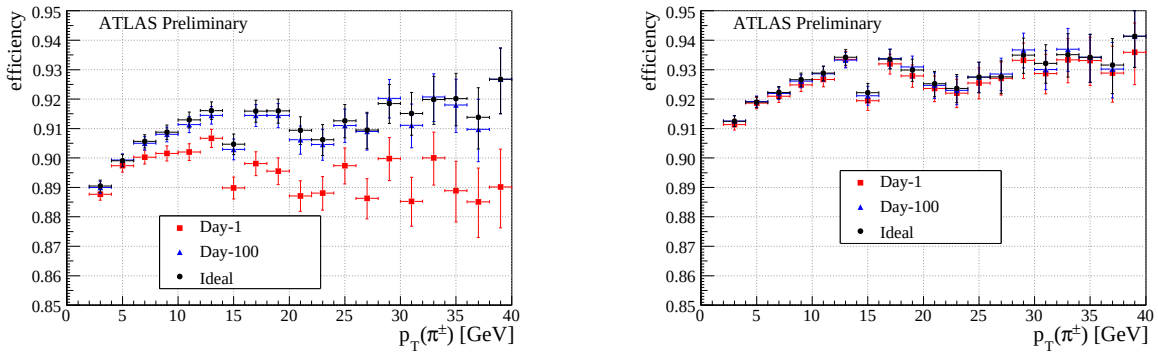

(a) TauRec other **(b)** TauRec leading (lowered p_T threshold)

Figure 4.6: Track reconstruction efficiency after track selection versus the pion transverse momentum of pions from tau decays in $Z \to \tau\tau$ events ($|\eta| < 1.5$). The track efficiency is evaluated using an ideal detector geometry and using misaligned detector geometries with two sets of random misalignments as they are expected shortly after LHC start up. The p_T threshold of the "TauRec leading" selection has been lowered to $p_T > 1\,\text{GeV}$.

impact parameter (*cf.* Table 4.2). Especially the track impact parameters with respect to the primary vertex are affected by misalignments in the detector modules (*cf.* Figure 4.7). This results in lower track selection efficiencies if higher level of misalignments are simulated (Figure 4.6). In this study an ideal detector geometry is taken as reference, *i.e.* the same positions of the detector modules were used in simulation and reconstruction. The results denoted with "day-1" and "day-100" used the same simulated Monte Carlo samples, but the positions of the Inner Detector modules have been randomly distorted in the detector description used in the reconstruction. The distortions of "day-1" correspond to the expected uncertainties in the detector alignment at LHC start up and "day-100" after the first round of data reprocessing incorporating knowledge from tracks in collision events. Special attention has been paid to so-called weak modes in the misalignment, which cannot easily be measured in data [107]. The differences between the ideal and the "day-100" geometry can therefore be taken as systematic uncertainties for early data from misalignments on the track reconstruction of charged pions in tau decays.

Finally the reduced impact parameter resolution and track selection efficiency propagates into the observables used to identify hadronic tau decays. However, it turns out that the impact of the systematic uncertainties in the detector alignment have a negligible effect on the tau identification. Figure 4.8 shows two of the track-based identification variables used in the TauRec algorithm, where one observes the largest impact, the transverse flight path significance and the invariant mass of the tracks in multi-prong candidates. The final impact on the tau identification efficiency and the rejection against QCD jets is therefore also negligible as shown in Figure 4.9. The impact of residual misalignments has not yet been studied in the context of the new PanTau approach, but the aforementioned results may be generalised to PanTau as well. Also in the case of PanTau one would expect only minor systematic effects from Inner Detector misalignments.

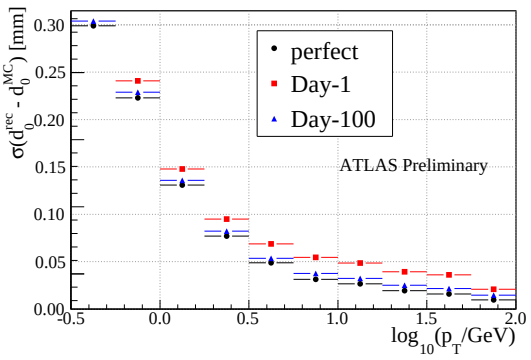

(a) d_0 resolution vs. track p_T, integrated over $|\eta| < 2.5$

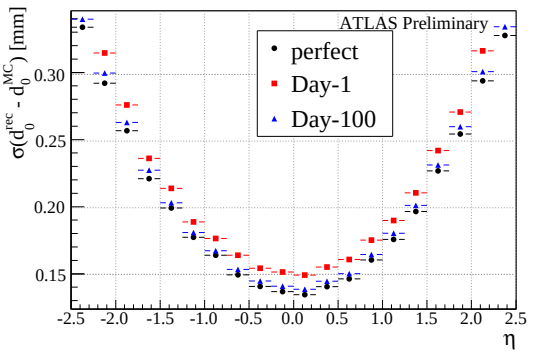

(b) d_0 resolution vs. track η

Figure 4.7: Resolution of the transverse impact parameter d_0 in $Z \to \tau\tau$ events for Day-1, Day-100 and perfect alignment. The resolution is defined as the RMS over a range spanning ± 3·RMS(full range).

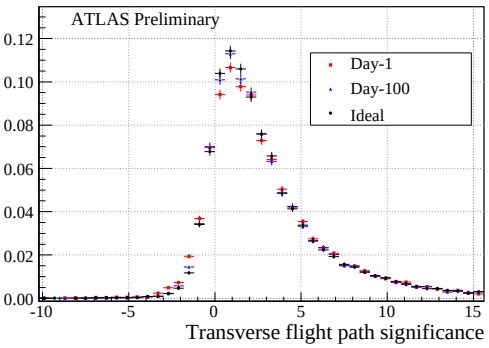

(a) Transverse flight path significance

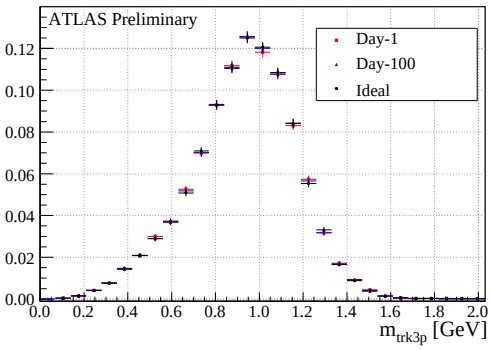

(b) Invariant mass of the track system for multi-track candidates

Figure 4.8: Distribution of identification variables for τ candidates with Monte Carlo truth match in $Z \to \tau\tau$ events for Day-1, Day-100 and perfect alignment.

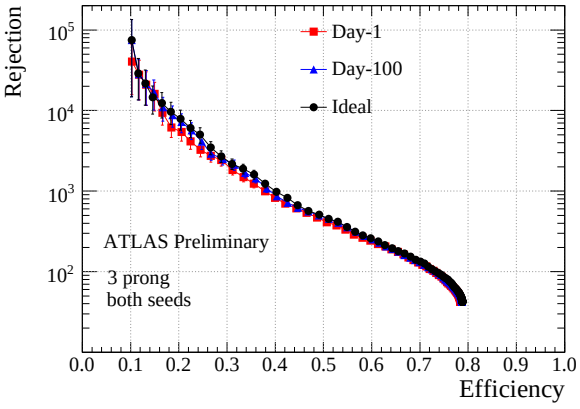

Figure 4.9: Tau efficiency versus jet rejection in the momentum range $10\,\text{GeV} < p_{T_{vis}}^{MCtruth} < 30\,\text{GeV}$ for $Z \to \tau\tau$ 3-prong candidates (efficiency) and QCD di-jet (rejection). The jet rejection is the inverse of the fake rate, for more details see Section 4.5.3. The performance curves are given for the standard Tau-Rec algorithm with different levels of misalignment of the Inner Detector.

4.3 Energy flow algorithms

In the low and medium energy range up to about 130 GeV the momentum resolution of the tracking system supersedes the energy resolution of the hadronic calorimeter. Figure 4.10 illustrates the general behaviour of the relative resolutions according to the following parametrisations

$$\sigma(1/p_{\mathrm{T}}) = 0.34\,\mathrm{TeV}^{-1}(1 \oplus 44\,\mathrm{GeV}/p_{\mathrm{T}}) \text{ (tracking)} \quad (4.1)$$

$$\sigma(E)/E = 50\,\%/\sqrt{E/\mathrm{GeV}} \oplus 3\,\% \text{ (had. calorimetry)} \quad (4.2)$$

taken from [62], where $\oplus$ denotes addition in quadrature. They are only approximately valid in the central barrel region of the detector for charged pions. More details on how the parametrisations have been derived can be found in [62, pp. 5, 163, 303]. Particles in tau and QCD jets of the relevant energies at the LHC exceed the threshold of 130 GeV only rarely. It is therefore a natural approach to take the measurements from the tracking system for charged particles and the calorimeter measurements for neutral particles only. Additionally the neutral component in tau jets is strongly dominated by neutral pions decaying immediately into photons, *i.e.* the neutral component can be measured by the electromagnetic calorimeter, which has a better energy resolution than the hadronic calorimeter (*cf.* Table 2.1).

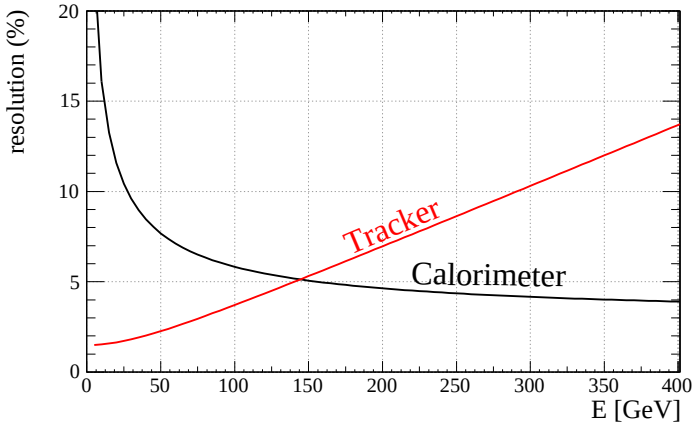

Figure 4.10: Relative energy and momentum resolution of the calorimetry and the Inner Detector tracking system in ATLAS, respectively. The graphs show only approximate resolutions for charged pions at low pseudo-rapidity $|\eta| \approx 0$ (see text).

The term *energy flow* or *particle flow* denotes algorithms implementing the idea to combine the tracking system and the calorimetry in order to improve the overall energy resolution. Energy flow algorithms have already been evaluated at the Large Electron Positron Collider (LEP) [108]. The detector design of certain detector concepts for the future International Linear Collider (ILC) are strongly based on the energy flow approach and one tries to optimise the calorimeter for energy flow [109, 110]. Note, that very different solutions are subsumed under the term energy flow. Furthermore, the actual implementation is constrained by the calorimeter used in the experiment.

The most crucial part of the energy flow reconstruction is the matching of tracks from charged particles to the corresponding energy deposits in the calorimeter. Matched

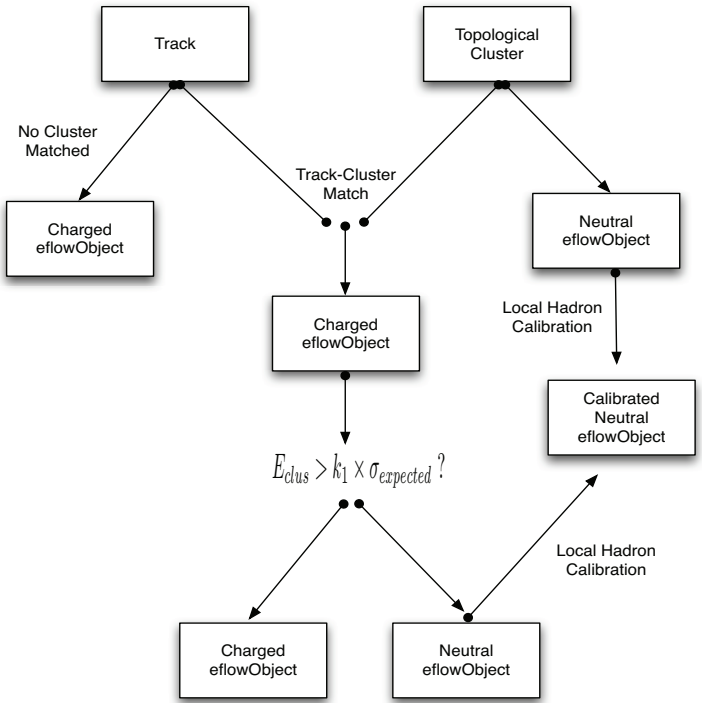

Figure 4.11: Sketch of the workflow of the eflowRec algorithm (from [111]).

energy deposits are subtracted from the calorimeter measurements to be left with the deposits of neutral particles, where the actual subtraction scheme can vary for different algorithms. In the following a short summary of the eflowRec algorithm implemented in the ATLAS software framework is given. A more detailed description of this algorithm can be found in reference [111].

Figure 4.11 sketches the general workflow of eflowRec. eflowRec uses so-called topological clusters built from the measurements in the calorimeter cells [81]. They correspond to spatially connected regions in the calorimeter, where the clusters can span the transverse direction within one calorimeter layer, but also longitudinally between different layers. Starting from seed cells above a certain energy threshold above the noise level of the calorimeter cell, surrounding cells are searched for until they fall below further energy thresholds. Different settings of the clusterisation have been investigated in the context of the tau reconstruction for PanTau as well [112], but the results will not be repeated here. Optimally one would have a one-to-one correspondence between calorimeter clusters and physical particles. In practice, however, a single topological cluster can contain showers from more than one particle and energy deposits of hadrons may be split into several clusters.

Reconstructed tracks are selected with very loose quality requirements and extrapolated into the second calorimeter layer. Here the nearest topological cluster in η and ϕ is selected, where the width of the clusters is taken into account. The energy E_{cluster} of

the matched cluster needs to fulfill the requirement

$$E_{\text{cluster}} > E_{\text{expected}} - k_2 \cdot \sigma_{\text{expected}} \tag{4.3}$$

where E_{expected} is the expected energy deposition of a charged pion corresponding to the track and σ_{expected} its uncertainty in order to make sure that the cluster does not have significantly less energy than one would expect. k_2 is an additional parameter which needs to be tuned. If the condition is satisfied, the expected energy is removed from the cluster using a special subtraction scheme described later. The track together with its matched cluster forms a so-called charged `eflowObject` (EFO), where the 4-momentum of the `eflowObject` is derived from the track information. This procedure is repeated for all other tracks matched to the cluster.

The energy-subtracted remnant cluster can still contain a certain amount of energy. If the remaining energy exceeds the threshold

$$E'_{\text{cluster}} > k_1 \cdot \sigma_{\text{expected}} \tag{4.4}$$

one assumes that the energy is not simply a fluctuation in the energy deposition, but was caused by additional neutral particles in the same direction. Those remnant clusters and topological clusters without any matched track form neutral `eflowObject`s where the 4-momentum is calculated from the cluster applying a local calibration of the cluster energy using cluster shapes (local hadron calibration, [113]). If no cluster with the above requirement can be matched to a track a charged `eflowObject` without an assigned cluster is created.

Electromagnetic showers of electrons and photons in the calorimeter are usually very regular and can be well described by shower models. The interactions of hadrons in the calorimeter on the contrary can be very irregular, *i.e.* a single hadron may create several non-connected energy deposits. In this case the energy of the particle is split between those clusters and requirement (4.3) is not fulfilled. Without this requirement one would therefore double count part of the energy, because only one of the clusters would be matched to the track and the others would be interpreted as additional neutral clusters. If a track and a cluster have been matched, while the requirement is not fulfilled, eflowRec uses a conservative approach. It creates a charged `eflowObject` with assigned track and cluster, but the energy is calculated from the cluster. This way the total energy is kept constant and double counting of energy is avoided, even though one gives up the good momentum resolution.

The energy requirement alone does not fully solve the problem, though, because in the above example one would end up with a charged EFO having the energy of the cluster and several additional neutral EFOs. This effect can be seen in Figure 4.12a, where the energy resolution of the charged component of $\tau^{\pm} \to \pi^{\pm}\pi^0\nu$ decays as reconstructed with eflowRec is shown. Obviously in a significant fraction of the tau decays the charged component is underestimated, while the neutral component is overestimated by the same amount. This has been fixed with the implementation of a *recovery algorithm* for split

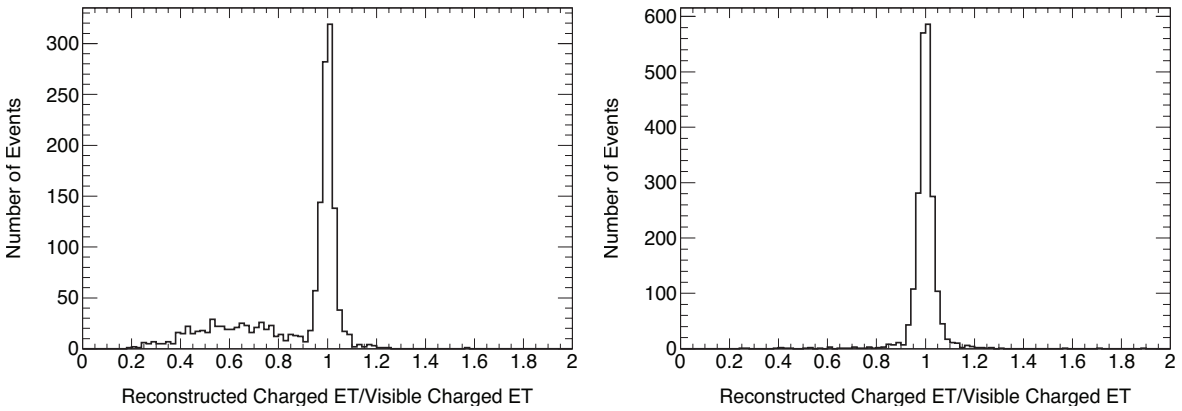

(a) without splitting recovery **(b)** with splitting recovery

Figure 4.12: Energy resolution of the charged component of $\tau^{\pm} \to \pi^{\pm}\pi^0\nu$ decays without (a) and with (b) recovery of the cluster splitting (from [111]).

clusters. The recovery searches for compatible clusters within a $\Delta R < 0.2$ cone around the extrapolated track path through the calorimeter. Afterwards the track energy is subtracted from all those clusters using the same subtraction procedure as before. The impact of the Split Shower Recovery algorithm can be seen in Figure 4.12b, where nearly all decays with significant underestimation of the charged component could be corrected.

One of the most important points, where energy flow algorithms differ is the way how the estimated energy of the extrapolated track is subtracted from the calorimeter clusters. eflowRec uses a cell ordered subtraction, *i.e.* one first defines a cell ordering and afterwards subtracts the contribution of each cell to the cluster until the expected energy of the track has been fully subtracted. The idea behind this approach is motivated by the properties of hadronic showers in the calorimeter (*cf.* [8] and references therein). At the position of the first interaction a prompt electromagnetic shower is created from the production of neutral pions decaying into photons. The photon induced showers create a core with high energy density. They are surrounded by a more diffuse shower of additional hadronic interactions creating a long tail in the energy distribution of the full shower. Therefore it seems natural to subtract the core first as it has the highest energy density and the more regular shape.

In the cell ordering the energy density per cell is weighted by the distance from the extrapolated track position using a two-dimensional Gaussian distribution with a width of 3.5 cm, approximating the Molière radius. Together with an estimate of the position of the first interaction of the shower one can derive "rings" around the extrapolated track in which the cells are ordered. Parametrisations of the mean radial shower profile allow to estimate the relative energy fraction expected to be deposited in each ring in the different calorimeter layers. This information is used to determine the ordering by energy density, but not to estimate the amount of energy to be subtracted.

eflowRec finally provides a collection of charged and neutral energy flow objects (EFO). They also include information on the cluster shape in the calorimeter allowing for a distinction between clusters from hadrons and electrons/photons. The energy flow objects are intended to yield a consistent picture of charged and neutral particles in the detector, while using the best knowledge from the tracking system and the calorimetry. They can be used *e.g.* to calculate the missing transverse energy $E_{\mathrm{T}}^{\mathrm{miss}}$ or – as in the case of PanTau– to reconstruct and identify jets from hadronic decays of tau leptons.

4.4 Common algorithms for tau reconstruction in ATLAS

Two approaches to the reconstruction and identification of hadronic tau decays are commonly used in the ATLAS experiment. The first approach, TauRec, is calorimeter-based and starts from clusters of energy deposits in the calorimeter [114]. It was supplemented by a second algorithm, tau1p3p, which is more track oriented and introduced the concept of energy flow into the tau reconstruction in ATLAS [115]. Both algorithms have been merged into a single algorithm in recent software releases under the name TauRec.

Only the basic principles of the merged TauRec algorithm will be presented here to clarify the differences to our new approach PanTau, which will be introduced in Section 4.5.1. Details about TauRec can be found in reference [116] and [67, 117]. In a first step the track-based approach uses "leading" tracks as seeds to obtain regions of interest for further investigation. Additional tracks around the leading seed track are considered within $\Delta R < 0.2$ satisfying other quality criteria. The track selection criteria and related issues have already been discussed in Section 4.2.1. Independent from the track-seeding TauRec builds calorimeter seeds by using cone jets with cone radius $\Delta R = 0.4$ made up from topological clusters in the calorimeter. The jets must have a transverse energy of $E_{\mathrm{T}} > 10\,\mathrm{GeV}$ and lie within $|\eta| < 2.5$ to be considered as seeds. Tracks with loose quality criteria are associated to the calorimeter seed within $\Delta R < 0.3$.

In a second step overlaps between the track- and calorimeter-based seeds are removed by matching them within $\Delta R < 0.2$. The η and ϕ directions of the candidates are reconstructed using a p_{T}-weighting of tracks for candidates with a track seed. In the case of candidates only seeded by the calorimeter the directions are calculated from the E_{T}-weighted barycenter of the calorimeter clusters. Similarly the energy of the tau candidate is determined by two different methods. For calorimeter-seeded candidates the energy is calculated from the calorimeter clusters inside the seed jet, where the general local calibration scheme of the cluster energies is applied. Additional correction factors of the tau energy are finally included. The energy is estimated with an energy flow approach only for candidates with a track seed.

The energy flow approach of tau1p3p divides the energy deposition of the tau candidate in the calorimeter in different components. The first component $E_{\mathrm{T}}^{\mathrm{emcl}}$ corresponds

to isolated clusters with energy purely in the electromagnetic calorimeter. The next two components $E_{\mathrm{T}}^{\mathrm{chrgEMtrk}}$ and $E_{\mathrm{T}}^{\mathrm{chrgHADtrk}}$ belong to energy depositions in the electromagnetic and hadronic calorimeter, respectively, which are in the vicinity of extrapolated track positions. Finally, $E_{\mathrm{T}}^{\mathrm{neuEM}}$ is given by energy depositions in the electromagnetic calorimeter being left over after the previous step. The two components $E_{\mathrm{T}}^{\mathrm{chrgEMtrk}}$ and $E_{\mathrm{T}}^{\mathrm{chrgHADtrk}}$ are replaced by the track momenta $\sum p_{\mathrm{T}}^{\mathrm{track}}$, where additional correction terms $\sum \mathrm{res}E_{\mathrm{T}}^{\mathrm{chrgEMtrk}}$ and $\mathrm{res}E_{\mathrm{T}}^{\mathrm{neuEM}}$ need to be introduced. The tau energy is then estimated by

$$E_{\mathrm{T}}^{\mathrm{eflow}} = E_{\mathrm{T}}^{\mathrm{emcl}} + \sum p_{\mathrm{T}}^{\mathrm{track}} + E_{\mathrm{T}}^{\mathrm{neuEM}} + \sum \mathrm{res}E_{\mathrm{T}}^{\mathrm{chrgEMtrk}} + \mathrm{res}E_{\mathrm{T}}^{\mathrm{neuEM}}. \qquad (4.5)$$

In contrast to eflowRec, the splitting of calorimeter clusters into the different contributions given above is done in a purely geometric way, *i.e.* calorimeter cells are flagged according to their η-ϕ distance to the tracks. No additional input like expected shower shapes or expected energy depositions is taken into account. This is the reason why the additional terms $\sum \mathrm{res}E_{\mathrm{T}}^{\mathrm{chrgEMtrk}}$ and $\mathrm{res}E_{\mathrm{T}}^{\mathrm{neuEM}}$ are needed to correct for overlapping energy depositions of π^0 and $\pi^\pm$ and for leakage of $\pi^\pm$ energy out of the assumed region around the track. Recently some attempts have been made to identify π^0 sub-clusters inside tau candidates by using parametrised shower shapes of charged pions in TauRec. However, these approaches suffer from the irregular shape of showers from $\pi^\pm$ in the calorimeter. They are not used in the default tau identification yet.

The tagging or identification of tau leptons based on the candidates is done independently from the actual reconstruction as described above. This allows for applying various discrimination methods in parallel. In addition the identification step can be redone with different tunings without the need to repeat the reconstruction steps.

4.5 PanTau – Tau ID with energy flow for ATLAS

In this Section we describe our new approach to tau identification in ATLAS, named PanTau. PanTau was developed in collaboration with Robindra Prabhu, who already published some results from PanTau in his doctoral thesis [112]. Further important contributions and ideas were provided by Peter Wienemann and Christian Limbach.

4.5.1 PanTau approach

In contrast to the conventional algorithms in ATLAS, PanTau is fully based on the results of energy flow algorithms, in our case eflowRec. Conceptually, this approach has several advantages, because it factorises the detector related steps in the reconstruction from the actual tau reconstruction and identification. For example the identification of tracks originating from conversion electrons may in principle be done by the energy flow

Category	classification requirements	
	number of charged EFOs	presence of neutral clusters
"1-prong"	1	○
"1-prong+neutral"	1	●
"2-prong"	2	○
"2-prong+neutral"	2	●
"3-prong"	3 or 4	○
"3-prong+neutral"	3 or 4	●
"other"	0 or > 4	○/●
"muon"	1, matched to identified muon	
"electron"	1, matched to identified electron	

Table 4.3: Classification scheme of PanTau for its tau candidates.

algorithm using common tools for conversion tagging[3]. Hence, the tau reconstruction does not have to consider conversion electrons itself, reducing its level of complexity. As mentioned before energy flow algorithms can improve the energy and angular resolution in many other applications than tau identification and all applications using a common energy flow approach can therefore profit from its development. The energy flow approach implemented inside TauRec on the other hand cannot be used for the reconstruction of jets or components of the missing transverse energy for example.

Another important concept of PanTau is the classification of tau candidates into categories already at an early stage in the tau reconstruction. The reconstructed classes conform with the decay modes of the tau lepton and are summarised in Table 4.3. The two leptonic classes "electron" and "muon" are not used by default, but have been introduced in the context of the identification of leptonic tau decays. The feasibility to identify tau decays into muons inside PanTau has been evaluated in a diploma thesis [103] and will not be considered in the following, even though it was shown that muonic tau decays have some potential, *e.g.* to improve the reconstruction of invariant sparticle masses in certain SUSY models. The decay mode classification can be of valuable input *e.g.* for studies of polarisation effects in SUSY decay chains including tau decays as mentioned before.

PanTau is fully integrated in the ATLAS software framework athena [118] and makes extensive use of its component model. It has been designed with flexibility and extensibility in mind and modularises the different steps in the tau reconstruction and identification. The ATLAS event data model (EDM) was extended with various Pan-

[3]At the time of writing the conversion identification is not used within eflowRec yet. This will also limit the performance of PanTau, but we will not consider this issue in the following.

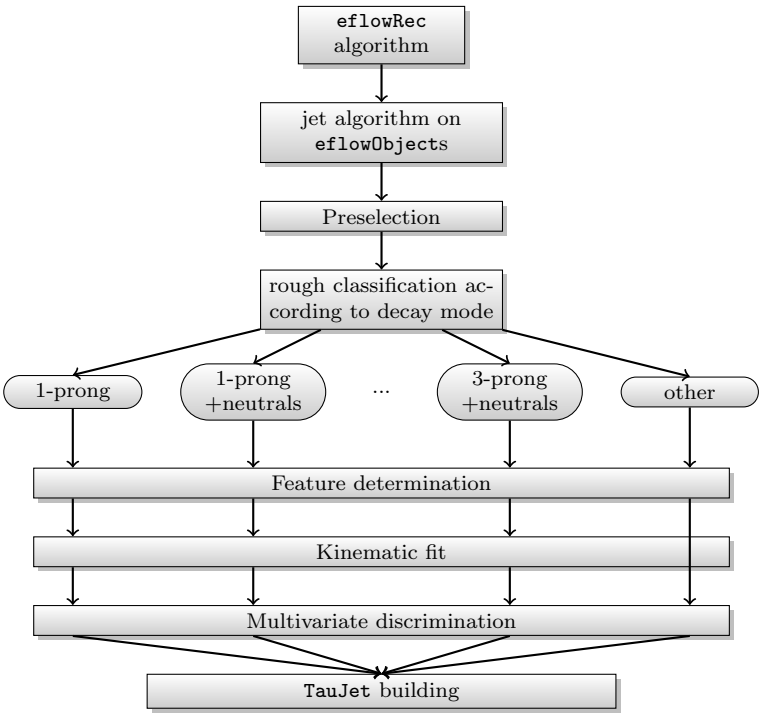

Figure 4.13: Workflow of the PanTau algorithm.

Tau-specific classes holding all data needed during the tau reconstruction. However, they have not yet been optimised in terms of CPU or memory requirements, but in terms of flexibility in the identification process, like the selection of variables used in the multivariate identification. The final result of PanTau is fully compatible with the output of the conventional TauRec algorithm and can therefore directly be used in physics analyses[4].

In the following no details about the software implementation and EDM classes will be given, leaving this for a technical ATLAS note. However, the basic ideas and concepts will be explained. Figure 4.13 sketches the work flow of PanTau. In the first step, the eflowRec algorithm is run independently from PanTau taking topological calorimeter clusters and tracks as input (*cf.* Section 4.3). Afterwards, a jet algorithm clusters the energy flow objects into jets, which are used as seeds for the tau reconstruction in PanTau. After a preselection, all seeds are classified in the aforementioned categories. Specific features are extracted for each seed, which can be used for the identification later on. Optionally, kinematic fits of the decay products can be performed for certain categories to further improve the energy resolution or to obtain information on how compatible with a true tau decay mode a seed is[5]. The multivariate discrimination of seeds against

[4] A bug was found in the TMVA version linked with the athena version used in this work, though, which necessitates to re-run the identification step outside of athena. This is outside the range of PanTau and will be fixed at some point.

[5] The kinematic fit of the tau decay products is not fully validated yet and has not been used for the following results.

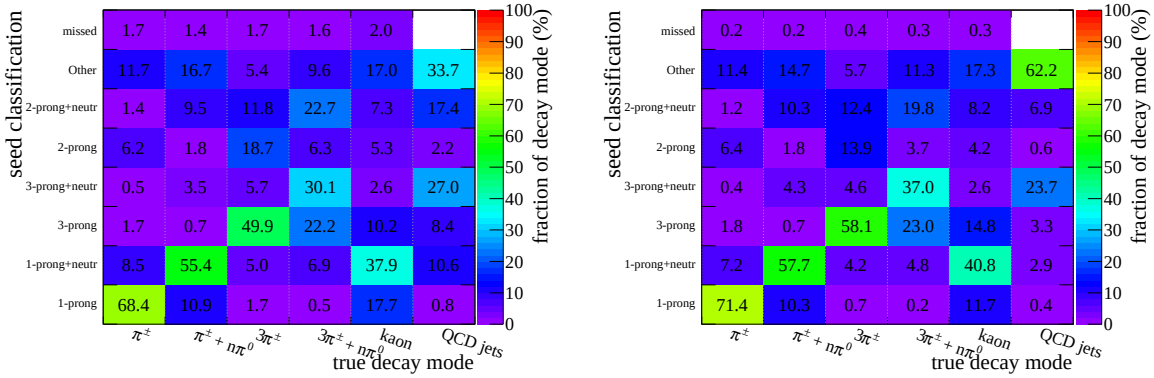

(a) $10\,\text{GeV} < p_\text{T}^\text{vis} < 25\,\text{GeV}$ **(b)** $25\,\text{GeV} < p_\text{T}^\text{vis} < 100\,\text{GeV}$

Figure 4.14: Performance of the seed classification in PanTau. Tau candidates in $\text{W} \rightarrow \tau\nu$ and $\text{Z} \rightarrow \tau\tau$ events are matched to true hadronic tau decays. Distributions are shown for Pythia (DW tune) Monte Carlo samples with tau candidates seeded from cone jets with $R = 0.4$ in the pseudo-rapidity range $|\eta^\text{vis}| < 2.0$. Candidates in QCD di-jet events are given for comparison, where the reconstructed E_T and η are used instead. The numbers give the percentage of candidates for a given true decay mode, *i.e.* they are normalised column-wise.

QCD jets is done in a separate step currently making use of the *TMVA Toolkit for Multivariate Data Analysis with ROOT* [119]. In a final step, seeds are converted into `TauJet` objects with the option to recalculate their kinematic properties based on the information obtained in the previous reconstruction steps.

Seeding and categorisation

By default, PanTau considers all energy flow objects (EFOs) belonging to the jet which is used as a seed. The region around the jet axis in which EFOs are taken into account is therefore determined by the jet algorithm and its parameters. This means the choice of the jet algorithms has significant impact on the identification efficiency and fake rate. If the jet radius is chosen too large several physical jets in an event may merge into a single seed. In this case jets from tau decays may look like QCD jets or can be hidden by those. On the other hand, if the radius is too small, the seed jets may not contain the full QCD jet and therefore look more like collimated tau jets. During the development of PanTau several different jet algorithms, like ATLAS cone (*cf.* [82–84]), SISCone [120], k_T [85, 86], anti-k_T [87] and Cambridge/Aachen [121, 122], have been investigated with distance parameters between 0.05 and 0.6. A distance parameter of 0.4 turned out to be a useful compromise for tau and QCD jets. The performance of the seeding was evaluated in Monte Carlo samples by inspecting the number of missing tau candidates, *i.e.* true hadronic tau decays without matching, versus the contamination of the different reconstructed categories with fakes from QCD jets. Additionally, the misclassification rate of true tau jets according to their decay mode was taken into account. Figure 4.14

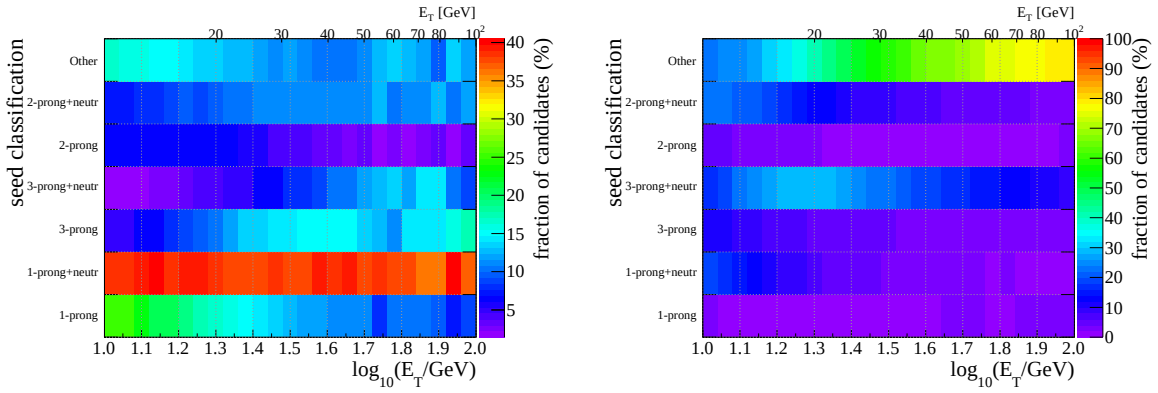

(a) $W \to \tau\nu$ and $Z \to \tau\tau$ **(b)** QCD di-jet

Figure 4.15: Dependency of the seed classification in PanTau on the (reconstructed) transverse energy. Tau candidates in $W \to \tau\nu$ and $Z \to \tau\tau$ events are matched to true hadronic tau decays, whereas the candidates in QCD di-jet events are required to have no tau truth match. Distributions are shown for MC09 samples with tau candidates seeded from cone jets with $R = 0.4$ in the pseudo-rapidity range $|\eta| < 2.0$. The histograms are normalised column-wise in E_{T} bins.

visualises the performance of the seed classification for seeds from ATLAS cone jets with distance parameter $R = 0.4$. The matrix shows the migration of seeds of a given decay mode into the reconstructed categories. Already at this early stage of the tau reconstruction a rather clean classification of the tau candidates can be achieved in PanTau.

However, it turns out that the number of missing seeds and fake seeds also depends on the topology of the events. $W \to \tau\nu$ and $Z \to \tau\tau$ events are relatively clean events without many additional quark or gluon-induced jets and choosing the radius parameter to be too large does not disturb the tau classification very much. In dense environments, like SUSY events, smaller cone sizes can give better classification performance and less missing seeds at the cost of a slightly higher QCD jet contamination.

In order to reduce the dependency of the seed classification on the actual jet algorithm PanTau also allows one to use the direction of the reconstructed jet only. In this case the information about the jet constituents is ignored, but instead all EFOs within a certain ΔR cone around the jet axis are considered by PanTau. This mode of operation allows for more flexibility in the choice of seeds and can be used to combine PanTau with the existing TauRec algorithm.

In Section 4.2.1 it was already shown how the track reconstruction efficiency depends on the the transverse momentum of the pions stemming from tau decays. This directly affects the classification of candidates from true tau decays, because more tracks are lost for low-energetic tau jets. In Figure 4.15a, it is clearly visible how the classification of tau candidates with a match to a true tau decay changes with increasing energy of the tau candidate. For example, the number of candidates classified as “other”, which is

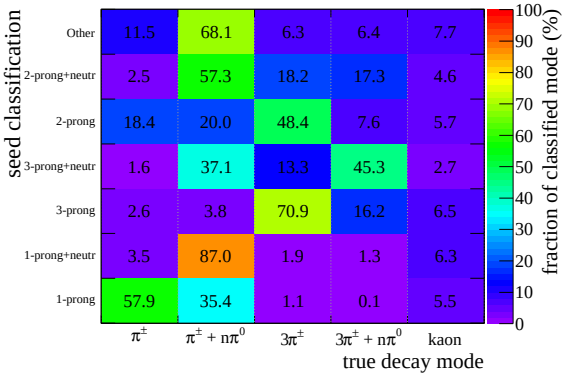

Figure 4.16: Composition of the reconstructed classes in PanTau. Only tau candidates in $W \to \tau\nu$ and $Z \to \tau\tau$ events which are matched to true hadronic tau decays are considered. Distributions are shown for Pythia samples (DW tune) with tau candidates seeded from cone jets with $R = 0.4$ in the pseudo-rapidity range $|\eta| < 2.0$ and $10\,\text{GeV} < E_\text{T} < 50\,\text{GeV}$. The histogram is normalised row-wise in the reconstructed classes.

dominated by candidates without any track is reduced with increasing energy. At the same time the number of candidates in the "3-prong" category is increasing. Entries in the "2-prong" category are also decreasing as more of them are categorised as "3-prong". Still a slightly higher fraction of candidates is observed in the "2-prong+neutrals" category due to contamination from true 1-prong+π^0 decays where the chance for photons converting to electron–positron pairs increases with energy. Additionally the fraction of "1-prong" candidates decreases as true tau decays with additional π^0 or true multi-prong candidates can be categorised more reliably as such. Figure 4.15b shows the same for fake candidates from QCD jets. Here the number of candidates in the "other" class increases with the energy because more and more candidates have more than four tracks. Conversely, the number of candidates in the n-prong categories decreases because the number of charged particles increases in QCD jets with energy up to a certain point, contrary to tau decays, where the number of charged particles does not depend on its energy.

Finally, Figure 4.16 shows the composition of the categories for tau candidates matched to true simulated tau decays using the Monte Carlo truth information. One can see that the "1-prong+neutrals" and the "3-prong" category have the by far best purity with respect to the true tau decay modes. This means for a candidate from those classes one can achieve high confidence in their true decay mode. In the "1-prong" category, on the other hand, one has a contamination of $\frac{1}{3}$ of true 1-prong decays with additional π^0.

Tau identification and variables in PanTau

Part of the philosophy of PanTau is the concept that all variables used in the tau identification are derived from energy flow quantities and not using *e.g.* the measurements of the calorimeter cells directly. This has the advantage of a better separation between the actual tau identification and the detector reconstruction. Additionally, quantities can be calculated that are not directly available in conventional approaches. PanTau makes use of the multivariate classification capabilities of the TMVA toolkit [119, 123]. All of its multivariate methods are directly usable by PanTau and can be applied in parallel or quickly be exchanged without the need to recompile the PanTau source code. Anyhow, if

need arises in the future to use other methods than the ones provided by TMVA or to use pre-compiled reference data they can easily be incorporated in PanTau. In the following we concentrate on the projective likelihood method for the tau identification. Even though this method is inferior to other methods – especially when correlations between variables arise – it is useful to demonstrate the feasibility of the PanTau approach.

In the next step after the seeding and categorisation of candidates several variables are determined that serve as features to distinguish tau jets and QCD jets. During the development phase of PanTau many different variables have been tested. Only a selection of those will be discussed here to demonstrate how the final selection was achieved. The first moment in $\Delta R(\text{jet}, \text{EFO}) = \sqrt{(\eta^{\text{jet}} - \eta^{\text{EFO}})^2 + (\varphi^{\text{jet}} - \varphi^{\text{EFO}})^2}$ is defined as

$$\langle \Delta R(\text{jet}, \text{EFO}) \rangle_{E_\text{T}}^{\mathcal{C}} = \frac{1}{\sum_{\text{EFO}^{\mathcal{C}}} {E_\text{T}}^{\text{EFO}}} \sum_{\text{EFO}^{\mathcal{C}}} {E_\text{T}}^{\text{EFO}} \cdot \Delta R(\text{jet}, \text{EFO}) \tag{4.6}$$

where the energy flow objects in the sum satisfy certain criteria $\mathcal{C}$[6]. In the following we use mainly two different criteria $\mathcal{C}$. The criterion "all" includes all energy flow objects with positive energy[7] independent of their charge or cluster type. The second criterion "charged" includes only energy flow objects which are charged, *i.e.* they must have a track assigned.

In addition to the weighting by E_T in equation (4.6) one can also weight the $\Delta R(\text{jet}, \text{EFO})$ by E.

$$\langle \Delta R(\text{jet}, \text{EFO}) \rangle_{E}^{\mathcal{C}} = \frac{1}{\sum_{\text{EFO}^{\mathcal{C}}} E^{\text{EFO}}} \sum_{\text{EFO}^{\mathcal{C}}} E^{\text{EFO}} \cdot \Delta R(\text{jet}, \text{EFO}) \tag{4.7}$$

The difference between weighting by E_T and weighting by E is expected to be small though, because the constituents within a tau candidate belong to a limited region in η such that the factors $E_\text{T} = E \cdot \sin(\theta) = E \cdot \frac{1}{\cosh(\eta)}$ are scaled with roughly the same value of $\sin(\theta)$.

Different isolation variables were defined as well that make use of the fact that tau jets are usually more collimated than QCD jets. Hence they have some similarity with the moments in ΔR of the energy flow objects, but still include extra information.

$$I_{\text{tot}}^{0.2;0.4} \equiv \frac{\sum_{0.2<\Delta R(\text{jet},\text{EFO})<0.4} {E_\text{T}}^{\text{EFO}}}{\sum {E_\text{T}}^{\text{EFO}}} \tag{4.8}$$

$$I_{R_{\text{outer}}}^{R_{\text{inner}}} \equiv \frac{\sum_{\Delta R(\text{jet},\text{EFO})<R_{\text{inner}}} {E_\text{T}}^{\text{EFO}}}{\sum_{\Delta R(\text{jet},\text{EFO})<R_{\text{outer}}} {E_\text{T}}^{\text{EFO}}} \tag{4.9}$$

[6] Note that the definition used here is different from the one used in Robindra Prabhu's thesis[112], where the first moment was defined as $\langle \Delta R(\text{jet}, \text{EFO}) \rangle^{\mathcal{C}} = \frac{1}{\sum_{\text{EFO}} {E_\text{T}}^{\text{EFO}}} \sum_{\text{EFO}^{\mathcal{C}}} {E_\text{T}}^{\text{EFO}} \cdot \Delta R(\text{jet}, \text{EFO})$.

[7] Due to the internal noise suppression of the topological clusterisation one introduces only a negligible bias by considering only clusters with positive energy.

For the jet sphericity S_{jet}, which quantifies how "spherical" the energy distribution is, we follow the definition from [90], defining the sphericity tensor as

$$S^{\alpha\beta} = \frac{\sum_i p_i^\alpha p_i^\beta}{\sum_i |\vec{p}_i|^2} \tag{4.10}$$

where $\alpha, \beta = 1, 2, 3$ correspond to the x, y and z components of the energy flow momentum $\vec{p}$ and i runs over all energy flow objects assigned to the tau candidate. By diagonalising $(S^{\alpha\beta})$ one finds the three eigenvalues $\lambda_1 \geqslant \lambda_2 \geqslant \lambda_3$ and defines the sphericity as

$$S_{\text{jet}} = \frac{3}{2}(\lambda_2 + \lambda_3). \tag{4.11}$$

Different angles between prominent energy flow objects within a candidate jet were defined, like the mean angle between the three leading charged energy flow objects

$$\bar{\alpha} = \frac{1}{3}(\alpha_{12} + \alpha_{13} + \alpha_{23}),\ \alpha_{ij} = \sphericalangle(\text{EFO}_{\text{i}}^{\pm}, \text{EFO}_{\text{j}}^{\pm}) \tag{4.12}$$

or the angle between the charged and neutral axis, $\sphericalangle(\vec{e}^{\,\text{charged}}, \vec{e}^{\,\text{neutral}})$, and the angle between the jet axis and the leading charged EFO, $\sphericalangle(\text{jet}, \text{EFO}^{\pm}_{\text{leading}})$. The angles try to exploit the fact that one often observes a hierarchy of the tau decay products with one dominating charged pion.

The transverse impact parameter significance $d_0/\sigma(d_0)$ of tracks from the leading charged EFOs is a complementary observable to the previous ones. Here the lifetime of the tau lepton is used for the identification. The invariant mass $m(\text{EFO}^{\mathcal{C}})$ of a certain class $\mathcal{C}$ of energy flow objects is a feature special to the energy flow approach. Furthermore the number of energy flow objects of a certain class provide separation power between tau decays and QCD jets.

Compared to the results presented in reference [112] most variables calculated from the mean of the distances of energy flow objects have been replaced by their E_{T}-weighted versions, like $\langle \Delta R(\text{jet}, \text{EFO}) \rangle^{\text{EM neutral}}_{E_{\text{T}}}$. This change comes at the cost of minor performance degradations in the Monte Carlo estimates, but is expected to be more robust to noise, because low energetic noise clusters contribute less. The only exception, where no E_{T}-weighting is performed, is the mean angular distance between the sub-leading and the leading charged EFO

$$\overline{\Delta R}(\text{EFO}^{\pm}, \text{EFO}^{\pm}_{\text{leading}}) = \frac{\sum_{\text{EFO}^{\pm}} \Delta R(\text{EFO}, \text{EFO}^{\pm}_{\text{leading}})}{N(\text{EFO}^{\pm}) {E_{\text{T}}}^{\text{jet}}} \tag{4.13}$$

Additionally the sum of charges $\sum_{\text{EFO}} q_i$ of energy flow objects belonging to a tau candidate was replaced by its absolute value in order to avoid a bias in the tau identification towards the charge asymmetry in $\text{W} \to \tau\nu$ events at the LHC[8].

Some variables, like the isolation variables $I_{\text{tot}}^{0.2;0.4}$ and $I_{R_{\text{outer}}}^{R_{\text{inner}}}$ are defined as ratios of energies in certain regions around the tau jet axis (equation (4.8) and (4.9)), are strongly peaked at zero and one. In such cases it is convenient to transform them with an inverse sigmoid ("logit") function defined as

$$\text{logit}(x) = \ln\left(\frac{x}{1-x}\right) \tag{4.14}$$

This function allows to "zoom" into the peaks at zero and one as illustrated in Figure 4.17. Especially for the likelihood method where reference distributions must be derived the transformed variables are more suitable.

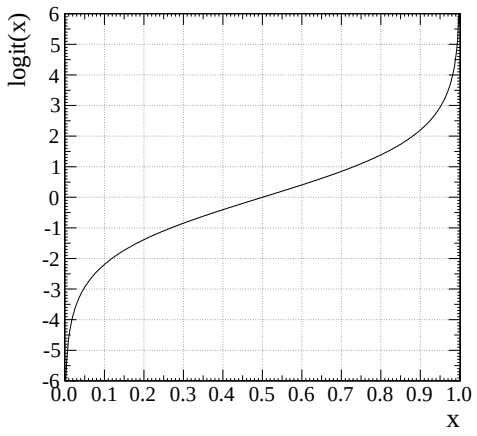

Figure 4.17: Graph of the logit function $\text{logit}(x) = \ln\left(\frac{x}{1-x}\right)$. Using the logit or inverse sigmoid function the whole real axis can mapped onto the interval $[0, 1]$.

Table 4.4 summarises the selection of identification variables that has been used as a base line. Different sets of variables have been used for the different reconstructed classes of tau candidates. This variation is needed, because some variables have only a small separation power or are even ill-defined in certain classes. Furthermore the selection distinguishes candidates in the transverse energy regimes $10\,\text{GeV} < E_{\text{T}} < 25\,\text{GeV}$, $25\,\text{GeV} < E_{\text{T}} < 50\,\text{GeV}$ and $E_{\text{T}} > 50\,\text{GeV}$. It is based on the selection used in [112] and tries to minimise the correlation between variables in each set. Multivariate methods that are less sensitive to correlations and default values in case of undefined variables may cope with a simpler selection and further variables.

[8] The LHC collides protons with protons and depending on the Bjorken-variable x of the participating partons there is a preference for the production of W^+ over W^-, due to the flavour content of the proton. See for example [124] and references therein.

	10-25GeV						25-50GeV			
variable	1p	1pn	3p	3pn	2p	2pn	1p/ 1pn	3p	3pn	2p/ 2pn
$N(\text{EFO}^{\pm})$	•					•				•
$N(\text{EFO}^{\pm *})$			•	•				•	•	
$\lvert\sum_{\text{EFO}} q_i\rvert$	•	•	•	•			•	•	•	
$\langle\Delta R(\text{jet},\text{EFO})\rangle_{E_\text{T}}^{\text{all}}$	•	•			•	•	•			•
$\langle\Delta R(\text{jet},\text{EFO})\rangle_{E_\text{T}}^{\text{charged}}$	•		•	•				•	•	
$\langle\Delta R(\text{jet},\text{EFO})\rangle_{E_\text{T}}^{\text{had. neutral}}$	•		•	•					•	
$\langle\Delta R(\text{jet},\text{EFO})\rangle_{E_\text{T}}^{\text{EM neutral}}$		•		•		•	•		•	•
$\text{logit}(I_{0.2}^{0.1})$	•									
$\text{logit}(I_{\text{tot}}^{0.2;0.4})$		•					•			
$\text{logit}(I_{0.4}^{0.1})$				•	•			•	•	
$\frac{1}{3}(\alpha_{12}+\alpha_{13}+\alpha_{23})$			•							
S_{jet}	•			•	•	•	•	•		•
$d_0/\sigma(d_0)$	•	•			•	•	•			•
$\sphericalangle(\text{jet},\text{EFO}_{\text{leading}}^{\pm})$		•				•				
$\sphericalangle(\vec{e}^{\text{charged}},\vec{e}^{\text{neutral}})$		•				•				
$\text{stddev}(E_\text{T}^{\text{EFO}})/E_\text{T}^{\text{jet}}$				•		•			•	•
$m(\text{EFO}^{\text{all}})$							•			

Table 4.4: Variables used as default for the tau identification in PanTau. A detailed description of the variables can be found in the text.

4.5.2 Energy dependency of tau identification variables

Achieving a stable performance of the tau identification over a wide range of visible tau momenta should be an aim for every algorithm for tau reconstruction. It is a priori not clear how "stable performance" is defined in this context. For example one can think of a flat tau identification efficiency or a flat rejection of QCD jets. We will leave this question open for the moment, but investigate the momentum dependency of the variables for tau identification in PanTau.

Figure 4.18 visualises the energy dependency of the first moment in $\Delta R(\text{jet},\text{EFO})$ of all energy flow objects for tau candidates belonging to true tau decays and fake candidates from QCD jets. In Figure 4.18a a clearly non-linear dependency on the reconstructed transverse energy E_T of the tau candidate is visible in the mean and median of both signal and background distributions. The median is shifted from 0.07 (0.18) at $p_\text{T} = 10\,\text{GeV}$ to 0.02 (0.05) at $p_\text{T} = 100\,\text{GeV}$ for the signal (respectively

background) distribution. This means the shift over this energy range is larger than the typical intervals spanning from 31.7 % to 68.3 %, *i.e.* the intervals corresponding to 1σ of a Gaussian. Such a strong dependency has a negative impact on multivariate methods which use this variable to identify tau lepton decays for the following reasons.

On the one hand, one does not want to use the tau energy directly as an input variable for the identification, because this would bias the identification towards the energy spectrum of the Monte Carlo samples used to train the methods. On the other hand all variables will be averaged over the energy range used in the training, if the method does not gain any knowledge about the energy of each tau candidate. This averaging washes out the separation power between true taus and QCD jets, if the energy

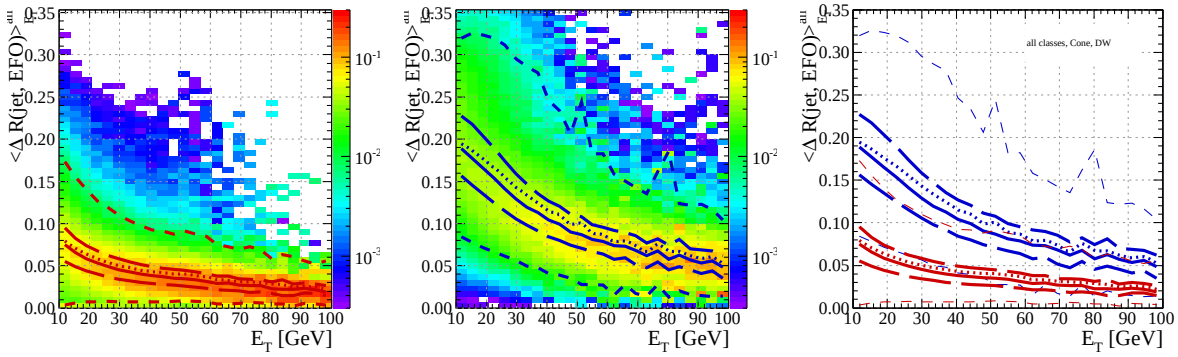

(a) E_{T} dependency

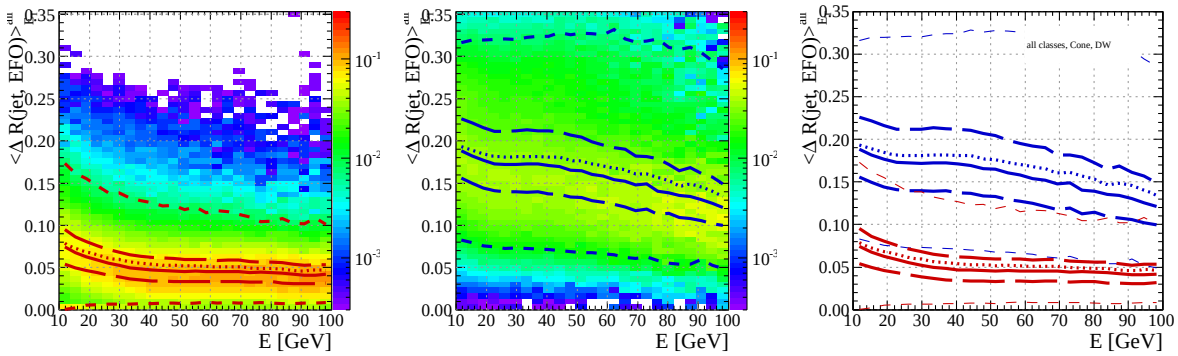

(b) E dependency

Figure 4.18: E_{T} and E dependency of the first moment $\langle \Delta R(\mathrm{jet}, \mathrm{EFO}) \rangle^{\mathrm{all}}_{E_{\mathrm{T}}}$ in $\Delta R(\mathrm{jet}, \mathrm{EFO})$ for all energy flow objects. The left graph includes tau candidates with a match to Monte Carlo true taus in $\mathrm{Z} \rightarrow \tau\tau$ and $\mathrm{W} \rightarrow \tau\nu$ events and the middle graph for tau candidates in QCD jet events. Both distributions are normalised column-wise in the energy bins and the color coding corresponds to the fraction of tau candidates. Overlaid to the two dimensional distributions are the median value (solid line), the mean value (dotted line) and the intervals of 95 %, 68.3 %, 31.7 % and 5 % (dashed lines) of all entries in each energy bin. On the right the energy dependency of mean and median value are repeated for signal (red) and background (blue) in the same graph. The η range of the tau candidates is restricted to $|\eta| < 2.0$.

dependency is too strong. Variables with only small energy dependencies are therefore preferable. One option to achieve this is to transform the variables as a function of the energy, such that the energy dependency vanishes or is at least minimised.

QCD jets are created from color-charged objects – either quarks or gluons – and a color flow exists between the jets in one collision event. In general transverse quantities are more suitable to describe their properties in hadron collider events, because one always has a boost along the beam axis as the partons in the hard interaction carry only a fraction of the hadron momenta. This does not necessarily hold for the tau decays, because the tau decay products are boosted along the tau momentum. Therefore the total energy E seems to be the more natural variable than the transverse energy E_{T} to describe the energy dependency in tau decays. However, Figure 4.18b shows a wider spread of the variable in each bin of the total energy E though and the energy dependency itself is not as pronounced as in a function of E_{T} (Figure 4.18a). For QCD jets one can clearly see, that E_{T} describes the energy dependency more precisely, but even for candidates matched to true tau decays E_{T} seems to be more suitable. In the following we will only show the E_{T} dependency of the variables.

Similar to the question whether E_{T} or E of the jet describe the energy dependency of the spread of tau jets better, one may ask, whether other quantities instead of ΔR should be used. One example would be the spherical angle $\sphericalangle(\mathrm{jet}, \mathrm{EFO})$ between the energy flow object and the jet direction (Figure 4.19c). One can also define an angular measure similar to ΔR by

$$\Delta R'(\mathrm{jet}, \mathrm{EFO}) = \sqrt{(\theta^{\mathrm{jet}} - \theta^{\mathrm{EFO}})^2 + (\varphi^{\mathrm{jet}} - \varphi^{\mathrm{EFO}})^2} \tag{4.15}$$

which does not show a "squeezing" of the measure for small angles to the beam pipe like the pseudo-rapidity η.

The different definitions of energy spread are compared in Figure 4.19. It turns out that the separation power of $\langle \Delta R(\mathrm{jet}, \mathrm{EFO}) \rangle_E^{\mathrm{all}}$ is better than the one of $\langle \Delta R'(\mathrm{jet}, \mathrm{EFO}) \rangle_E^{\mathrm{all}}$ and $\langle \sphericalangle(\mathrm{jet}, \mathrm{EFO}) \rangle_E^{\mathrm{all}}$. The latter reduces the energy dependency only slightly. We will therefore proceed with the investigation of $\Delta R(\mathrm{jet}, \mathrm{EFO})$.

The simplest way to reduce the energy dependency of $\langle \Delta R(\mathrm{jet}, \mathrm{EFO}) \rangle_{E_{\mathrm{T}}}^{\mathrm{all}}$ is to multiply its value by the transverse energy E_{T} itself (Figure 4.20a). However, this transformation leads to an overcompensation and one observes a rise in $\langle \Delta R(\mathrm{jet}, \mathrm{EFO}) \rangle_{E_{\mathrm{T}}}^{\mathrm{all}} \cdot E_{\mathrm{T}}$ with increasing E_{T}. Still the dependency is slightly more linear in the signal distribution than before, but a very strong dependency is visible in the background distribution especially for $E_{\mathrm{T}} < 20\,\mathrm{GeV}$. Hence, this simple transformation is not sufficient to remove the energy dependency. Another undesirable feature is visible in the distribution of $\langle \Delta R(\mathrm{jet}, \mathrm{EFO}) \rangle_{E_{\mathrm{T}}}^{\mathrm{all}} \cdot E_{\mathrm{T}}$ especially at low transverse energies. By construction the mean ΔR distance is limited by $\langle \Delta R(\mathrm{jet}, \mathrm{EFO}) \rangle_{E_{\mathrm{T}}}^{\mathrm{all}} \lesssim 0.4$, if the candidates are built from energy flow objects in a cone jet with cone size $\Delta R = 0.4$. This limit transforms into a linear boundary by multiplying the E_{T}-weighted mean distance with the transverse energy of the candidate, which is clearly visible in Figure 4.20a. For the same reason one observes a "knee" in the E_{T} dependency of $\langle \Delta R(\mathrm{jet}, \mathrm{EFO}) \rangle_{E_{\mathrm{T}}}^{\mathrm{all}} \cdot E_{\mathrm{T}}$ at about $E_{\mathrm{T}} \approx 20\,\mathrm{GeV}$.

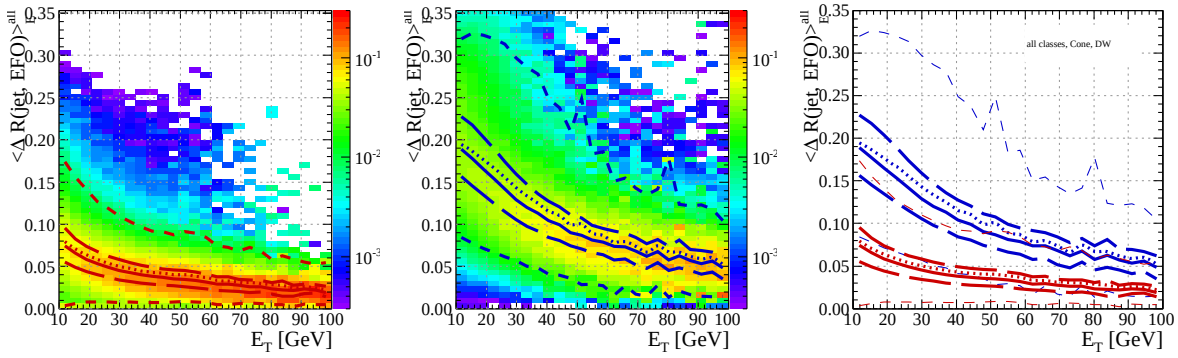

(a) $\langle \Delta R(\text{jet}, \text{EFO}) \rangle_E^{\text{all}}$

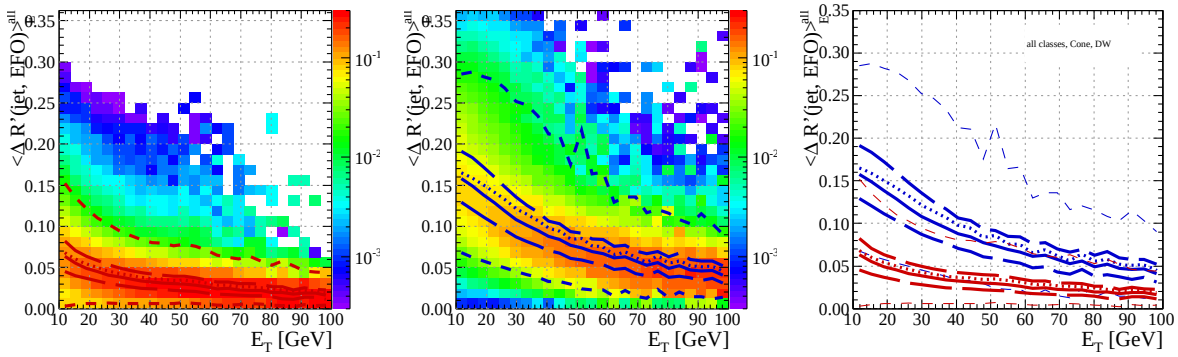

(b) $\langle \Delta R'(\text{jet}, \text{EFO}) \rangle_E^{\text{all}}$

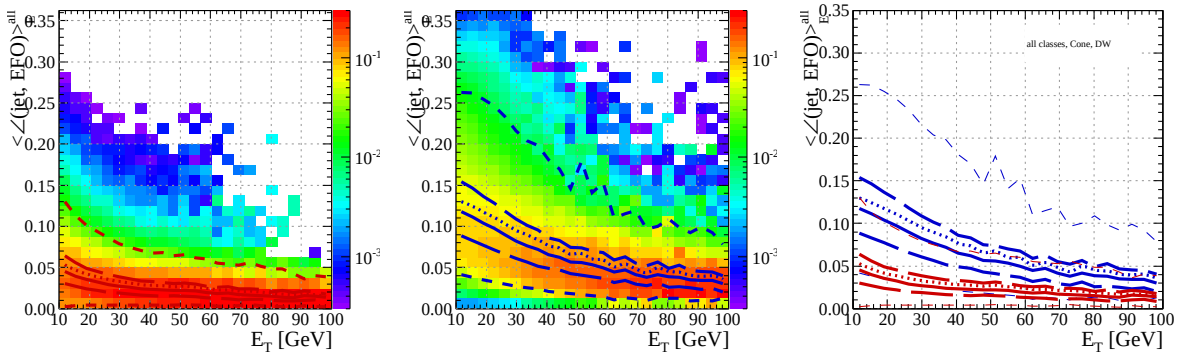

(c) $\langle \sphericalangle(\text{jet}, \text{EFO}) \rangle_E^{\text{all}}$

Figure 4.19: Energy dependency of the first moments of ΔR, $\Delta R'$ and the angle between the energy flow objects and the jet direction. The quantities are weighted with the energy E of the energy flow objects here. Coding of colors and lines follows the same convention as in Figure 4.18.

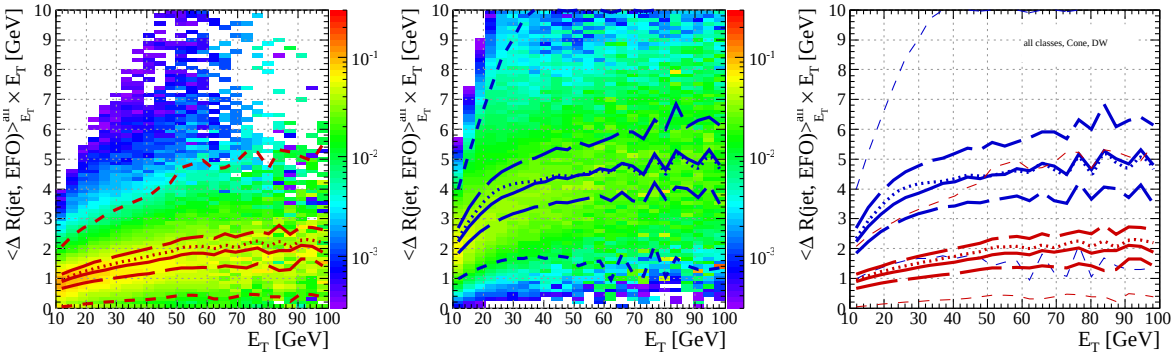

(a) $\langle \Delta R(\text{jet}, \text{EFO}) \rangle^{\text{all}}_{E_\text{T}} \cdot E_\text{T}$

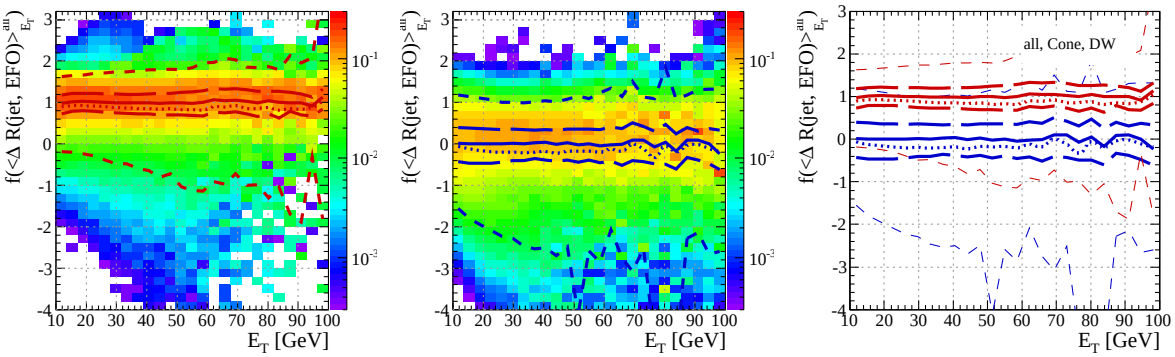

(b) $\langle \Delta R(\text{jet}, \text{EFO}) \rangle^{\text{all}}_{E_\text{T}}$, flattened

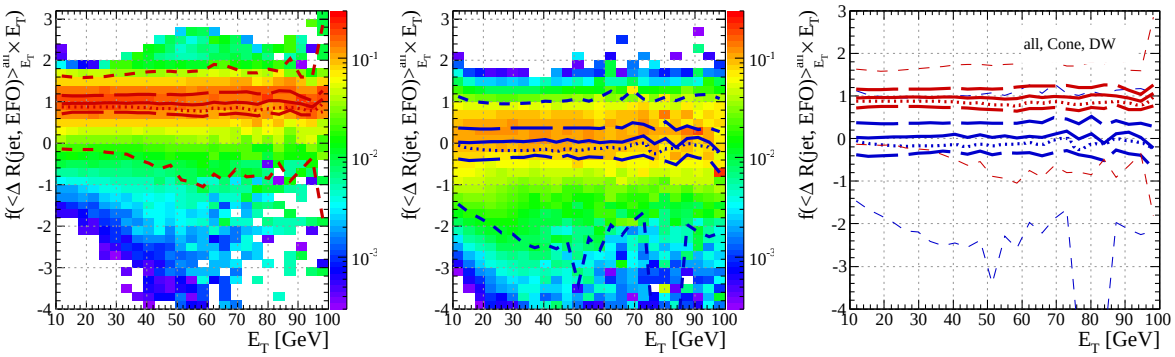

(c) $\langle \Delta R(\text{jet}, \text{EFO}) \rangle^{\text{all}}_{E_\text{T}} \cdot E_\text{T}$, flattened

Figure 4.20: Energy dependency of the first moment of ΔR in different transformations. Coding of colors and lines follows the same convention as in Figure 4.18.

Another option to reduce the energy dependency is to flatten the distributions by fitting an appropriate function to the background and signal distribution and use this functions as a basis to transform the variable. Here we fitted a fourth order polynomial to the median of the signal and background distributions to obtain the functions

$$S(E_{\mathrm{T}}) = s_0 + s_1 E_{\mathrm{T}} + s_2 {E_{\mathrm{T}}}^2 + s_3 {E_{\mathrm{T}}}^3 + s_4 {E_{\mathrm{T}}}^4 \quad (4.16)$$

$$B(E_{\mathrm{T}}) = b_0 + b_1 E_{\mathrm{T}} + b_2 {E_{\mathrm{T}}}^2 + b_3 {E_{\mathrm{T}}}^3 + b_4 {E_{\mathrm{T}}}^4 \quad (4.17)$$

With the following mapping $x \mapsto x' = f(x)$ one can ensure that the median of the distribution of x' for the signal is located at 1 and the median of the background at 0

$$x' = f(x) = \frac{x - B(E_{\mathrm{T}})}{S(E_{\mathrm{T}}) - B(E_{\mathrm{T}})} = \frac{x - \sum_{n=0}^{4} b_n {E_{\mathrm{T}}}^n}{\sum_{n=0}^{4} (s_n - b_n) {E_{\mathrm{T}}}^n} \quad (4.18)$$

A similar procedure was used in TauRec by R. Reece et al. to derive energy dependent cuts for a cut-based tau identification, but has not been applied to transform variables as an input for multivariate methods, before.

Figure 4.20b shows the flattening procedure applied to $\langle \Delta R(\mathrm{jet}, \mathrm{EFO}) \rangle^{\mathrm{all}}_{E_{\mathrm{T}}}$. The fit of the background and signal distributions is performed for each reconstructed class individually, because the different classes show slightly different behaviour (see Appendix C.2). For the median of the flattened variable it does not make any difference, whether the flattening is done with $\langle \Delta R(\mathrm{jet}, \mathrm{EFO}) \rangle^{\mathrm{all}}_{E_{\mathrm{T}}}$ or $\langle \Delta R(\mathrm{jet}, \mathrm{EFO}) \rangle^{\mathrm{all}}_{E_{\mathrm{T}}} \cdot E_{\mathrm{T}}$. The spread of the transformed variable, however, can be different. For this reason the same procedure is applied to $\langle \Delta R(\mathrm{jet}, \mathrm{EFO}) \rangle^{\mathrm{all}}_{E_{\mathrm{T}}} \cdot E_{\mathrm{T}}$ in Figure 4.20c. In both cases the transformed variable shows indeed a strongly improved energy dependency. Both the median and the the intervals corresponding to 1σ of a Gaussian are nearly flat in E_{T} now. Just in the tails of the distributions some minor energy dependencies remain.

Similar to the energy dependencies of the variables their dependency on the pseudorapidity η has been investigated. Again a strong η dependency would "wash out" the separation power of identification variables. In Figure 4.21 the η dependency is shown for $\langle \Delta R(\mathrm{jet}, \mathrm{EFO}) \rangle^{\mathrm{all}}_{E_{\mathrm{T}}}$, its E_{T}-flattened version and the angle between the energy flow objects and the jet direction. The distribution of $\langle \Delta R(\mathrm{jet}, \mathrm{EFO}) \rangle^{\mathrm{all}}_{E_{\mathrm{T}}}$ is nearly flat in η within the available statistics. Even though the spatial and energy resolution of the tracking system and the calorimeters changes with η, this has no significant effect on the width of the distributions. The E-weighted mean of the angle between energy flow objects and the jet direction $\langle \sphericalangle(\mathrm{jet}, \mathrm{EFO}) \rangle^{\mathrm{all}}_{E}$, however, shows a very strong η dependency. It is not only visible in the distribution for QCD jets, but also in the distribution of tau candidates matched to true hadronic tau decays. Here we find another reason, why $\Delta R(\mathrm{jet}, \mathrm{EFO})$ is preferable to $\sphericalangle(\mathrm{jet}, \mathrm{EFO})$. One should keep in mind though, that the distributions are biased towards flatness in $\Delta R(\mathrm{jet}, \mathrm{EFO})$, because only energy flow objects belonging to a jet formed by cone jet algorithm with $\Delta R = 0.4$ are considered here. This means the jets are more and more "squeezed" in the polar angle θ with increasing η.

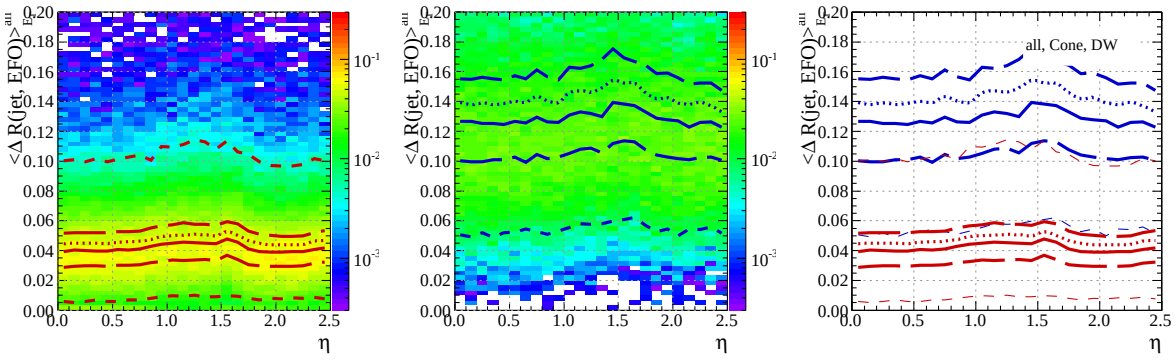

(a) $\langle \Delta R(\text{jet}, \text{EFO}) \rangle^{\text{all}}_{E_{\text{T}}}$

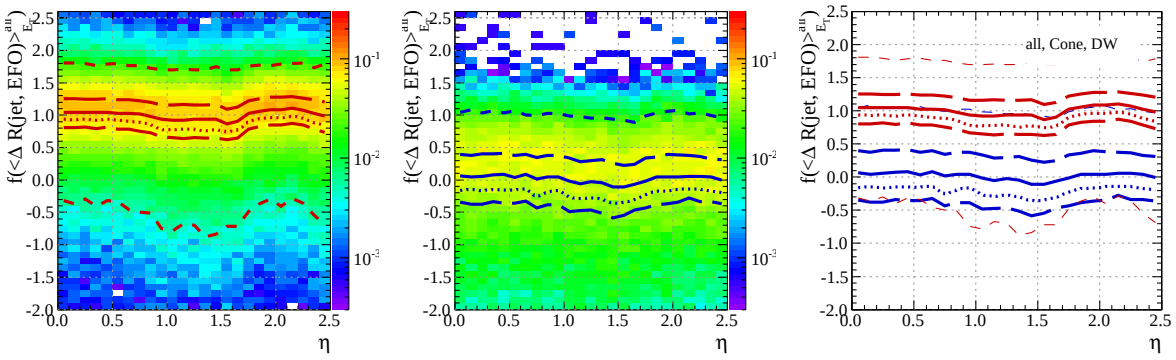

(b) $\langle \Delta R(\text{jet}, \text{EFO}) \rangle^{\text{all}}_{E_{\text{T}}}$, flattened in E_{T}

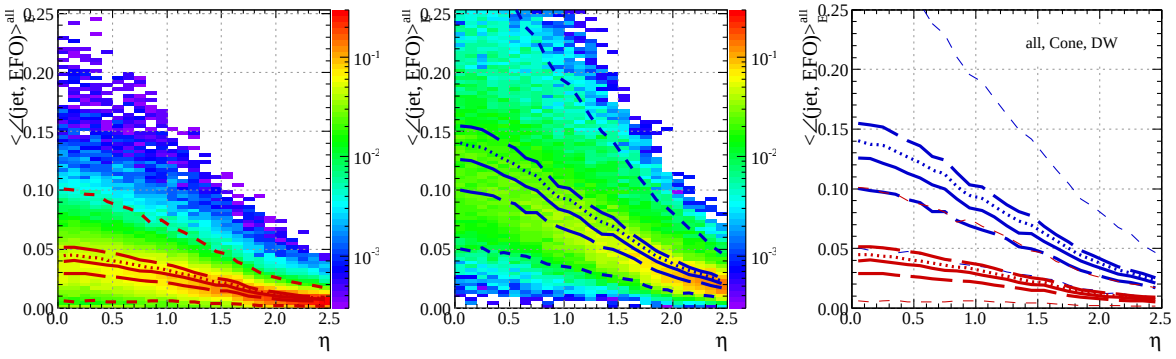

(c) $\langle \sphericalangle(\text{jet}, \text{EFO}) \rangle^{\text{all}}_{E}$

Figure 4.21: η dependency of the first moments of ΔR, its E_{T}-flattened version and the angle between the energy flow objects and the jet direction. All candidates in the energy range $25\,\text{GeV} < E_{\text{T}} < 50\,\text{GeV}$ have been considered. Coding of colors and lines follows the same convention as in Figure 4.18.

Crucial for the identification is the difference in a variable between signal (τ jets) and background (QCD jets). We define two measures of the separation power, the separation $\langle S^2 \rangle$ [119] and the overlap O of a variable x by

$$\langle S^2 \rangle = \frac{1}{2} \int \frac{(S(x) - B(x))^2}{S(x) + B(x)} \mathrm{d}x \approx \frac{1}{2} \sum_i \frac{(S_i - B_i)^2}{S_i + B_i} \tag{4.19}$$

$$O = \int \min(S(x), B(x)) \mathrm{d}x \approx \sum_i \min(S_i, B_i) \tag{4.20}$$

where $S(x)$ and $B(x)$ are the probability distribution functions of x for signal and background, respectively, *i.e.* $\int S(x)\mathrm{d}x = \int B(x)\mathrm{d}x = 1$. Both functions are approximated by the bin contents S_i, B_i of the corresponding histograms. Unfortunately this approximation is very sensitive to the binning as $\langle S^2 \rangle$ always goes to 1 if the binning is too fine and to 0 if the binning is too coarse. Consequently these two measures need to be taken with caution, but they can at least give a hint about the separation power of a variable. The separation $\langle S^2 \rangle$ is defined in a way that $\langle S^2 \rangle = 1$, if the distributions are completely disjoint and $\langle S^2 \rangle = 0$, if the distributions are identical. The definition of the overlap O is just the other way around.

Neglecting the energy dependency of variables can even be misleading in quantifying the separation power of variables. Figure 4.22a shows the same E_T dependency of $\langle \Delta R(\mathrm{jet}, \mathrm{EFO}) \rangle_E^{\mathrm{all}}$ as Figure 4.18a on page 74, but without normalising the distributions in bins of E_T such that the energy spectrum of the used Monte Carlo samples gets visible. One can easily see that the energy spectra of the signal and background sample are different. Figure 4.22b shows the projection of the distribution, *i.e.* averaged over E_T. The separation between signal and background sample seems to be better here than it really is, because the low-E_T dominated background sample is biased towards larger values of $\langle \Delta R(\mathrm{jet}, \mathrm{EFO}) \rangle_E^{\mathrm{all}}$. Figure 4.22e shows the energy dependency in a waterfall plot including the overlap between signal and background in each energy bin. The overlap in each bin is greater than the overlap of the averaged distributions, even though the E_T dependency smears out the averaged distributions. This can only be explained by the different energy spectra of the signal and background samples.

Figure 4.22 additionally includes the same graphics for the E_T-flattened version of the variable. In this case the aforementioned effect is not visible, because the flattened variable does not have a strong E_T dependency by construction. The projection (Figure 4.22d) of the distribution (Figure 4.22c) possesses about the same overlap between signal and background as the individual E_T bins in the waterfall plot, Figure 4.22f. Within the statistical fluctuations the overlap is identical in each E_T bin in the original and the flattened version of the variable as expected. Still the projection of the original variable seems to have a better separation than the projection of the flattened version due to the different energy spectra of the Monte Carlo samples for signal and background. One therefore should be careful not to reject the flattened variable, in spite of the artificial separation power of the original variable.

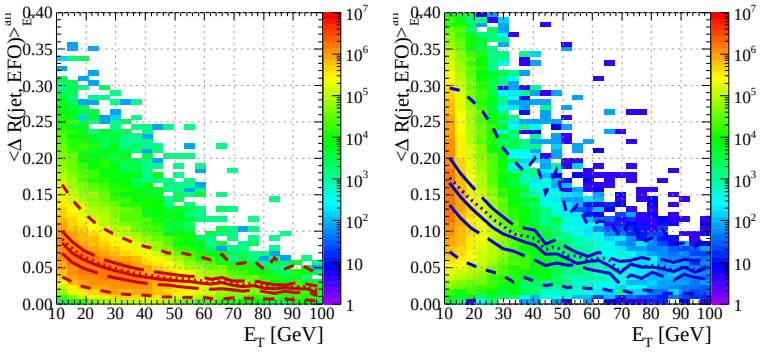

(a) E_{T} dependency

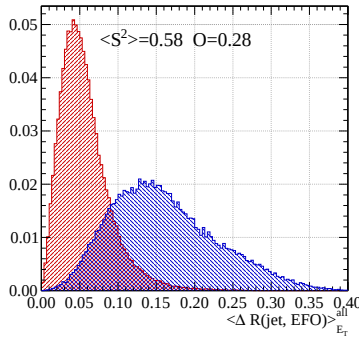

(b) Averaged distribution

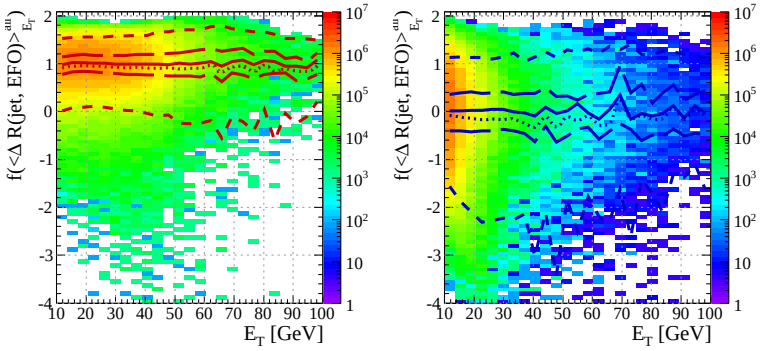

(c) E_{T} dependency, flattened variable

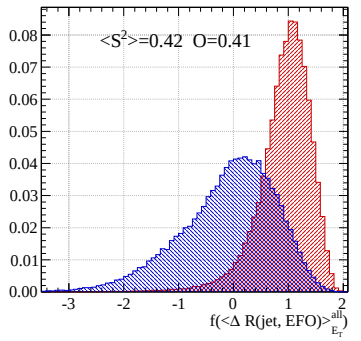

(d) Averaged distribution, flattened variable

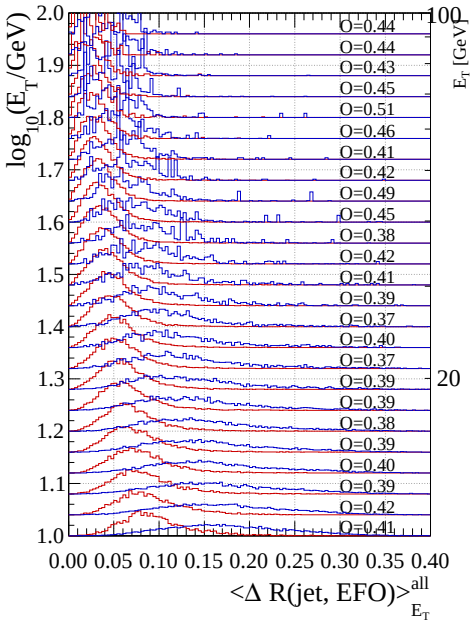

(e) E_{T} dependency

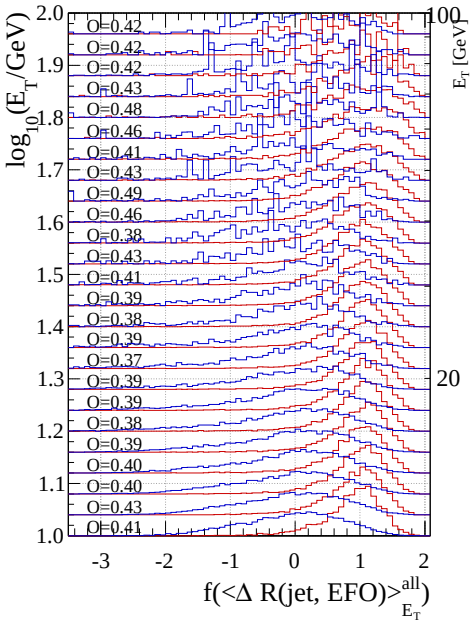

(f) E_{T} dependency, flattened variable

Figure 4.22: Comparison of the variable $\langle \Delta R(\mathrm{jet}, \mathrm{EFO}) \rangle^{\mathrm{all}}_{E_{\mathrm{T}}}$ before ((a), (b), (e)) and after ((c), (d), (f)) flattening in the transverse energy E_{T} of the tau candidates. Coding of colors and lines follows the same convention as in Figure 4.18. Only tau candidates belonging to the "1-prong with neutrals" class are used here. (b) is the projection of (a), *i.e.* ignoring the E_{T} dependency. (e) visualises the E_{T} dependency like (a), but as a waterfall plot.

4.5.3 Performance of the PanTau identification in Monte Carlo samples

In the PanTau approach, tau candidates are classified according to their decay mode at an early stage and the discrimination against QCD jets is performed class-wise. In the simplest case the candidates from each class are put together again after the multivariate analysis by treating the classifier output of each class identically. However, the a priori probabilities for a tau candidate to be a true tau are quite different for the classes, *cf.* Section 4.5.1. For example the "Other" class is mainly dominated by QCD jets, whereas the "1-prong" class is already rather pure. Treating all classes identically therefore mixes likelihood ratios of different quality and leads to serious performance degradations.

The likelihood ratios $\frac{L_S}{L_B}$ of tau candidates from different classes k can be combined into a new measure p by

$$\text{logit}(p) = \tau \cdot \text{logit}(a_k) + \ln\left(\frac{L_S}{L_B}\right) , \tag{4.21}$$

where a_k is the prior probability for a candidate in class k to be true tau lepton. The factor τ is an empirically introduced factor that reweights the contribution of the prior probabilities versus the likelihood ratio. For $\tau = 1$ one can interpret p as the posterior probability of a candidate to stem from a true tau lepton. Appendix C.1 discusses this method in more detail.

In principle one can derive energy dependent a priori probabilities $a_k(E_\text{T})$ from Monte Carlo samples and to use them in equation (4.21). However, this may introduce additional systematic uncertainties and only results with fixed a_k are shown in the following. The a priori probabilities are just separated in two energy regimes corresponding to the energy ranges of the used in the likelihood method, *cf.* Table 4.4. Another method to combine the classifier outputs of different classes would be the calculation of a new likelihood ratio on top of the output for each class, which takes the a priori probabilities into account. This new test statistics would also include information about the different separation power between signal and background in the reconstruction classes and should therefore further improve the performance of the combined result. It also has the advantage to be applicable to other classifiers, like Boosted Decision Trees, whose outputs are not easily interpretable in terms of probabilities. One may also apply artificial neural networks with multiple output nodes, each corresponding to one decay mode. This is currently not yet available in TMVA and its implementation out of the scope of this thesis.

A note on the MC truth matching of tau candidates Tau candidates are matched to the Monte Carlo particles using the ΔR between the reconstructed momentum and the true visible momentum p_T^vis. The visible momentum p_T^vis includes only the visible decay products of the tau leptons and ignores the neutrinos. This matching procedure of reconstructed tau candidates to the Monte Carlo truth particles was investigated in a

detailed study. It turned out that the ΔR matching is not optimal in dense environments, where many jets exist in a single event. In such cases it can even matter, whether the matching starts from the truth particles or the reconstructed tau candidates. It has been shown that a more reliable matching can be achieved by using the detailed track information as follows. The ATLAS detector simulation provides truth information about any simulated hit in the tracking system giving a measure how much a certain truth particle contributed to a hit. The reconstructed tracks can therefore be matched to the truth particles with high confidence using their measurements. One can take the tracks assigned to a tau candidate and relate them with the above information to the charged pions from the tau decay. In $\mathrm{Z} \to \tau\tau$ events both methods agree very well and one observes differences in less than a per mill of all events. In SUSY events, however, one can observe differences in up to about 10 % of all events. The differences are mainly due to tau candidates with badly reconstructed directions, such that the ΔR between reconstructed momentum and true visible momentum gets too large even though the correct tracks have been assigned. In the following we will use the ΔR matching, because it is the default in ATLAS and allows to compare the results to previous publications more easily.

Definition of identification efficiency and jet rejection The tau identification efficiency $\epsilon^{\tau\mathrm{had}}$ is defined with respect to all hadronic tau decays using the Monte Carlo truth information,

$$\epsilon^{\tau\mathrm{had}} = \frac{N(\tau \text{ jet, MC matched} \wedge \text{tagged})}{N(\text{MC } \tau)}\,, \tag{4.22}$$

where the kinematic selection cuts for both are performed on the true visible energy. "Tagged" in this context means that the reconstructed τ jet has a likelihood ratio or respective classifier larger than a given cut. Only $\mathrm{W} \to \tau\nu$ and $\mathrm{Z} \to \tau\tau$ events are included here.

Furthermore one defines the rejection R^{jet} against QCD jets by

$$R^{\mathrm{jet}} = \frac{1 - \epsilon^{\mathrm{jet}}}{\epsilon^{\mathrm{jet}}}\,, \tag{4.23}$$

$$\epsilon^{\mathrm{jet}} = \frac{N(\tau \text{ jet,}\neg\text{MC matched} \wedge \text{tagged})}{N(\text{MC jet})}\,. \tag{4.24}$$

In this case a small asymmetry in the kinematic selection cuts cannot be avoided and one uses the reconstructed momenta for the reconstructed τ jets ($N(\tau\text{jet,}\neg\text{MC matched} \wedge \text{tagged})$) and the truth momentum for the jets from Monte Carlo particles ($N(\text{MC jet})$)[9]. Anyhow, $N(\text{MC jet})$ is only an overall scaling factor of the fake rate and therefore identical in case of comparisons of different identification methods. During this study also other definitions of the rejection have been used for example normalising on the

[9] $N(\text{MC jet})$ is calculated from the number jets found by the anti-k_T algorithm with radius parameter $R = 0.4$ run on all final state Monte Carlo particles.

number of reconstructed calorimeter jets – not tau jets – in the kinematic range. Even in this definition the kinematic selection is asymmetric as the reconstructed energy between tau jets and calorimeter jets can be different. In the calculation of the jet rejection only simulated QCD di-jet events are regarded.

Figure 4.23 shows the efficiency-versus-rejection curve (receiver operating characteristic) for the projective likelihood of PanTau with the selection of variables given in Table 4.4. Depending on the cut on the classifier one selects another working point of the identification algorithm on this curve. For comparison the same curve is shown for the TauRec algorithm using its likelihood classification. Without re-weighting the different reconstruction classes the performance of PanTau performance is rather poor, because of the reasons mentioned earlier. By re-weighting the reconstructed decay modes with their

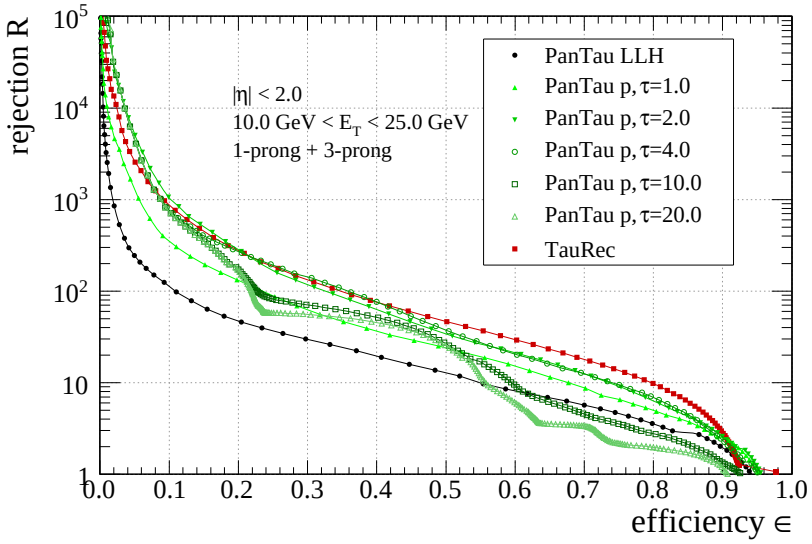

(a) $10\,\text{GeV} < E_\text{T} < 25\,\text{GeV}$

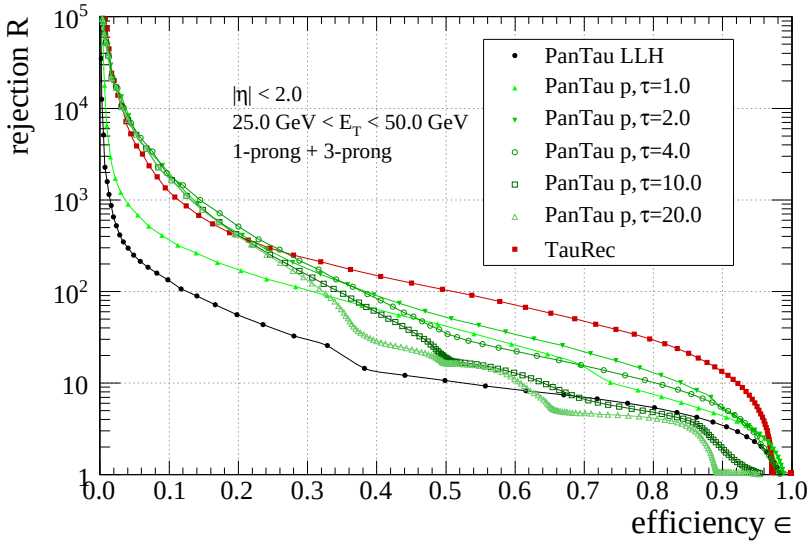

(b) $25\,\text{GeV} < E_\text{T} < 50\,\text{GeV}$

Figure 4.23: QCD jet rejection R^jet versus tau efficiency $\epsilon^{\tau\text{had}}$ for PanTau and TauRec using the likelihood identification (MC09 J0-J4 QCD di-jet and $\text{W} \to \tau^\text{had}\nu$, $\text{Z} \to \tau\tau$ Monte Carlo samples).

a priori probabilities, one can already achieve a good performance in the important low energy regime $10\,\text{GeV} < E_\text{T} < 25\,\text{GeV}$ (Figure 4.23a), which is comparable or slightly better than the TauRec result. A rescaling factor of about $\tau \approx 4$ was observed to give the best performance. In the higher energy regime (Figure 4.23b) the current PanTau selection is not fully satisfactory yet and reaches or outperforms the TauRec performance only for efficiencies below 30 %. Anyhow Figure 4.23 demonstrates the potential of the PanTau approach, because the selection of identification variables is not fully optimised yet and additional variables, not being used yet, are known to have a good separation power.

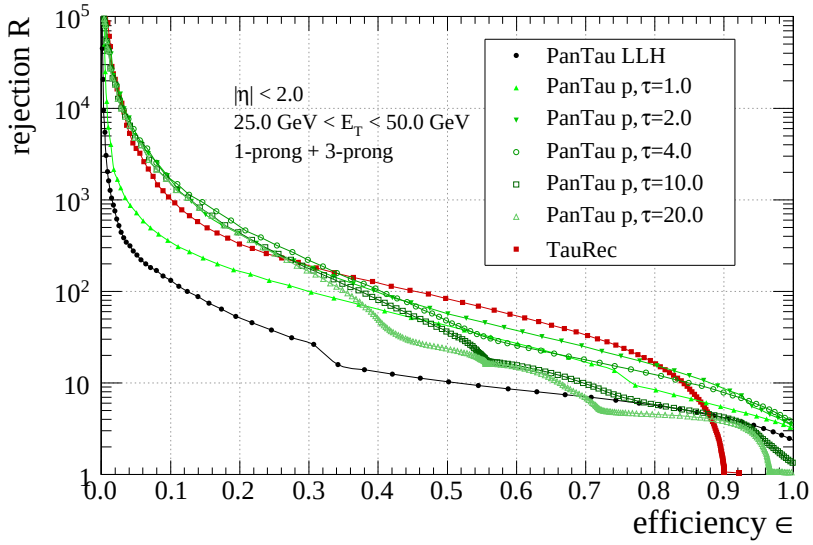

Figure 4.24: QCD jet rejection R^jet versus tau efficiency $\epsilon^{\tau\text{had}}$ in the energy range $25\,\text{GeV} < E_\text{T}^\text{reco} < 50\,\text{GeV}$. In contrast to Figure 4.23b the kinematic cuts (η, E_T) are done on reconstructed quantities for both the signal and the background (see text).

Note that the definition of efficiency and rejection used here is also asymmetric in the kinematic selection of tau candidates between efficiency and rejection, because the first uses the truth E_T^vis whereas the latter uses the reconstructed E_T^reco. This is not optimal if systematic shifts between reconstructed and true visible energy occur. Even if the uncertainty of the reconstructed energy is not systematically biased this can lead to a net shift at the values of the energy cut, if the energy spectrum is steeply falling as it is the case for QCD jets, because on average more candidates are shifted from higher to lower energy than vice versa. This asymmetry can be avoided by cutting on the reconstructed energy also in the definition of the efficiency. However, this will lead to an asymmetric definition by itself, because in the calculation of $N(\text{MC}\ \tau)$ one needs to rely on the truth E_T^vis as no reconstructed information is available for true decays not matched to any reconstructed candidate. For comparison Figure 4.24 shows the same efficiency versus rejection as Figure 4.23b, but cutting on E_T^reco and η^reco in the calculation of $\epsilon^{\tau\text{had}}$. In this case efficiencies above 1 are possible, due to differences in E_T^reco and E_T^vis. No optimal solution exists for the definition of the efficiency and rejection and we therefore use the first definition in the following as it is the default in ATLAS. Anyhow the reader should be aware of subtle differences in the definitions when comparing efficiency-vs-rejection curves from different publications.

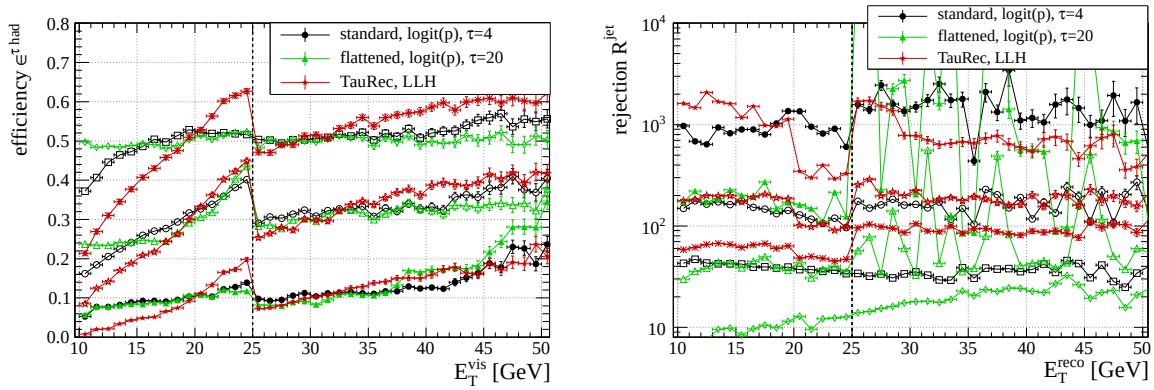

(a) Efficiency $\epsilon^{\tau\,\mathrm{had}}$ **(b)** Rejection R^{jet}

Figure 4.25: Tau efficiency and QCD jet rejection versus the transverse energy ${E_\mathrm{T}}^{\mathrm{vis}}$ and ${E_\mathrm{T}}^{\mathrm{reco}}$, respectively, for TauRec and PanTau with standard variable selection and E_T-flattened variables. The energy dependencies are shown for mean efficiencies of 10 %, 30 % and 50 %, where the mean efficiencies have been calculated in the energy ranges $15\,\mathrm{GeV} < E_\mathrm{T} < 25\,\mathrm{GeV}$ and $25\,\mathrm{GeV} < E_\mathrm{T} < 40\,\mathrm{GeV}$, which leads to a "jump" at $E_\mathrm{T} = 25\,\mathrm{GeV}$, but keeps the efficiencies more comparable over the whole range. A second "jump" is observed in the TauRec rejection at $E_\mathrm{T} = 20\,\mathrm{GeV}$ due to the binning used in its reference distributions. The uncertainties of the jet rejection need to be taken with care and are most likely underestimated, because the different jet samples have very different scale factors.

The energy dependency of the tau efficiency and the jet rejection depicts Figure 4.25. Even without applying the flattening of variables in the transverse energy one observes that the PanTau efficiency and rejection is more stable in E_T than TauRec. At a mean efficiency of 50 % a significant drop in efficiency is only observed for transverse visible energies below 15 GeV. For comparison the energy dependency is shown after replacing the variables $\langle \Delta R(\mathrm{jet}, \mathrm{EFO}) \rangle^{\mathcal{C}}_{E_\mathrm{T}}$ for all criteria $\mathcal{C}$ with their flattened versions. Indeed the energy dependency of the efficiency gets smaller at least for higher efficiencies, but the rejection is largely reduced for the reasons discussed above. The rejection without E_T-flattened variables is relatively stable within the statistical uncertainties even though it gets worse by about a factor of two for lower energies as one would expect.

From the described experiences with the flattening procedure we can conclude that this method cannot be used by default yet. Even though the rejection appears to be worse only artificially one needs further tuning to achieve competitive results. In special applications the flattening can still be very useful, *e.g.* in analyses including the reconstruction of an invariant di-tau mass $m_{\tau\tau}$ one would profit from very low E_T-dependencies of the efficiency, because it minimises biases in the energy spectra of the tau leptons. Furthermore other multivariate methods may be less sensitive to the described effect. It may also be helpful to reweight the events in the training or reference sample to obtain a flat E_T spectrum of the reference. Such a re-weighting was not pos-

sible with the given Monte Carlo samples as it needs higher statistics in order to avoid large statistical fluctuations due to large scale factors[10].

Energy resolution

One of the main objectives of the energy flow approach is the improvement of the energy resolution. Figure 4.26 therefore shows the relative energy resolution $E_{\mathrm{T}}^{\mathrm{reco}}/E_{\mathrm{T}}^{\mathrm{vis}}$ achieved for the main true decay modes of tau leptons. It is clearly visible that the energy resolution can be significantly improved with respect to the TauRec algorithm for 1- and 3-prong tau decays without additional neutral particles (Figure 4.26a, Figure 4.26c). However, the energy is slightly overestimated and tails are observed to higher energies. This effect is most likely caused by the splitting of hadronic clusters and remnants from the subtraction procedure (*cf.* Section 4.3). The improvement in tau decays with additional particles is not as large and again one observes a systematic overestimation of the tau energy (Figure 4.26b, Figure 4.26d). Note, that no additional correction of the tau jet energy is applied for PanTau, yet, as it is the case for TauRec.

Only recently the full Monte Carlo truth information about the energy deposition of individual particles in each calorimeter cell is available in athena. These data will most likely help to identify remaining problems in the energy flow approach of eflowRec and to correct for the above effects. eflowRec is still under heavy development and many improvements are expected in this respect.

The energy dependency of the energy resolution, the "linearity", is visualised in Figure 4.27. PanTau clearly shows a more stable behaviour than TauRec especially for tau decay modes without neutral pions. Still the bias is not completely flat in the transverse energy. Energy dependent correction factors may be derived from the mean shift in Figure 4.27 to improve the final energy reconstruction.

[10] Note the special technical demands to employ eflowRec at the moment. eflowRec requires ESD files with full calorimeter information as input. Currently only a fraction of the Monte Carlo samples in ATLAS are kept with ESD information and eflowRec is not yet run in the default reconstruction. It was therefore only possible to use limited Monte Carlo statistics in this analysis.

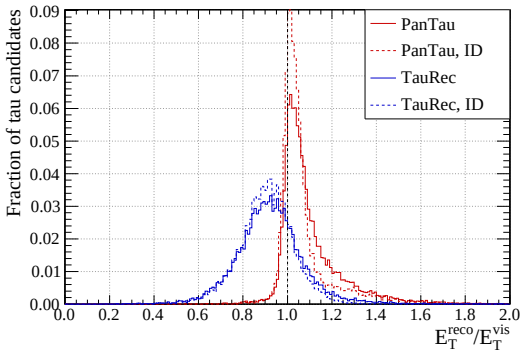

(a) true 1-prong decays

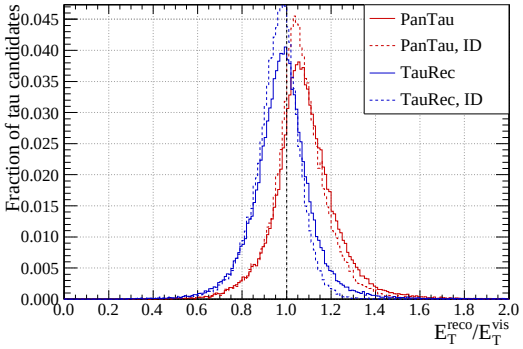

(b) true 1-prong decays with neutral particles

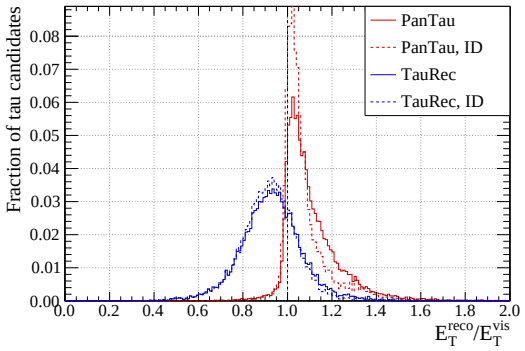

(c) true 3-prong decays

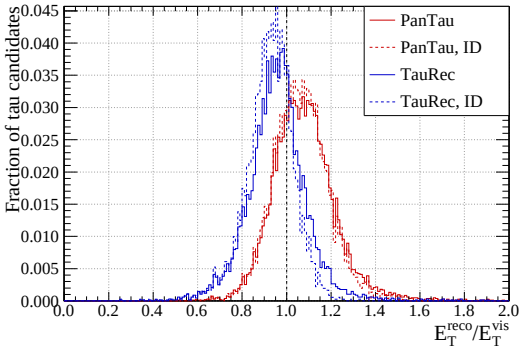

(d) true 3-prong decays with neutral particles

Figure 4.26: Relative energy resolution of PanTau in the energy range $10\,\text{GeV} < E_\text{T}^\text{vis} < 50\,\text{GeV}$ in $\text{W} \to \tau^\text{had}\nu$ and $\text{Z} \to \tau\tau$ MC09 samples. The solid line corresponds to all reconstructed candidates with truth match, and the dashed line to candidates after identification using the likelihood with an efficiency of approximately $\epsilon^{\tau\text{had}} \approx 50\,\%$. The same quantities for TauRec are shown for comparison.

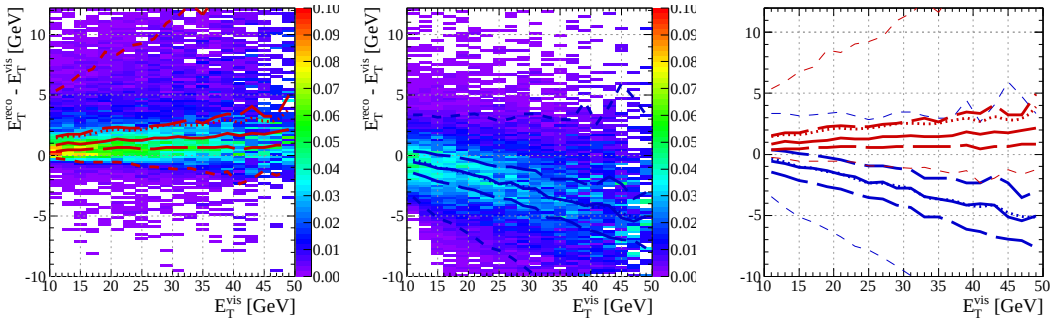

(a) true 1-prong decays without neutral particles

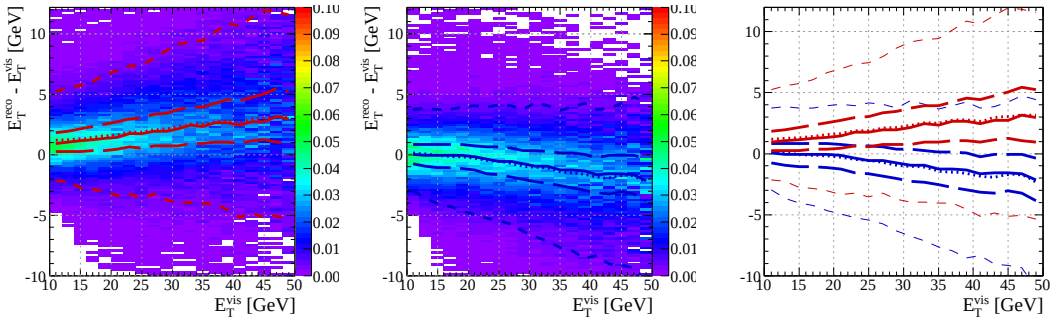

(b) true 1-prong decays with neutral particles

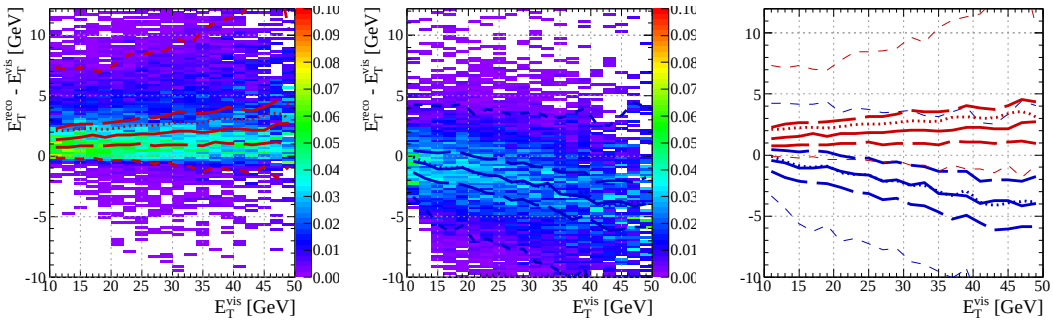

(c) true 3-prong decays without neutral particles

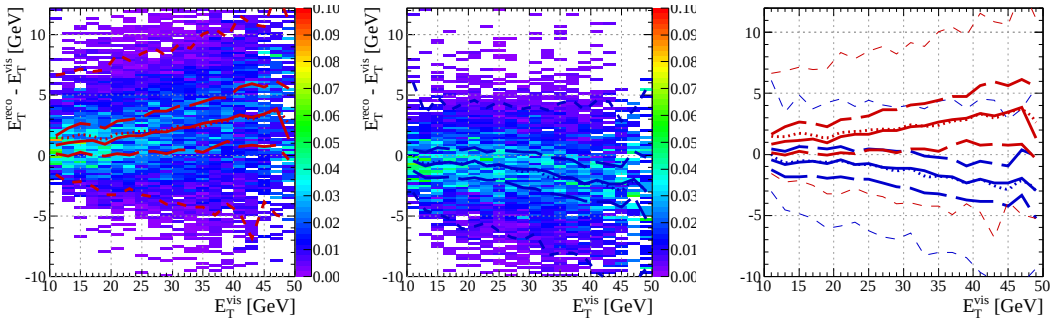

(d) true 3-prong decays with neutral particles

Figure 4.27: Energy resolution of PanTau (left) and TauRec (middle) versus the true transverse energy $E_{\mathrm{T}}^{\mathrm{vis}}$ in $\mathrm{W} \to \tau^{\mathrm{had}}\nu$ and $\mathrm{Z} \to \tau\tau$ MC09 samples. Overlaid to the two dimensional distributions are the median value (solid line), the mean value (dotted line) and the intervals of 95 %, 68.3 %, 31.7 % and 5 % (dashed lines) of all entries in each energy bin. On the right the energy dependency of mean and median value are repeated for PanTau (red) and TauRec (blue) in the same graph. The η range of the tau candidates is restricted to $|\eta^{\mathrm{vis}}| < 2.0$.

4.5.4 Data – Monte Carlo comparison of energy flow quantities

In the following some comparisons of energy flow quantities and PanTau identification variables between Monte Carlo samples and measured data are performed. This test is important to demonstrate that the PanTau approach is not only an academic idea, but also a reliable algorithm in the real experimental environment, which always includes more side effects than incorporated in Monte Carlo simulations. For this purpose collision data at a centre-of-mass energy of $\sqrt{s} = 7\,\text{TeV}$ mainly from the run period D of 2010 are used, comprising approximately $\mathcal{L} \approx 358\,\text{nb}^{-1}$ of integrated luminosity. A detailed list of the runs and data samples used in the comparison can be found in Appendix A.1. The analysis follows the ATLAS recommendations and applies similar event selection and cleaning cuts as references [125] and [126] which compared the standard TauRec algorithm in Monte Carlo and data.

As a first event cleaning cut a so-called *good runs list* (GRL) is applied [127] to select only luminosity blocks inside a run, where all sub-detectors needed for the tau reconstruction are operational. In a central production the ESD datasets have been skimmed to "performance DPDs", *i.e.* some event selection cuts have already been applied[11]. To make a comparison to the Monte Carlo prediction it is therefore needed to apply at least one event selection cut that is equal or harder than the DPD skimming in both Monte Carlo and data samples. Therefore we require to have at least one tau candidate in each event found by the TauRec algorithm with transverse energy $E_\text{T} > 30\,\text{GeV}$. This cut requires only a tau candidate and no identification at all, *i.e.* it is fulfilled by nearly all jets above this energy threshold. All events are required to pass the L1_TAU5 *trigger condition*, defined as having at least one tau jet at trigger level 1 passing a 5 GeV threshold. In order to remove events with mismeasurements in the calorimeter and jets with bad timing behaviour all events with *"bad" or "ugly" jets are rejected*, where the jets are classified using a dedicated tool (JetCaloQualityUtils), following a recommendation of the ATLAS jet group [128]. Furthermore at least one reconstructed *primary vertex* with four or more associated tracks is required. Finally a very loose *di-jet selection* is performed with at least two tau candidates with $E_\text{T} > 15\,\text{GeV}$ which are separated in azimuthal angle by $\Delta\varphi > 2.7$.

The leading, *i.e.* most energetic, tau candidate in each event is not used in the following analysis. This reduces systematic uncertainties on the trigger selection, because the leading candidate is usually connected to the object triggering the L1_TAU5 condition. Additionally it avoids interference with the leading tau cut of $E_\text{T} > 30\,\text{GeV}$ in the energy regime below this value. Table 4.5 summarises the cut flow for data and Monte Carlo. The Monte Carlo samples are normalised to data after the GRL, trigger and leading tau requirement. With the given event selection cuts only a negligible amount of true tau candidates from $\text{W} \to \tau\,\nu$ and $\text{Z} \to \tau^-\,\tau^+$ events are expected in the investigated data

[11] The usage of performance DPDs derived from the ESD data format is needed for this analysis, because the energy flow reconstruction (eflowRec) has to be run privately and needs data objects like the energy deposition in every calorimeter cell which is not available in the AOD format usually used for physics analyses. Details on the DPD skimming can *e.g.* be found in [125].

sample. Hence, the following comparison of energy flow quantities between Monte Carlo samples and data only considers QCD jet backgrounds.

Already in early studies [129] it was shown that the MC09 tune [130] of Pythia does not describe the jet shapes in data very well. Instead the DW tune [131] of Pythia was shown to be more appropriate and is therefore used here. Unfortunately, the amount of officially available QCD di-jet samples with the DW tune of Pythia is rather limited at the time of writing. Especially the Monte Carlo samples in the energy range up to $E_{\mathrm{T}} < 17\,\mathrm{GeV}$ and $E_{\mathrm{T}} < 35\,\mathrm{GeV}$ have large scale factors between the statistics of the Monte Carlo samples and the expected number of events of the order of $\mathcal{O}(2000)$ and $\mathcal{O}(150)$, respectively, causing significant fluctuations in the following distributions. From the J0 sample ($E_{\mathrm{T}} < 17\,\mathrm{GeV}$) only one event out of its Monte Carlo sample of about 400 000 events passes the event selection cuts, mainly because of the requirement for a leading TauRec candidate with $E_{\mathrm{T}} > 30\,\mathrm{GeV}$. Therefore the J0 sample was completely skipped in the following analysis. Without larger Monte Carlo datasets as they are produced at the time of writing it is therefore not useful to further increase the considered amount of data. In order to reflect the relative contributions of the different di-jet Monte

cut	$\mathrm{Z} \to \tau\tau$	$\mathrm{W} \to \tau\nu$	QCD jets		data	
Good Runs List	81.3	866.9	$5.960(9) \times 10^7$		6 396 104	
leading tau	22.5	114.5	$3.124(14) \times 10^6$	5.2%	3 089 984	48.3%
Trigger L1_TAU5	22.4	112.8	$2.876(13) \times 10^6$	92.0%	2 875 777	93.1%
jet cleaning	22.1	111.5	$2.841(13) \times 10^6$	98.8%	2 804 790	97.5%
primary vertex	22.1	111.5	$2.840(13) \times 10^6$	100.0%	2 798 661	99.8%
tau candidates	14.7	48.6	$1.961(10) \times 10^6$	69.1%	1 978 937	70.7%
tau back-to-back pair	5.6	12.0	$7.84(6) \times 10^5$	40.0%	807 235	40.8%
number of sub-leading PanTau candidates	7.9	16.6	$9.20(13) \times 10^5$		1 063 523	

Table 4.5: Cut-flow of the data to Monte Carlo comparison. The uncertainties include statistical uncertainties of the Monte Carlo samples only, where the statistical uncertainties of the $\mathrm{W} \to \tau\nu$ and $\mathrm{Z} \to \tau\tau$ samples are negligible. In addition to the number of events the table also shows the event yield with respect to the previous cut in percent. Monte Carlo samples are scaled with respect to each other according to their predicted cross sections and scaled to data after applying the *Good Runs List*, *leading tau* and *trigger* selection. The last row shows the total number of sub-leading PanTau candidates in the kinematic range $p_{\mathrm{T}} > 15\,\mathrm{GeV}$, $|\eta| < 2.0$.

Carlo samples (labeled J1 to J4 with increasing transverse energy) their histograms have been stacked on top of each other in the following figures.

The distribution of the pseudo-rapidity η differs in the range where PanTau candidates are reconstructed for the n-prong classes and the "other" class due to the η coverage of the Inner Detector, because the n-prong classes require a certain number of reconstructed tracks, whereas also candidates without qualified tracks can end up in the "other" class. Above $|\eta| > 2.5$ the track requirement cannot be fulfilled, which is visible in the comparison of the η distribution of all PanTau candidates (Figure 4.28a) and ignoring the "other" class (Figure 4.28c). In the higher momentum range $25\,\text{GeV} < p_\text{T} < 50\,\text{GeV}$ (Figure 4.28b and Figure 4.28d) this difference in not as expressed as in the low-momentum range $10\,\text{GeV} < p_\text{T} < 25\,\text{GeV}$, because for higher momenta the "other" class is dominated by candidates with more than seven qualified tracks.

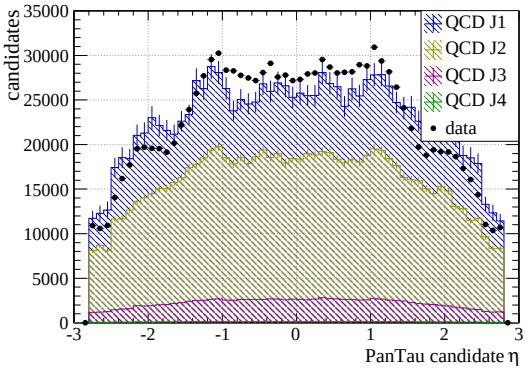

(a) $10\,\text{GeV} < p_\text{T} < 25\,\text{GeV}$

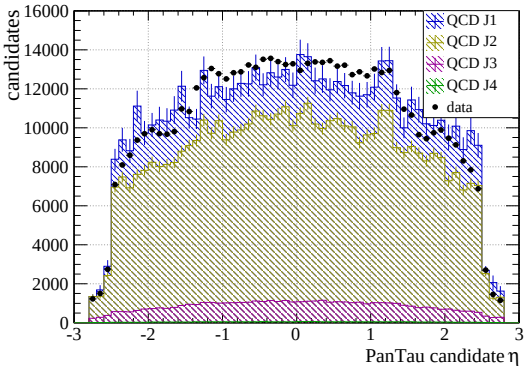

(b) $25\,\text{GeV} < p_\text{T} < 50\,\text{GeV}$

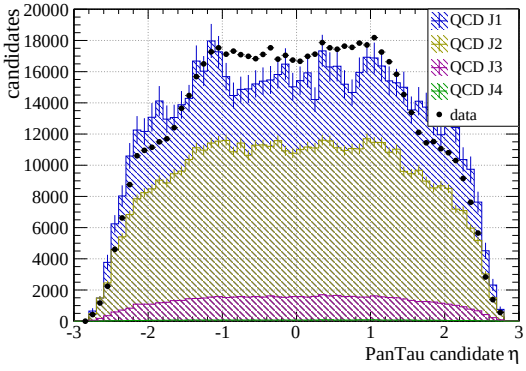

(c) $10\,\text{GeV} < p_\text{T} < 25\,\text{GeV}$, without "other"

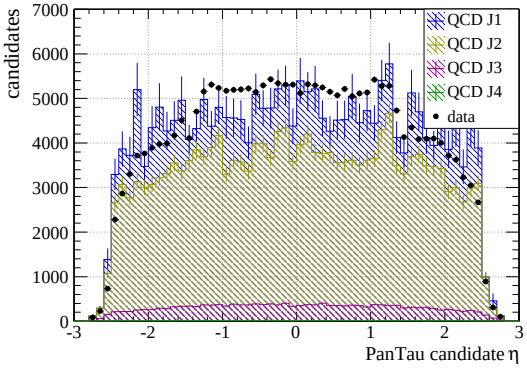

(d) $25\,\text{GeV} < p_\text{T} < 50\,\text{GeV}$, without "other"

Figure 4.28: Pseudorapidity η distribution of sub-leading PanTau candidates in Monte Carlo and data at $\sqrt{s} = 7\,\text{TeV}$. The Monte Carlo distribution is normalised to data by area and the different contributions of the QCD di-jet MC (J1 - J4, DW tune) are stacked on top of each other.

Both for all candidates and ignoring the "other" class one observes differences between the QCD di-jet Monte Carlo prediction and the measured η distribution. Even though the Monte Carlo sample size is limited one can see, that the measurements are more central than the Monte Carlo prediction. This is a known feature of the Pythia DW tune and is also observed in the η distribution of the TauRec candidates [125]. The ATLAS tau performance group decided to use the Pythia DW tune anyhow, because it describes the individual ID variables and jet shapes better. In order to reduce the effect of differences in the pseudo-rapidity distribution we restrict the pseudo-rapidity range to $|\eta| < 2.0$ in the following.

Considering all PanTau candidates in the pseudo-rapidity range $|\eta| < 2.0$ one observes differences in the distribution of the reconstructed transverse momentum p_{T} especially at low momenta (Figure 4.29a). The "other" class is expected to be most sensitive to noise clusters in the calorimeter and other mismeasurements, because it includes candidates

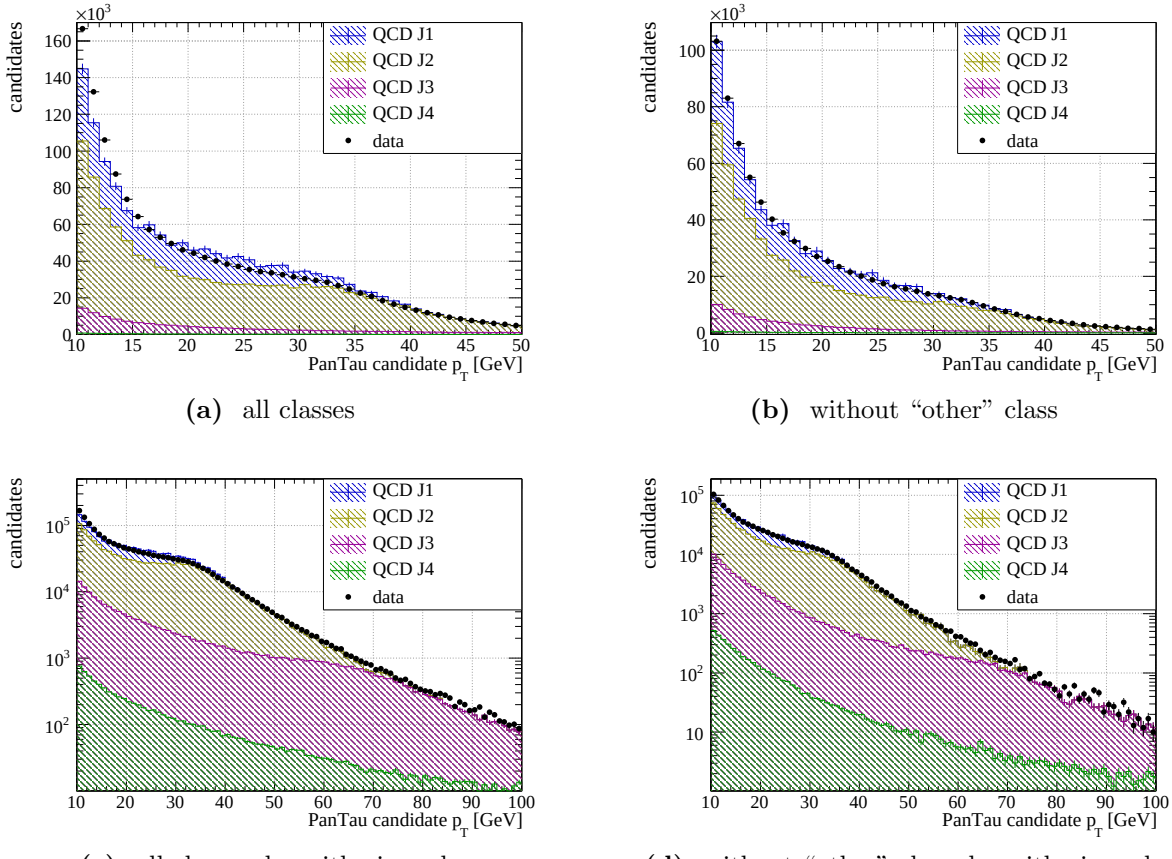

(a) all classes

(b) without "other" class

(c) all classes, logarithmic scale

(d) without "other" class, logarithmic scale

Figure 4.29: Transverse momentum distribution of sub-leading PanTau candidates in Monte Carlo and data at $\sqrt{s} = 7\,\mathrm{TeV}$ in the pseudo-rapidity range $|\eta| < 2.0$. The Monte Carlo distribution is normalised to data by area and the different contributions of the QCD di-jet MC (J1 - J4, DW tune) are stacked on top of each other. The left figures include all PanTau candidates, the right ones all candidates except for those belonging to the "other" class. Note the different range of the p_{T} axis for the logarithmic plots.

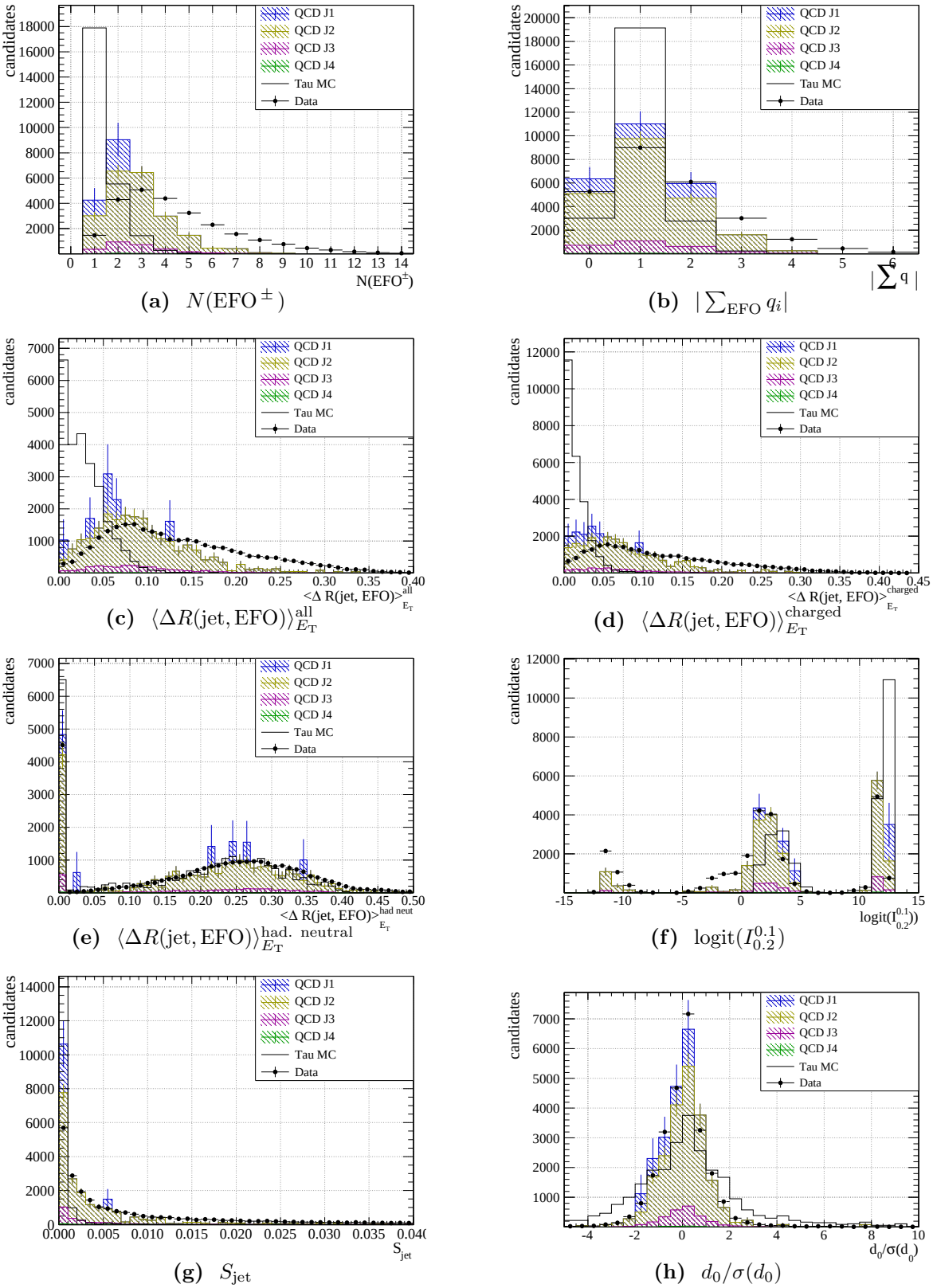

(a) $N(\mathrm{EFO}^{\pm})$ **(b)** $|\sum_{\mathrm{EFO}} q_i|$

(c) $\langle \Delta R(\mathrm{jet}, \mathrm{EFO}) \rangle^{\mathrm{all}}_{E_{\mathrm{T}}}$ **(d)** $\langle \Delta R(\mathrm{jet}, \mathrm{EFO}) \rangle^{\mathrm{charged}}_{E_{\mathrm{T}}}$

(e) $\langle \Delta R(\mathrm{jet}, \mathrm{EFO}) \rangle^{\mathrm{had.\ neutral}}_{E_{\mathrm{T}}}$ **(f)** $\mathrm{logit}(I^{0.1}_{0.2})$

(g) S_{jet} **(h)** $d_0/\sigma(d_0)$

Figure 4.30: Distribution of the identification variables for the "1-prong" class in the transverse momentum range $10\,\mathrm{GeV} < p_{\mathrm{T}} < 25\,\mathrm{GeV}$. The stacked histograms correspond to the different QCD di-jet samples and the black dots are measured data. Monte Carlo samples have been scaled to the integral of the data. The black line shows the distribution for $\mathrm{W} \rightarrow \tau\nu$ and $\mathrm{Z} \rightarrow \tau\tau$ events for comparison.

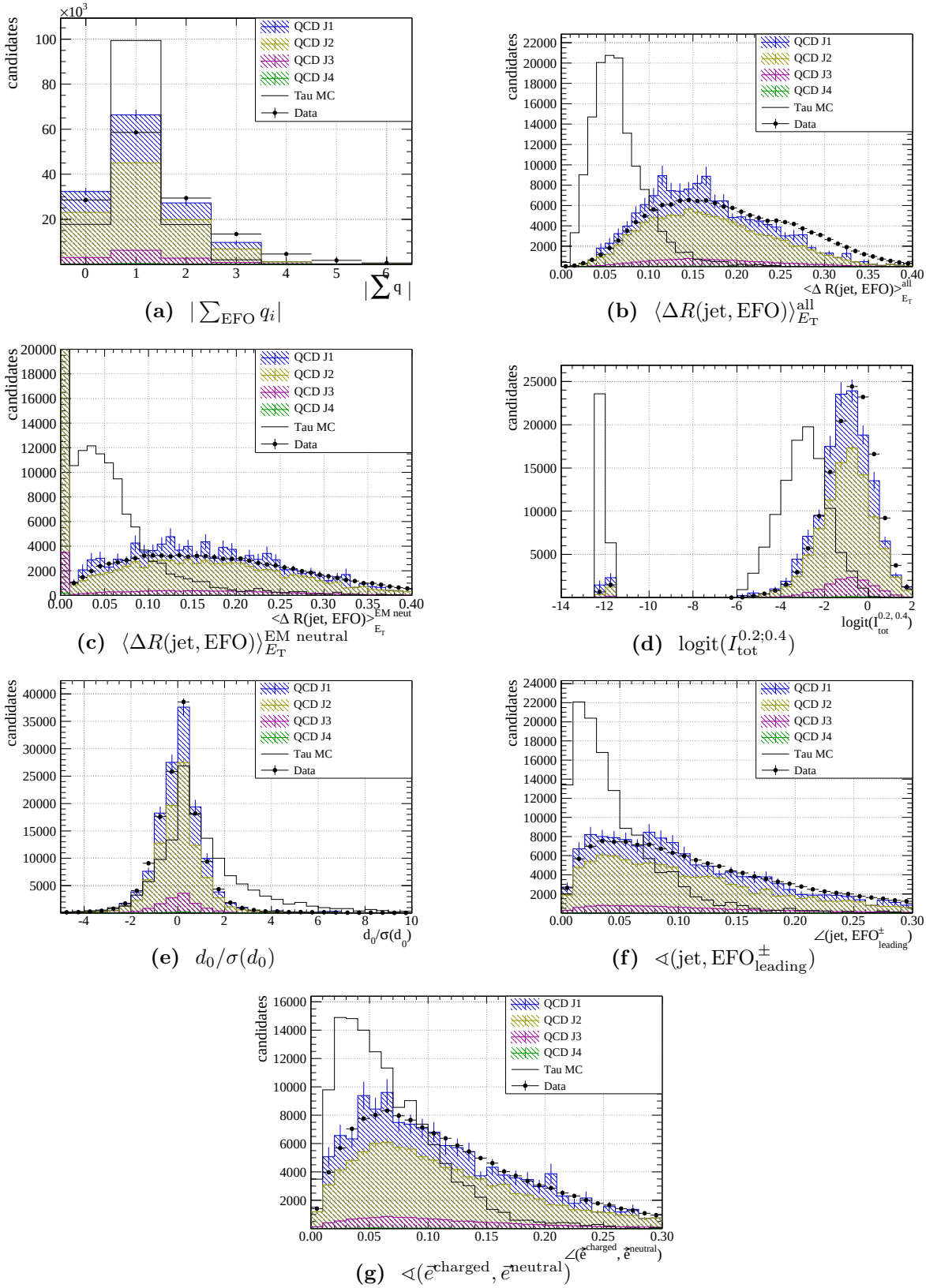

(a) $|\sum_{\mathrm{EFO}} q_i|$ **(b)** $\langle \Delta R(\mathrm{jet}, \mathrm{EFO}) \rangle^{\mathrm{all}}_{E_{\mathrm{T}}}$

(c) $\langle \Delta R(\mathrm{jet}, \mathrm{EFO}) \rangle^{\mathrm{EM\ neutral}}_{E_{\mathrm{T}}}$ **(d)** $\mathrm{logit}(I^{0.2;0.4}_{\mathrm{tot}})$

(e) $d_0/\sigma(d_0)$ **(f)** $\sphericalangle(\mathrm{jet}, \mathrm{EFO}^{\pm}_{\mathrm{leading}})$

(g) $\sphericalangle(\vec{e}^{\mathrm{charged}}, \vec{e}^{\mathrm{neutral}})$

Figure 4.31: Distribution of the identification variables for the "1-prong+neutral" class in the transverse momentum range $10\,\mathrm{GeV} < p_{\mathrm{T}} < 25\,\mathrm{GeV}$. The stacked histograms correspond to the different QCD di-jet samples and the black dots are measured data. Monte Carlo samples have been scaled to the integral of the data. The black line shows the distribution for $\mathrm{W} \rightarrow \tau\nu$ and $\mathrm{Z} \rightarrow \tau\tau$ events for comparison.

without any qualified track as well as candidates with more than seven tracks. Indeed one observes a very good agreement between Monte Carlo prediction and data, when the "other" class is neglected in the transverse momentum distribution (Figure 4.29b, Figure 4.29d).

Figure 4.30, 4.31 and Figure C.8 to C.19 in Appendix C.3 compare the ID variables for each individual category in data and in Pythia Monte Carlo (DW tune). To illustrate the difference between QCD jets and tau jets the comparisons also include the Monte Carlo prediction for tau candidates in $W \to \tau\,\nu$ and $Z \to \tau^-\,\tau^+$ events with truth match. Figure 4.30, 4.31 and Figure C.8 – C.12 show the variables in the transverse momentum range $10\,\text{GeV} < p_\text{T} < 25\,\text{GeV}$ and Figure C.13 – C.19 in the range $25\,\text{GeV} < p_\text{T} < 50\,\text{GeV}$.

In general a good agreement between the Monte Carlo prediction for QCD jets and the measured data is achieved within the statistical uncertainties of the Monte Carlo samples. Some variables show larger discrepancies, though, and they are especially pronounced in the "1-prong" category (Figure 4.30). For example the number of charged energy flow objects $N(\text{EFO}^{\pm})$ (Figure 4.30a) and the sum of charges $|\sum_{\text{EFO}} q_i|$ (Figure 4.30b) in the "1-prong" category are significantly larger in the data than in the Monte Carlo prediction. Also the E_T-weighted mean distance of charged energy flow objects (Figure 4.30d) has significantly larger tails to higher values in contrast to the same distribution for neutral, hadronic energy flow objects (Figure 4.30e).

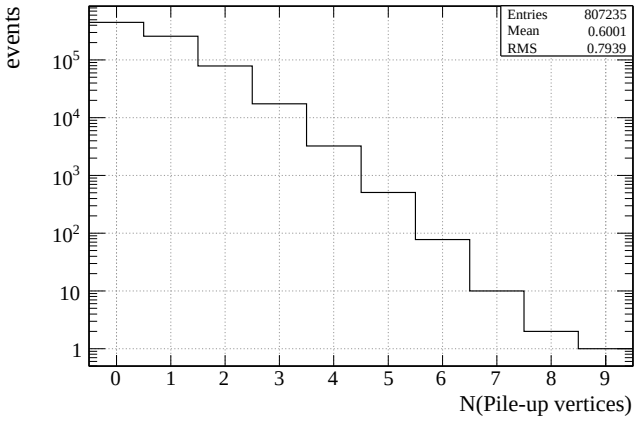

Figure 4.32: Number of reconstructed pile-up vertices in the data events used for the Monte Carlo to data comparisons in this Section. Only events passing the selection cuts given in Table 4.5 are included here.

We will see that the discrepancies can mostly be explained by pile-up effects in data. Due to the high number of protons in each of the proton bunches in the LHC, more than one pair of protons may interact in a single bunch crossing (*cf.* Section 2.1). Even though the number of protons in the bunches were small in the LHC runs in 2010 compared to the design parameters of the LHC one still observed a sizable fraction of events with additional pile-up vertices. Figure 4.32 shows the number of reconstructed pile-up vertices in the events used for the comparisons. Even though most events do not include additional pile-up interactions yet, there are even a few events with five or more reconstructed pile-up vertices. In total a mean number of 0.6 pile-up vertices is found. The Monte Carlo samples on the other hand do not include simulated pile-up vertices.

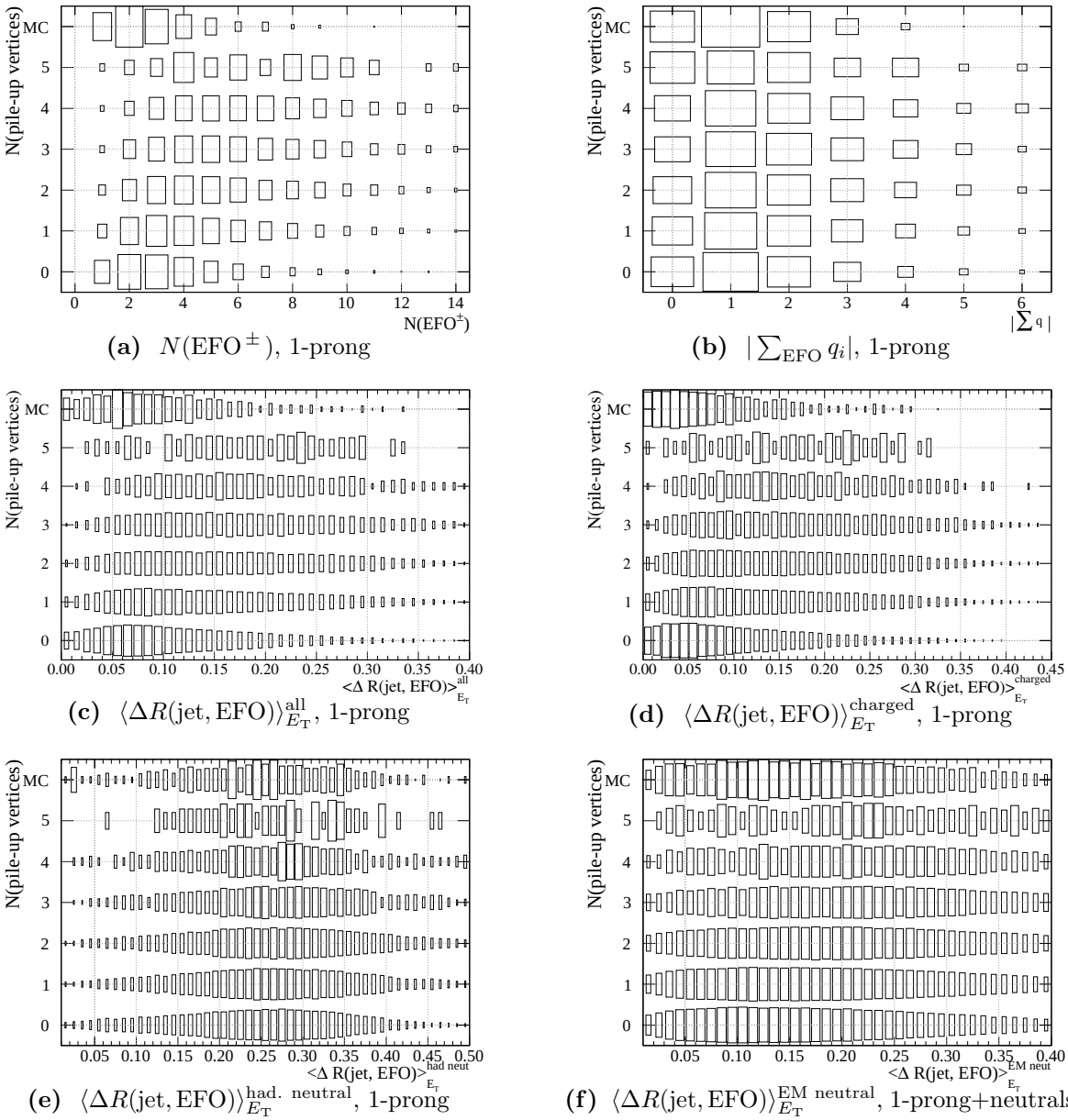

(a) $N(\mathrm{EFO}^{\pm})$, 1-prong **(b)** $|\sum_{\mathrm{EFO}} q_i|$, 1-prong

(c) $\langle \Delta R(\mathrm{jet}, \mathrm{EFO}) \rangle^{\mathrm{all}}_{E_{\mathrm{T}}}$, 1-prong **(d)** $\langle \Delta R(\mathrm{jet}, \mathrm{EFO}) \rangle^{\mathrm{charged}}_{E_{\mathrm{T}}}$, 1-prong

(e) $\langle \Delta R(\mathrm{jet}, \mathrm{EFO}) \rangle^{\mathrm{had.\ neutral}}_{E_{\mathrm{T}}}$, 1-prong **(f)** $\langle \Delta R(\mathrm{jet}, \mathrm{EFO}) \rangle^{\mathrm{EM\ neutral}}_{E_{\mathrm{T}}}$, 1-prong+neutrals

Figure 4.33: Pile-up dependency of PanTau identification variables in the transverse momentum range $10\,\mathrm{GeV} < p_{\mathrm{T}} < 25\,\mathrm{GeV}$. The variable distribution is given for different numbers of reconstructed pile-up vertices. The top row shows the Pythia Monte Carlo prediction (DW tune) for comparison, which does not include simulated pile-up. Entries are normalised in each row.

Figure 4.33 visualises the pile-up dependency for selected variables. Especially the total number of charged energy flow objects $N(\mathrm{EFO}^{\pm})$ (Figure 4.33a) shows a strong pile-up dependency. The distributions for events without pile-up vertices matches the MC prediction much better. Figure 4.34 allows for a better comparison with the MC prediction by showing events with no additional pile-up vertices. Note, that $N(\mathrm{EFO}^{\pm})$

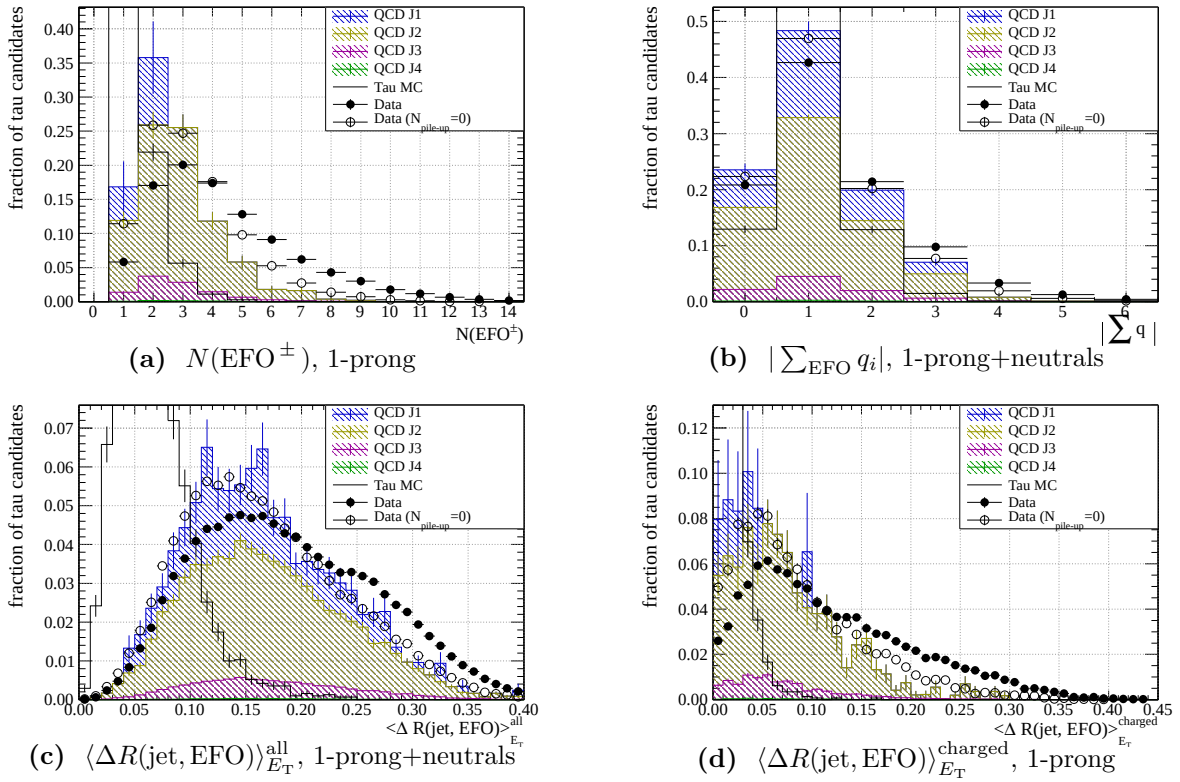

(a) $N(\mathrm{EFO}^{\pm})$, 1-prong **(b)** $|\sum_{\mathrm{EFO}} q_i|$, 1-prong+neutrals

(c) $\langle \Delta R(\mathrm{jet}, \mathrm{EFO}) \rangle^{\mathrm{all}}_{E_{\mathrm{T}}}$, 1-prong+neutrals **(d)** $\langle \Delta R(\mathrm{jet}, \mathrm{EFO}) \rangle^{\mathrm{charged}}_{E_{\mathrm{T}}}$, 1-prong

Figure 4.34: Distribution of selected identification variables in the transverse momentum range $10\,\mathrm{GeV} < p_{\mathrm{T}} < 25\,\mathrm{GeV}$. The stacked histograms correspond to the different QCD di-jet samples and the black dots denote measured data. Open circles represent events in data without additional measured vertices ($N_{\text{pile-up}} = 0$). All histograms are normalised and show the fraction of tau candidates in each bin.

includes all charged energy flow objects without further track selection cuts. The same holds for the sum of charges $|\sum_{\mathrm{EFO}} q_i|$ (Figure 4.33b and Figure 4.34b). In general one observes a stronger dependency on the number of pile-up vertices for those variables including charged EFOs. This is fortunate as track-based observables can be made pile-up proof more easily than purely calorimeter-based observables for the following reason. The pile-up vertices are shifted up to a few cm along the z-axis with respect to the primary vertex due to the length of the colliding proton bunches. These shifts can be resolved by the Inner Detector tracking. The tracks of charged particles can be selected to keep only tracks compatible with the primary vertex. Such a selection is not possible for calorimeter clusters without track match, because the angular pointing resolution of the calorimeter clusters is by far not good enough to resolve different pile-up vertices along the beam pipe. It should therefore be sufficient to re-tune the track selection cuts for non-qualified energy flow objects in PanTau to minimise the pile-up sensitivity of the identification variables or to use only charged EFOs with qualified tracks in the calculation of variables. Note that the non-qualified selection is independent from the selection of qualified charged objects used in the categorisation, *cf.* Section 4.5.1.

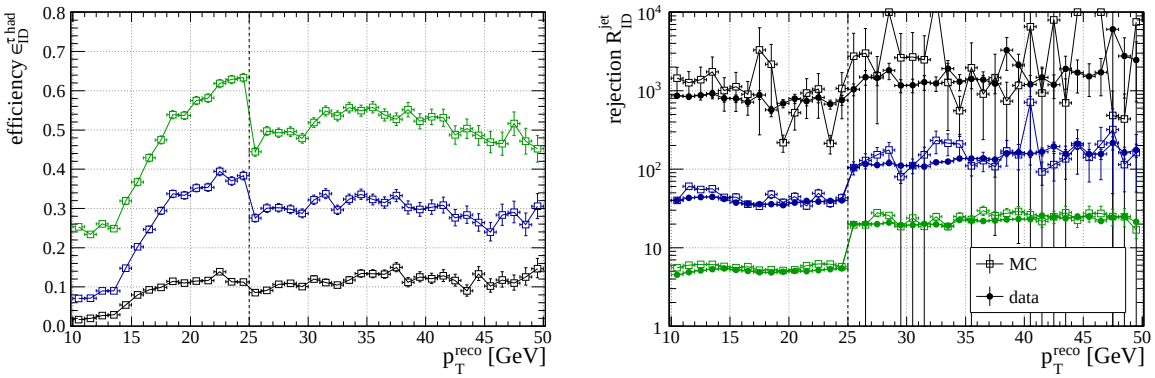

(a) Identification efficiency $\epsilon_{\mathrm{ID}}^{\tau\mathrm{had}}$ **(b)** Jet rejection $R_{\mathrm{ID}}^{\mathrm{jet}}$

Figure 4.35: Tau identification efficiency and jet rejection versus the transverse momentum $p_{\mathrm{T}}^{\mathrm{reco}}$, for Monte Carlo and data with standard variable selection (logit(p) with $\tau = 4$). The momentum dependencies are shown for mean efficiencies of 10 %, 30 % and 50 %, where the mean efficiencies have been calculated in the energy ranges 15 GeV $< E_{\mathrm{T}} <$ 25 GeV and 25 GeV $< E_{\mathrm{T}} <$ 40 GeV, which leads to a "jump" at $E_{\mathrm{T}} = 25$ GeV, but keeps the efficiencies more comparable over the whole range. In contrast to Figure 4.25 only the efficiency and rejection of the identification step is given here, *i.e.* the efficiencies and rejections are normalised to the number of reconstructed tau candidates, not true taus or true jets. The uncertainties of the jet rejection need to be taken with care and are most likely underestimated, because the different jet samples have very different scale factors.

In conclusion of the previous results Figure 4.35 shows the efficiency and rejection of the tau identification in PanTau as a function of the reconstructed transverse momentum of the tau candidates. In contrast to Figure 4.25 only the efficiency and rejection of the identification step is given here, *i.e.* the efficiencies and rejections are normalised to the number of reconstructed tau candidates, not true taus or true jets. This allows to easily apply the same calculation for the jet rejection to measured data. Figure 4.35b compares the jet rejection as estimated from the Monte Carlo samples with the estimates from data. Again one assumes that no or only negligible contributions from true tau decays exist in the data sample. Like before one observes a reasonably good agreement between the Monte Carlo estimate and the measured data. Only in the transverse momentum range below 15 GeV the rejection in data seems to be slightly worse. More sophisticated methods to estimate the jet rejection like tag-and-probe methods can be applied to QCD jets, but they will reduce the available statistics significantly and will not improve the results as long as true tau decays do not contribute. The extended methods have the advantage though that further systematic effects may be studied as well, like the difference between quark and gluon induced QCD jets, see *e.g.* reference [132].

Apart from the pile-up dependency of some identification variables the comparison of energy flow quantities and the PanTau jet rejection in Monte Carlo predictions and data show that the eflowRec and PanTau approaches are robust and work reliably not

only on simulated events, but also in "real life". The sensitivity to pile-up can easily be improved by further track selection criteria as argued before.

4.6 Summary

The reconstruction and identification of tau leptons and especially their hadronic decays is an important ingredient for many searches for new phenomena beyond the Standard Model. However, only the tau decay products can be detected in collision events at ATLAS. The decays into hadrons occur in well-known modes via resonances making it possible to distinguish the resulting jets from jet production by the hadronisation of quarks and gluons.

Mainly decays into one or three charged pions with additional neutral pions occur. As this is one of the important signatures for tau decays, one needs reliable algorithms for the reconstruction of the pion tracks. The criteria for the selection of reconstructed tracks is crucial to obtain a high efficiency at a low rate of fake tracks. The main source of fake tracks inside tau jets is the conversion of photons into e^+e^- pairs. Inefficiencies in the track reconstruction mainly arise from hadronic interactions of the charged pions in the Inner Detector volume. Several track selection criteria were investigated based on Monte Carlo simulations of tau and QCD jets and tuned to give the most reliable classification of tau jets into their decay modes. Additionally the effect of misalignments of the Inner Detector on the track reconstruction for tau decays and the tau identification itself were studied, where no significant impact was found.

Energy flow algorithms combine the measurements of the tracking system with measurements in the calorimeters to improve the energy resolution of objects like jets. They are especially useful for the reconstruction of tau leptons and are already used for some time in this field. Here a new approach to tau lepton reconstruction was presented, which fully relies on the energy flow algorithm eflowRec which is not specific to tau reconstruction. This has several conceptional advantages to existing approaches and makes use of the good performance of eflowRec which uses a more detailed energy flow scheme than the energy flow algorithm in the conventional tau reconstruction of ATLAS. A better separation of the recovery from detector effects and the actual tau reconstruction can thus be achieved. The new tau algorithm, named PanTau, also implements new concepts in the categorisation according to tau decay modes. The categorisation was studied in detail and it could be shown that especially for the important modes with one charged pion with and without neutral pions a rather reliable classification can be achieved. Furthermore the dependency on the tau energy and pseudo-rapidity of the observables used to distinguish tau jets from QCD jets was investigated. Several methods to reduce the energy dependency of the variables were tested. However, it turned out that the final performance of the identification efficiency is sensitive to the sample composition, such that no general recommendation can be given, whether transformed variables are better to use. Significant improvements in the energy resolution with respect to the conventional tau reconstruction algorithm TauRec could be achieved in the classes without

additional neutral pions. In the classes with neutral pions the improvements are smaller than expected from previous studies [111], showing that further tunings of the eflowRec algorithm are needed.

The Monte Carlo estimates for the ID variables of PanTau were tested with measured collision data of the ATLAS experiment. In general a good agreement is observed, but some variables show a significant dependency on the number of additional pile-up vertices. Mainly variables including charged quantities are affected, therefore the dependency can be strongly reduced by additional track selection criteria. Remaining discrepancies are in agreement with studies of the conventional tau ID algorithm and can mostly be accounted for the modeling of the underlying event and the parton shower in the Monte Carlo generator. The rejection of QCD jets in the tau identification as estimated from data, matches the Monte Carlo prediction very well for candidates with $p_{\mathrm{T}} > 15\,\mathrm{GeV}$.

Chapter 5

Discovery potential for R-parity violating Supersymmetry

"Count what is countable, measure what is measurable, and what is not measurable, make measurable."
— Galileo Galilei

Section 1.2.3 theoretically motivated the R-parity violating SUSY models with the scalar partner of the tau, the so-called stau ($\widetilde{\tau}$), as lightest supersymmetric particle (LSP). We have seen that these models are theoretically appealing and may provide promising signatures for early discoveries at the LHC. Still R-parity violating scenarios with prompt LSP decays are only poorly studied by the ATLAS collaboration [133–137], in contrast to R-parity conserving scenarios with large missing transverse energy due to the escaping, neutral LSP where a huge number of studies exists (see *e.g.* reference [67] and references therein).

This Chapter will help to close this gap for R-parity violating models with stau LSP and lepton number violation. The BC 1 scenario, which is especially interesting for early discoveries, will be investigated in detail. Section 1.2.3 already described some of its basic properties. In this scenario the $\widetilde{\tau}$-LSP decays predominantly via a 4-body decay $\widetilde{\tau}_1^{\pm} \to \tau^{\pm}\, \ell^+\, \ell^-\, \nu$ into leptons. The electrons and muons in this decay are of special interest to identify such events in the background of Standard Model processes, which have up to several orders of magnitude higher cross sections. At first a cut-based event selection will be presented based on this specific benchmark scenario. Its cut-flow and expected signal significance for an integrated luminosity of $\int \mathcal{L} \mathrm{d}t = 500\,\mathrm{pb}^{-1}$ at a centre-of-mass energy of $\sqrt{s} = 7\,\mathrm{TeV}$ is given. This includes the full ATLAS detector simulation and the relevant Standard Model backgrounds as well as estimates for the most important systematic uncertainties and the trigger selection.

The analysis will go beyond the specific benchmark scenario by using fast detector simulations to estimate the expected signal significance in the SUSY parameter space around this scenario. Scanning the parameter space proves that the proposed event selection is general enough to select stau LSP scenarios with lepton number violation (λ_{121}

coupling) with reasonable efficiency and negligible Standard Model background. Finally, a method is proposed to reconstruct the mass of the stau LSP in case of a discovery. Even though the mass reconstruction suffers from large combinatorial backgrounds and missing energy due to the many neutrinos in the events, it allows to give mass estimates already with a few fb^{-1}.

The event selection is an update and extension with full detector simulation of the fast simulation results, which were already published in reference [59]. Similarly the parameter scan is updated with respect to the reference. The estimate of the stau LSP mass is identical to the previously published result [59].

5.1 Event Selection

The expected SUSY particles have larger masses than most SM particles. Additionally the $\widetilde{\tau}$-LSP decays into leptons in the considered R-parity violating scenario. Hence, the SUSY events have to some extent very different properties from the Standard Model background. These properties are studied based on Monte Carlo predictions for the BC 1 signal as well as for the Standard Model events.

In what follows, mainly Standard Model backgrounds are considered that can lead to at least one (parton level) electron, muon or tau in the final state. Furthermore, from most of the SUSY events additional hard jets are expected, that arise from decays in the upper parts of the decay chain. The most important Standard Model processes with compatible signature are therefore the production of *top quark pairs* ($\mathrm{t\bar{t}}$) and the production of *vector bosons* with additional jets. For the W boson the leptonic decays into a charged lepton and a neutrino are considered. Z boson decays into a pair of charged leptons are relevant as well. For both $\mathrm{Z} \to \ell^+ \ell^-$ and $\mathrm{W} \to \ell \nu$ only the production with at least one hard jet at parton level need to be considered, because of the large amounts of energy from jets expected in the SUSY events. Finally the di-boson (WW, WZ and ZZ) production is important to be taken into account. In principle, tri-boson production may also contribute to the SM background. It is still neglected here as its cross section is much smaller than the di-boson cross section [138]. *QCD di-jet* events with light flavors are expected to play no significant role despite their huge cross section compared to the expected signal, because isolated leptons should only occur very rarely in such events. They are still included in the following analysis, even though the Monte Carlo predictions of di-jet events are usually not reliable, because even minor mismodeling in Monte Carlo can lead to visible effects and it is mostly impossible to simulate QCD jet events with sufficient statistics due to the huge cross section.

A detailed list of the Monte Carlo samples and generators used in this analysis can be found in Appendix A.2. All samples use the `MC09` tune [130] of the event generators and include the full ATLAS detector simulation. The assumed cross sections are taken from the official Monte Carlo productions of the ATLAS collaboration. k-factors have

particle	min. p_{T}/GeV	max. $\lvert\eta\rvert$	algorithm/ID
electron	10	2.5	medium
muon	10	2.5	Staco, isolation $E_{\mathrm{T}}(\Delta R < 0.2) < 10\,\mathrm{GeV}$
tau	10	2.5	TauRec, medium likelihood selection, $\lvert q\rvert = 1e$, $n_{\mathrm{tracks}} = 1, 3$
jet	20	2.5	anti-k_T ($R = 0.4$) [87] from topological calorimeter clusters with global (H1) calibration

Table 5.1: Cuts for the particle pre-selection. The algorithms for particle reconstruction are described in Section 2.2.5.

been applied to the cross sections of the Standard Model samples to reproduce NLO and NNLO predictions according to reference [139].

Special to the BC 1 scenario are the 4-body $\not{R}_p$ decays $\widetilde{\tau}_1^{\pm} \to \tau^{\pm}\,\ell^+\,\ell^-\,\nu$ of the $\widetilde{\tau}$-LSP. They also need a special treatment in the Monte Carlo event generator. An extended version of Herwig 6.510 [140], which includes the additional 4-body decays according to reference [40] is used. This extension has been introduced in the ATLAS software framework athena to allow for the official simulation of such signals by the ATLAS collaboration. However, in this analysis privately produced Monte Carlo samples are used for the BC 1 signal which apply the settings of the MC09 tune by ATLAS, because official samples contained an error in the event generation. The full simulation and reconstruction chain was employed coherently to the official background samples inside the ATLAS software framework (*cf.* Appendix A.2).

5.1.1 Selection of reconstructed objects

Section 2.2.5 summarised the different algorithms of the ATLAS experiment for the reconstruction and identification of physical objects, like leptons or jets. In the case of muons and jets different algorithms exist, which can be chosen according to the requirements of the studied process. Likewise, the algorithms for lepton identification provide different ID levels with certain efficiencies and purities of the selected lepton samples.

The particle selection used here was guided by the definitions of the ATLAS collaboration for SUSY studies, *cf.* reference [67, pp. 1518], but has been updated to more recent recommendations in the course of this work. The pre-selection cuts are given in Table 5.1. See Section 2.2.5 for the description of the algorithms and the parameters of the object ID. Similarly the guidelines for the overlap removal of reconstructed objects were followed. An overlap removal is needed, because a single particle may be reconstructed as several different objects.

For the overlap removal simply the distance in pseudo-rapidity η and azimuthal angle ϕ was used, defined as $\Delta R = \sqrt{(\Delta\phi)^2 + (\Delta\eta)^2}$. Objects are selected in the following order:

1. Muons, if no jet and no previously selected muon is present within $\Delta R < 0.4$.
2. Electrons, if no jet is present within $0.2 < \Delta R < 0.4$ and no previously selected electron within $\Delta R < 0.4$.
3. Hadronically decaying taus, if no electron or tau has already been selected within $\Delta R < 0.4$.
4. Jets, if no electron, tau or another jet has already been selected within $\Delta R < 0.4$.

These cuts take care of the fact that electrons and taus are usually also reconstructed as jets. Furthermore, electrons are more reliably identifiable than taus. In addition, one does not want to select electrons or muons, that stem from heavy flavor decays within jets.

Due to the so-called crack-region of the ATLAS EM calorimeter (*cf.* Section 2.2.2) the identification capabilities for electrons are degraded within the range $1.37 < |\eta| < 1.52$. Even more critical is the fact that the detector simulation in this region is not as reliable as in other regions of the detector, because the material distribution is very complicated there. In order to avoid an excess of events due to wrongly identified electrons, all events with identified electrons in this crack region are disregarded. This is done in a pre-selection step for all the following results.

5.1.2 Particle multiplicities and kinematic properties

Having defined the object selection criteria, the particle multiplicities and kinematic properties of the BC 1 scenario are presented next. The comparison of the SUSY scenario with Monte Carlo predictions for the relevant Standard Model processes allows to derive event selection cuts. The following histograms are scaled to an integrated luminosity of $\int \mathcal{L} dt = 1\,\text{fb}^{-1}$ at a centre-of-mass energy of $\sqrt{s} = 7\,\text{TeV}$ using the predicted cross sections and k-factors of the different Monte Carlo samples. They do not include any event selection cuts, despite the pre-selection to avoid electrons in the crack region as described before. The various Standard Model contributions are grouped in the categories W + jets, Z + jets, di-boson production, $\text{t}\bar{\text{t}}$ and QCD di-jets. They are stacked on top of each other, while the BC 1 signal is shown in front of the Standard Model distributions.

In Figure 5.1 the number of selected electrons, muons, hadronic tau decays and jets per event are shown. One can immediately see the large excess of isolated electrons in the BC 1 signal compared to the Standard Model events. The mean number of muons (Figure 5.1b) is also relatively large compared to some of the Standard Model processes.

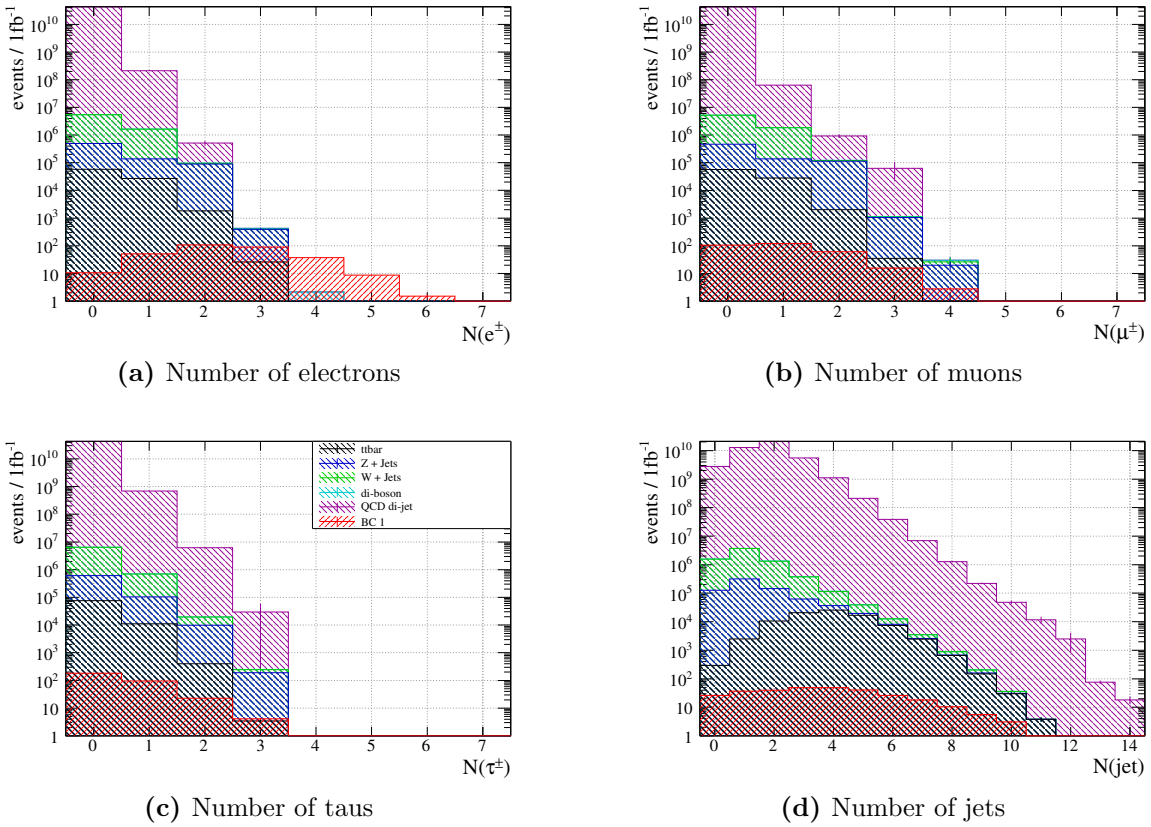

(a) Number of electrons

(b) Number of muons

(c) Number of taus

(d) Number of jets

Figure 5.1: Number of reconstructed and identified objects in BC 1 signal and Standard Model background. The quality requirements for the electrons, muons and (hadronically decayed) taus considered here are described in the text. Additionally the mentioned overlap removal procedure between reconstructed objects was performed. No event selection cuts, despite the pre-selection explained in Section 5.1.1, were applied. The different background contributions are stacked on top of each other in the following order: $t\bar{t}$, Z + jets, W + jets, di-boson, QCD jet production. The BC 1 signal (red) is drawn in front of the background histograms.

The large number of electrons and muons in the final state provides the most striking signature of the BC1 scenario.

In the ratio between electrons and muons an interesting property of the benchmark scenario BC 1 is visible. One observes a mean number of two to three electrons per BC 1 event, whereas the muon distribution peaks at one. This is the expected behaviour from the parton-level signatures reviewed in Section 1.2.3, *cf.* especially the row for the λ_{121} coupling in Table 1.4. The decay of two $\widetilde{\tau}$-LSPs in a typical BC 1 event leads at parton level to two to four electrons and up to two muons. Therefore the ratio of the number of reconstructed electrons and muons carries information about the involved B_3 coupling. λ_{121} couples two lepton superfields of the first generation to one of the second generation. In this case the $\widetilde{\tau}$-LSP decays produce more electrons than muons. If one

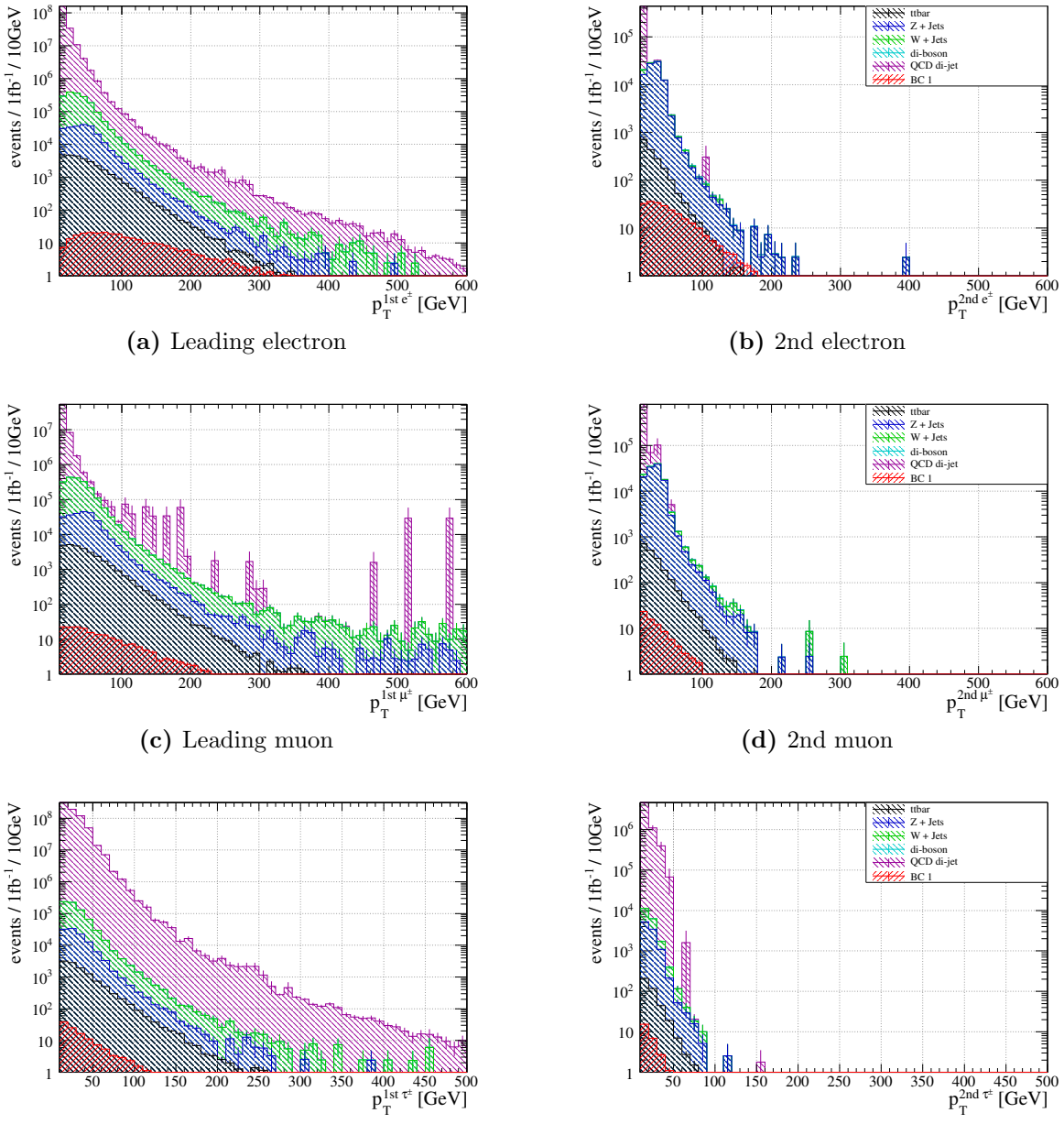

(a) Leading electron

(b) 2nd electron

(c) Leading muon

(d) 2nd muon

(e) Leading tau

(f) 2nd tau

Figure 5.2: Transverse momentum p_T of the leading and the second reconstructed and identified leptons in each event for the BC 1 signal and Standard Model background. Color scheme and selection are as in Figure 5.1. The "spikes" in the QCD di-jet distribution are caused by large scale factors that apply for some QCD Monte Carlo samples due to limited statistics.

assumes $\lambda_{122} \neq 0$ instead, the situation would be reversed and the average number of muons to electrons would be roughly three.

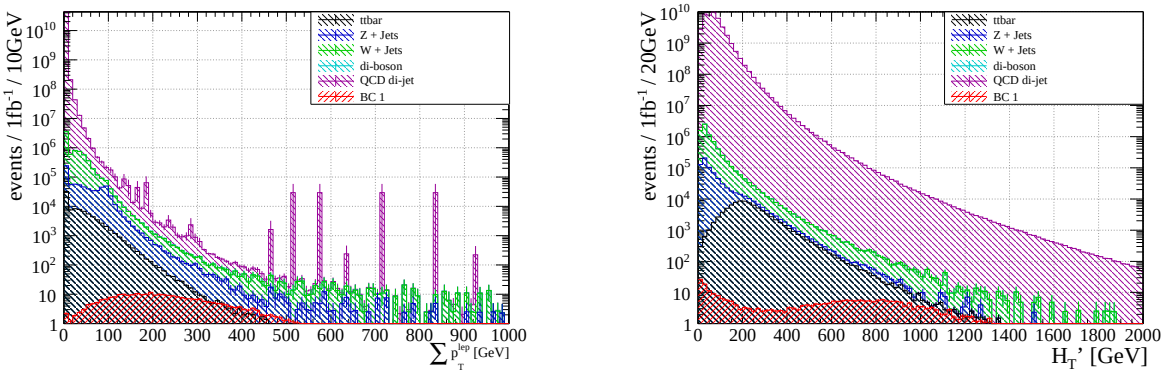

(a) $\sum_{\text{lep}} p_{\text{T}}$ **(b)** H'_{T}

Figure 5.3: $\sum_{\text{lep}} p_{\text{T}}$ and H'_{T} in BC 1 signal and Standard Model background. No event selection cuts, despite the cleaning cuts explained in the text, were applied.

Not only the bare numbers of the selected leptons per event are of interest, but also their transverse momenta. Figure 5.2 presents the p_{T} distributions of the two hardest electrons and the two hardest muons. The p_{T} distribution of the background falls off more rapidly than the signal especially for electrons. For large momenta ($p_{\text{T}} \gtrsim 100\,\text{GeV}$) of the second electron (Figure 5.2b) one can see that the signal already gets competitive with the important $\text{t}\bar{\text{t}}$ background. The transverse momenta of the leading and second leading electrons and muons will be used in the selection of BC 1 events.

Due to their large multiplicity and large transverse momenta, also leptons beyond the sub-leading electron and muon can contribute significantly to the energy deposition of all leptons. The scalar p_{T} sum, $\sum_{\text{lep}} p_{\text{T}}$, of all electrons and muons (Figure 5.3a) is therefore another variable to be used in the event selection and accounts for the fact that the momenta of the signal lepton are on average larger than the background. The lepton momenta in BC 1 can be large because they are produced at the end of the decay chain of heavy SUSY particles.

The number of jets per event (Figure 5.1d) does not show a strongly expressed maximum for BC 1 events. This can be explained by the different sparticles produced and their various decay modes that contribute in the upper parts of the SUSY decay chain and gluon radiation. In the prototype case of squark pair production and decay via the lightest neutralino into the stau-LSP one would expect two high-momentum jets:

$$qq/\text{gg} \to \widetilde{q}\widetilde{q} \to jj\widetilde{\chi}_1^0\widetilde{\chi}_1^0 \to jj(\widetilde{\tau}\tau)(\widetilde{\tau}\tau) \to jj(\tau\tau\ell^+\ell^-\nu)(\tau\tau\ell^+\ell^-\nu). \tag{5.1}$$

Gluino ($\widetilde{\text{g}}$) pair production instead of squark pair production will usually give two additional jets, *e.g.* via the decay $\widetilde{\text{g}} \to j\widetilde{q}$. Additional jets to those from the decay chain can occur from parton showers or non-identified hadronic tau decays. Indeed one observes that most events include between two and five jets. The distribution of the number of jets looks very different in the semi-leptonic $\text{t}\bar{\text{t}}$ decays for example. Here one expects two b-jets and two light quark jets from one of the W bosons. This behaviour is also

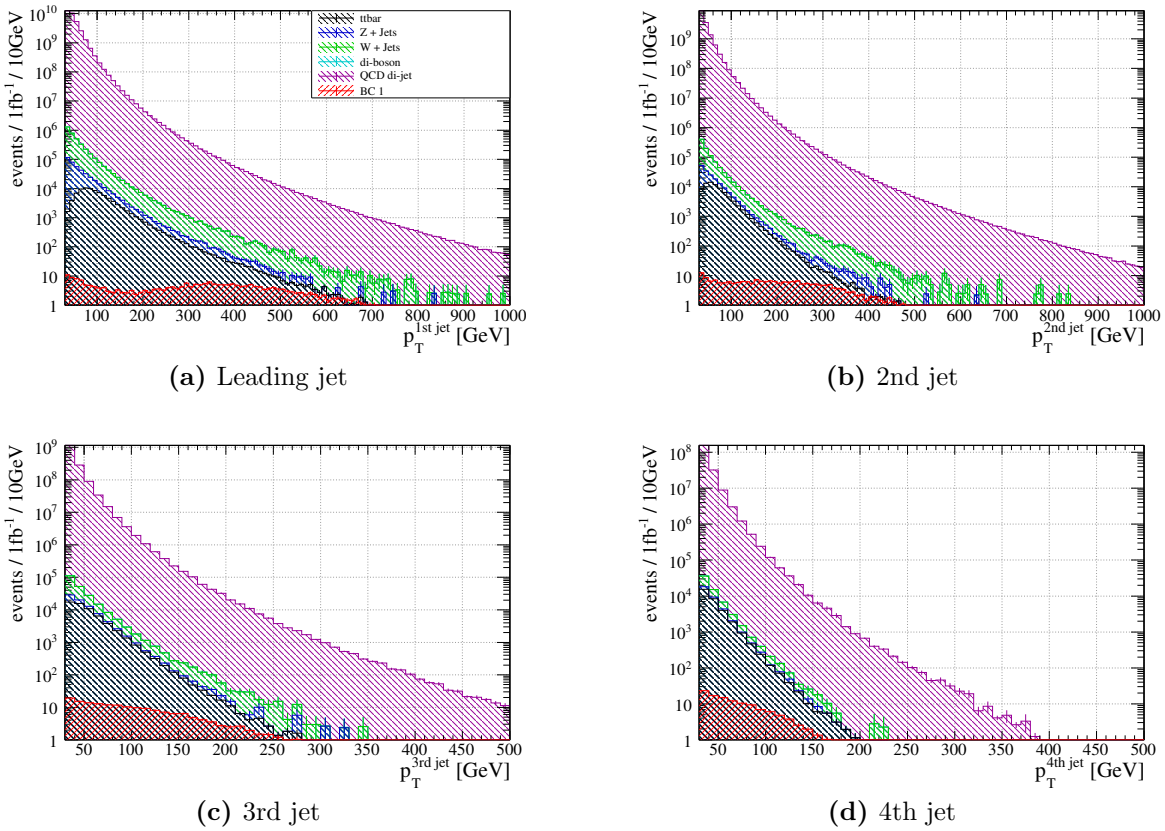

(a) Leading jet **(b)** 2nd jet

(c) 3rd jet **(d)** 4th jet

Figure 5.4: Transverse momentum p_T of the four leading jets for the BC 1 signal and the Standard Model background. No event selection cuts, despite the cleaning cuts explained in the text, were applied.

visible in the background distribution. The fact that less entries with no jets than with one jet are observed in the W + jets and Z + jets samples is an artifact of the selection of Monte Carlo samples. Only W and Z Monte Carlo events with at least one additional parton in the hard process are taken into account here, because only those are relevant as background.

The p_T spectra of the four hardest jets are visualised in Figure 5.4. It is clear that the jet spectra are fully dominated by QCD jet events. Anyhow, jets provide important information to suppress Standard Model background from W+jets and Z+jets events. The jet spectra for the BC 1 signal are relatively flat over a wide range of transverse momenta, whereas they are much more steeply falling for the background. In the spectrum of the leading jet (Figure 5.4a) one can see a maximum in the region of $p_T = 350\,\text{GeV}$ to $400\,\text{GeV}$. This wide peak is mainly caused by the decay of squarks into the lightest neutralino $\widetilde{\chi}_1^0$. The mass difference between most of the squarks and the $\widetilde{\chi}_1^0$ is about 400 to 500 GeV in BC 1 [43, 59].

Additional softer jets may arise from the decay of gluinos into squarks. Here the mass differences are usually only around 100 GeV, so those jets appear in the sub-leading p_T

distributions Figure 5.4c and 5.4d. From Figure 5.4 one can see that the signal-to-background ratio will improve by demanding very hard jets. This leads to the definition of the so-called visible hadronic mass $H'_{\mathrm{T}} = \sum_{\text{jet 1–4}} p_{\mathrm{T}}$ as the scalar sum of the transverse momenta of the four leading jets. Summing over more jets would reduce the separation to $\mathrm{t\bar{t}}$ events, where more jets are expected than in BC 1 (*cf.* Figure 5.1d). The distribution of H'_{T} in Figure 5.3b reflects the above considerations.

It may be surprising at first sight that the number of selected hadronic tau decays per BC 1 event in Figure 5.1c does only rarely exceed two. In most BC 1 events no hadronic tau lepton is selected at all. Naively one would expect four tau leptons in the basic process (5.1) from which about 65 % each should decay hadronically. It turns out that only a small fraction of the hadronic tau decays can be identified as such in the BC 1 events. One reason is the low energy of the $\tau^{\pm}$, which often causes the visible part of the tau decay to have transverse momenta below 10 GeV. The η-p_{T} distribution of hadronically decaying taus in BC 1 is depicted in Figure 5.5. It is clearly visible that a significant fraction of the τ leptons is outside the acceptance region (dashed line) of the τ identification.

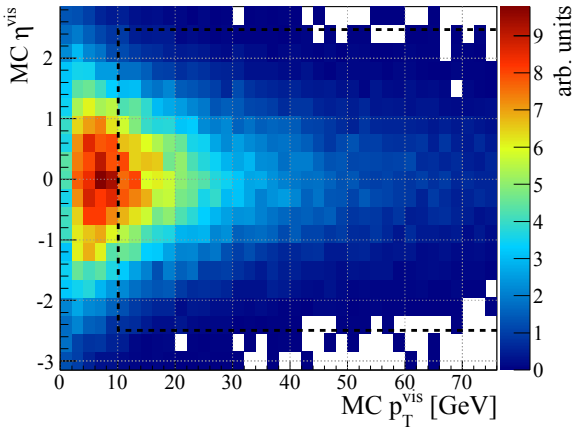

Figure 5.5: Distribution in the η^{vis}-$p_{\mathrm{T}}^{\mathrm{vis}}$ plane of hadronically decaying taus in BC 1. All true hadronic decays are included here, *i.e.* no detector simulation or acceptance cuts were applied. Only the visible component of the tau decay products is considered. The dashed line illustrates the acceptance region for hadronic tau decays in the analysis.

Another important reason, why much less τ are found than naively expected, is the event topology of the BC 1 signal. Many tau leptons are "hidden" by electrons, muons or other jets in the events, because of the relatively large abundance of those objects. This effect can be seen in Figure 5.6 where the efficiency for the reconstruction and identification of hadronic tau decays is shown as a function of the Monte Carlo truth momentum. Even at the same visible tau momentum the efficiency in BC 1 events (open symbols) is reduced by more than a factor of two compared to $\mathrm{Z} \to \tau^- \tau^+$ events (solid symbols), the "standard candle" for the tau identification. In the Figure only the efficiency for the reconstruction and identification is included to visualise the effect on the τ ID itself. Additional losses in the efficiency occur due to the overlap removal applied in the analysis.

For completeness the momentum distributions of the leading and sub-leading selected tau lepton are shown in Figure 5.2e and 5.2f. From the discussion above it is clear that the tau leptons cannot be used reasonably well to distinguish BC 1 signal from Standard

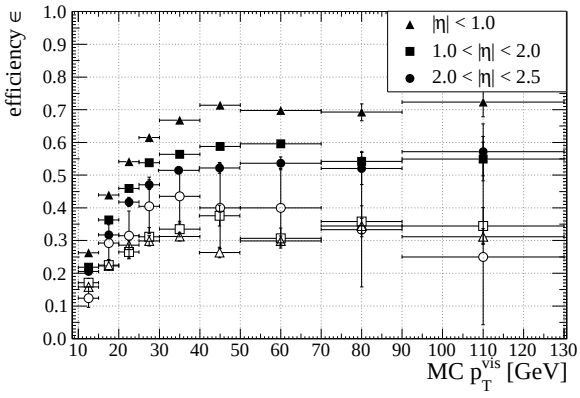

Figure 5.6: Reconstruction and identification efficiency of hadronically decaying taus in BC 1 (open symbols) and $Z \to \tau^- \tau^+$ events (solid symbols). The τ candidates are selected as given in Table 5.1, but no overlap removal was applied here.

Model background. Still their identification will be important for the reconstruction of the mass of the $\widetilde{\tau}$-LSP as we will see in Section 5.3.

The missing transverse energy $E_{\mathrm{T}}^{\mathrm{miss}}$ is an important observable in the case of R-parity conserving SUSY models, where the LSP is stable and leaves the experiment undetected, *cf.* the discussion in Section 1.2.2. In R-parity violating models this argument does not hold and the missing transverse energy is expected to be much smaller than in RPC models. However, the observed $E_{\mathrm{T}}^{\mathrm{miss}}$ in Figure 5.7 can be significant compared to Standard Model processes with $E_{\mathrm{T}}^{\mathrm{miss}}$, like di- and semi-leptonic $\mathrm{t\bar{t}}$ events. The reason for this are the neutrinos from the $\widetilde{\tau}$-LSP decays

$$\begin{aligned} \widetilde{\chi}_1^0 &\to \widetilde{\tau}_1 + \tau \\ &\quad \big\lfloor \longrightarrow \tau \ell^+ \ell^- \nu \end{aligned} \tag{5.2}$$

and the neutrinos from the successive τ decays. However, no explicit cut on $E_{\mathrm{T}}^{\mathrm{miss}}$ will be applied in the event selection in order to keep the analysis complementary to searches for R-parity conserving SUSY in ATLAS.

It should be kept in mind, that the discovery of an $E_{\mathrm{T}}^{\mathrm{miss}}$ signal does not necessarily contradict $\not{R}_p$ models. $E_{\mathrm{T}}^{\mathrm{miss}}$ alone is not sufficient to distinguish R-parity violating from

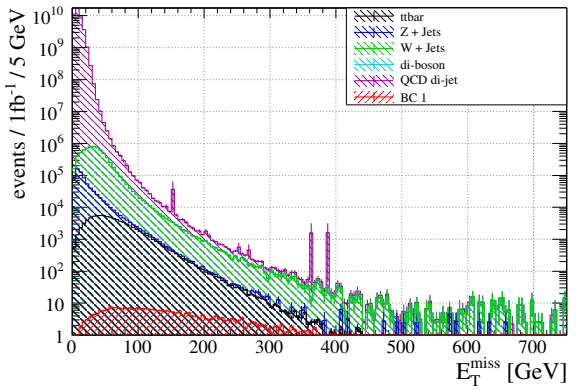

Figure 5.7: Distribution of the missing transverse energy $E_{\mathrm{T}}^{\mathrm{miss}}$ in BC 1 and Standard Model background. No event selection cuts, despite the cleaning cuts explained in the text, were applied.

R-parity conserving SUSY. Finally, a lepton (linear) collider may be needed to clarify the nature of the LSP and the source of the missing energy [35]. Further observables, like kinematic edges, allow to gain insights in the SUSY mass spectrum to constrain the SUSY models [141].

5.1.3 Event selection and cut flow

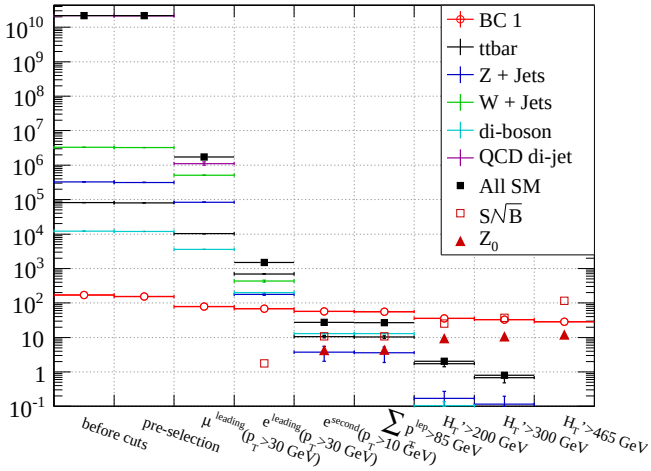

Figure 5.8: Cut flow in BC 1 at $\sqrt{s} = 7\,\text{TeV}$. As in Table 5.2, entries are scaled to an integrated luminosity $\int \mathcal{L}\mathrm{d}t = 500\,\text{pb}^{-1}$ and error bars include statistical uncertainties only. The significance Z_0 assumes a systematic uncertainty of 25 % in addition to the statistical uncertainty of the background estimate. Details on the definition of Z_0 are given in Section 5.1.5.

Without any event selection the Standard Model background is several orders of magnitude larger than the expected SUSY signal. For an integrated luminosity of $\int \mathcal{L}\mathrm{d}t = 500\,\text{pb}^{-1}$ one expects about 150 BC 1 events prior to event selection. From the kinematic properties presented in the previous Section the following cuts were derived. They and the resulting cut flow are summarised in Table 5.2 and visualised in Figure 5.8.

p_T(1st $\mu^\pm$) > 30 GeV At least one muon with $p_\text{T} > 30\,\text{GeV}$ is demanded in the final state. This cut reduces the QCD background already significantly.

p_T(1st e$^\pm$) > 30 GeV The leading electron must have a transverse momentum larger than 30 GeV. One obtains a great improvement of the signal to background ratio to $\mathcal{O}(0.01)$ by demanding one isolated muon and one isolated electron ($p_\text{T} > 30\,\text{GeV}$) in the final state. At this stage the main backgrounds stem from leptonic decays of $\mathrm{t\bar{t}}$ and from leptonic decays of di-bosons, which can produce an electron and a muon at parton level. In addition, also W + jets events contribute to the background. Here, the second electron or muon stems mainly from jets that are misidentified as a charged lepton.

p_T(2nd e$^\pm$) > 10 GeV Demanding at least a second electron in the event. Note, that $p_\text{T} > 10\,\text{GeV}$ corresponds to the electron pre-selection cut, *cf.* Table 5.1. This makes use of the fact, that a large number of isolated electrons are expected due to the two $\widetilde{\tau}$-LSP decays in the BC 1 events. With this cut the BC 1 signal already supersedes

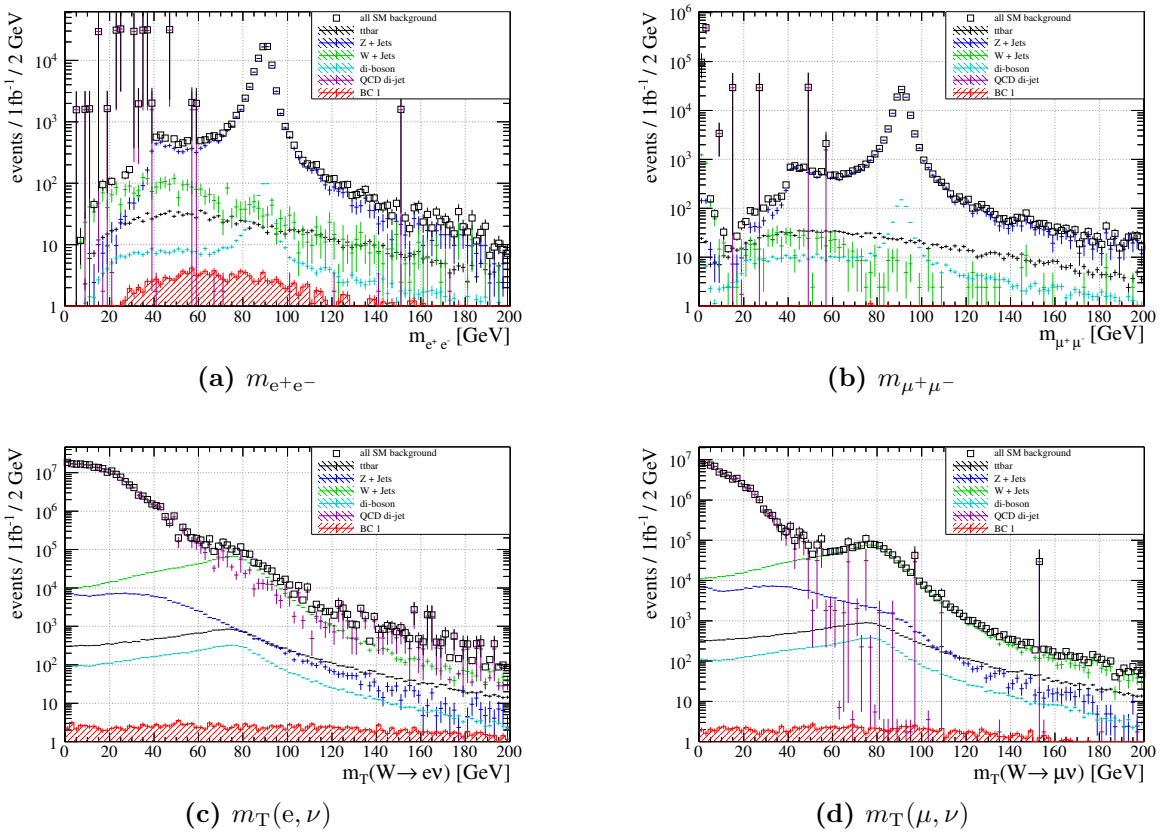

(a) $m_{e^+e^-}$ **(b)** $m_{\mu^+\mu^-}$

(c) $m_T(e,\nu)$ **(d)** $m_T(\mu,\nu)$

Figure 5.9: Distributions of the invariant mass of lepton pairs, $m_{\ell^+\ell^-}$, and the transverse W mass $m_T(\ell,\nu)$ for BC 1 signal and Standard Model background. No event selection cuts, despite the cleaning cuts explained in the text, were applied. The "spikes" in the distribution arise from QCD di-jet Monte Carlo samples with large scale factors, due to limited MC statistics.

the Standard Model background. The remaining background is dominated by $t\bar{t}$ and di-boson events.

$\sum_{lep} p_T > 85$ GeV The scalar p_T sum of all electrons and muons needs to be larger than 85 GeV, reflecting the large number of high-p_T electrons and muons in BC 1 (Figures 5.1a and 5.1b).

$H'_T > 200, 300, 465$ GeV Different cuts are applied on the p_T sum of the four hardest jets, where the base-line selection uses the cut $H'_T > 300$ GeV. The previous cuts only employed the electrons and muons that stem mainly from the $\widetilde{\tau}$-LSP decays. The main production mechanism for the signal is the pair production of strongly interacting sparticles. They cascade down to the LSP and produce hard jets. The cut on the hadronic energy H'_T is especially useful to suppress the remaining di-boson background. For $H'_T > 200$ GeV the di-boson events are nearly completely suppressed. With a harder cut of $H'_T > 300$ GeV only $t\bar{t}$ background remains.

Finally with $H'_{\mathrm{T}} > 465\,\mathrm{GeV}$ one can even obtain a (nearly) background free sample of about 30 signal events.

The cut selection was optimized with the help of the TMVA[1] toolkit [119, 123]. The cuts were chosen such to improve the signal to background ratio $\frac{S}{\sqrt{B}}$, based on simulated annealing [142]. This was iterated with different sets of event selection variables, while some cuts were left fixed. Several other variables, like the $m_{\ell^+\ell^-}$ invariant mass as Z-veto or the W transverse mass, were tested as well. However, they turned out to be of less relevance in combination with the variables finally used.

Cuts on the invariant mass of lepton pairs ($m_{\mathrm{e}^+\mathrm{e}^-}$ and $m_{\mu^+\mu^-}$, Figure 5.9a and 5.9b) have only minor impact on the final $\mathrm{Z} \to \ell^+\,\ell^-$ background, because this background is anyhow strongly suppressed by demanding two electrons, as well as a muon in the event. Only the di-boson background (WZ and ZZ) can be slightly reduced, if the cut on the scalar sum of the transverse jet momenta H'_{T} is omitted. Including the cut on H'_{T} all di-boson events are anyhow well suppressed. One may argue that the jet spectra in di-boson events are not well described in the Monte Carlo simulation and the H'_{T} cut may therefore include higher systematic uncertainties than a cut on $m_{\ell^+\ell^-}$. Still one looses signal efficiency by cutting on $m_{\ell^+\ell^-}$ and it is therefore preferred not to apply the cut. Once an excess over the Standard Model prediction has been observed using the proposed event selection, one should check the $m_{\ell^+\ell^-}$ distribution in the selected events to make sure that indeed no peak at the Z mass is observed to gain confidence in a BSM signal. The same argument holds for the transverse mass m_{T} constructed from the leading electron or muon in the event and the missing transverse energy $E_{\mathrm{T}}^{\mathrm{miss}}$ (Figures 5.9c and 5.9d). $\mathrm{W} \to \ell\,\nu$ events do not play a role in the final event selection and no events survive in the Monte Carlo sample (*cf.* Table 5.2). The $m_{\mathrm{T}}(\mathrm{e}, \nu)$ and $m_{\mathrm{T}}(\mu, \nu)$ distributions may serve as an extra check that an observed excess does not stem from $\mathrm{t\bar{t}}$ production.

5.1.4 Systematic uncertainties

In this Section systematic uncertainties of the event selection are investigated. The following effects are considered as the most important ones: Energy scale uncertainties of jets and leptons directly affect the selection efficiencies of signal and background. Theoretical uncertainties of the predicted Standard Model background arise from uncertainties of the cross section, the parton distribution functions, as well as the prediction of parton showers and the underlying event. Furthermore, the selection efficiency of electrons and muons and their fake rates need to be considered. Finally, the selection of leptons depends on the isolation criteria, which are required to distinguish leptons from the hard process from leptons produced in heavy flavor decays inside jets.

[1] TMVA 4.01.00 with a special patch to handle larger number of input events was applied. The cut optimisation was performed only on a fraction of the whole Monte Carlo sample to avoid overtraining on statistical artifacts.

cut	$t\bar{t}$	Z + Jets	W + Jets	di-boson	all SM	BC 1	Z_0
pre-selection	$80\,854 \pm 138$	$3.163(4) \times 10^5$	$3.231(3) \times 10^6$	$11\,914 \pm 18$	$2.161(2) \times 10^{10}$	153.4 ± 1.7	—
$p_T(1\text{st } \mu^\pm) > 30\,\text{GeV}$	$10\,225 \pm 29$	$8.43(2) \times 10^4$	$5.13(1) \times 10^5$	$3\,597 \pm 10$	$1.72(12) \times 10^6$	78.5 ± 1.2	—
$p_T(1\text{st } e^\pm) > 30\,\text{GeV}$	697 ± 7	177 ± 10	434 ± 30	200 ± 2.5	$1\,508 \pm 33$	67.9 ± 1.1	—
$p_T(2\text{nd } e^\pm) > 10\,\text{GeV}$	10.6 ± 0.9	3.7 ± 1.7	$\lesssim 1$	13.0 ± 0.3	27.4 ± 2.0	56.4 ± 1.0	4.3
$\sum p_T^\ell > 85\,\text{GeV}$	10.3 ± 0.9	3.6 ± 1.7	$\lesssim 1$	12.9 ± 0.3	26.8 ± 2.0	56.3 ± 1.0	4.4
$H'_T > 200\,\text{GeV}$	1.7 ± 0.3	0.2 ± 0.1	$\lesssim 1$	0.1 ± 0.1	2.0 ± 0.4	35.8 ± 0.8	9.5
$H'_T > 300\,\text{GeV}$	0.7 ± 0.2	0.1 ± 0.1	$\lesssim 1$	$\lesssim 0.1$	0.8 ± 0.2	33.2 ± 0.8	10.8
$H'_T > 465\,\text{GeV}$	0.1 ± 0.1	$\lesssim 0.1$	$\lesssim 1$	$\lesssim 0.1$	0.1 ± 0.1	28.7 ± 0.7	12.1

Table 5.2: Cut flow for the BC 1 signal and the considered Standard Model background. The number of events are scaled to an integrated luminosity of $\int \mathcal{L} dt = 500\,\text{pb}^{-1}$. The number of QCD events after pre-selection are $(2.160 \pm 0.002) \times 10^{10}$ and $(1.1 \pm 0.1) \times 10^6$ after requiring $p_T(1\text{st } \mu^\pm) > 30\,\text{GeV}$. After the cut on the leading electron no events survive in the QCD Monte Carlo sample. The given uncertainties on the number of events include statistical errors only. The significance Z_0 includes a systematic uncertainty of 25 % in addition to the statistical uncertainties. For the first three rows Z_0 is not well-defined. Details on the definition of Z_0 are given in Section 5.1.5, where also other definitions of significance are included.

cut	MC@NLO +Herwig	AcerMC +Pythia	PowHeg +Herwig	PowHeg +Pythia
$p_{\mathrm{T}}(\mathrm{2nd\ e}^{\pm}) > 10\,\mathrm{GeV}$	41.3 ± 2.3	$47.7 \pm 4.6 (+15\%)$	$41.6 \pm 4.3 (+1\%)$	$46.0 \pm 4.9 (+11\%)$
$\sum p_{\mathrm{T}}^{\ell} > 85\,\mathrm{GeV}$	32.6 ± 2.0	$40.6 \pm 4.3 (+24\%)$	$35.3 \pm 4.0 (+8\%)$	$37.3 \pm 4.4 (+14\%)$
$H'_{\mathrm{T}} > 100\,\mathrm{GeV}$	14.8 ± 1.4	$17.4 \pm 2.8 (+17\%)$	$20.1 \pm 3.0 (+36\%)$	$11.8 \pm 2.5 (-21\%)$
$H'_{\mathrm{T}} > 200\,\mathrm{GeV}$	4.9 ± 0.8	$6.2 \pm 1.7 (+28\%)$	$4.9 \pm 1.5 (+1\%)$	$6.1 \pm 1.8 (+26\%)$
$H'_{\mathrm{T}} > 300\,\mathrm{GeV}$	1.7 ± 0.5	$2.2 \pm 1.0 (+28\%)$	$0.4 \pm 0.4 (-74\%)$	$2.6 \pm 1.1 (+47\%)$

Table 5.3: Event yields for different Monte Carlo generators in $\mathrm{t\bar{t}}$ events without fully hadronic $\mathrm{t\bar{t}}$ decays. MC@NLO+Herwig/Jimmy is used as base line. AcerMC+Pythia and PowHeg with Herwig/Jimmy and Pythia are used for comparison. Errors include statistical uncertainties of the respective samples only. The relative deviation from MC@NLO+Herwig/Jimmy is given in percent.

Even though nearly background free samples of BC 1 events can be selected at sufficient signal efficiencies, it is crucial to gain reliable estimates of the remaining backgrounds. Especially in parameter regions beyond BC 1, which have lower cross sections and lower selection efficiencies as BC 1, only a precise knowledge of the Standard Model background can allow for a discovery of the SUSY signal (*cf.* Section 5.2).

It has been shown in the previous Section, that the leptonic and semi-leptonic decays of top-quark pairs ($\mathrm{t\bar{t}}$) form the dominant SM background. Therefore, $\mathrm{t\bar{t}}$ events need special attention in the study of systematic uncertainties. The theoretical uncertainties in the prediction of the $\mathrm{t\bar{t}}$ background shapes are accounted for by comparing the results of different Monte Carlo event generators.

Table 5.3 summarises the cut flow for various $\mathrm{t\bar{t}}$ MC samples produced with different combinations of matrix element generators (AcerMC, MC@NLO) and parton shower Monte Carlo (Pythia and Herwig). We use MC@NLO with Herwig as baseline for $\mathrm{t\bar{t}}$ as recommended by the ATLAS top working group. In all cases the cross sections have been scaled with k-factors to reach the prediction by reference [143]. Within the statistical uncertainties of the Monte Carlo samples the predictions fairly agree. However, there is some evidence that larger $\mathrm{t\bar{t}}$ background contributions are predicted by the event generators with Pythia parton shower. Taking the relative deviation from the prediction by MC@NLO+Herwig/Jimmy would certainly overestimate the systematic uncertainty because of the relatively large statistical uncertainties of the available Monte Carlo sample. An additionally systematic uncertainty of 10 % on the $\mathrm{t\bar{t}}$ prediction is therefore assumed here.

In recent studies of the ATLAS electron/gamma working group [144] (*cf.* also [145]) using tag-and-probe methods in $\mathrm{W} \to \mathrm{e}\,\nu$ and $\mathrm{Z} \to \mathrm{e}^{-}\,\mathrm{e}^{+}$ events, the electron efficiency was found to be slightly lower in collision data than estimated from Monte Carlo simulations. For the medium electron selection scale factors between Monte Carlo and data have been derived between 95.4 % and ≈ 100 % depending on the range of pseudo-

rapidity η and the transverse energy E_{T}. Therefore we assumed a systematic uncertainty of $-5\,\%$ on the electron identification efficiency. Following the recommendations from reference [146] the energy scale uncertainty for electrons was estimated with $3\,\%$. Barrel and end-cap are treated fully correlated, *i.e.* the same scale factor was used over whole range $|\eta| < 2.5$.

Various sources of jet energy scale (JES) uncertainties have been studied by the ATLAS collaboration in reference [147]. Based on Monte Carlo studies a maximum relative JES uncertainty of $7.5\,\%$ to $8.8\,\%$ ($20\,\mathrm{GeV} < p_{\mathrm{T}}^{\mathrm{jet}} < 60\,\mathrm{GeV}$) and $5.8\,\%$ to $6.8\,\%$ ($p_{\mathrm{T}}^{\mathrm{jet}} > 60\,\mathrm{GeV}$) in the pseudo-rapidity region $|\eta| < 2.8$ was derived for anti-$k_{\perp}$ jets with $R = 0.4$ in this reference. The estimates have lately been updated [148] and parametrisations as a function of $p_{\mathrm{T}}^{\mathrm{jet}}$ and η^{jet} were provided.Over wide ranges of η^{jet} and $p_{\mathrm{T}}^{\mathrm{jet}}$ the updated uncertainties are between about $3.5\,\%$ and $4.5\,\%$ with higher values up to $8\,\%$ below $100\,\mathrm{GeV}$. This study used the parametrised JES uncertainty and was cross checked with a fixed value assuming a mean uncertainty of $5\,\%$.

Recent investigations of the ATLAS muon combined performance group [149] showed that the reconstruction and identification efficiency is only slightly lower in collision data than in the Monte Carlo estimates. The scale factors were found to be about $98\,\%$ on average for the Staco muon reconstruction algorithm (*cf.* Section 2.2.5), where no significant dependency of the scale factor on the muon momentum appeared. However, some regions in pseudo-rapidity η were found where the scale factor is significantly lower (down to $90\,\%$). Here the impact of a mean drop in efficiency of $95\,\%$ was investigated.

The muon momentum scale and resolution was found to be described extremely well by the Monte Carlo simulation [150]. Discrepancies in the momentum scale are mostly well below $0.5\,\%$ and reach $1\,\%$ only in the region $1.7 < |\eta| < 2.0$ [151, 152]. Therefore, the systematic uncertainty of the muon energy scale was estimated with $1\,\%$ to be conservative.

The impact of additional fake, *i.e.* wrongly identified, electrons and muons was estimated by increasing their fake rate by $10\,\%$. Fake leptons from other events of the same Monte Carlo (sub-)sample were added to the events in order to obtain a reasonable momentum spectrum of the additional fake leptons. Their mean number was estimated with Monte Carlo truth information and randomly chosen with Poisson statistics.

In the event selection a cut is applied on the scalar sum $\sum p_{\mathrm{T}}^{\ell}$ of the transverse momenta of the electrons and muons. In order to check the combination of the systematic uncertainties due to the jet energy scale and the electron and muon momentum scales toy experiments have been performed in which the energy and momentum scales were randomly varied according to their respective systematic uncertainties. The variations were drawn from independent Gaussian distributions with the related widths. The outcome of such pseudo-experiments is shown in Figure 5.10.

Following the ATLAS recommendations the uncertainty of the determination of the integrated luminosity is estimated with an overall scaling uncertainty of $11\,\%$. Additionally the uncertainty of the expected cross sections of the Standard Model processes

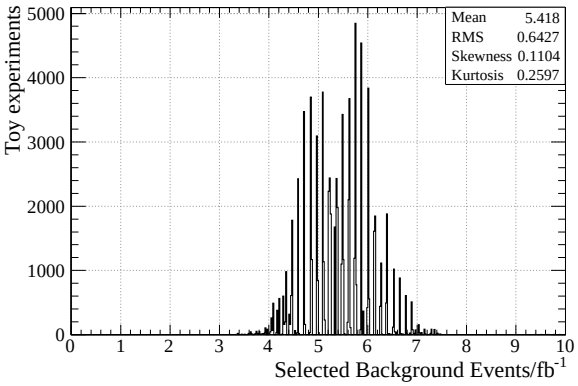

Figure 5.10: Event yield for Standard Model background in pseudo-experiments to check the systematic uncertainty of the background prediction. In the pseudo-experiments the jet energy scale and the muon and electron momentum scales have been randomly varied according to their systematic uncertainties given in the text. The variations were drawn from independent Gaussian distributions with the related widths.

needs to be taken into account. For most processes the cross section uncertainty is taken to be 5 %. The uncertainty of the QCD estimate is usually expected to be much larger (of the order of 100 %), because even minor effects in the modelling of fake leptons may have significant impact due to the very large QCD cross section. However, in our Monte Carlo sample no QCD events survive even after requiring one muon and one electron each with a lowered threshold of $p_{\mathrm{T}} > 20\,\mathrm{GeV}$. Based on this Monte Carlo prediction it is therefore very difficult to reliably estimate the QCD background. It will anyhow be extracted from data, *e.g.* using template fits [67]. In the case of the important $\mathrm{t\bar{t}}$ background the uncertainty of the cross section was assumed to be $^{+6.9}_{-9.5}\%$ in compliance with reference [153].

The systematic uncertainties of the estimated number of background events have been determined with respect to the event yield after all event selection cuts. However, the selection cuts on the lepton momenta were relaxed to $p_{\mathrm{T}}(1\mathrm{st}\ \mu^{\pm}) > 20\,\mathrm{GeV}$,

source	Δ_+ (%)	Δ_- (%)
jet energy scale	+9.4	−14.0
$\mu^{\pm}$ momentum scale	+2.3	0.0
$\mathrm{e}^{\pm}$ momentum scale	+4.4	−6.8
μ efficiency $\epsilon_{\mu^{\pm}}$		−5.2
e efficiency $\epsilon_{\mathrm{e}^{\pm}}$		−9.7
fake $\mu^{\pm}$	+1.1	
fake $\mathrm{e}^{\pm}$	+0.7	
luminosity	+11.0	−11.0
cross section σ	+6.1	−7.6
$\mathrm{t\bar{t}}$ generators	+10.0	−10.0

Table 5.4: Relative systematic uncertainties of the Standard Model background estimate in percent. The uncertainties correspond to the event yield after all event selection cuts, while relaxing the cuts on the lepton momenta to $p_{\mathrm{T}}(1\mathrm{st}\ \mu^{\pm}) > 20\,\mathrm{GeV}$, $p_{\mathrm{T}}(1\mathrm{st}\ \mathrm{e}^{\pm}) > 20\,\mathrm{GeV}$ and the hadronic mass to $H'_{\mathrm{T}} > 200\,\mathrm{GeV}$.

$p_{\mathrm{T}}(1\mathrm{st}\ \mathrm{e}^{\pm}) > 20\,\mathrm{GeV}$ and the hadronic mass to $H'_{\mathrm{T}} > 200\,\mathrm{GeV}$ compared to the final selection in order to remain with enough background events in the Monte Carlo samples. It was checked that the results can be referred to the final selection, even though the statistical sample of Monte Carlo background events gets very small then. Table 5.4 summarises the relative uncertainties for the various sources. In each of the categories the maximum absolute value of the upward and downward shifts has been taken. By adding up these contributions in quadrature one obtains a total systematic uncertainty of 25 % on the background estimate.

The proposed cuts for the signal selection heavily rely on reconstructed electrons and muons. As already mentioned, one has to apply isolation criteria to them. The isolation, however, is potentially affected by noise and additional energy deposits due to pile-up. Pile-up arises in ATLAS, because several protons of a bunch may interact in the same bunch crossing and the additional interactions are overlaid on top of the process of interest. The impact of pile-up events on the lepton reconstruction has been investigated with special a Monte Carlo sample of BC 1. In this sample a mean number of 5 additional minimum bias events were overlaid to each simulated signal event during the digitisation step. No significant impact on the number of selected events was found due to the pile-up. The selection efficiency is only decreased well within the statistical uncertainties of the Monte Carlo samples.

5.1.5 Significance definitions

The expected signal significance for a given set of event selection cuts depends on the significance definition used and the estimated systematic uncertainties. Some definitions are compared in Table 5.5, which make different assumptions on the underlying statistical properties. In the following a very short review of those is given. For details the reader is referred to the references [154, 155].

In all cases the p-value of a given number of observed events under the background-only hypothesis with a certain number of expected background events is related to the significance Z by

$$p = \int_Z^\infty \frac{1}{\sqrt{2\pi}} e^{-x^2/2} dx = 1 - \Phi(Z) \ , \tag{5.3}$$

where Φ is the cumulative distribution of the standard Gaussian.

For simplicity one uses the so-called Asimov dataset, *i.e.* one estimates the expected number of signal (S) and background (B) events by the Monte Carlo estimate and the expected number of observed events by $n_{\mathrm{obs}} = S + B$. Assuming Poisson statistics the p-value of observing n_{obs} events when B background events are expected is

$$p_{\mathrm{P}} = \sum_{n=n_{\mathrm{obs}}}^{\infty} P_{\mathrm{P}}(n; B) = \sum_{n=n_{\mathrm{obs}}}^{\infty} \frac{B^n}{n!} e^{-B} \ , \tag{5.4}$$

where P_{P} is the Poisson distribution. Using Wilks' theorem the corresponding significance $Z_{\mathrm{P}} = \Phi^{-1}(1 - p_{\mathrm{P}})$ can be approximated as

$$Z_{\mathrm{W}} = \sqrt{2(S+B)\ln(1+S/B) - 2S} \tag{5.5}$$

in the limit of large statistics. Even in our case this approximation is very good and Z_{W} and Z_{P} have nearly identical values. Z_{W} itself can be approximated with the simple $S/\sqrt{B}$ in the limit of $S \ll B$ by expanding the logarithm. This approximation is clearly not valid for our nearly background free sample and this is the reason for the discrepancy between $S/\sqrt{B}$ and Z_{P} in Table 5.5.

The significance is reduced by uncertainties on the background estimate. As the background is estimated from Monte Carlo itself, limited statistics of the background Monte Carlo translates into uncertainties on the estimate of B, which are not included in the previous definitions of significance. The ratio between Monte Carlo and data luminosity $\tau = \frac{L^{\mathrm{MC}}}{L^{\mathrm{data}}}$ is used to relate the m Monte Carlo background events passing the cuts to the background estimate $b = m/\tau$. The probability to observe $n = S + B$ events is therefore

$$\begin{aligned} P(n, m; S+B, \tau B) &= P_{\mathrm{P}}(n; S+B) \cdot P_{\mathrm{P}}(m; \tau B) \\ &= P_{\mathrm{P}}(n+m; S+B+\tau B) \\ &\quad \cdot P_{\mathrm{Bi}}(n | n+m; \rho)\,, \end{aligned} \tag{5.6}$$

with $\rho = \frac{S+B}{S+B+\tau B}$ and P_{Bi} denoting the binomial distribution. One can test the background only hypothesis ($S = 0$) with a standard frequentist binomial parameter test, giving the p-value

$$p_{\mathrm{Bi}} = \sum_{j=n}^{n+m} P_{\mathrm{Bi}}\left(j | n+m; 1/(1+\tau)\right)\,. \tag{5.7}$$

The estimated uncertainty of estimating the true $b\tau$ by m is $\sqrt{m}$, which gives the correspondence $\sigma_b = \sqrt{m}/\tau$ and with the estimate of b finally $\tau = b/\sigma_b^2$. This relationship can be used to provide an ad-hoc background uncertainty σ_b to the Binomial p-value, *cf.* equation (5.7). This method is used in the definition of $Z_0(50\,\%)$ to set a fixed relative background uncertainty of $f = 50\%$, *i.e.* in summary

$$\tau' = 1/(b \cdot f^2)\,, \tag{5.8}$$

$$n'_{\mathrm{off}} = b \cdot \tau'\,, \tag{5.9}$$

$$n'_{\mathrm{on}} = s + b\,, \tag{5.10}$$

$$p_0 = \sum_{k=n'_{\mathrm{on}}}^{n'_{\mathrm{on}}+n'_{\mathrm{off}}} P_{\mathrm{Bi}}(k | n'_{\mathrm{off}} + n'_{\mathrm{on}}; 1/(1+\tau'))\,, \tag{5.11}$$

$$Z_0 = \Phi^{-1}(1 - p_0)\,. \tag{5.12}$$

cut	all SM	BC 1	$S/\sqrt{B}$	Z_0	Z_0, 50 %	Z_P	Z_W	Z_Bi
pre-selection	$2.161(2) \times 10^{10}$	153.4 ± 1.7	0.0	—	—	—	—	—
$p_\mathrm{T}(\text{1st } \mu^\pm) > 30\,\mathrm{GeV}$	$1.72(12) \times 10^6$	78.5 ± 1.2	0.1	—	—	0.1	0.1	0.1
$p_\mathrm{T}(\text{1st } e^\pm) > 30\,\mathrm{GeV}$	$1\,508 \pm 33$	67.9 ± 1.1	1.7	—	—	1.7	1.7	1.7
$p_\mathrm{T}(\text{2nd } e^\pm) > 10\,\mathrm{GeV}$	27.4 ± 2.0	56.4 ± 1.0	10.8	4.3	2.3	8.6	8.6	8.6
$\sum_\mathrm{lep} p_\mathrm{T} > 85\,\mathrm{GeV}$	26.8 ± 2.0	56.3 ± 1.0	10.9	4.4	2.4	8.6	8.7	8.6
$H'_\mathrm{T} > 100\,\mathrm{GeV}$	6.6 ± 1.4	40.7 ± 0.9	15.8	6.4	4.7	10.2	10.2	10.1
$H'_\mathrm{T} > 200\,\mathrm{GeV}$	2.0 ± 0.4	35.8 ± 0.8	25.2	9.5	7.5	12.2	12.3	11.9
$H'_\mathrm{T} > 300\,\mathrm{GeV}$	0.8 ± 0.2	33.2 ± 0.8	37.0	10.8	9.7	13.7	13.7	13.0
$H'_\mathrm{T} > 465\,\mathrm{GeV}$	0.1 ± 0.1	28.7 ± 0.7	115.0	12.1	14.6	17.1	17.2	12.2

Table 5.5: Cut flow and different significance definitions for BC 1. An integrated luminosity of $\int \mathcal{L}\mathrm{d}t = 500\,\mathrm{pb}^{-1}$ at $\sqrt{s} = 7\,\mathrm{TeV}$ was assumed here. The given uncertainties on the number of events include statistical errors only. The significance Z_0 includes a systematic uncertainty of 25 % in addition to the statistical uncertainties of the Monte Carlo estimates. For the first three rows Z_0 is not well-defined. Additionally, Z_0, 50 % denotes the calculation of Z_0 with a fixed uncertainty of the background estimate of 50 %.

For large number of background events, as in the MC sample before cuts, this can lead to $p_0 > 0.5$, *i.e.* the significance is not well-defined anymore. In this analysis two contributions to the background uncertainty are considered in the calculation of Z_0. First the systematic uncertainty of 25 % is assumed according to Section 5.1.4. Additionally the statistical uncertainty of the Monte Carlo sample is taken into account. This leads to smaller values of Z_0 than $Z_0(50\,\%)$ in the last row of Table 5.5, because of the large relative statistical uncertainty.

Finally a profile likelihood method was used to incorporate the uncertainty on the Monte Carlo estimate of the background in the significance. This has the advantage with respect to the Binomial significance Z_Bi (*cf.* equation (5.7)), that different scale factors τ_i for different sub-samples i of the background can be treated correctly. A description of the method can be found in the documentation of the `SigCalc` code [155].

5.1.6 Trigger efficiencies

In Section 5.1.2 event selection cuts for BC 1 events have been derived, which require high momentum electron and muons. Therefore, the trigger is not a critical issue for those event topologies. In Table 5.6 the Event Filter trigger items (*cf.* Section 2.2.4) are summarised, which are interesting for the BC 1 signal in the first year of data taking [156–158]. The considered `EF_mu20` muon trigger with a threshold of 20 GeV shows an individual efficiency of about 85 % with respect to the offline event selection ($p_\mathrm{T}(\text{1st } \mu^\pm) > 30\,\mathrm{GeV}, p_\mathrm{T}(\text{1st } \mathrm{e}^\pm) > 30\,\mathrm{GeV}, p_\mathrm{T}(\text{2nd } \mathrm{e}^\pm) > 10\,\mathrm{GeV}, \sum p_\mathrm{T}^\ell > 85\,\mathrm{GeV}, H'_\mathrm{T} > 300\,\mathrm{GeV}$). At first this may be surprising as the offline selection requires a reconstructed muon with

a transverse momentum $p_{\mathrm{T}} > 30\,\mathrm{GeV}$, but the overall efficiency of the muon trigger at the plateau above its threshold is only about 80 % in the barrel region (*cf.* [67, pp. 649]). The loss in efficiency comes from the limited geometrical coverage of the resistive plate chambers (RPC), which are used by the muon trigger system. Figure 5.11b shows the trigger efficiency of the `EF_mu10` and `EF_mu20` trigger chains for BC 1 events as a function of the transverse momentum of the leading muon in the event. The efficiency at the plateau above the trigger threshold around is 85 % and 90 %, respectively, and higher than the reference value, because more than one muon may exist per BC 1 event.

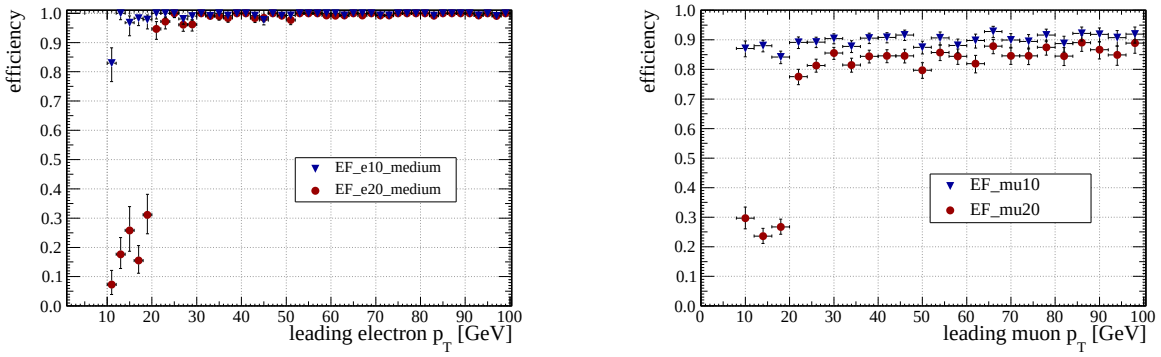

(a) Electron trigger **(b)** Muon trigger

Figure 5.11: Efficiency of the used electron and muon triggers in BC 1 events versus the (offline reconstructed) transverse momentum of the leading electron or muon in the event, respectively. No offline event selection is applied here.

The electron trigger chains `EF_e10_medium` and `EF_e20_medium` alone are nearly fully efficient with respect to the offline selection. As baseline trigger for BC 1 events the combinations `EF_mu10 or EF_e10_medium` (at an instantaneous luminosity of $10^{31}\,\mathrm{cm}^{-2}\,\mathrm{s}^{-1}$) and `EF_mu20 or EF_e20_medium` ($10^{32}\,\mathrm{cm}^{-2}\,\mathrm{s}^{-1}$ and $10^{33}\,\mathrm{cm}^{-2}\,\mathrm{s}^{-1}$) can be used. They are expected to be used without trigger prescale and the Monte Carlo estimate shows, that they are fully efficient for BC 1 events. In Table 5.6 also several other trigger combinations with higher thresholds are listed, which are nearly fully efficient ($> 98\,\%$). They may be used instead, if `EF_mu20 or EF_e20_medium` need to be pre-scaled at a later stage.

trigger	ϵ (%)		prescale at luminosity (in $\mathrm{cm^{-2}\,s^{-1}}$) 10^{31}	10^{32}	10^{33}
EF_mu10	90.56	$^{+0.66}_{-0.69}$	**1**	1,10,10	
EF_mu15	87.08	$^{+0.76}_{-0.78}$	1	1,1,10	
EF_mu20	85.28	$^{+0.80}_{-0.83}$	1	1	**1**
EF_mu40	72.05	$^{+1.02}_{-1.04}$	1	1	
EF_mu20i_loose	69.78	$^{+1.05}_{-1.06}$	1	1	
EF_2mu6	53.16	$^{+1.15}_{-1.15}$	1	1	
EF_2mu10	47.89	$^{+1.15}_{-1.15}$	1	–	**1**
EF_2mu20	13.71	$^{+0.80}_{-0.78}$	1	1	
EF_3mu6	19.73	$^{+0.92}_{-0.90}$	1	1	
EF_2mu6_e10_loose	53.16	$^{+1.15}_{-1.15}$	1	1	
EF_e20_loose	98.47	$^{+0.27}_{-0.30}$	**1**	–	
EF_e20_medium	99.74	$^{+0.10}_{-0.14}$	–	1	**1**
EF_e20i_medium	99.84	$^{+0.08}_{-0.11}$	–	**1**	
EF_e25_medium	99.89	$^{+0.06}_{-0.10}$	–	1	
EF_e55_loose1	86.66	$^{+0.77}_{-0.79}$	1	**1**	
EF_e105_loose1	52.95	$^{+1.15}_{-1.15}$	1	**1**	
EF_2e5_medium	99.10	$^{+0.20}_{-0.24}$	**1**	10,1,1	
EF_2e15_medium	94.20	$^{+0.52}_{-0.55}$	1	**1**	**1**
EF_e10_loose_mu6	91.88	$^{+0.61}_{-0.64}$	1	**1**	
(EF_mu20 or EF_e20_medium)	100.00	$^{+0.00}_{-0.06}$	1	1	1
(EF_mu20 or EF_e20i_medium)	99.79	$^{+0.09}_{-0.13}$	–	1	
(EF_mu20 or EF_e25_medium)	100.00	$^{+0.00}_{-0.06}$	–	1	
(EF_mu20 or EF_2e15_medium)	99.53	$^{+0.14}_{-0.18}$	1	1	
(EF_mu20 or EF_e55_loose1)	98.84	$^{+0.23}_{-0.26}$	1	1	

Table 5.6: Trigger chains and their trigger efficiency for BC 1 events as derived from Monte Carlo simulation. The expected pre-scale settings are given for luminosities of $10^{31}\,\mathrm{cm^{-2}\,s^{-1}}$ to $10^{33}\,\mathrm{cm^{-2}\,s^{-1}}$ (numbers may change to accommodate for actual trigger rates). Numbers in bold face denote so-called primary triggers. Efficiencies are calculated with respect to the offline event selection ($p_\mathrm{T}(\text{1st } \mu^\pm) > 30\,\mathrm{GeV}, p_\mathrm{T}(\text{1st e}^\pm) > 30\,\mathrm{GeV}, p_\mathrm{T}(\text{2nd e}^\pm) > 10\,\mathrm{GeV}, \sum p_\mathrm{T}^\ell > 85\,\mathrm{GeV}, H_\mathrm{T}' > 300\,\mathrm{GeV}$).

5.2 Parameter scans

The analysis concentrated on a specific benchmark scenario up to now. This section will go beyond this restriction to show that the developed event selection cuts can lead to a discovery in wider ranges of the mSUGRA parameter space. For this purpose regions of the lepton number violating (B_3) mSUGRA parameter space with different mass spectra compared to BC 1 but with the same non-vanishing lepton number violating coupling have been evaluated.

Simply by constraints on the computing time it is not reasonably possible to use the full-fledged ATLAS detector simulation in those parameter scans. Therefore the following analysis is based on the generic detector simulation Delphes 1.9 [94]. As shown in Section 3.2 one gets a reasonable agreement between Delphes and the full ATLAS detector simulation, that is at least sufficient to study the influence of the SUSY mass spectrum on the discovery potential.

In this parameter scan Monte Carlo samples of the signal were generated with the extended Herwig version [140] implemented in the ATLAS software framework and afterwards processed with the Delphes detector simulation. Hence, the settings of the event generator are those of the MC09 tune. In our first publication on the discovery potential of the BC 1 scenario [59] the signal as well as the Standard Model background were independently generated and simulated using Delphes. The settings of the event generators were guided by the MC09 tune, but produced completely independent from the ATLAS software framework. Here the background estimates obtained with the ATLAS full simulation are used instead.

The SUSY mass spectra were calculated with SOFTSUSY 3.0 [159, 160]. The SOFTSUSY output was fed into ISAWIG 1.200 and ISAJET 7.75 [161] in order to calculate the decay widths of the SUSY particles [59].

In the scan, the parameters $M_{1/2}$ and $\tan(\beta)$ have been varied for the following reasons. With increasing $M_{1/2}$ especially the masses of the strongly interacting sparticles raise. By varying $M_{1/2}$ one can thus investigate the discovery potential as a function of the SUSY mass scale. In contrast, changing $\tan(\beta)$ does not affect most of the sparticle masses and therefore also leaves the total sparticle production cross section nearly unchanged, *cf.* Figure 5.12a. However, increasing $\tan(\beta)$ decreases the stau LSP mass by RGE running due to an increased tau Yukawa coupling [46]. Therefore, with the help of $\tan(\beta)$ one can change the kinematics of the LSP decay products. The mean momentum of the stau LSP itself changes according to the the mass difference between the $\widetilde{\chi}_1^0$ and the $\widetilde{\tau}_1$, because the mass of the $\widetilde{\chi}_1^0$ is nearly independent of $\tan(\beta)$.

The black regions in the parameter space in Figure 5.12 correspond to parameter values which either include tachyons [40] or which violate the Higgs mass or stau mass bounds from LEP [41, 42]. One can see in Figure 5.12b, that the selection is relatively stable over wide regions of the considered parameter range and drops from about 20% to 10% for larger values of $\tan(\beta)$. This shows, that the chosen event selection cuts are not

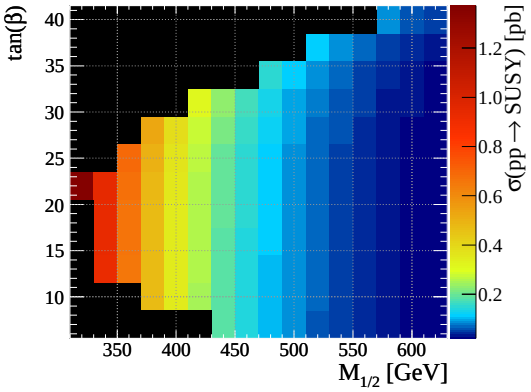

(a) Signal cross section in pb

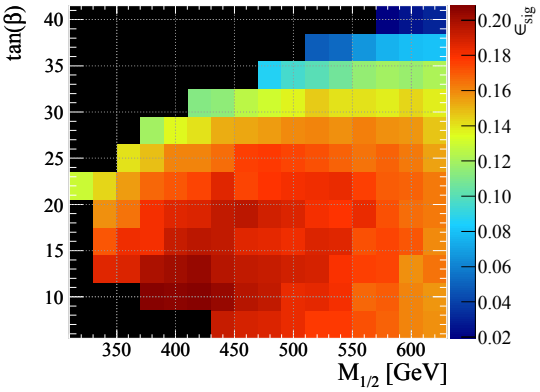

(b) Selection efficiency for the signal events

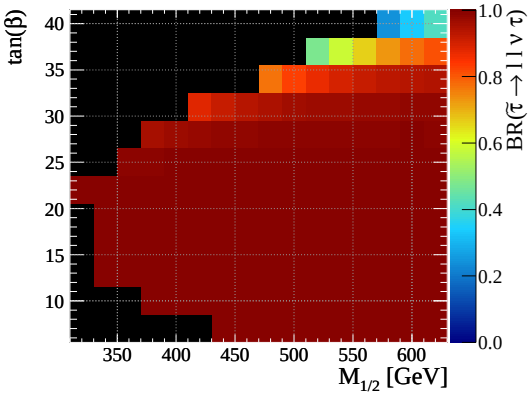

(c) $\mathcal{B}(\tilde{\tau}_1^{\pm} \to \tau^{\pm}\, \ell^+\, \ell^-\, \nu)$

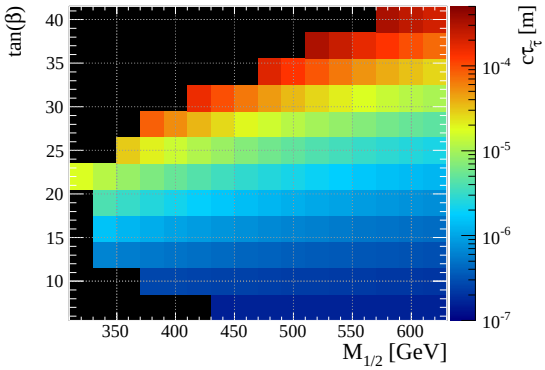

(d) Lifetime $c\tau_{\tilde{\tau}_1}$

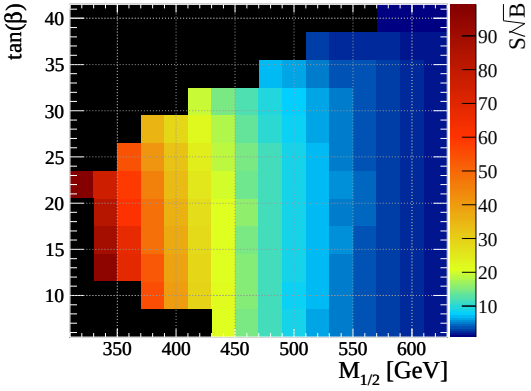

(e) Significance $S/\sqrt{B}$

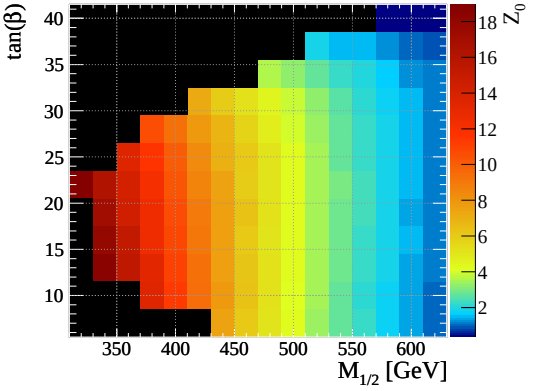

(f) Significance Z_0

Figure 5.12: Parameter scans in the $M_{1/2}$–tan(β) plane at a centre-of-mass energy of $\sqrt{s} = 7\,\text{TeV}$. The other mSUGRA parameters are those of BC 1, *i.e.* $M_0 = A_0 = 0\,\text{GeV}$ and $\text{sgn}(\mu) = +1$. The significances are given for an integrated luminosity of $500\,\text{pb}^{-1}$, where a relative systematic background uncertainty of 25 % is assumed in addition to the statistical uncertainty for the calculation of the binomial significance Z_0.

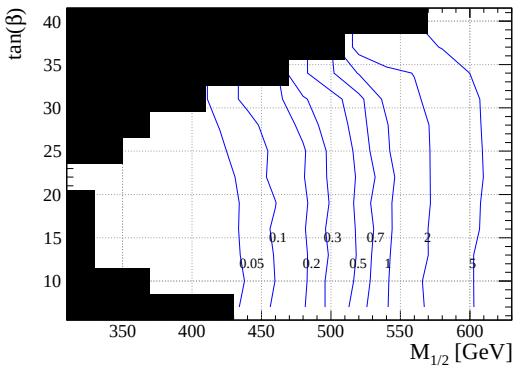

(a) Estimated contours of minimum required integrated luminosity (fb^{-1}) to reach $S/\sqrt{B} > 5$

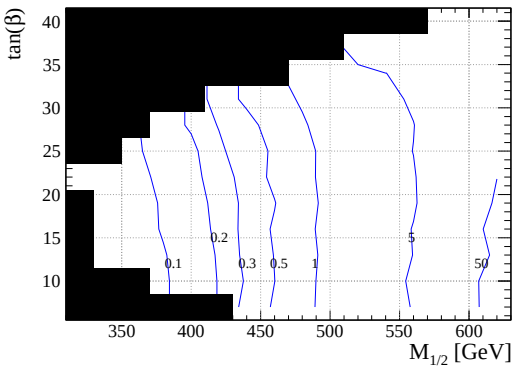

(b) Estimated contours of minimum required integrated luminosity (fb^{-1}) to reach $Z_0 > 5$ assuming a relative systematic background uncertainty of 25 % in addition to the statistical uncertainty

Figure 5.13: Minimum required integrated luminosity for a 5σ discovery at $\sqrt{s} = 7\,\mathrm{TeV}$ without (a) and with (b) systematic background uncertainties included. The parameters are as in Figure 5.12.

over-tuned to a special benchmark scenario. The dependency on $\tan(\beta)$ can be explained by the aforementioned dependency of the $\widetilde{\tau}_1$-$\widetilde{\chi}_1^0$ mass difference, giving harder $\widetilde{\tau}$ decay products for higher values of $\tan(\beta)$. The mass spectrum is shifted upwards for higher values of $M_{1/2}$, *i.e.* in general all produced particles from the SUSY decay chain get higher momenta. For very high values of $M_{1/2}$ one observes a slight degradation again, which can be explained by highly boosted decay products. In this case the leptons may not pass the isolation cuts anymore, because the particles are too collimated.

Furthermore, it is interesting to look at the fraction of 4-body decays in the LSP decay, *i.e.* the branching ratio $\mathcal{B}(\widetilde{\tau}_1^{\pm} \to \tau^{\pm}\,\ell^+\,\ell^-\,\nu)$ in Figure 5.12c as obtained in Monte Carlo simulation. In the given parameter space the $\widetilde{\tau}$ decays predominantly in four-body decays, with the assumed signature. However, for high $\tan(\beta)$ two-body decays ($\widetilde{\tau} \to \mu\nu/\tau\nu$) get important and the events do not provide the signature anymore which is assumed in the event selection. A detailed discussion of the branching fractions into two- and four-body decays can be found in reference [45]. Related to this is the lifetime of the $\widetilde{\tau}$-LSP (Figure 5.12d). In all of the parameter space $c\cdot\tau_{\widetilde{\tau}}$ is well below the mm range. This means the $\widetilde{\tau}$ will decay inside the tracking volume of the detector even for large boost factors $\gamma = E_{\widetilde{\tau}}/m_{\widetilde{\tau}}$. Particles with large decay lengths may be identified in the detector by the reconstruction of displaced vertices while even larger displacements can lead to losses in the reconstruction efficiency of the secondary particles. For some points with long lifetimes the mass difference between $\widetilde{\chi}_1^0$ and $\widetilde{\tau}_1$ can be large ($\approx 150\,\mathrm{GeV}$), compared to the stau mass ($\approx 90\,\mathrm{GeV}$). Still the decay length is small for the assumed strength of the $\not{R}_p$ coupling, such that effects from displaced decay vertices are not relevant here.

The ratio $S/\sqrt{B}$ is proportional to the absolute number of events passing the cuts at a given integrated luminosity and is mainly determined by the signal cross section (Figure 5.12a), whereas the selection efficiency plays a minor role in the given parameter range. However, $S/\sqrt{B}$ overestimates the expected signal significance strongly and the binomial significance Z_0 gives a more realistic estimate. In its calculation the systematic uncertainty of 25 % (*cf.* Section 5.1.4) as well as the statistical uncertainty of the background estimate have been taken into account.

One can translate the expected signal significance into the required luminosity to reach the discovery significance of 5σ. The significance definition of Z_0 cannot easily be inverted analytically and therefore a numerical method was used to calculate the contours of required luminosity given in Figure 5.13. Especially for high values of $M_{1/2}$ the binomial significance requires unreasonable amounts of data (Figure 5.13b), because the number of selected signal events gets that low, that the significance is fully dominated by the systematic uncertainty of the background estimate. In this region of parameter space an increase of the collected integrated luminosity does not help anymore, but only better estimates of the Standard Model background allow for a discovery of the SUSY signal.

5.3 Prospects for stau mass determination

Once a signal of beyond the Standard Model events has been established, one needs to measure certain observables, which can give hints on the nature of the BSM process. In the case of supersymmetric models one of the first measurements will be the mass scale of the SUSY particles. In the case of *R*-parity violating SUSY where the lightest SUSY particle decays promptly, one important step towards a determination of the sparticle spectrum would be the measurement of the mass of the LSP itself.

In the case of the two-body decay $\widetilde{\tau}_1 \to \mathrm{u}\,\mathrm{d}$ in the benchmark scenario BC 2 ($\lambda'_{311} > 0$, *cf.* Section 1.2.3), the LSP would be visible as a mass peak in the invariant mass spectrum of two-jet combinations. This is however not the case for the four-body decay

$$\widetilde{\tau}_1^{\pm} \to \tau^{\pm}\, \ell^+\, \ell^-\, \nu \tag{5.13}$$

of the $\widetilde{\tau}$-LSP in and around the benchmark scenario BC 1 ($\lambda'_{121} > 0$). Here the undetectable neutrino in the $\widetilde{\tau}_1$ decay and the additional neutrino in the subsequent τ decay lead to a loss of information and complicate the mass measurement. Against this background the prospects for the determination of the $\widetilde{\tau}_1$ mass in the BC 1 scenario are investigated in this Section. A full treatment of all systematic uncertainties of the mass determination is omitted here and left to the time when a signal has been established.

As one expects two $\widetilde{\tau}$-LSP per event and due to additional taus in the decay $\widetilde{\chi}_1^0 \to \widetilde{\tau}_1\,\tau$ one cannot simply use the missing transverse energy $E_{\mathrm{T}}^{\mathrm{miss}}$ in the calculation of the $\widetilde{\tau}_1$ (transverse) mass. Even though not all decay products of the $\widetilde{\tau}$-LSP are visible one can

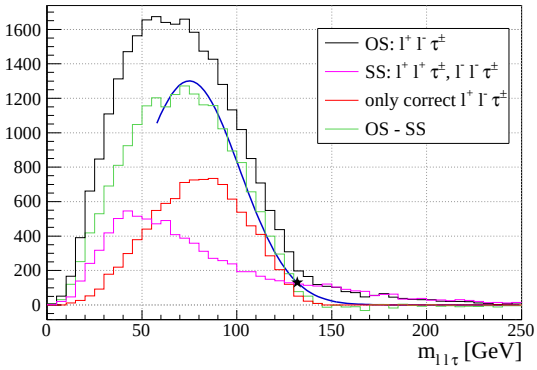

Figure 5.14: Invariant mass distribution of the visible part of the hardest tau, $\tau^{\pm}$, with the two nearest (in ΔR) charged leptons, ℓ, of the first or second generation. The black line (purple line) gives the distribution for the opposite-sign (same-sign) lepton pair, $\ell^+\ell^-$ ($\ell^{\pm}\ell^{\mp}$), plus the tau. The distribution is denoted by OS (SS). The green line shows the difference of the OS and SS distributions. The red histogram corresponds to the correct $\tau^{\pm}\ell^+\ell^-$ combination, *i.e.* all three leptons stem from the same $\widetilde{\tau}_1$ decay. A Gaussian (blue line) has been fitted to the OS−SS distribution.

still build the invariant mass of the $\ell^+\ell^-$ pair with the visible part of the (hadronically decaying) τ. Here and in the following $\ell^{\pm}$ denotes $e^{\pm}$ or $\mu^{\pm}$. One then expects a kinematic endpoint in the invariant mass distribution, which should lie at the true stau LSP mass.

It has already been shown in Section 5.1.2 that (nearly) background-free samples of BC 1 events can be selected with efficiencies of roughly 20 %. Therefore, Standard Model backgrounds need not to be considered in the following investigations. However the combinatorial background due to wrong combinations of $\ell^+\ell^-\tau^{\text{had}}$ selections turns out to be sizable. The black line in Figure 5.14 (labelled OS for opposite sign) shows the invariant mass distribution of the $\ell^+\ell^-$ pair combined with the visible part of the tau. The histogram contains 50 000 BC 1 signal events simulated at a centre-of-mass energy of $\sqrt{s} = 7\,\text{TeV}$. The red histograms includes only such combinations where the correct combination was chosen, *i.e.* all three particles belong to the same stau decay.

Note, that no detector simulation is employed here. Electrons and muons are only selected if their transverse momentum p_{T} is larger than 7 GeV and $|\eta| < 2.5$. Hadronically decaying taus are identified if their visible momentum exceeds $p_{\text{T}}^{\text{vis}} > 10\,\text{GeV}$ and $|\eta^{\text{vis}}| < 2.5$. In general more than one $\tau^{\pm}\ell^+\ell^-$ combination exists per event. In fact one would be fully dominated by wrong combinations, if all such combinations would be taken into account. This means it is crucial to develop a method having a high probability to select the correct combinations. In principle two correct combinations may exist in a single event, if both taus stemming from the two $\widetilde{\tau}_1$-LSPs decay hadronically. However, it is quite unlikely that all electrons, muons and taus in the event can be reconstructed and therefore only one combination is kept per event at maximum. As an additional cut only those selected combinations are used, where the distance in ΔR between both

leptons and the tau is smaller than 1.5. In principle this cut may distort the invariant mass spectrum, especially for very high stau masses. Both options with and without this cut have been checked and both give nearly identical results in the precision of the estimated stau mass. A detailed discussion of the combinatorial backgrounds and a comparison of different combination schemes is given in Appendix D.

5.3.1 Stau mass estimation

In order to reduce the combinatorial backgrounds at least statistically and thus to sharpen the kinematic endpoint of the invariant mass, one can combine the hardest tau with the nearest same sign (SS) lepton pair, $\ell^{\pm}\ell^{\pm}$. The respective invariant mass distribution is given by the purple line in Figure 5.14 (labelled SS). After subtraction of the same sign $\tau\ell^{\pm}\ell^{\pm}$ distribution (purple line) from the opposite sign $\tau\ell^{+}\ell^{-}$ distribution (black line) one obtains the OS−SS distribution given by the green line.

The OS−SS invariant mass distribution follows much closer the distribution that arises from the correct $\tau\ell^{+}\ell^{-}$ triplet (red histogram in Figure 5.14) than the original OS distribution. Without the cut on the angular distance between the two leptons and the tau the same sign distribution shows a long tail at high invariant masses, which leads to an over-subtraction at high masses. This can be explained by the fact, that one of the same sign leptons mostly stems from the other stau decay in the event or another source and therefore often has a larger angle to the first lepton leading to higher invariant masses.

The resulting OS−SS distribution has an endpoint near the true endpoint at the simulated $\widetilde{\tau}_1$ mass of 148 GeV. However, it is difficult to define in measured data, where the endpoint exactly lies as always a few entries will remain with higher invariant masses. One therefore needs to find an observable which is sensitive to the stau mass. Here a Gaussian distribution is fitted to the OS−SS distribution and the value calculated, where it drops to 10% of its maximum (marked by a star in Figure 5.14). The fit range is crucial and has been determined in an iterated Gaussian fit, which starts with the maximum bin position and the root mean square (RMS) of the histogram and uses the range $\mu - \sqrt{2\ln(2)}/2 \cdot \sigma$ to 200 GeV, where μ is the mean of the previous Gaussian fit and σ^2 its variance. The effect of the fit range needs to be treated as a systematic uncertainty of the method. Although this observable lies below the simulated stau mass of 148 GeV, one can use it to estimate the true mass as long as there is a clear and known correlation between the two. Such a procedure has already been successfully demonstrated on simulated Monte Carlo samples in the context of sparticle mass measurements *e.g.* in reference [67, 102].

Other functions for the fit have been tested as well, like the log-normal distribution or a Gaussian distribution with an additional offset. From all the tested functions the simple Gaussian with the above mentioned fit range turned out the give the most stable fit results, while describing the invariant mass distribution sufficiently well. Similarly, other definitions of the observable were used, like the mean of the Gaussian or its upper

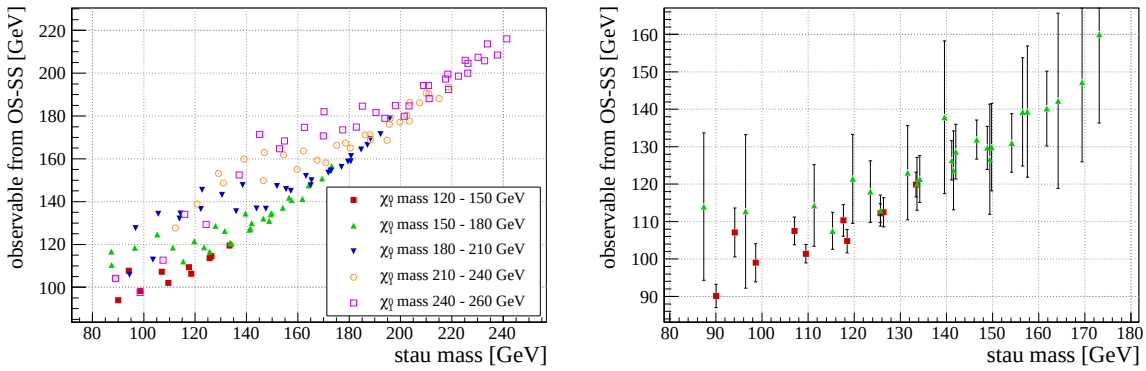

(a) All parameter points

(b) Including event selection cuts and assuming $\int \mathcal{L} dt = 5\,\text{fb}^{-1}$

Figure 5.15: Stau mass sensitive observable versus true stau mass (see text for definition) for the scenarios presented in Section 5.2. Different colours of the points correspond to different intervals of the $\widetilde{\chi}_1^0$ (NLSP) mass. (a) includes all parameter points, where 10 000 signal events were simulated each. (b) shows estimates for an integrated luminosity of $5\,\text{fb}^{-1}$ at $\sqrt{s} = 7\,\text{TeV}$ including event selection cuts. Only scenarios where at least 150 events pass the cuts are used in (b). The error bars show to what precision the estimated stau mass can be measured. The errors correspond to statistical fluctuations and are estimated as described in the text.

half maximum value. Again, the definition finally used showed the best correlation with the true stau mass.

Indeed a clear correlation between the aforementioned observable and the true $\widetilde{\tau}$ mass is observed in Figure 5.15a. Here the stau LSP scenarios of the parameter scans from Section 5.2 were taken. 10 000 signal events were simulated for each scenario and the observable determined from the OS−SS invariant mass distribution as described above. The different marker styles in Figure 5.15a correspond to different masses of the $\widetilde{\chi}_1^0$, which is the next-to-lightest supersymmetric particle (NLSP) here. There is only a small systematic dependency of the estimated mass on the $\widetilde{\chi}_1^0$ mass. For example, for a stau mass of 120 GeV the observable can increase from roughly 100 GeV to 140 GeV, if the $\widetilde{\chi}_1^0$ mass increases from 120 GeV to 240 GeV. This is expected because a heavier $\widetilde{\chi}_1^0$ leads to a harder tau from the $\widetilde{\chi}_1^0$ decay.

One can use Figure 5.15a to translate the observable to the true stau mass. Such an analysis is even possible in a limited way with early LHC data, as can be seen in Figure 5.15b, where the observable is again plotted against the true stau mass. Here event selection cuts were applied and only scenarios were included, where at least 150 events in $5\,\text{fb}^{-1}$ pass the event selection cuts. Otherwise, there would not be enough statistics for the mass reconstruction. The error bars correspond to the precision with which the observable can be measured assuming an integrated luminosity of $5\,\text{fb}^{-1}$. Systematic uncertainties are not included here.

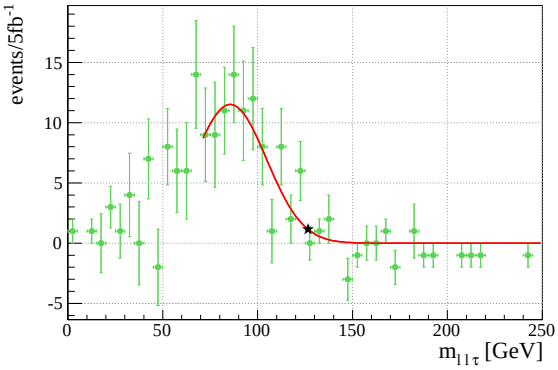

Figure 5.16: OS−SS distribution as in Figure 5.14, but here including event selection cuts and randomly selecting events corresponding to an integrated luminosity of $5\,\text{fb}^{-1}$, *i.e.* uncertainties and fluctuations correspond to those expected for $5\,\text{fb}^{-1}$ at $\sqrt{s} = 7\,\text{TeV}$. The star marks the value of the chosen observable.

The statistical uncertainties in Figure 5.15b were estimated in the following way. Out of 10 000 simulated signal events, events have been randomly chosen to get a sub-sample corresponding to an integrated luminosity of $5\,\text{fb}^{-1}$. This procedure was repeated 100 times for each point to obtain different sub-samples. The observables of these sub-samples follow a Gaussian distribution, where its width corresponds to the statistical uncertainties in Figure 5.15b. Figure 5.14 shows an example of one sub-sample for the BC 1 scenario.

From the above investigations one can conclude that rough estimates of the stau LSP mass in BC 1-like scenarios should be possible with an integrated luminosity of $5\,\text{fb}^{-1}$ at $\sqrt{s} = 7\,\text{TeV}$. An interpretation of candidate events within the assumed model will be feasible with a mass resolution of about 20 GeV depending on the actual $\widetilde{\tau}$ mass. More detailed studies of the systematic effects on the mass determination have to be done once a BSM signal has been established and their specific event topologies are known.

5.4 Summary

The first full Monte Carlo analysis including an estimate of the systematic uncertainties on the Standard Model backgrounds were given for the BC 1 scenario, in which the $\widetilde{\tau}$-LSP mainly undergoes the four-body decay $\widetilde{\tau}_1^{\pm} \to \tau^{\pm}\,\ell^+\,\ell^-\,\nu$. Already with an integrated luminosity of a few hundred pb^{-1} a discovery should be possible with the ATLAS experiment. With $\int \mathcal{L}\text{d}t = 500\,\text{pb}^{-1}$ one would even be able to select a nearly background free sample of about 30 BC 1 events, corresponding to a signal significance of about $Z_0 \approx 12$, taking systematic uncertainties of the background estimate into account. Even though many tau leptons are expected in the final states of BC 1 events, their reconstruction efficiency is very low, because most tau leptons have low momenta ($p_{\text{T}}^{\text{vis}} < 10\,\text{GeV}$). Additionally the BC 1 events include many other electrons, muons and jets, which hide the tau leptons and reduce their efficiency further. Hence, no observables based on identified tau leptons were used in the event selection, instead the kinematics of electrons, muons and jets are used to distinguish the SUSY signal from Standard Model background.

Not only the benchmark scenario itself shows a high discovery potential at the LHC, but also the mSUGRA parameter space around this specific point can be covered. With $1\,\mathrm{fb}^{-1}$ a 5σ discovery should be possible in the mass range up to about $M_{1/2} \lesssim 500\,\mathrm{GeV}$ over the theoretically allowed range of $5 \lesssim \tan(\beta) \lesssim 30$. The determination of the $\widetilde{\tau}_1$ mass, once a signal has been established, is not straight forward due to the many neutrinos in the final states for the assumed $\not{R}_p$ coupling and due to the combinatorial background within the signal events. Anyhow it was shown that estimates of the $\widetilde{\tau}_1$ mass should be possible with $\int \mathcal{L}\mathrm{d}t \approx 5\,\mathrm{fb}^{-1}$, where different methods for the mass estimation were compared.

Chapter 6

Conclusions and Outlook

The guiding topic of this thesis was the search for supersymmetric extensions of the Standard Model including R-parity violation with the ATLAS experiment. SUSY is very well studied in many models in theory and in experiment, because it is theoretically appealing and may lead to a grand unified theory of particle physics. However, R-parity is usually taken to be conserved giving signatures with a stable, undetectable lightest supersymmetric particle in collision experiments. Even though R-parity violating ($\not{R}_p$) models are equally well motivated, they were mostly ignored in previous studies by the ATLAS collaboration.

The present study concentrated on SUSY models in the mSUGRA framework and more precisely on models where the scalar partner of the tau lepton, the stau $\widetilde{\tau}$, is the lightest supersymmetric particle (LSP). Such models are empirically excluded in R-parity conserving models, but arise naturally when assuming lepton number violating $\not{R}_p$. It was shown that multi-lepton signatures as they arise for many $\not{R}_p$ couplings can be discovered with the ATLAS experiment already in the first years of operation. A full Monte Carlo investigation of one benchmark scenario (BC 1) was used to derive a set of cuts to separate the $\not{R}_p$ signal events from the Standard Model background. The integrated luminosity of $\int \mathcal{L} \mathrm{d}t = 500\,\mathrm{pb}^{-1}$, which is available by summer 2011, would lead to a nearly background free sample of about 30 BC 1 events, corresponding to a significance of about $Z_0 \approx 12$, taking systematic uncertainties of the background estimate into account. A scan of the parameter space around the benchmark scenario allowed to derive estimates for the expected luminosity which is needed for a 5σ discovery. Assuming $1\,\mathrm{fb}^{-1}$ a discovery should be possible in the parameter range up to about $M_{1/2} \lesssim 500\,\mathrm{GeV}$.

After the discovery of a potential $\not{R}_p$ SUSY signal one wants to measure the properties of the new phenomenon. The mass of the LSP will be one of the first parameters to be determined. It was shown that an estimate of the $\widetilde{\tau}_1$ mass should be possible with a few fb^{-1}. However, the mass determination suffers from a large combinatorial background and the many neutrinos in the final state for the assumed class of models. A method was presented to derive the $\widetilde{\tau}_1$ mass from its visible decay products including a scheme to select the best matching combination of reconstructed particles.

With this study the awareness for R-parity violating SUSY within the ATLAS collaboration grew. The grid of parameter points prepared in Section 5.2 will be used as an official reference grid to be studied with the data, which will be collected in 2011 by the ATLAS experiment.

Important for the $\not{R}_p$ SUSY studies, but also of more general interest, is the reconstruction of tau leptons and the fast simulation of detector effects. Both topics were addressed in this thesis as well. The fast track simulation FATRAS provides detailed Monte Carlo estimates of measurements in the ATLAS tracking system, while being about a factor of 50 faster than the fully fledged simulation of the Inner Detector. Still a good agreement with first collision data of the ATLAS experiment was achieved. FATRAS is of increasing importance for the ATLAS collaboration and as part of ATLFAST-IIF applied for many studies. It also played an important role in studies of upgrades for the Inner Detector. Generic detector simulations were compared to the simulation of the ATLAS detector and it was shown that the Delphes program yields reasonably good results for electrons, muons and jets in the SUSY signal events. Tau leptons, however, are badly modeled in this simple approach.

The reliable identification of (hadronically decayed) tau leptons relies strongly on the reconstruction of tracks from charged pions. Track selection criteria were developed to obtain the best results in the classification of tau leptons according to their decay mode. The studies showed that inefficiencies in the track reconstruction are mostly due to hadronic interactions in the Inner Detector. Systematic uncertainties due to Inner Detector misalignments on the other hand can be neglected.

Finally a new approach to the reconstruction of tau leptons in ATLAS was introduced, fully based on results of the energy flow algorithm eflowRec. This algorithm, named PanTau, has a high potential in the identification of individual tau decay modes, which is an important ingredient for certain SUSY studies. Relying on energy flow results has conceptional advantages in the tau reconstruction. Furthermore the individual treatment of the different tau decay modes improves the identification performance. The dependency of the identification variables on the tau energy was studied in detail and methods were applied to reduce it. However, no general recommendation can be given, whether the reduced dependency improves the overall performance as this strongly depends on the application of the tau ID and the energy spectrum of the tau candidates under investigation.

The performance of eflowRec and PanTau on QCD jets in the first data of the ATLAS experiment at $\sqrt{s} = 7\,\text{TeV}$ was found to be well modeled in the Monte Carlo prediction. Effects from pile-up were found in some ID variables. The tuning of PanTau parameters and the selection of variables will be slightly modified to minimise pile-up effects. At the time of writing efforts are ongoing by the ATLAS tau performance group to incorporate the PanTau approach into the common tau reconstruction of the ATLAS experiment, thus making it available for all analyses. PanTau will be an important contribution to the aim of including more information about the sub-structure of tau jets and the identification of individual charged and neutral pions in the jets.

Appendix A

Monte Carlo samples and software versions

The Monte Carlo samples used in this thesis in general follow the MC09 simulation of the ATLAS experiment. Base line release of the ATLAS software for event reconstruction is athena 15.6.9.8. All Monte Carlo samples have been simulated with a centre-of-mass energy of $\sqrt{s} = 7\,\text{TeV}$, despite the comparisons to first collision data at $\sqrt{s} = 900\,\text{GeV}$ (Section 3.1.2) and the studies of misalignment (Section 4.2.2). In addition to the MC09 tunes [130] of the event generators the Pythia DW tune [131] was used for some of the tau studies.

A.1 Tau studies

The energy flow algorithm eflowRec is not run by default in the official ATLAS event reconstruction. Therefore, all eflowRec and PanTau related studies need to run eflowRec on ESD datasets. The samples in Table A.1 have been processed in athena 15.6.9.8 with the following additional packages:

package	tag
Reconstruction/eflowAthenaPool	eflowAthenaPool-00-00-05
Reconstruction/eflowEvent	eflowEvent-00-02-50
Reconstruction/eflowEventTPCnv	eflowEventTPCnv-00-00-15
Reconstruction/eflowRec	eflowRec-00-02-36

The PanTau reconstruction and analysis of the data samples was done in athena 15.6.9.8 with the following additional packages:

package	tag
PhysicsAnalysis/PanTauAnalysis	
Reconstruction/PanTau/PanTauAlgs	
Reconstruction/PanTau/PanTauEvent	
Reconstruction/PanTau/PanTauInterfaces	
Reconstruction/PanTau/PanTauUtils	
DataQuality/GoodRunsLists	GoodRunsLists-00-00-84
DataQuality/GoodRunsListsUser	GoodRunsListsUser-00-00-12
Database/CoolRunQuery	CoolRunQuery-00-03-01
LumiBlock/LumiBlockComps	LumiBlockComps-00-01-13
Reconstruction/MissingETGoodness	MissingETGoodness-00-00-59
PhysicsAnalysis/D3PDMaker/D3PDMakerConfig	D3PDMakerConfig-00-01-75
PhysicsAnalysis/D3PDMaker/JetD3PDMaker	JetD3PDMaker-00-01-17
PhysicsAnalysis/D3PDMaker/MissingETD3PDMaker	MissingETD3PDMaker-00-05-12
PhysicsAnalysis/D3PDMaker/TauD3PDMaker	TauD3PDMaker-00-05-03
PhysicsAnalysis/D3PDMaker/TrigMissingETD3PDMaker	TrigMissingETD3PDMaker-00-00-04
PhysicsAnalysis/D3PDMaker/TrigTauD3PDMaker	TrigTauD3PDMaker-00-00-05
PhysicsAnalysis/TauID/TauTrackEvent	TauTrackEvent-00-00-10
PhysicsAnalysis/TauID/TauTrackTools	TauTrackTools-00-02-02
Reconstruction/Jet/JetRec	JetRec-01-01-89
Reconstruction/Jet/JetUtils	JetUtils-01-01-27
Reconstruction/RecExample/RecExCommon	RecExCommon-00-12-09
Trigger/TrigAnalysis/TriggerMenuNtuple	TriggerMenuNtuple-00-01-24

Older Monte Carlo datasets at a centre-of-mass energy of $\sqrt{s} = 10\,\text{TeV}$ have been used to estimate the impact of Inner Detector misalignments on the reconstruction of hadronic tau decays in Section 4.2.2. In this case the full track reconstruction chain including pattern recognition has been re-run from ESD files in athena 15.0.0.2. The detector geometry ATLAS-GEO-02-01-00 and three sets of alignment constants [107] have been applied for each sample summarised in Table A.2. The impact parameter resolutions have been estimated from the last sample in Table A.2, where the full Inner Detector reconstruction was run on RDO files.

Dataset	Process	Simulation tag	Events	cross section/pb	Comments
106052	$Z \to \tau\tau$	e468_s765_s767_r1302	201 971	8.54×10^2	MC09
106023	$W \to \tau^{had}\nu$	e468_s765_s767_r1302	100 987	8.93×10^3	
105009	QCD, J0	e468_s766_s767_r1303	1 399 184	9.86×10^9	
105010	QCD, J1	e468_s766_s767_r1303	1 394 383	6.78×10^8	
105011	QCD, J2	e468_s766_s767_r1303	1 398 078	4.09×10^7	
105012	QCD, J3	e468_s766_s767_r1303	1 397 430	2.19×10^6	
105013	QCD, J4	e468_s766_s767_r1303	1 397 401	8.77×10^4	
107413	$Z \to \tau\tau$	e579_s766_s767_r1303	498 590	7.30×10^2	Pythia DW tune
107414	$W \to \tau\nu$	e579_s766_s767_r1303	417 319	7.79×10^3	
115859	QCD, J0	e570_s766_s767_r1303	399 639	7.77×10^9	
115860	QCD, J1	e570_s766_s767_r1303	398 143	5.04×10^8	
115861	QCD, J2	e570_s766_s767_r1303	399 793	2.93×10^7	
115862	QCD, J3	e570_s766_s767_r1303	399 747	1.56×10^6	
115863	QCD, J4	e570_s766_s767_r1303	399 486	6.45×10^4	
116194	$A^0 \to \tau\tau$	e601_s765_s767_r1302	59 967	2.74×10^{-2}	for study of
106052	$Z \to \tau\tau$	e468_s765_s767_r1302	1 998 598	8.54×10^2	track efficiency

Table A.1: MC samples for tau studies ($\sqrt{s} = 7\,\text{TeV}$)

Dataset ID	Process	Simulation tag	Events	cross section/pb	Comments
106052	$Z \to \tau\tau$	e347_s462_r541	200 000	1.13×10^3	
105010	QCD, J1	e344_s465_r544		8.67×10^8	
105011	QCD, J2	e344_s465_r544		5.60×10^7	
106052	$Z \to \tau\tau$	e347_s462_d126	20 000	1.13×10^3	full reconstruction

Table A.2: MC samples for tau misalignment studies. MC08 samples at a centre-of-mass energy of $\sqrt{s} = 10\,\text{TeV}$. The full track reconstruction including pattern recognition has been re-run from ESD in athena 15.0.0.2 with geometry ATLAS-GEO-02-01-00 and three sets of alignment constants for each sample.

Run	$\mathcal{L}/\text{nb}^{-1}$	Events	Period	Reconstruction tag
159203	8.50	300 051	D6	f275_m549
159202	11.49	375 478	D6	f275_m549
159113	29.59	1 332 684	D5	f275_m549
159086	60.04	2 517 048	D4	f275_m549
159041	29.68	1 399 596	D4	f275_m549
158975	23.23	1 131 772	D3	f275_m549
158632	5.97	329 048	D3	f274_m544
158582	17.68	1 009 892	D2	f273_m544
158549	4.01	233 745	D2	f273_m544
158548	11.95	617 739	D2	f273_m544
158545	1.50	74 747	D2	f273_m544
158392	8.55	616 009	D1	f271_m544
158299	1.39	88 945	D1	f271_m534
158269	3.57	197 680	D1	f271_m534
158116	16.27	1 021 468	D1	f271_m534
158045	1.00	64 890	D1	f270_m534
155678	1.21	301 698	C1	f261_m497

Table A.3: Data samples for tau studies at a centre-of-mass energy of $\sqrt{s} = 7\,\text{TeV}$. Given here is the approximated integrated luminosity during "stable beams" periods of each run. Samples are taken from the `physics_L1Calo` stream in `DESD_MET` format.

A.2 Search for R-parity violating SUSY

The analysis of the discovery potential for R-parity violating SUSY was done on MC09 Monte Carlo samples of the ATLAS experiment, which have been simulated at a centre-of-mass energy of $\sqrt{s} = 7\,\text{TeV}$.

Dataset	Process	Simulation tag	Events	cross section/pb	Comments
107681	$W \to e\nu + 1$	e511_s765_s767_r1302_r1306	258 408	1293	Alpgen/Jimmy
107682	$W \to e\nu + 2$	e511_s765_s767_r1302_r1306	163 899	377.1	
107683	$W \to e\nu + 3$	e511_s765_s767_r1302_r1306	50 477	100.9	
107684	$W \to e\nu + 4$	e511_s765_s767_r1302_r1306	12 991	25.3	
107685	$W \to e\nu + 5$	e511_s765_s767_r1302_r1306	3449	6.9	
107691	$W \to \mu\nu + 1$	e511_s765_s767_r1302_r1306	255 909	1281.2	Alpgen/Jimmy
107692	$W \to \mu\nu + 2$	e511_s765_s767_r1302_r1306	187 860	375.3	
107693	$W \to \mu\nu + 3$	e511_s765_s767_r1302_r1306	50 887	101.1	
107694	$W \to \mu\nu + 4$	e511_s765_s767_r1302_r1306	12 991	25.7	
107695	$W \to \mu\nu + 5$	e511_s765_s767_r1302_r1306	3498	7.0	
107701	$W \to \tau\nu + 1$	e511_s765_s767_r1302_r1306	254 753	1276.8	Alpgen/Jimmy
107702	$W \to \tau\nu + 2$	e511_s765_s767_r1302_r1306	188 446	376.6	
107703	$W \to \tau\nu + 3$	e511_s765_s767_r1302_r1306	50 472	100.8	
107704	$W \to \tau\nu + 4$	e511_s765_s767_r1302_r1306	12 996	25.7	
107705	$W \to \tau\nu + 5$	e511_s765_s767_r1302_r1306	3998	7.0	
107651	$Z \to ee + 1$	e529_s765_s767_r1302_r1306	63 440	126.5	Alpgen/Jimmy
107652	$Z \to ee + 2$	e529_s765_s767_r1302_r1306	19 497	38.2	
107653	$Z \to ee + 3$	e529_s765_s767_r1302_r1306	5499	10.6	
107654	$Z \to ee + 4$	e529_s765_s767_r1302_r1306	1499	2.6	
107655	$Z \to ee + 5$	e529_s765_s767_r1302_r1306	500	0.7	
107661	$Z \to \mu\mu + 1$	e529_s765_s767_r1302_r1306	62 996	126	Alpgen/Jimmy
107662	$Z \to \mu\mu + 2$	e529_s765_s767_r1302_r1306	18 993	37.6	
107663	$Z \to \mu\mu + 3$	e529_s765_s767_r1302_r1306	5497	10.5	
107664	$Z \to \mu\mu + 4$	e529_s765_s767_r1302_r1306	1499	2.7	
107665	$Z \to \mu\mu + 5$	e529_s765_s767_r1302_r1306	499	0.7	
107671	$Z \to \tau\tau + 1$	e529_s765_s767_r1302_r1306	63 481	126.2	Alpgen/Jimmy
107672	$Z \to \tau\tau + 2$	e529_s765_s767_r1302_r1306	19 492	38.3	
107673	$Z \to \tau\tau + 3$	e529_s765_s767_r1302_r1306	5497	10.5	
107674	$Z \to \tau\tau + 4$	e529_s765_s767_r1302_r1306	1499	2.7	
107675	$Z \to \tau\tau + 5$	e529_s765_s767_r1302_r1306	499	0.7	
105985	WW	e521_s765_s767_r1302_r1306	249 837	11.7	Herwig/Jimmy

Continued on next page

Table A.4 – continued from previous page

Dataset	Process	Simulation tag	Events	cross section/pb	Comments
105987	WZ	e521_s765_s767_r1302_r1306	249 830	3.5	Herwig/Jimmy
105986	ZZ	e521_s765_s767_r1302_r1306	249 725	0.98	Herwig/Jimmy
105200	$t\bar{t}$, no full had.	e510_s765_s767_r1302_r1306	924 434	80.2	MC@NLO/Herwig/Jimmy
105204	$t\bar{t}$, full had.	e540_s765_s767_r1302_r1306	149 899	64.0	MC@NLO/Herwig/Jimmy
105205	$t\bar{t}$	e552_s765_s767_r1302_r1306	199 891	58.2	AcerMC
105860	$t\bar{t}$	e540_s765_s767_r1302_r1306	199 882	79.1	PowHeg/Herwig/Jimmy
105861	$t\bar{t}$	e521_s765_s767_r1302_r1306	199 838	79.1	PowHeg/Pythia
105011	QCD, J2	e468_s766_s767_r1303_r1306	1 398 078	4.1×10^7	
105012	QCD, J3	e468_s766_s767_r1303_r1306	1 322 431	2.2×10^6	
105013	QCD, J4	e468_s766_s767_r1303_r1306	1 372 402	8.8×10^4	
105014	QCD, J5	e468_s766_s767_r1303_r1306	1 391 612	2.3×10^3	
105015	QCD, J6	e468_s766_s767_r1303_r1306	1 222 660	3.4×10^1	
	BC 1	s766_r1303	9300		
	BC 1	s766_r1394_r1303	9300		pile-up

Table A.4: MC samples for RPV studies ($\sqrt{s} = 7\,\text{TeV}$, full ATLAS detector simulation).

Appendix B

Details on the generic detector simulations

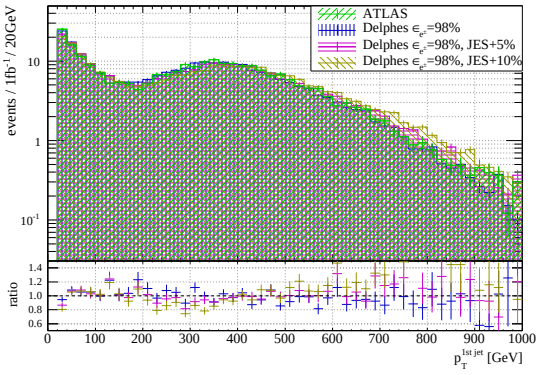

(a) Leading jet

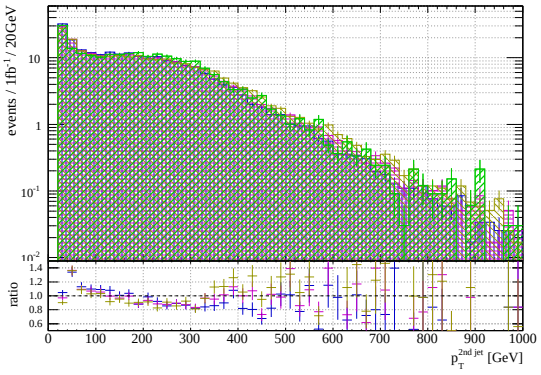

(b) 2nd jet

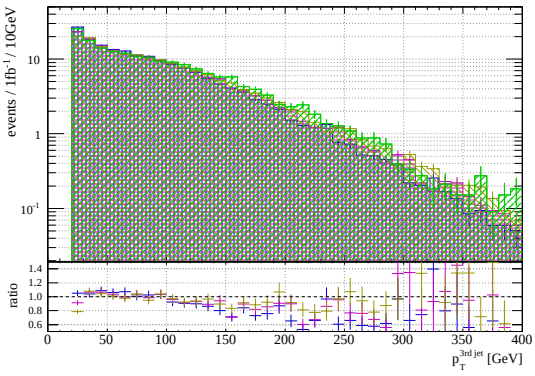

(c) 3rd jet

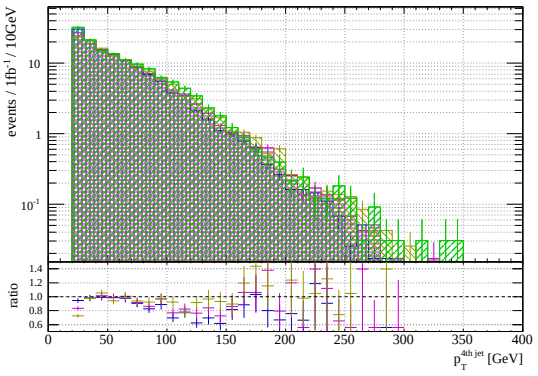

(d) 4th jet

Figure B.1: JES variation in Delphes.

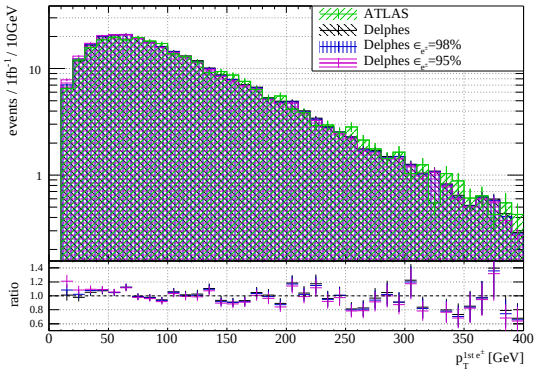

(a) Leading electron

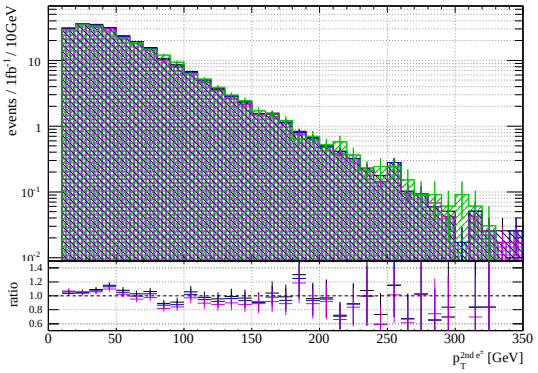

(b) 2nd electron

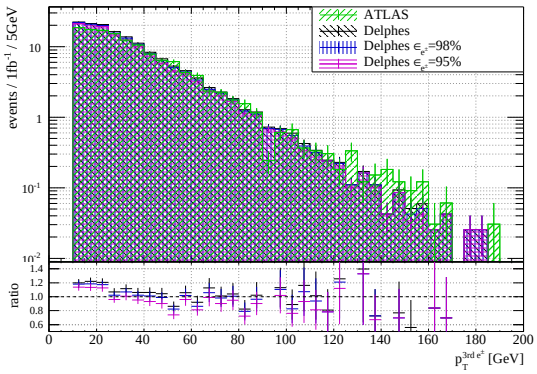

(c) 3rd electron

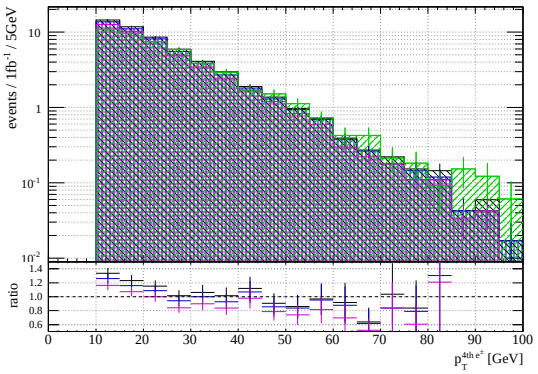

(d) 4th electron

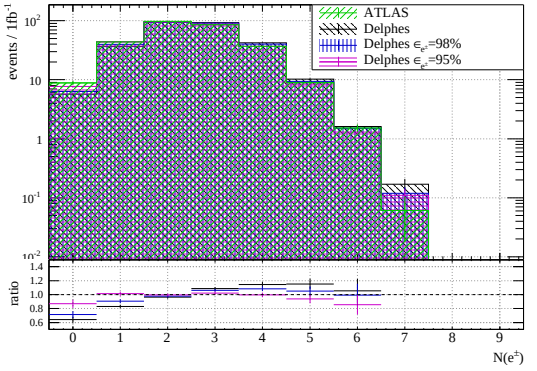

(e) Number of electrons

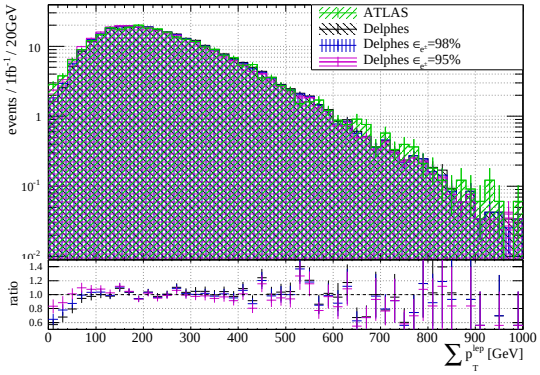

(f) $\sum_{\text{lep}} p_{\text{T}}$

Figure B.2: Delphes with reduced electron efficiency.

Appendix C

Details on PanTau studies

In this Appendix more details on the performance studies of PanTau will be given. At first the combination of the output of the likelihood classifier for different tau decay categories is discussed. The second section includes further plots of the energy dependency of PanTau ID variables.

C.1 Combination of Likelihood ratios for different classes

The output of the projective likelihood classifier in the TMVA toolkit is defined as

$$y = \frac{L_S}{L_S + L_B} \tag{C.1}$$

where

$$L_{\mathcal{C}} = \prod_k p_{\mathcal{C}k}(x_k), \mathcal{C} = S, B \text{ and } \int_{-\infty}^{\infty} p_{\mathcal{C}k}(x_k)\mathrm{d}x_k = 1 \tag{C.2}$$

i.e. the signal and background reference distributions $p_{\mathcal{C}k}(x_k)$ of the variable x_k are normalised individually. y can be interpreted as the probability for a candidate to be a true tau, if the a priori probabilities for signal and background are assumed to be equal. It can be turned into a logarithmic likelihood ratio with the help of the inverse sigmoid function logit(y) (*cf.* equation (4.14))

$$\mathrm{logit}(y) = -\ln\left(\frac{1}{y} - 1\right) = \ln\left(\frac{L_S}{L_B}\right) \tag{C.3}$$

According to Bayes' theorem the posterior probability for being signal can be calculated as

$$p = \frac{aL_S}{aL_S + bL_B} = \frac{aL_S}{aL_S + (1-a)L_B} = \frac{ay}{1 - a - y + 2ay} \tag{C.4}$$

where a is the a priori probability of the signal and $b = 1 - a$ the a priori probability of background (for a comprehensive introduction see *e.g.* [162]). By means of the inverse sigmoid transformation one gets a log-likelihood equivalent

$$\text{logit}(p) = \ln\left(\frac{a}{1-a}\frac{L_S}{L_B}\right) = \ln\left(\frac{a}{1-a}\right) + \ln\left(\frac{L_S}{L_B}\right) \tag{C.5}$$

i.e. the log-likelihood contribution of the a priori probability a can be interpreted as $\ln\left(\frac{a}{1-a}\right) = \text{logit}(a)$.

Empirically one can introduce another factor τ to give a relative weight to the a priori contribution

$$\text{logit}(a) \mapsto \tau \cdot \text{logit}(a): \quad \text{logit}(p) = \tau \cdot \text{logit}(a) + \ln\left(\frac{L_S}{L_B}\right) \tag{C.6}$$

For $\tau = 1$ the effect of using $\text{logit}(p)$ instead of $\ln\left(\frac{L_S}{L_B}\right)$ (or equivalently y) is very small. For larger values of τ the shift between the different classes gets important and one observes a significant improvement in the rejection. However, only the case $\tau = 1$ is mathematically fully valid in terms of a posterior probability.

Scaling all a priori probabilities a_k (where k denotes the reconstructed decay mode or class) by the same constant c (equivalent to rescaling the cross sections between $\text{Z} \to \tau\tau$, $\text{W} \to \tau\nu$ and QCD di-jet events) leads to a relative shift which is class dependent

$$a_k \mapsto c \cdot a_k: \quad \text{logit}(p) = \tau \ln\left(\frac{c \cdot a_k}{1 - c \cdot a_k}\right) + \cdot \ln\left(\frac{L_S}{L_B}\right) \tag{C.7}$$

However, the relative shift between different classes j and k is

$$\text{logit}(c \cdot a_j) - \text{logit}(c \cdot a_k) = \ln\left(\frac{a_1}{a_2}\right) + \ln\left(\frac{1 - c \cdot a_2}{1 - c \cdot a_1}\right) \tag{C.8}$$

$\ln\left(\frac{1-c\cdot a_2}{1-c\cdot a_1}\right)$ is usually very small, because the $c \cdot a_k$ are still small (besides maybe for one class), *i.e.* the relative shifts in the distributions of $\text{logit}(p)$ are simply $\ln\left(\frac{a_1}{a_2}\right)$ and therefore independent of c.

The a priori probabilities a_k itself strongly depend on the energy spectra of the considered signal and background samples. However, only the signal to background contributions of the classes relative to each other are important as equation (C.8) shows. Still we already observed a change in the classification of QCD jets with increasing energy in Figure 4.15b, because more charged and neutral particles are produced in the hadronisation with increasing energy. Even the tau candidates matched to true tau decays are classified differently (Figure 4.15a), presumably because of energy dependencies of the track reconstruction efficiency and photon conversions.

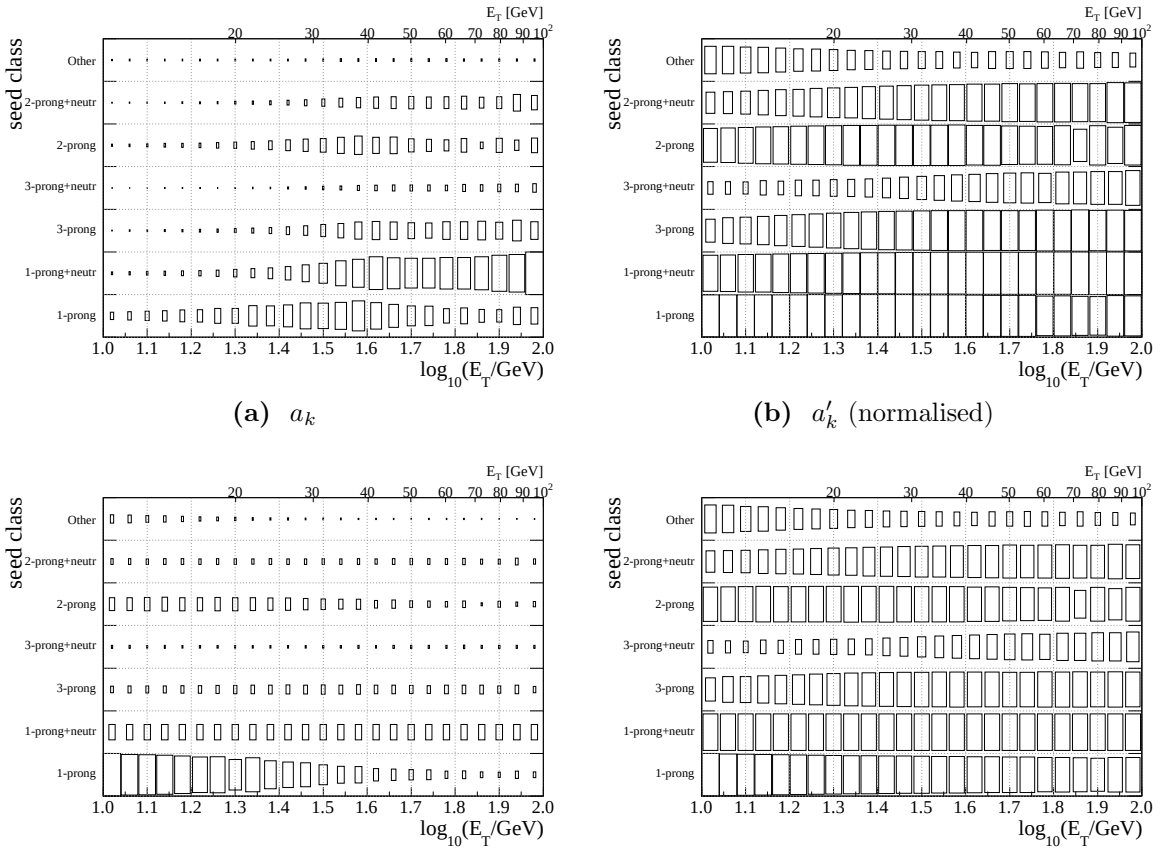

(a) a_k **(b)** a'_k (normalised)

(c) a_k, scaled to "1-prong with neutrals" **(d)** a'_k, scaled to "1-prong with neutrals"

Figure C.1: Dependency of the a priori probabilities in PanTau for taus in a certain reconstructed class on the transverse energy E_{T}.

To get a better understanding of the energy dependency of the a priori probabilities and their relative magnitudes they are visualised in Figure C.1 in four different ways. For Figure C.1a the probabilities are calculated as

$$a_k(E_{\mathrm{T}}) = \frac{N_k^{\mathrm{tau}}(E_{\mathrm{T}})}{N_k^{\text{QCD jet}}(E_{\mathrm{T}}) + N_k^{\mathrm{tau}}(E_{\mathrm{T}})} \tag{C.9}$$

where the number of QCD jets and truth matched taus are weighted by the cross sections of the QCD jet, $\mathrm{W} \to \tau\nu$ and $\mathrm{Z} \to \tau\tau$ events. It is clearly visible how the a priori probabilities increase with the energy, which is mainly an effect of the steeply falling energy spectrum of the QCD jet samples used here. To remove this effect all probabilities have been scaled to the probability of the "1-prong with neutrals" class, which has the largest fraction of true taus of all classes (*cf.* Figure 4.15a), in Figure C.1c. The "other" class gets more background dominated with increasing energy, because the QCD jets contain more particles. The term $N_k^{\mathrm{tau}}(E_{\mathrm{T}})$ in the denominator can be neglected here because in all cases $N_k^{\mathrm{tau}}(E_{\mathrm{T}}) \ll N_k^{\text{QCD jet}}(E_{\mathrm{T}})$ holds. In the following formula the explicit E_{T} dependency is omitted for the sake of conciseness. A normalised version of

the probabilities is shown in Figure C.1b, using

$$a'_k = \frac{N_k^{\text{tau}}/N^{\text{tau}}}{N_k^{\text{QCD jet}}/N^{\text{QCD jet}} + N_k^{\text{tau}}/N^{\text{tau}}} \tag{C.10}$$

which is equivalent to assuming identical numbers of QCD jets and taus in each energy bin over all classes. This completely removes the dependency on the energy spectra of the samples used. However, this also increases the influence of the number of taus in the denominator and therefore reduces the hierarchy between the different classes as it neglects the fact that in all classes in general more QCD jets exist than true taus. The scaling to the "1-prong with neutrals" class (Figure C.1d) gives only minor changes for a'_k and is only shown for completeness here.

In principle the above procedure allows to derive energy dependent a priori probabilities $a_k(E_{\text{T}})$ and to use them in equation (C.5). However, this may introduce additional systematic uncertainties and we will only show results with fixed a_k in following. The a priori probabilities are just separated in two energy regimes corresponding to the energy ranges of the used in the likelihood method, *cf.* Table 4.4. Another method to combine the classifier outputs of different classes would be the calculation of a new likelihood ratio on top of the output for each class, which takes the a priori probabilities into account. This new test statistics would also include information about the different separation power between signal and background in the reconstruction classes and should therefore further improve the performance of the combined result. It also has the advantage to be applicable to other classifiers, like Boosted Decision Trees, whose outputs are not easily interpretable in terms of probabilities.

C.2 Energy dependency of PanTau variables

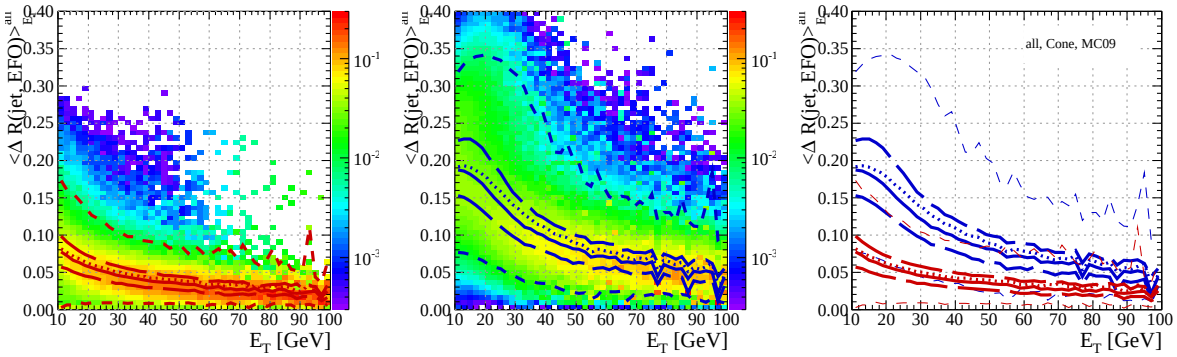

(a) all categories

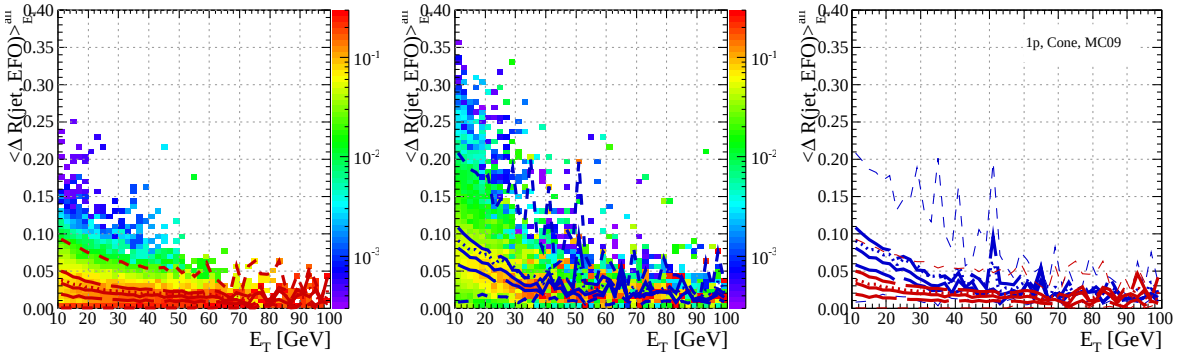

(b) 1-prong

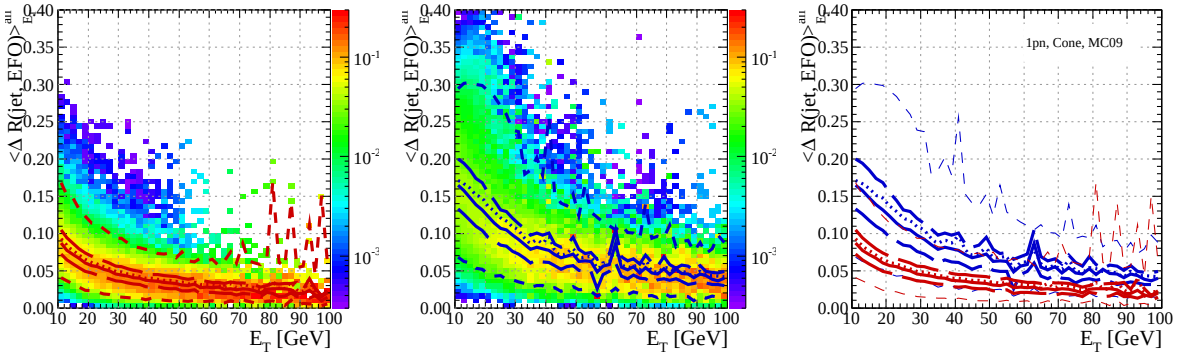

(c) 1-prong+neutrals

Figure C.2: Energy dependency of the first moment $\langle \Delta R(\text{jet}, \text{EFO}) \rangle^{\text{all}}_{E_{\text{T}}}$ in $\Delta R(\text{jet}, \text{EFO})$ for all energy flow objects. The left graph includes tau candidates with a match to Monte Carlo true taus in $\text{Z} \rightarrow \tau\tau$ and $\text{W} \rightarrow \tau\nu$ events and the middle graph for tau candidates in QCD jet events. Both distributions are normalised column-wise in the energy bins and the color coding corresponds to the fraction of tau candidates.

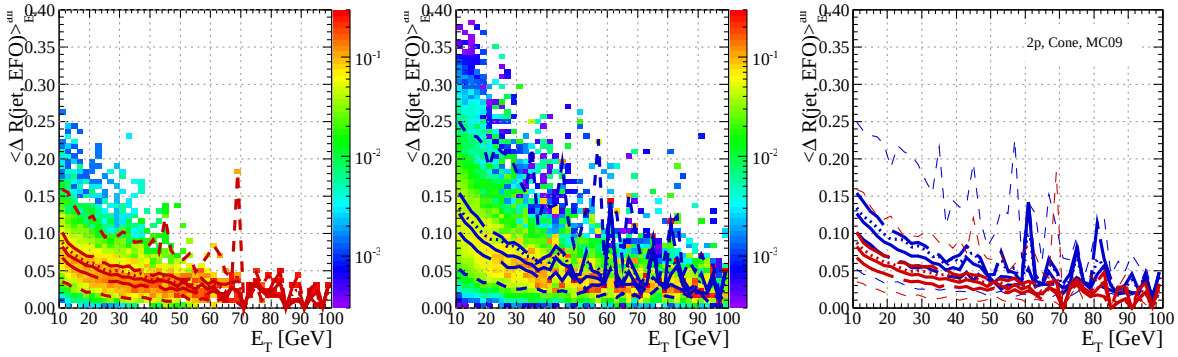

(a) 2-prong

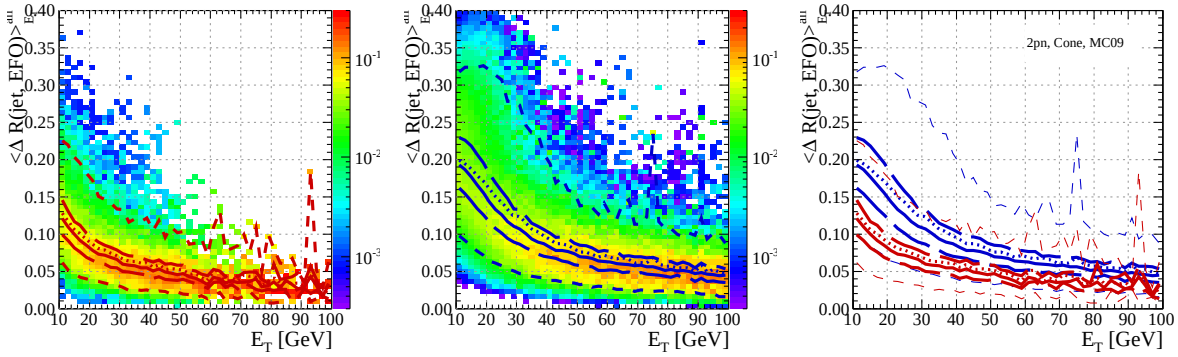

(b) 2-prong+neutrals

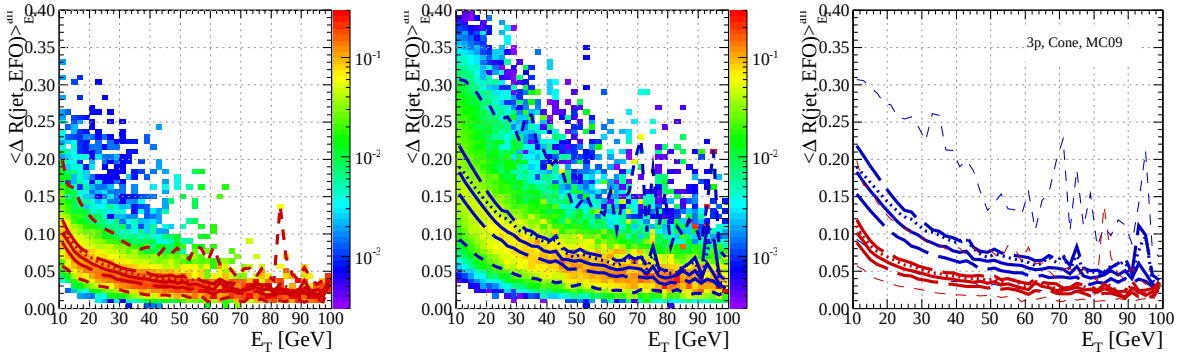

(c) 3-prong

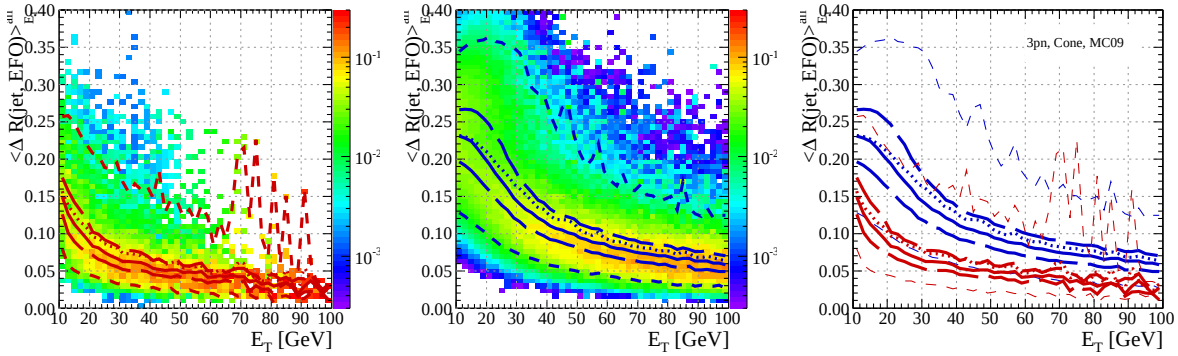

(d) 3-prong+neutrals

Figure C.3: Energy dependency of the first moment $\langle \Delta R(\text{jet}, \text{EFO}) \rangle^{\text{all}}_{E_T}$.

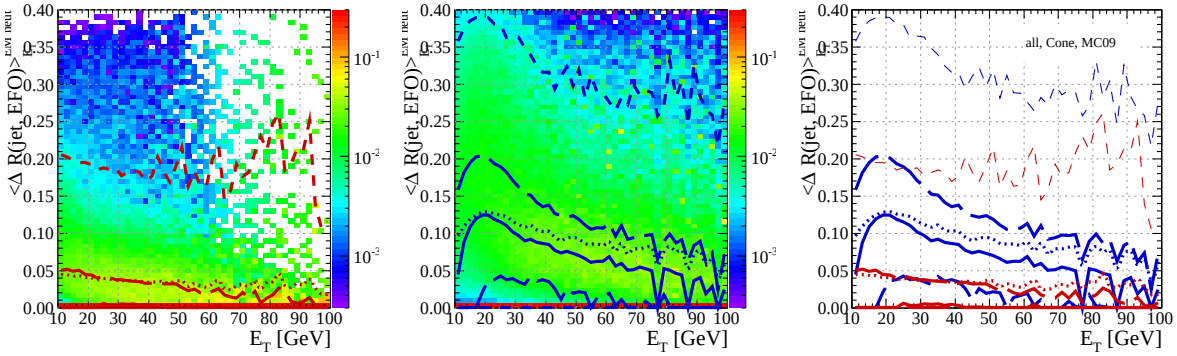

(a) all categories

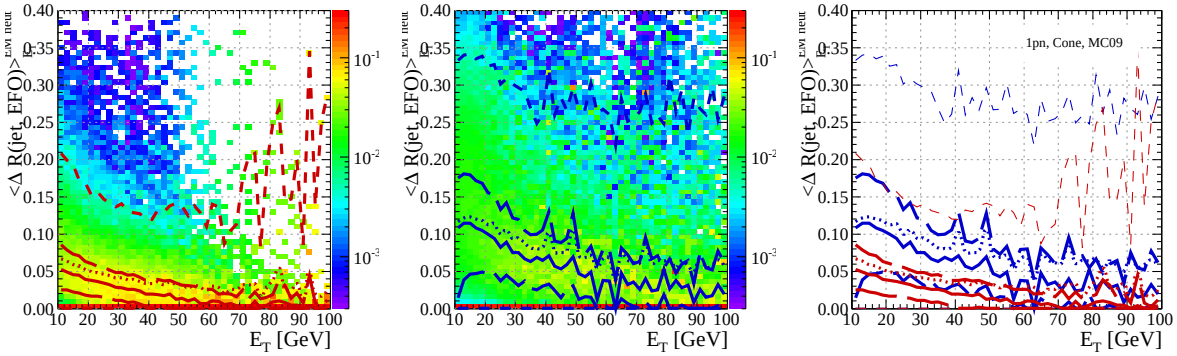

(b) 1-prong+neutrals

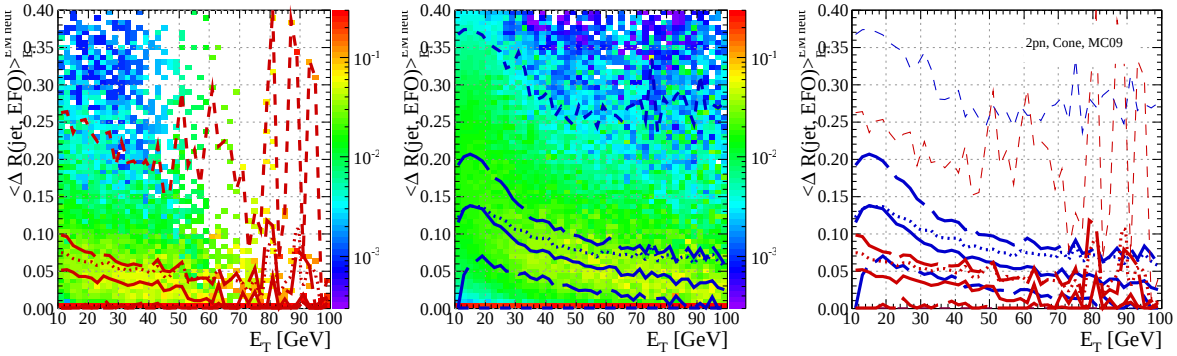

(c) 2-prong+neutrals

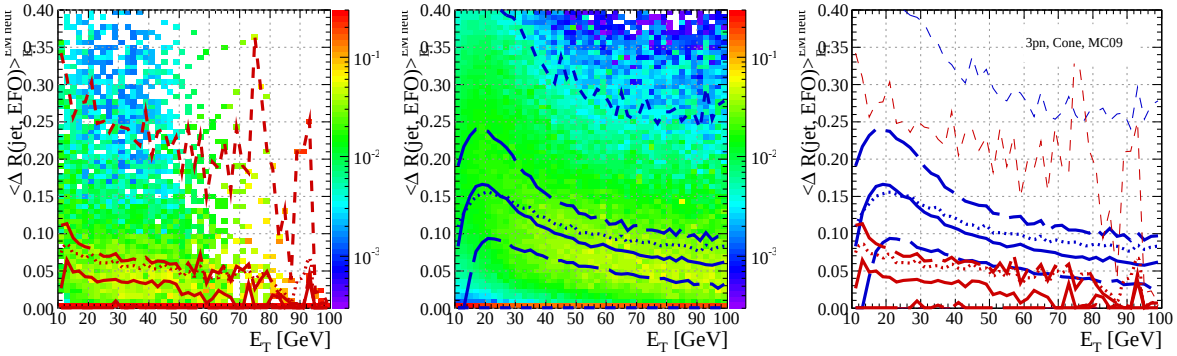

(d) 3-prong+neutrals

Figure C.4: Energy dependency of $\langle\Delta R(\text{jet}, \text{EFO})\rangle^{\text{had}}_{E_T}$.

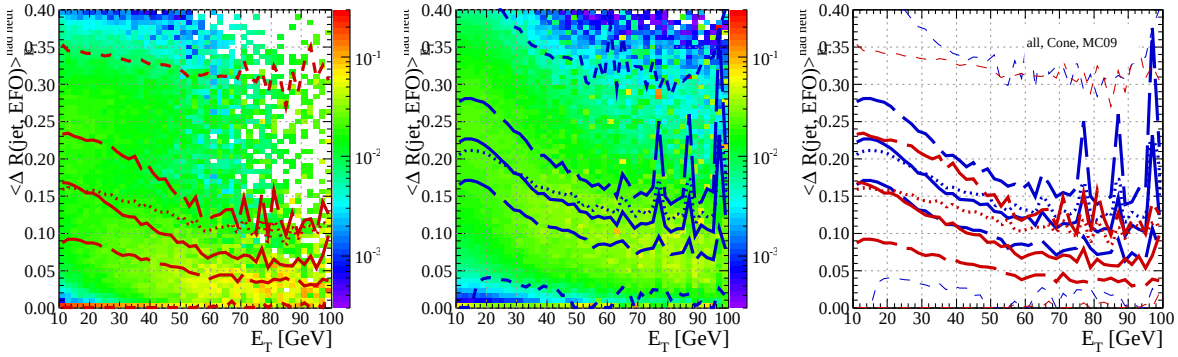

(a) all categories

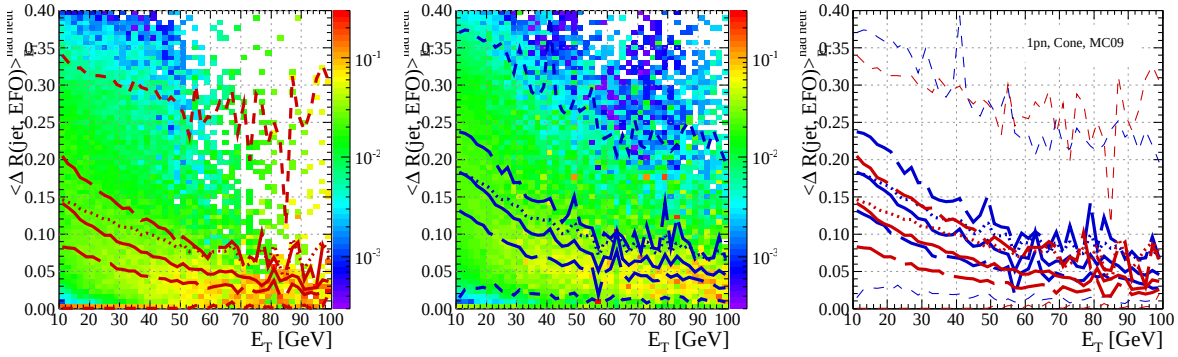

(b) 1-prong+neutrals

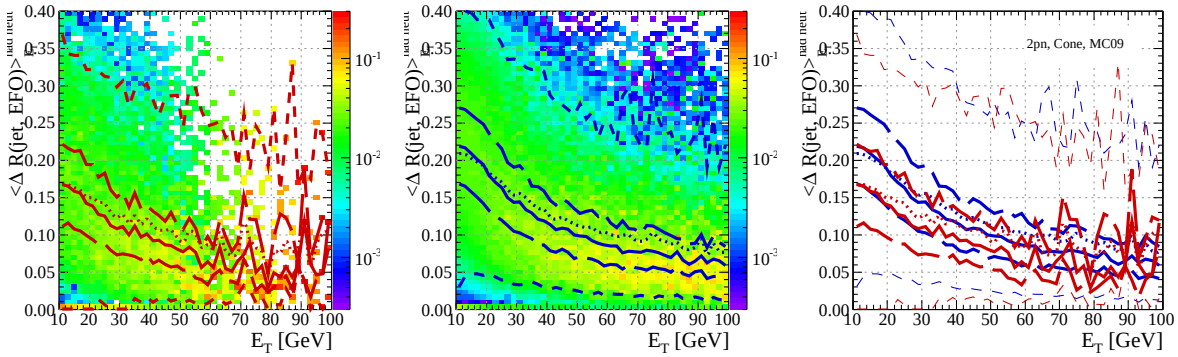

(c) 2-prong+neutrals

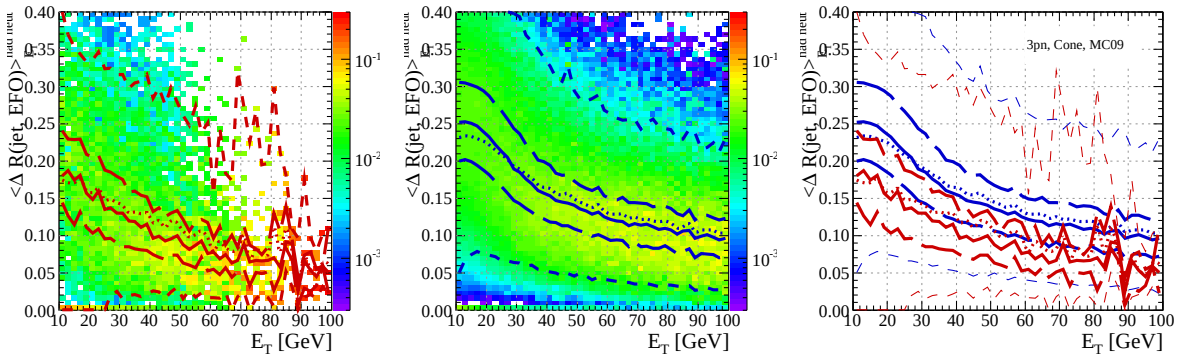

(d) 3-prong+neutrals

Figure C.5: Energy dependency of $\langle \Delta R(\text{jet}, \text{EFO}) \rangle^{\text{EM}}_{E_{\text{T}}}$.

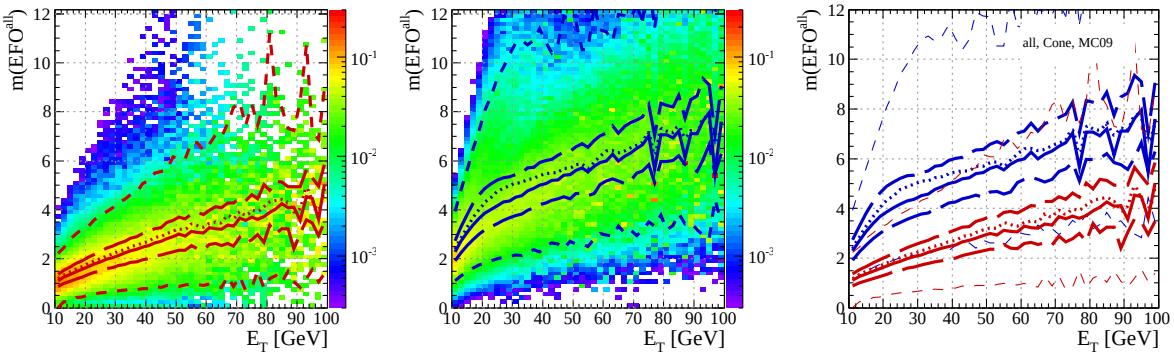

(a) all categories

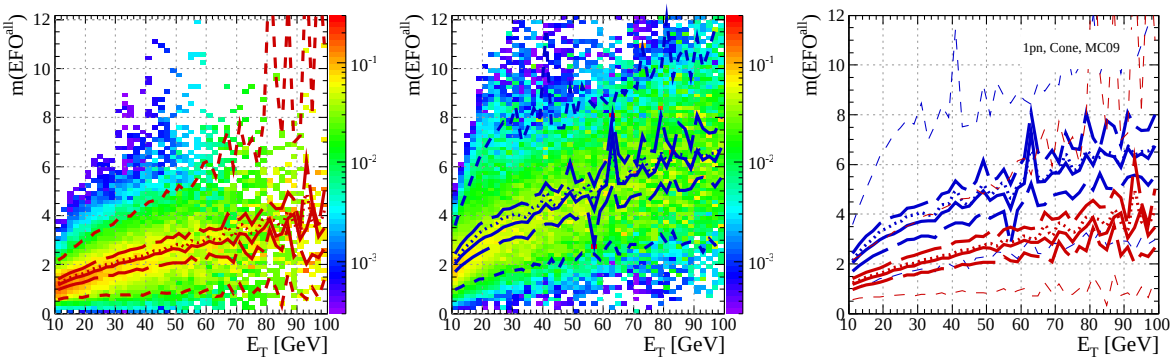

(b) 1-prong+neutrals

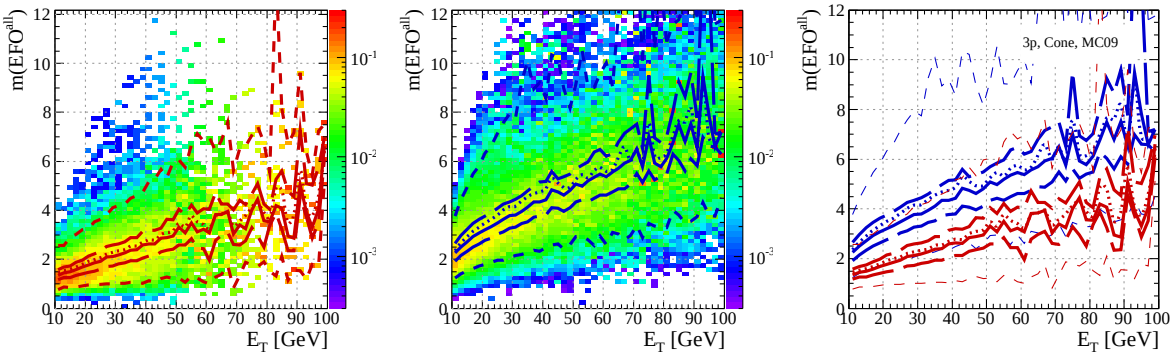

(c) 3-prong

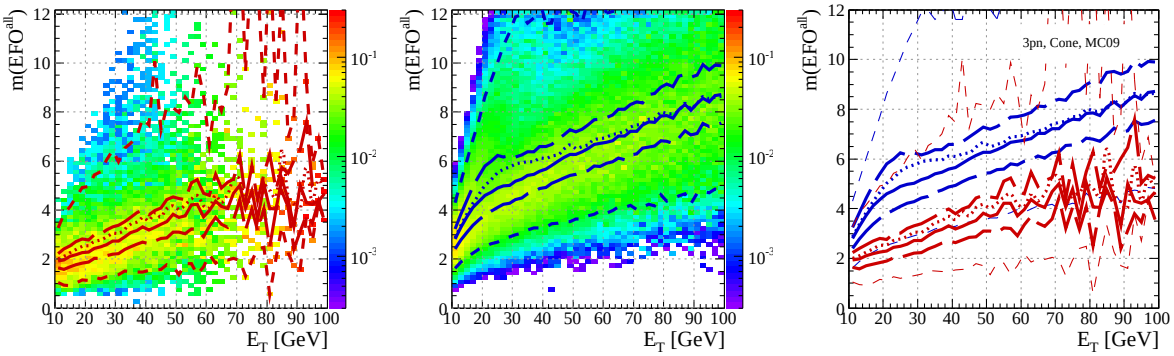

(d) 3-prong+neutrals

Figure C.6: Energy dependency of the invariant mass of all energy flow objects.

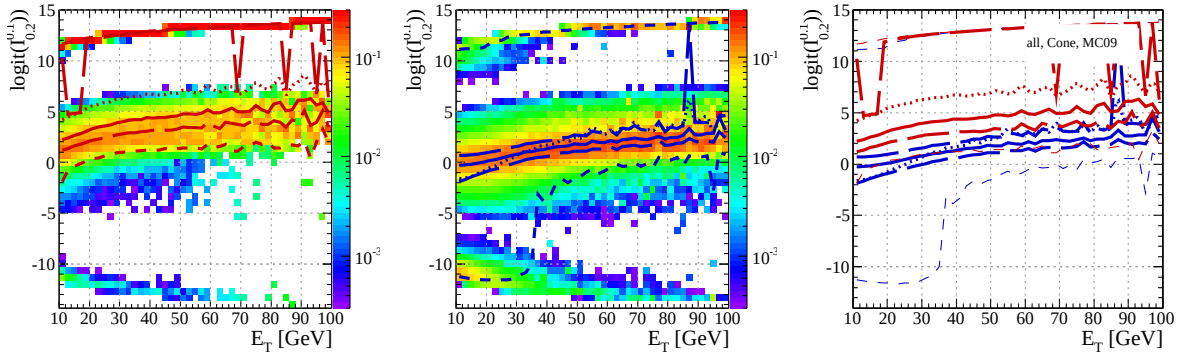

(a) logit($I_{0.2}^{0.1}$), all categories

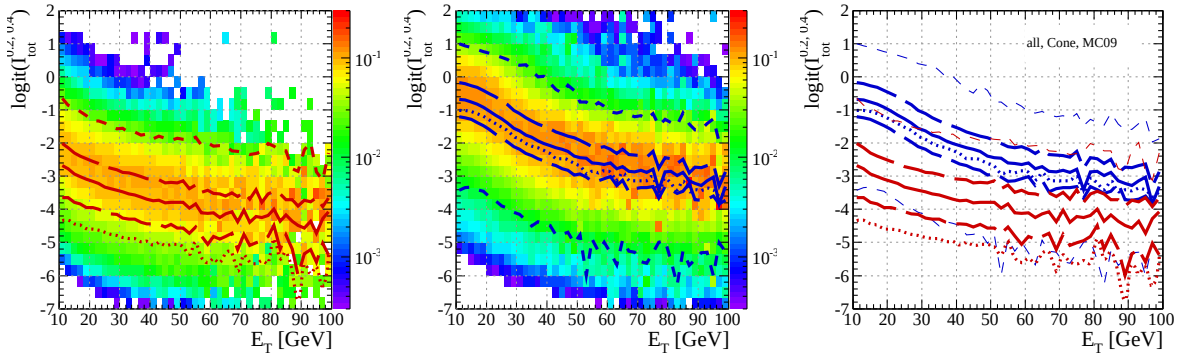

(b) logit($I_{\mathrm{tot}}^{0.2;0.4}$), all categories

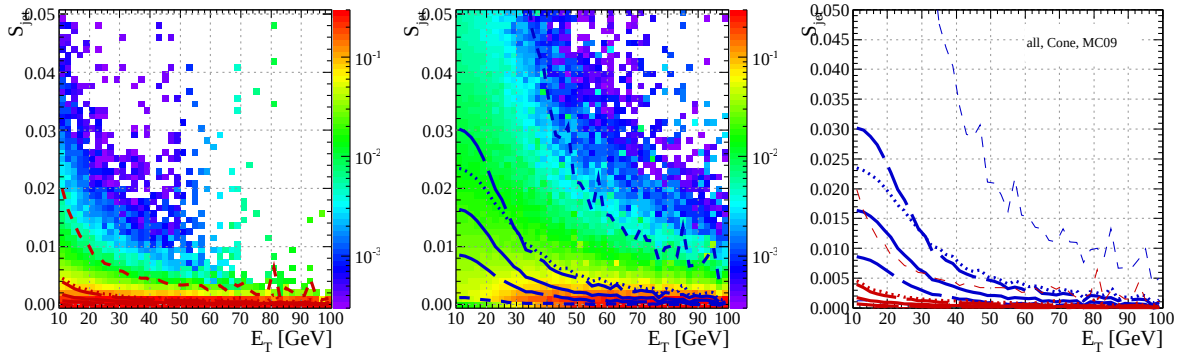

(c) jet sphericity S_{jet}, all categories

Figure C.7: Energy dependency of the isolation variables and the jet sphericity S_{jet}.

C.3 Data – Monte Carlo comparison of energy flow quantities

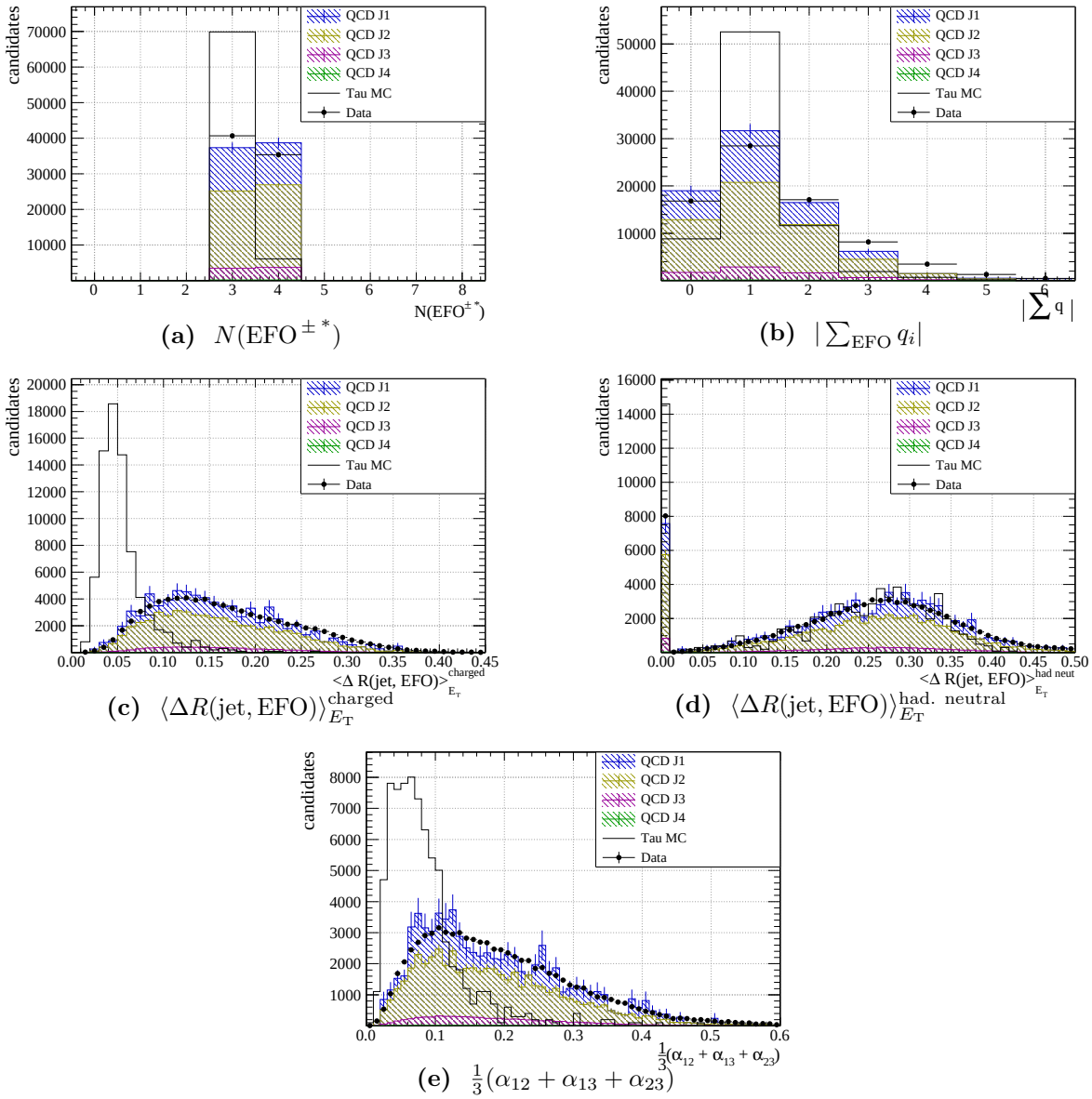

(a) $N(\mathrm{EFO}^{\pm *})$ (b) $|\sum_{\mathrm{EFO}} q_i|$

(c) $\langle \Delta R(\mathrm{jet}, \mathrm{EFO}) \rangle^{\mathrm{charged}}_{E_{\mathrm{T}}}$ (d) $\langle \Delta R(\mathrm{jet}, \mathrm{EFO}) \rangle^{\mathrm{had.\ neutral}}_{E_{\mathrm{T}}}$

(e) $\frac{1}{3}(\alpha_{12} + \alpha_{13} + \alpha_{23})$

Figure C.8: Distribution of the identification variables for the "3-prong" class in the transverse momentum range $10\,\mathrm{GeV} < p_{\mathrm{T}} < 25\,\mathrm{GeV}$. The stacked histograms correspond to the different QCD di-jet samples and the black dots are measured data. Monte Carlo samples have been scaled to the integral of the data. The black line shows the distribution for $\mathrm{W} \rightarrow \tau\nu$ and $\mathrm{Z} \rightarrow \tau\tau$ events for comparison.

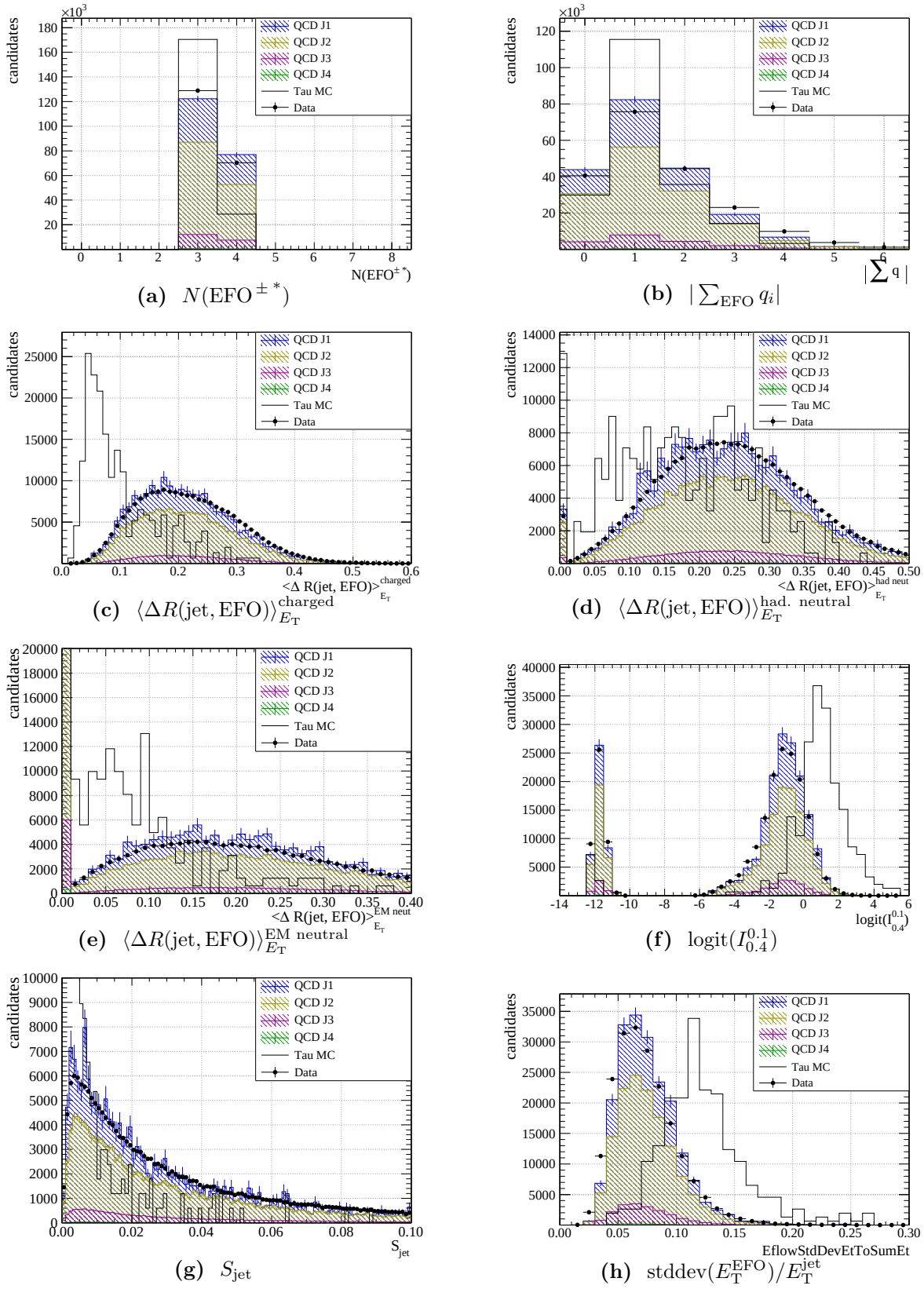

(a) $N(\mathrm{EFO}^{\pm *})$ **(b)** $|\sum_{\mathrm{EFO}} q_i|$

(c) $\langle \Delta R(\mathrm{jet}, \mathrm{EFO}) \rangle^{\mathrm{charged}}_{E_\mathrm{T}}$ **(d)** $\langle \Delta R(\mathrm{jet}, \mathrm{EFO}) \rangle^{\mathrm{had.\ neutral}}_{E_\mathrm{T}}$

(e) $\langle \Delta R(\mathrm{jet}, \mathrm{EFO}) \rangle^{\mathrm{EM\ neutral}}_{E_\mathrm{T}}$ **(f)** $\mathrm{logit}(I^{0.1}_{0.4})$

(g) S_{jet} **(h)** $\mathrm{stddev}(E^{\mathrm{EFO}}_{\mathrm{T}})/E^{\mathrm{jet}}_{\mathrm{T}}$

Figure C.9: Distribution of the identification variables for the "3-prong+neutral" class in the transverse momentum range $10\,\mathrm{GeV} < p_\mathrm{T} < 25\,\mathrm{GeV}$. The stacked histograms correspond to the different QCD di-jet samples and the black dots are measured data. Monte Carlo samples have been scaled to the integral of the data. The black line shows the distribution for $\mathrm{W} \to \tau\nu$ and $\mathrm{Z} \to \tau\tau$ events for comparison.

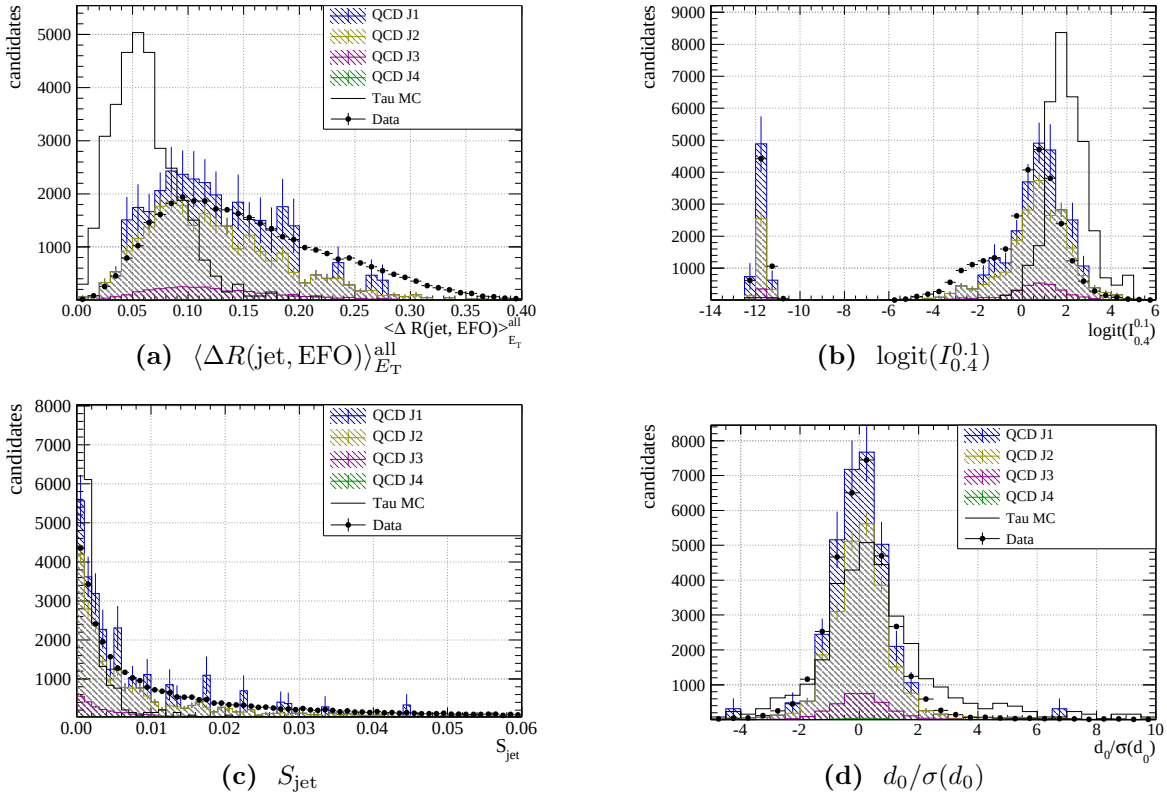

(a) $\langle \Delta R(\text{jet}, \text{EFO}) \rangle^{\text{all}}_{E_{\text{T}}}$ **(b)** $\text{logit}(I^{0.1}_{0.4})$

(c) S_{jet} **(d)** $d_0/\sigma(d_0)$

Figure C.10: Distribution of the identification variables for the "2-prong" class in the transverse momentum range $10\,\text{GeV} < p_{\text{T}} < 25\,\text{GeV}$. The stacked histograms correspond to the different QCD di-jet samples and the black dots are measured data. Monte Carlo samples have been scaled to the integral of the data. The black line shows the distribution for $\text{W} \rightarrow \tau\nu$ and $\text{Z} \rightarrow \tau\tau$ events for comparison.

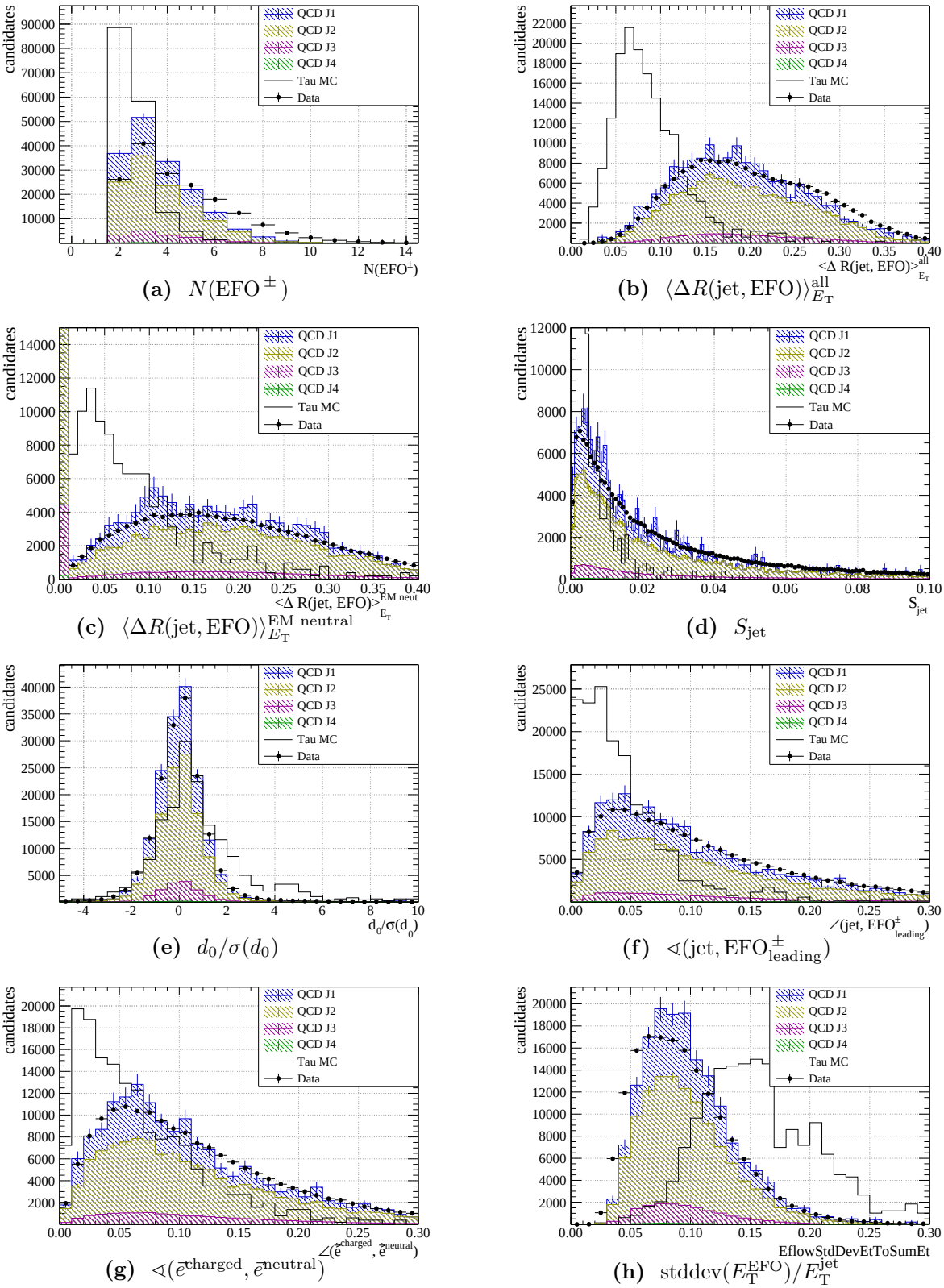

(a) $N(\mathrm{EFO}^{\pm})$ **(b)** $\langle \Delta R(\mathrm{jet}, \mathrm{EFO}) \rangle^{\mathrm{all}}_{E_{\mathrm{T}}}$

(c) $\langle \Delta R(\mathrm{jet}, \mathrm{EFO}) \rangle^{\mathrm{EM\ neutral}}_{E_{\mathrm{T}}}$ **(d)** S_{jet}

(e) $d_0/\sigma(d_0)$ **(f)** $\sphericalangle(\mathrm{jet}, \mathrm{EFO}^{\pm}_{\mathrm{leading}})$

(g) $\sphericalangle(\vec{e}^{\,\mathrm{charged}}, \vec{e}^{\,\mathrm{neutral}})$ **(h)** $\mathrm{stddev}(E_{\mathrm{T}}^{\mathrm{EFO}})/E_{\mathrm{T}}^{\mathrm{jet}}$

Figure C.11: Distribution of the identification variables for the "2-prong+neutral" class in the transverse momentum range $10\,\mathrm{GeV} < p_{\mathrm{T}} < 25\,\mathrm{GeV}$. The stacked histograms correspond to the different QCD di-jet samples and the black dots are measured data. Monte Carlo samples have been scaled to the integral of the data. The black line shows the distribution for $\mathrm{W} \to \tau\nu$ and $\mathrm{Z} \to \tau\tau$ events for comparison.

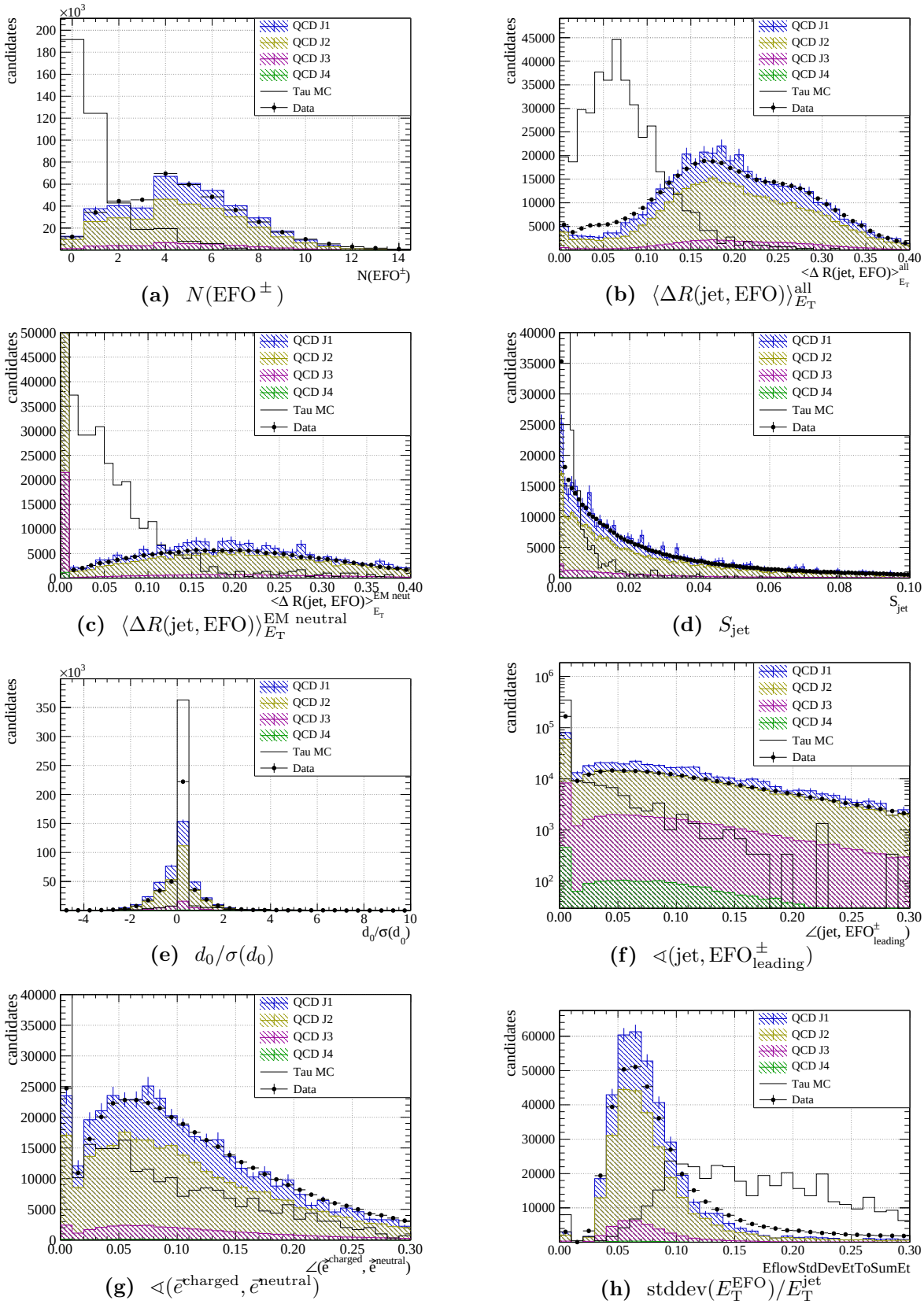

(a) $N(\mathrm{EFO}^{\pm})$ **(b)** $\langle \Delta R(\mathrm{jet}, \mathrm{EFO}) \rangle^{\mathrm{all}}_{E_{\mathrm{T}}}$

(c) $\langle \Delta R(\mathrm{jet}, \mathrm{EFO}) \rangle^{\mathrm{EM\ neutral}}_{E_{\mathrm{T}}}$ **(d)** S_{jet}

(e) $d_0/\sigma(d_0)$ **(f)** $\sphericalangle(\mathrm{jet}, \mathrm{EFO}^{\pm}_{\mathrm{leading}})$

(g) $\sphericalangle(\vec{e}^{\,\mathrm{charged}}, \vec{e}^{\,\mathrm{neutral}})$ **(h)** $\mathrm{stddev}(E_{\mathrm{T}}^{\mathrm{EFO}})/E_{\mathrm{T}}^{\mathrm{jet}}$

Figure C.12: Distribution of the identification variables for the "other" class in the transverse momentum range $10\,\mathrm{GeV} < p_{\mathrm{T}} < 25\,\mathrm{GeV}$. The stacked histograms correspond to the different QCD di-jet samples and the black dots are measured data. Monte Carlo samples have been scaled to the integral of the data. The black line shows the distribution for $\mathrm{W} \rightarrow \tau\nu$ and $\mathrm{Z} \rightarrow \tau\tau$ events for comparison.

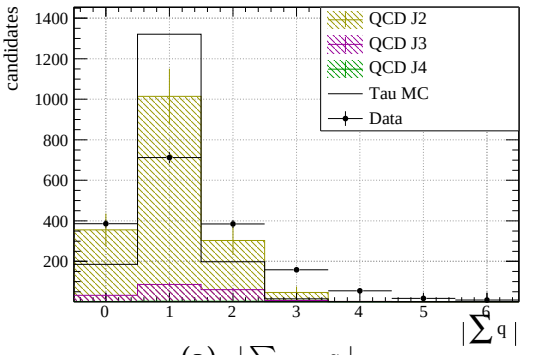

(a) $|\sum_{\mathrm{EFO}} q_i|$

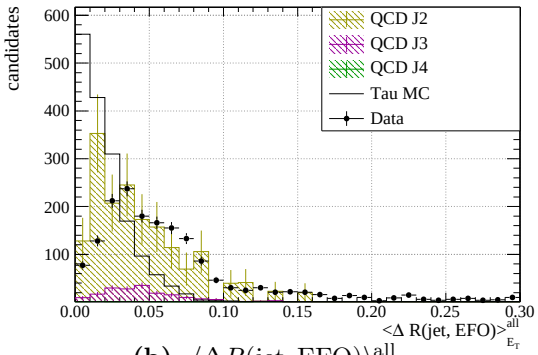

(b) $\langle \Delta R(\mathrm{jet}, \mathrm{EFO}) \rangle^{\mathrm{all}}_{E_{\mathrm{T}}}$

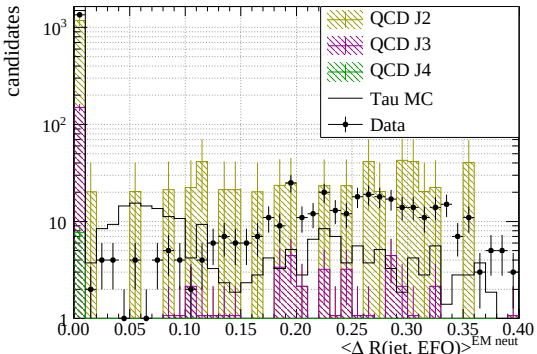

(c) $\langle \Delta R(\mathrm{jet}, \mathrm{EFO}) \rangle^{\mathrm{EM\ neutral}}_{E_{\mathrm{T}}}$

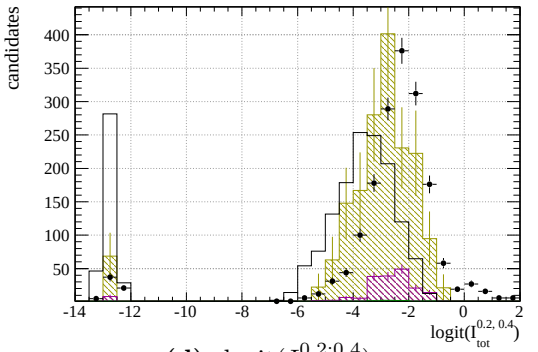

(d) $\mathrm{logit}(I_{\mathrm{tot}}^{0.2;0.4})$

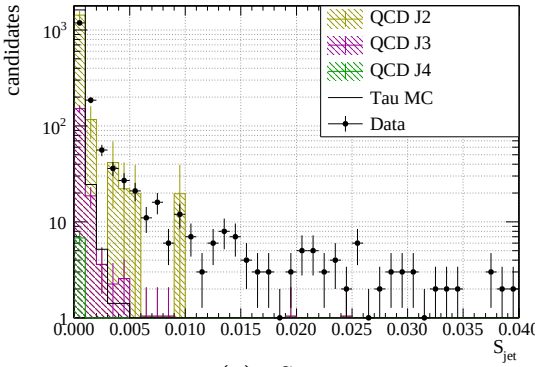

(e) S_{jet}

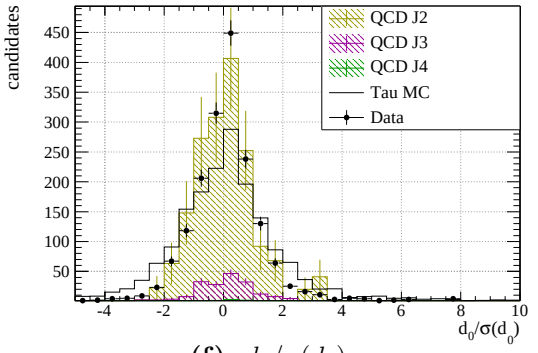

(f) $d_0/\sigma(d_0)$

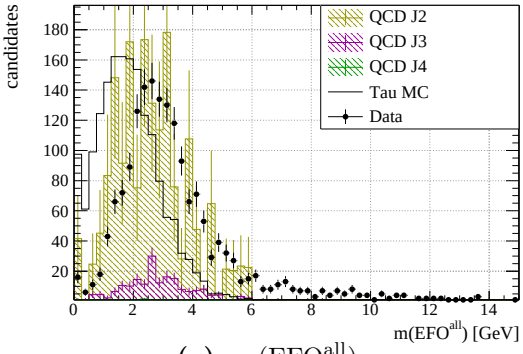

(g) $m(\mathrm{EFO}^{\mathrm{all}})$

Figure C.13: Distribution of the identification variables for the "1-prong" class in the transverse momentum range 25 GeV $< p_{\mathrm{T}} <$ 50 GeV. The stacked histograms correspond to the different QCD di-jet samples and the black dots are measured data. Monte Carlo samples have been scaled to the integral of the data. The black line shows the distribution for $\mathrm{W} \rightarrow \tau\nu$ and $\mathrm{Z} \rightarrow \tau\tau$ events for comparison.

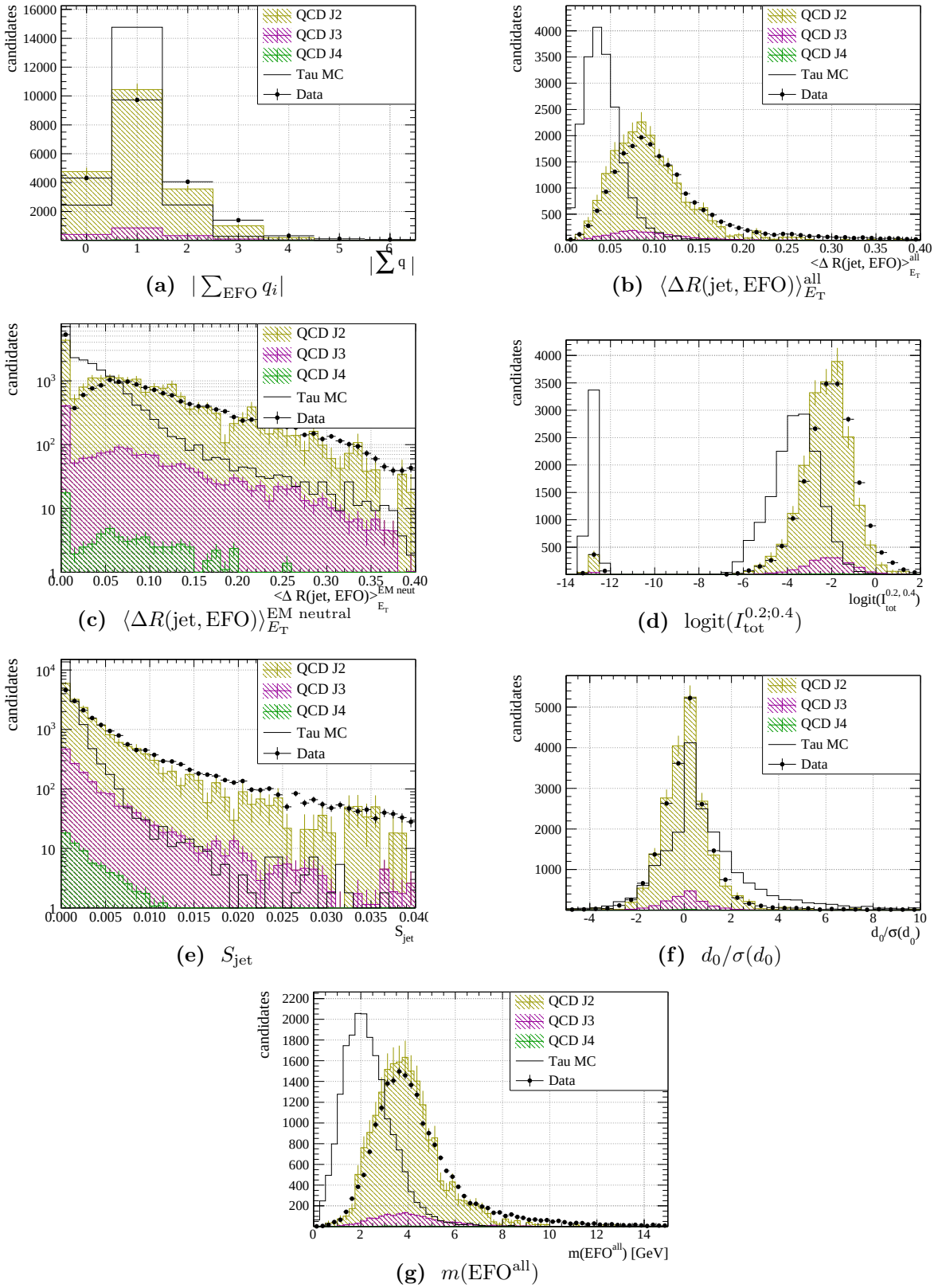

(a) $|\sum_{\mathrm{EFO}} q_i|$ **(b)** $\langle \Delta R(\mathrm{jet}, \mathrm{EFO}) \rangle^{\mathrm{all}}_{E_{\mathrm{T}}}$

(c) $\langle \Delta R(\mathrm{jet}, \mathrm{EFO}) \rangle^{\mathrm{EM\ neutral}}_{E_{\mathrm{T}}}$ **(d)** $\mathrm{logit}(I^{0.2;0.4}_{\mathrm{tot}})$

(e) S_{jet} **(f)** $d_0/\sigma(d_0)$

(g) $m(\mathrm{EFO}^{\mathrm{all}})$

Figure C.14: Distribution of the identification variables for the "1-prong+neutrals" class in the transverse momentum range $25\,\mathrm{GeV} < p_{\mathrm{T}} < 50\,\mathrm{GeV}$. The stacked histograms correspond to the different QCD di-jet samples and the black dots are measured data. Monte Carlo samples have been scaled to the integral of the data. The black line shows the distribution for $\mathrm{W} \to \tau\nu$ and $\mathrm{Z} \to \tau\tau$ events for comparison.

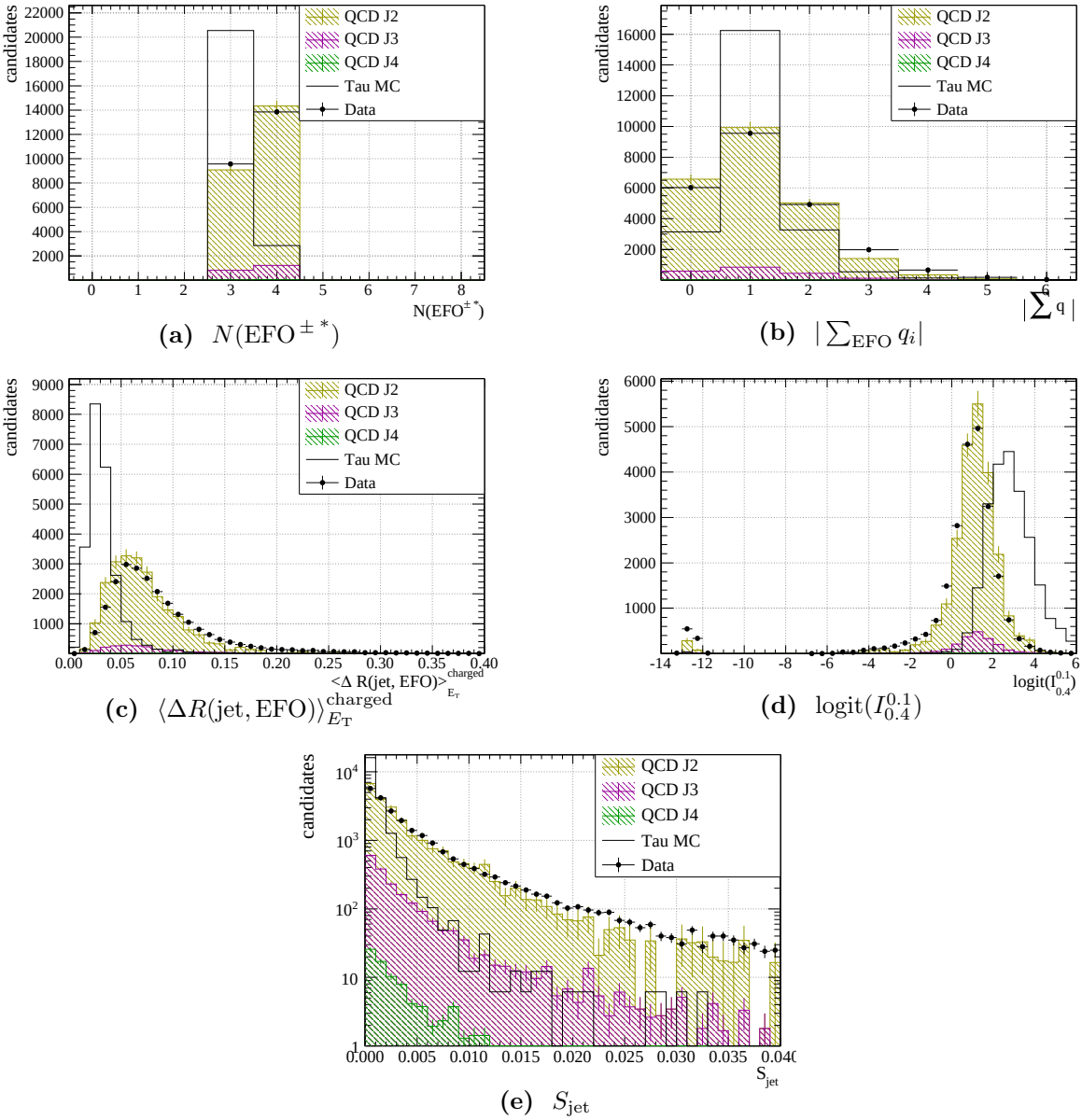

(a) $N(\mathrm{EFO}^{\pm *})$ **(b)** $|\sum_{\mathrm{EFO}} q_i|$

(c) $\langle \Delta R(\mathrm{jet}, \mathrm{EFO}) \rangle^{\mathrm{charged}}_{E_{\mathrm{T}}}$ **(d)** $\mathrm{logit}(I^{0.1}_{0.4})$

(e) S_{jet}

Figure C.15: Distribution of the identification variables for the "3-prong" class in the transverse momentum range $25\,\mathrm{GeV} < p_{\mathrm{T}} < 50\,\mathrm{GeV}$. The stacked histograms correspond to the different QCD di-jet samples and the black dots are measured data. Monte Carlo samples have been scaled to the integral of the data. The black line shows the distribution for $\mathrm{W} \to \tau\nu$ and $\mathrm{Z} \to \tau\tau$ events for comparison.

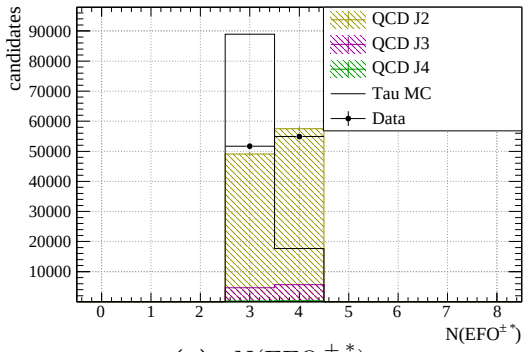

(a) $N(\mathrm{EFO}^{\pm *})$

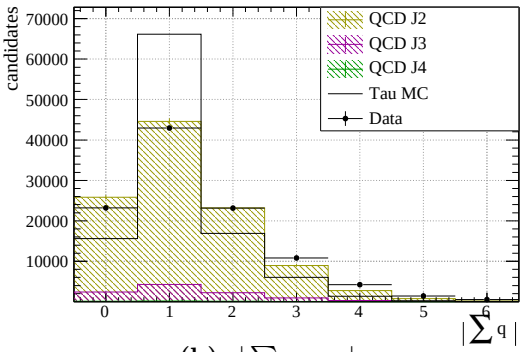

(b) $|\sum_{\mathrm{EFO}} q_i|$

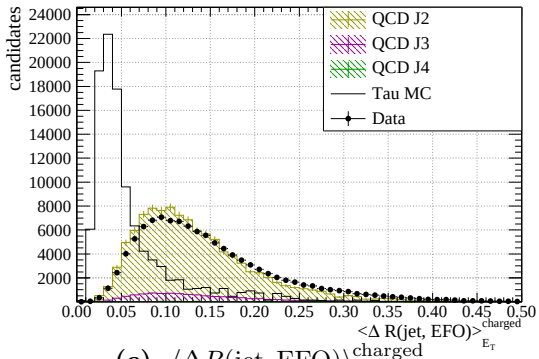

(c) $\langle \Delta R(\mathrm{jet}, \mathrm{EFO}) \rangle^{\mathrm{charged}}_{E_{\mathrm{T}}}$

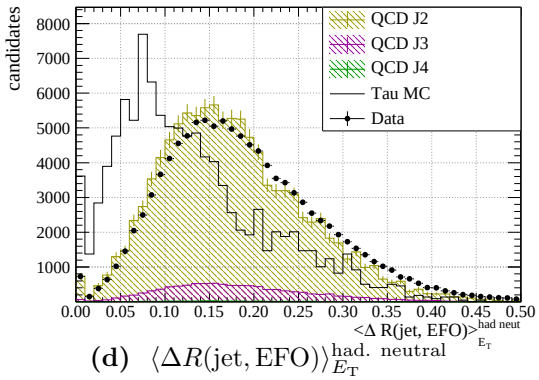

(d) $\langle \Delta R(\mathrm{jet}, \mathrm{EFO}) \rangle^{\mathrm{had.\ neutral}}_{E_{\mathrm{T}}}$

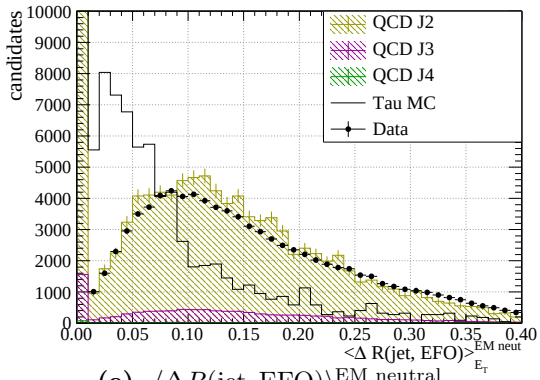

(e) $\langle \Delta R(\mathrm{jet}, \mathrm{EFO}) \rangle^{\mathrm{EM\ neutral}}_{E_{\mathrm{T}}}$

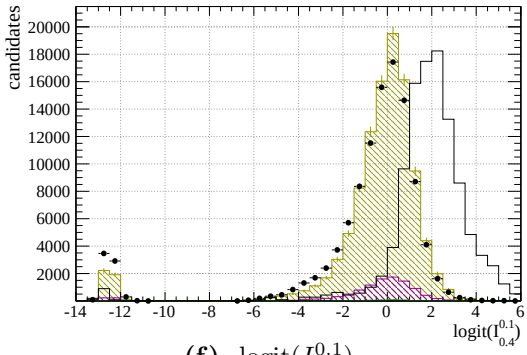

(f) $\mathrm{logit}(I^{0.1}_{0.4})$

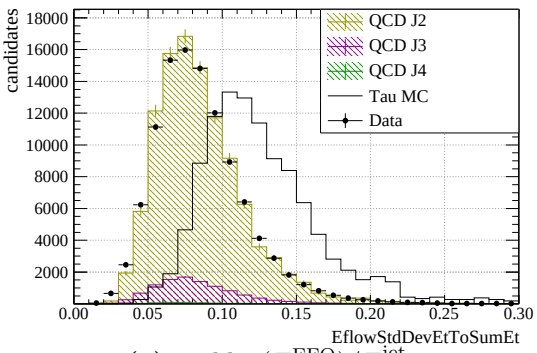

(g) $\mathrm{stddev}(E_{\mathrm{T}}^{\mathrm{EFO}})/E_{\mathrm{T}}^{\mathrm{jet}}$

Figure C.16: Distribution of the identification variables for the "3-prong+neutral" class in the transverse momentum range $25\,\mathrm{GeV} < p_{\mathrm{T}} < 50\,\mathrm{GeV}$. The stacked histograms correspond to the different QCD di-jet samples and the black dots are measured data. Monte Carlo samples have been scaled to the integral of the data. The black line shows the distribution for $\mathrm{W} \to \tau\nu$ and $\mathrm{Z} \to \tau\tau$ events for comparison.

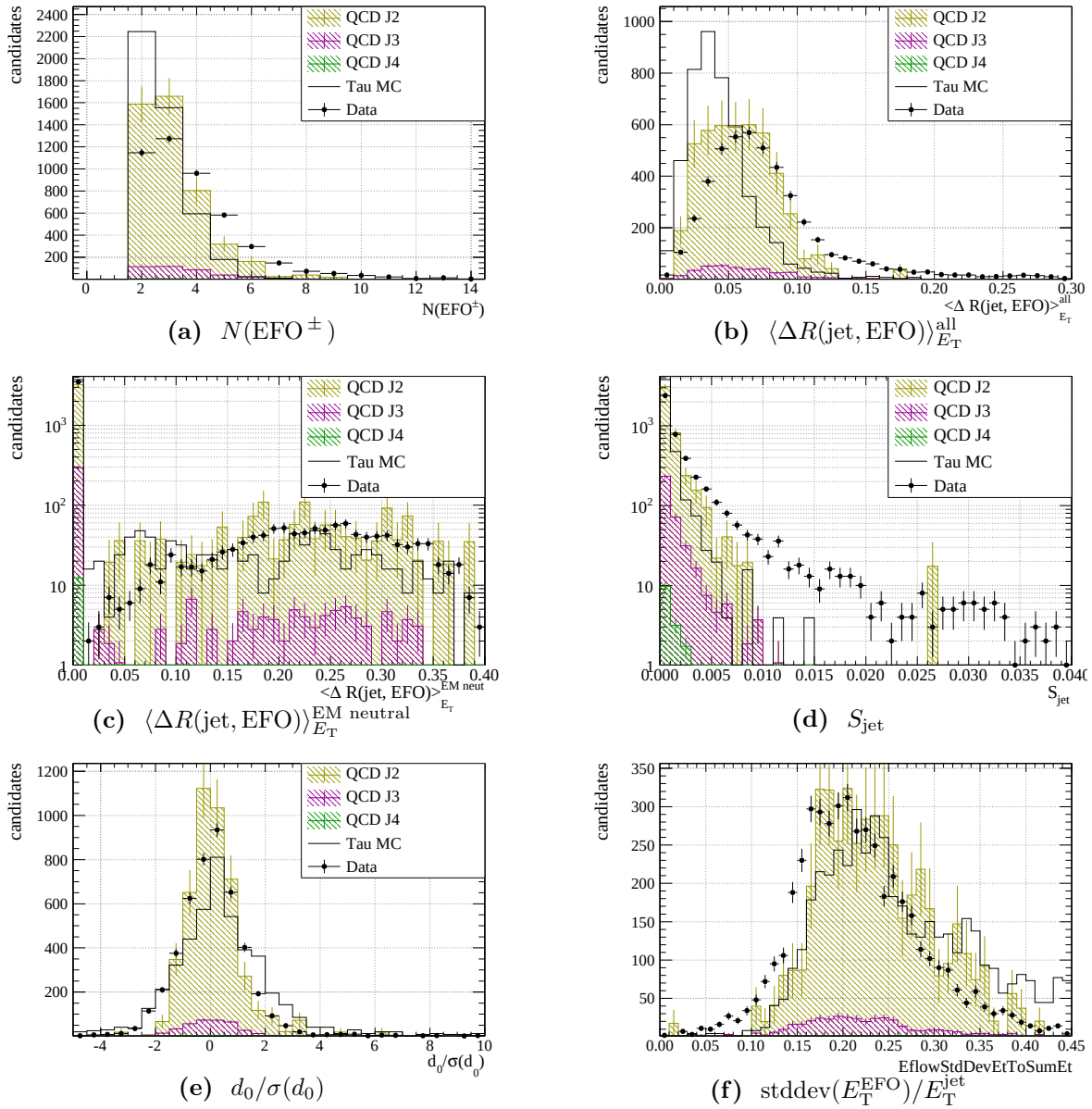

(a) $N(\mathrm{EFO}^{\pm})$ **(b)** $\langle \Delta R(\mathrm{jet}, \mathrm{EFO}) \rangle^{\mathrm{all}}_{E_{\mathrm{T}}}$

(c) $\langle \Delta R(\mathrm{jet}, \mathrm{EFO}) \rangle^{\mathrm{EM\ neutral}}_{E_{\mathrm{T}}}$ **(d)** S_{jet}

(e) $d_0/\sigma(d_0)$ **(f)** $\mathrm{stddev}(E_{\mathrm{T}}^{\mathrm{EFO}})/E_{\mathrm{T}}^{\mathrm{jet}}$

Figure C.17: Distribution of the identification variables for the "2-prong" class in the transverse momentum range $25\,\mathrm{GeV} < p_{\mathrm{T}} < 50\,\mathrm{GeV}$. The stacked histograms correspond to the different QCD di-jet samples and the black dots are measured data. Monte Carlo samples have been scaled to the integral of the data. The black line shows the distribution for $\mathrm{W} \rightarrow \tau\nu$ and $\mathrm{Z} \rightarrow \tau\tau$ events for comparison.

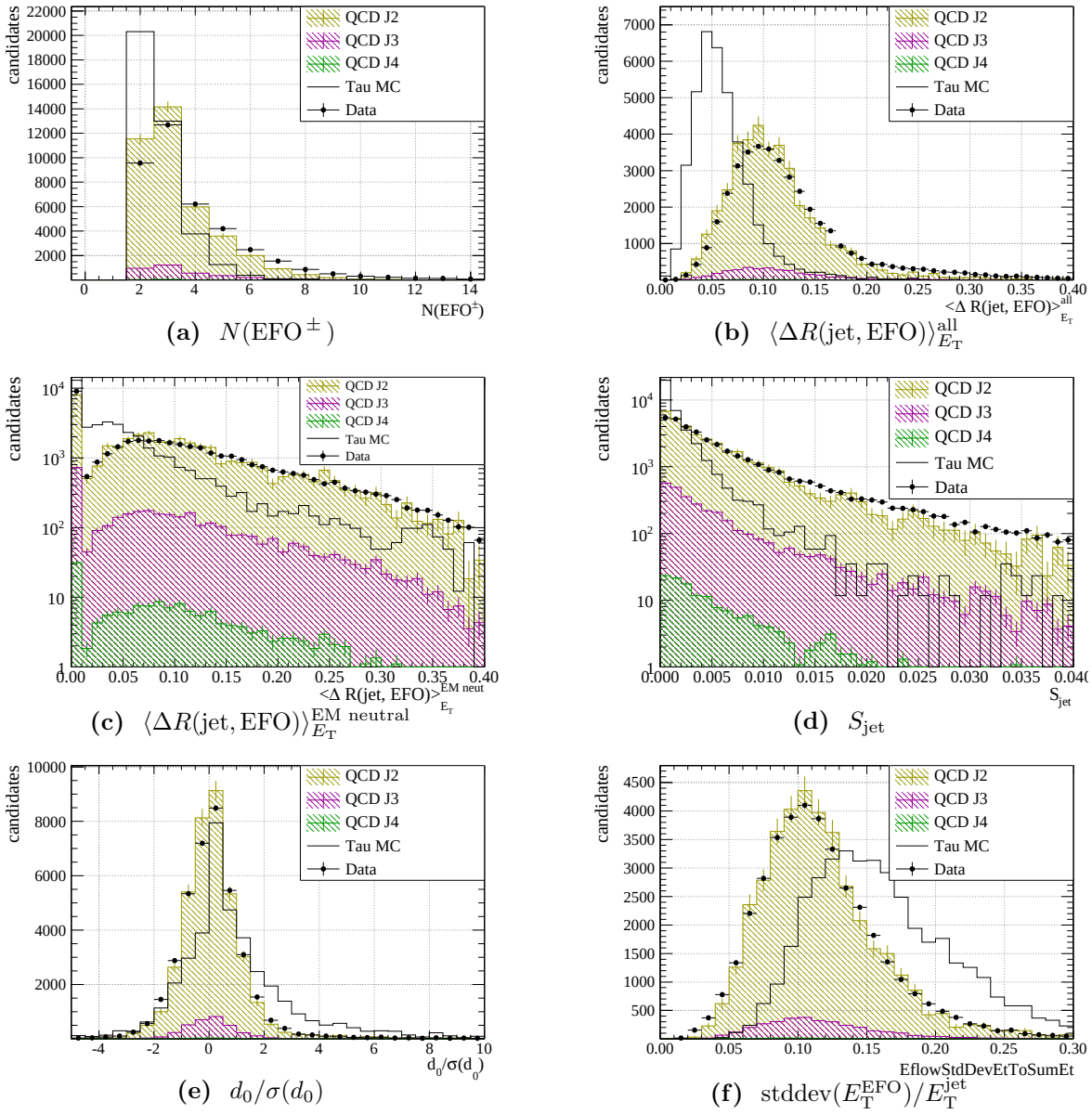

(a) $N(\mathrm{EFO}^{\pm})$ **(b)** $\langle \Delta R(\mathrm{jet}, \mathrm{EFO}) \rangle^{\mathrm{all}}_{E_{\mathrm{T}}}$

(c) $\langle \Delta R(\mathrm{jet}, \mathrm{EFO}) \rangle^{\mathrm{EM\ neutral}}_{E_{\mathrm{T}}}$ **(d)** S_{jet}

(e) $d_0/\sigma(d_0)$ **(f)** $\mathrm{stddev}(E_{\mathrm{T}}^{\mathrm{EFO}})/E_{\mathrm{T}}^{\mathrm{jet}}$

Figure C.18: Distribution of the identification variables for the "2-prong+neutral" class in the transverse momentum range $25\,\mathrm{GeV} < p_{\mathrm{T}} < 50\,\mathrm{GeV}$. The stacked histograms correspond to the different QCD di-jet samples and the black dots are measured data. Monte Carlo samples have been scaled to the integral of the data. The black line shows the distribution for $\mathrm{W} \rightarrow \tau\nu$ and $\mathrm{Z} \rightarrow \tau\tau$ events for comparison.

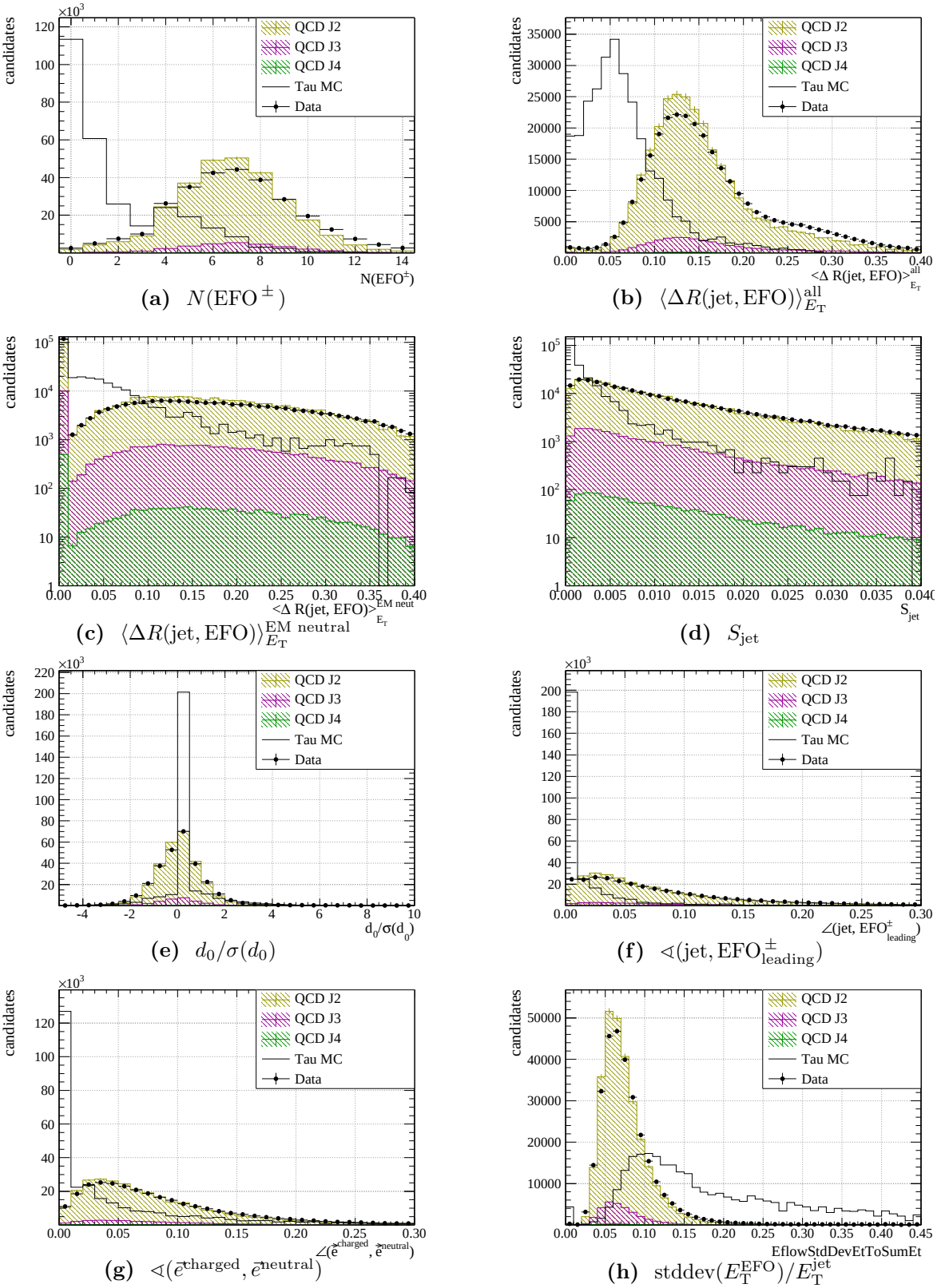

(a) $N(\mathrm{EFO}^{\pm})$ **(b)** $\langle \Delta R(\mathrm{jet}, \mathrm{EFO}) \rangle^{\mathrm{all}}_{E_{\mathrm{T}}}$

(c) $\langle \Delta R(\mathrm{jet}, \mathrm{EFO}) \rangle^{\mathrm{EM\ neutral}}_{E_{\mathrm{T}}}$ **(d)** S_{jet}

(e) $d_0/\sigma(d_0)$ **(f)** $\sphericalangle(\mathrm{jet}, \mathrm{EFO}^{\pm}_{\mathrm{leading}})$

(g) $\sphericalangle(\vec{e}^{\,\mathrm{charged}}, \vec{e}^{\,\mathrm{neutral}})$ **(h)** $\mathrm{stddev}(E_{\mathrm{T}}^{\mathrm{EFO}})/E_{\mathrm{T}}^{\mathrm{jet}}$

Figure C.19: Distribution of the identification variables for the "other" class in the transverse momentum range $25\,\mathrm{GeV} < p_{\mathrm{T}} < 50\,\mathrm{GeV}$. The stacked histograms correspond to the different QCD di-jet samples and the black dots are measured data. Monte Carlo samples have been scaled to the integral of the data. The black line shows the distribution for $\mathrm{W} \to \tau\nu$ and $\mathrm{Z} \to \tau\tau$ events for comparison.

Appendix D

Treatment of combinatorial backgrounds in the stau mass reconstruction

This Section explains the method used to choose the $\ell^+\ell^-\tau^{\text{had}}$ combination and investigates the origin of the combinatorial background in the reconstruction of the invariant mass of the $\widetilde{\tau}_1$ in BC 1. It also motivates the final combination scheme *the hardest tau with the nearest* $\ell^+\ell^-$ *pair in* ΔR which was finally used.

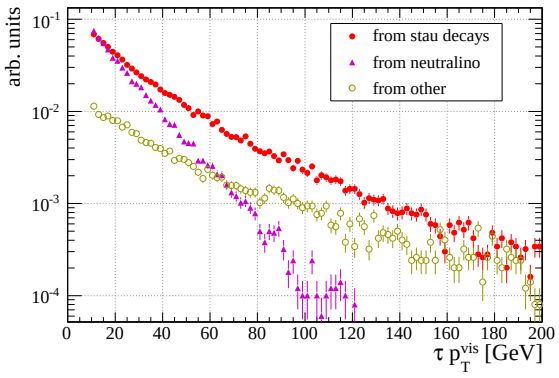

Figure D.1: Visible transverse momentum of taus from different sources in BC 1. The tau leptons are categorised according to Monte Carlo truth information and stem either from $\widetilde{\tau}$ LSP decays (solid red dots), $\widetilde{\chi}_1^0$ decays (purple solid triangles) or other sources (open yellow dots). Error bars represent statistical uncertainties.

In Figure D.1 the visible $p_{\text{T}}^{\text{vis}}$ distribution of selected taus from different sources is shown. A sample of 50 000 BC 1 signal events is used. One first observes that there are one order of magnitude less taus from other sources than from $\widetilde{\tau}_1$ LSP and $\widetilde{\chi}_1^0$ decays. In the low-p_{T} region, *i.e.* for transverse momenta below a few tens of GeV, one finds nearly as much taus from $\widetilde{\chi}_1^0$ decays as from stau decays. Fortunately, the p_{T} distribution from $\widetilde{\chi}_1^0$ decays falls off more rapidly when going to higher p_{T} values than the p_{T} distribution from stau decays. One can thus naturally reduce the combinatorial backgrounds if the hardest tau in each event is taken for the mass reconstruction.

Figure D.2 presents the number of taus from different sources in the same notation as in Figure D.1. One can see that in 33 % of all signal events only one tau is selected. Furthermore, in 47 % and 37 % of all events exactly one tau from the stau LSP and the $\widetilde{\chi}_1^0$ decays is identified, respectively. In 15 % of all events exactly one tau from other sources occurs.

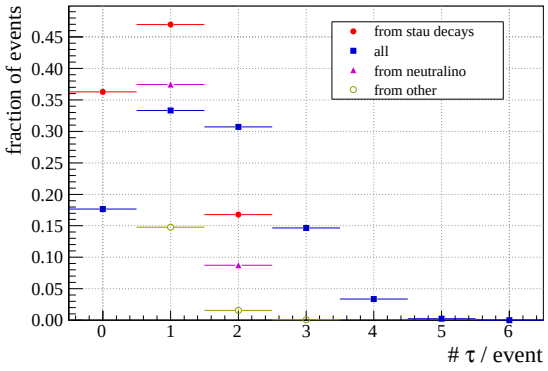

Figure D.2: Number of identified tau leptons per event from different sources in the scenario BC 1. The same notation like in Figure D.1 is used. In addition the sum of all taus is denoted by blue solid squares. In the zero bin, fractions for taus from $\widetilde{\chi}_1^0$ decays and other sources are out of the axis range.

method	correct	τ from $\widetilde{\chi}_1^0$	τ from other source	wrong ℓ^+ and ℓ^-	wrong ℓ^-	wrong ℓ^+	no $\tau^\pm\ell^+\ell^-$
A	24.7	21.8	11.6	5.9	8.9	9.1	18.0
B	9.4	21.7	11.6	20.2	8.9	10.1	18.0
C	17.5	30.4	7.6	13.5	5.9	7.1	18.0
D	13.8	35.1	6.8	8.8	8.6	9.0	18.0
E	24.7	20.6	10.8	5.2	8.1	8.2	22.4

Table D.1: Origin of charged leptons of the $\tau^\pm\ell^+\ell^-$ combination that is used for mass reconstruction in percent. Different selection methods are employed. Note that method A corresponds to the method finally used. The other methods are described in the text.

The most important observation from Figure D.2 is that combinatorial backgrounds cannot be avoided at all. One sees that in roughly 36 % of all events no tau from the stau LSP decays was identified. On the other hand only about 18 % of the events have no hadronically decaying tau. Therefore, in 36 % − 18 % = 18 % of all events one ends up with at least one identified tau, where none of the taus stem from stau LSP decays.

Various combination schemes have been investigated and compared with respect to their probability to select the correct combination. Amongst them are the following

method A Starting from the hardest (hadronically decayed) $\tau^\pm$ and combine it with the nearest $\ell^+\ell^-$ pair in ΔR ($\ell^\pm = \mathrm{e}^\pm, \mu^\pm$).

method B Same as method A, but with $\Delta\phi$ instead of ΔR match

method C Starting from the hardest $\ell^\pm$ and combine it with the nearest τ and $\ell^\mp$ in ΔR

method D For each event build all combinations $\tau^\pm\ell^+\ell^-$ and take the one with the smallest invariant mass

method E Same as method A, but do not allow the combination $\tau\mu^+\mu^-$

The first method (method A) corresponds to the method finally employed.

Table D.1 summarises the origin of the charged leptons of the $\tau^{\pm}\ell^{+}\ell^{-}$ combination that is used for the mass reconstruction. The different columns correspond to different sources, where the following classes were defined

correct All leptons of the triplet $\tau^{\pm}\ell^{+}\ell^{-}$ stem from the same stau LSP decay.

τ from $\widetilde{\chi}_1^0$ The tau in the relevant $\tau^{\pm}\ell^{+}\ell^{-}$ combination originates from the neutralino decay $\widetilde{\chi}_1^0 \to \widetilde{\tau}_1\tau$.

τ from other source The tau in the $\tau^{\pm}\ell^{+}\ell^{-}$ triplet stems neither from a stau LSP decay nor a $\widetilde{\chi}_1^0$ decay.

wrong ℓ^+ and ℓ^- The $\ell^{+}\ell^{-}$ pair is not from the same stau LSP decay like the tau.

wrong ℓ^+ (ℓ^-) The ℓ^+ (ℓ^-) originates not from the same stau LSP decay like the tau.

no $\tau^{\pm}\ell^{+}\ell^{-}$ No combination $\tau^{\pm}\ell^{+}\ell^{-}$ is possible in the event.

Note, that in the last three cases the tau always stems from the decay of a stau LSP.

For method A in 24.7 % of all events the correct $\tau^{\pm}\ell^{+}\ell^{-}$ combination is chosen, *i.e.* a lepton triplet that stems from the same stau LSP decay. However, in 33.4 % of all events, one starts with a tau that is not a stau LSP decay product. Within the class of wrong taus, most of them (21.8 %) are from $\widetilde{\chi}_1^0$ decays. This is also expected from Figure D.1 and Figure D.2. One has to keep in mind that two decays $\widetilde{\chi}_1^0 \to \widetilde{\tau}_1\tau$ are present in nearly every SUSY event, because most decay chains involve the $\widetilde{\chi}_1^0$.

Very often the wrong tau from the $\widetilde{\chi}_1^0$ decay and the $\ell^{+}\ell^{-}$ pair belong to the same decay chain, *i.e.* they stem *e.g.* from $\widetilde{q} \to q\widetilde{\chi}_1^0 \to \widetilde{\tau}_1\tau$. Due to the fact, that the $\widetilde{\chi}_1^0$ and the stau originate from the decay of a heavy sparticle like a squark, they are boosted in the same direction. Therefore, the ΔR criterion does not help to avoid these combinatorial backgrounds. However, taking only the hardest tau helps as described above.

None of the other methods described here leads to a better fraction of correct combinations. In most cases the amount of combinatorial backgrounds is even enhanced. For example, by relaxing the ΔR criterion by combining the three leptons that are nearest in $\Delta\phi$ (method B), the fraction of correct combinations is reduced to 9.4 %. The reason is, that very often a tau from one decay chain is combined with the $\ell^{+}\ell^{-}$ pair from the other decay chain then, *cf.* the fifth column for method B.

A small improvement is possible by vetoing the combination $\tau\mu^{+}\mu^{-}$ (method E). This does not increase the fraction of correct combinations but it reduces the number of wrong combinations. This can be seen in the last column of Table D.1. Going from method A to method E increases the fraction of no valid combinations from 18 % to 22.4 %. At the same time, the fraction of correct combinations is unchanged. The reason is, that the stau LSP cannot decay to $\tau\mu^{+}\mu^{-}\nu$ via a coupling λ_{121}, *cf.* Section 1.2.3. Therefore, the analysis of Section 5.3.1 was done with method A and E, but no significant improvement

was found for method E. It was thus decided not to veto the $\tau\mu^+\mu^-$ combination. In addition, the analysis is also more model independent. If a λ_{212} coupling is assumed instead of λ_{121} the stau decay to $\tau\mu^+\mu^-\nu$ would be the dominant one whereas the decay to $\tau e^+e^-\nu$ would no longer exist.

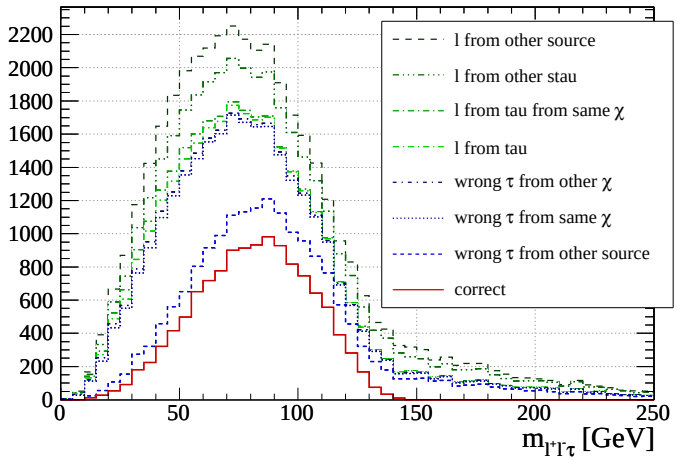

Figure D.3: Invariant mass distribution of the visible part of the hardest $\tau^\pm$ with the two nearest (in ΔR) charged leptons, ℓ as selected by method A. The contributions due to wrong $\tau^\pm\ell^+\ell^-$ combinations are split by the origin of the selected particles. "Correct" combinations are those where the selected $\tau^\pm\ell^+\ell^-$ all stem from the same $\widetilde{\tau}$ decay. "Wrong τ from same $\widetilde{\chi}_1^0$" includes a τ from a $\widetilde{\chi}_1^0 \to \widetilde{\tau}_1\tau$ decay and the leptons from the subsequent $\widetilde{\tau}$ decay. "ℓ from τ" are contributions with a selected lepton stemming from a leptonic τ decay and "ℓ from τ from same $\widetilde{\chi}_1^0$" with a lepton stemming from the τ decay of the $\widetilde{\chi}_1^0 \to \widetilde{\tau}_1\tau$. "$\ell$ from other $\widetilde{\tau}$" include at least one lepton stemming from the decay of the other $\widetilde{\tau}$ in the event and "ℓ from other source" leptons that stem from neither $\widetilde{\tau}$ nor $\widetilde{\chi}_1^0$ decays.

The contributions to the invariant mass distribution due to wrong $\tau^\pm\ell^+\ell^-$ combinations may distort the distribution. More precisely the combinations from different sources may even affect the invariant mass distribution differently and lead to a bias for example due to differences in the $\Delta\phi$ between leptons and taus which is used in the calculation of the invariant mass. For this reason Figure D.3 shows again the invariant mass distribution of selected $\tau^\pm\ell^+\ell^-$ combinations using method A, but here the contributions by wrong combinations have been split according to the origin of the selected particles. It is clearly visible that combinations with taus and leptons from other sources, *i.e.* neither $\widetilde{\tau}$ nor $\widetilde{\chi}_1^0$, contribute strongly at high invariant masses above the simulated $\widetilde{\tau}$ mass of 148 GeV. Their mean angular distance to the other particles is larger for them as they are more or less uncorrelated to them. Another significant contribution at high masses comes from combinations where one lepton belongs to the other $\widetilde{\tau}$ decay in the event than the selected τ. The dominant background, which shifts the total distribution to smaller invariant masses, comes from combinations where the selected τ stems from the $\widetilde{\chi}_1^0 \to \widetilde{\tau}_1\tau$ decay and the selected leptons from the subsequent $\widetilde{\tau}$ decay.

Bibliography

[1] S. Glashow, "Partial Symmetries of Weak Interactions", *Nucl.Phys.* **22** (1961) 579–588.

[2] S. Weinberg, "A Model of Leptons", *Phys.Rev.Lett.* **19** (1967) 1264–1266.

[3] M. Gell-Mann, "A Schematic Model of Baryons and Mesons", *Phys. Lett.* **8** (1964) 214–215.

[4] G. Zweig, "An SU_3 model for strong interaction symmetry and its breaking; Part II", Feb 1964.

[5] I. J. R. Aitchison and A. J. G. Hey, "Gauge theories in particle physics i", Institute of physics publishing, Bristol, 3rd ed., 2003.

[6] I. J. R. Aitchison and A. J. G. Hey, "Gauge theories in particle physics ii", Institute of physics publishing, Bristol, 3rd ed., 2004.

[7] N. Arkani-Hamed, S. Dimopoulos, and G. R. Dvali, "The hierarchy problem and new dimensions at a millimeter", *Phys. Lett.* **B429** (1998) 263–272, `hep-ph/9803315`.

[8] **Particle Data Group**, K. Nakamura *et al.*, "Review of particle physics", *J. Phys.* **G37** (2010) 075021.

[9] **Super-Kamiokande Collaboration**, Y. Ashie *et al.*, "A Measurement of atmospheric neutrino oscillation parameters by SUPER-KAMIOKANDE I", *Phys.Rev.* **D71** (2005) 112005, `arXiv:hep-ex/0501064`.

[10] **The SNO Collaboration**, B. Aharmim *et al.*, "Electron energy spectra, fluxes, and day-night asymmetries of B-8 solar neutrinos from the 391-day salt phase SNO data set", *Phys. Rev.* **C72** (2005) 055502, `nucl-ex/0502021`.

[11] **The Muon G-2 Collaboration**, G. W. Bennett *et al.*, "Final report of the muon E821 anomalous magnetic moment measurement at BNL", *Phys. Rev.* **D73** (2006) 072003, `hep-ex/0602035`.

[12] J. P. Miller, E. de Rafael, and B. L. Roberts, "Muon g-2: Review of Theory and Experiment", *Rept. Prog. Phys.* **70** (2007) 795, `hep-ph/0703049`.

[13] G. Kane and S. Watson, "Dark Matter and LHC: What is the Connection?", *Mod. Phys. Lett.* **A23** (2008) 2103–2123, `arXiv:0807.2244`.

[14] J. M. Campbell, J. W. Huston, and W. J. Stirling, "Hard Interactions of Quarks and Gluons: A Primer for LHC Physics", *Rept. Prog. Phys.* **70** (2007) 89, hep-ph/0611148.

[15] Z. Maki, M. Nakagawa, and S. Sakata, "Remarks on the unified model of elementary particles", *Prog.Theor.Phys.* **28** (1962) 870–880.

[16] D. J. Gross and F. Wilczek, "Ultraviolet behavior of non-abelian gauge theories", *Phys. Rev. Lett.* **30** (1973) 1343–1346.

[17] F. Englert and R. Brout, "Broken symmetry and the mass of gauge vector mesons", *Phys. Rev. Lett.* **13** (1964) 321–322.

[18] P. W. Higgs, "Broken symmetries and the masses of gauge bosons", *Phys. Rev. Lett.* **13** (1964) 508–509.

[19] S. P. Martin, "A Supersymmetry Primer", hep-ph/9709356v5.

[20] M. Drees, "An Introduction to supersymmetry", hep-ph/9611409.

[21] I. J. R. Aitchison, "Supersymmetry and the MSSM: An Elementary introduction", hep-ph/0505105.

[22] H. K. Dreiner, "An introduction to explicit R-parity violation", arXiv:hep-ph/9707435.

[23] H. K. Dreiner, H. E. Haber, and S. P. Martin, "Two-component spinor techniques and Feynman rules for quantum field theory and supersymmetry", *Phys. Rept.* **494** (2010) 1–196, arXiv:0812.1594.

[24] R. Barbier *et al.*, "R-parity violating supersymmetry", *Phys. Rept.* **420** (2005) 1–202, hep-ph/0406039.

[25] J. Wess and B. Zumino, "Supergauge Transformations in Four-Dimensions", *Nucl.Phys.* **B70** (1974) 39–50.

[26] S. Dimopoulos and H. Georgi, "Softly Broken Supersymmetry and SU(5)", *Nucl.Phys.* **B193** (1981) 150.

[27] H. K. Dreiner, C. Luhn, and M. Thormeier, "What is the discrete gauge symmetry of the MSSM?", *Phys. Rev.* **D73** (2006) 075007, hep-ph/0512163.

[28] G. 't Hooft, "Naturalness, chiral symmetry, and spontaneous chiral symmetry breaking", *NATO Adv.Study Inst.Ser.B Phys.* **59** (1980) 135.

[29] S. R. Coleman and J. Mandula, "All possible symmetries of the S matrix", *Phys.Rev.* **159** (1967) 1251–1256.

[30] R. Haag, J. T. Lopuszanski, and M. Sohnius, "All Possible Generators of Supersymmetries of the S Matrix", *Nucl.Phys.* **B88** (1975) 257.

[31] J. R. Ellis, J. Hagelin, S. Kelley, and D. V. Nanopoulos, "Aspects of the Flipped Unification of Strong, Weak and Electromagnetic Interactions", *Nucl.Phys.* **B311** (1988) 1.

[32] U. Amaldi, W. de Boer, and H. Fürstenau, "Comparison of grand unified theories with electroweak and strong coupling constants measured at LEP", *Phys. Lett.* **B260** (1991) 447–455.

[33] A. Brignole, L. E. Ibanez, and C. Munoz, "Soft supersymmetry-breaking terms from supergravity and superstring models", `hep-ph/9707209`.

[34] H. Flacher *et al.*, "Gfitter - Revisiting the Global Electroweak Fit of the Standard Model and Beyond", *Eur. Phys. J.* **C60** (2009) 543–583, `arXiv:0811.0009`.

[35] P. Bechtle, K. Desch, M. Uhlenbrock, and P. Wienemann, "Constraining SUSY models with Fittino using measurements before, with and beyond the LHC", *Eur. Phys. J.* **C66** (2010) 215–259, `arXiv:0907.2589`.

[36] D. Stöckinger, "The muon magnetic moment and supersymmetry", *J. Phys.* **G34** (2007) R45–R92, `hep-ph/0609168`.

[37] Y. Grossman and H. E. Haber, "(S)neutrino properties in R-parity violating supersymmetry. I: CP-conserving phenomena", *Phys. Rev.* **D59** (1999) 093008, `hep-ph/9810536`.

[38] J. R. Ellis, J. S. Hagelin, D. V. Nanopoulos, K. A. Olive, and M. Srednicki, "Supersymmetric relics from the big bang", *Nucl. Phys.* **B238** (1984) 453–476.

[39] J. R. Ellis, K. A. Olive, Y. Santoso, and V. C. Spanos, "Supersymmetric Dark Matter in Light of WMAP", *Phys. Lett.* **B565** (2003) 176–182, `hep-ph/0303043`.

[40] B. C. Allanach, A. Dedes, and H. K. Dreiner, "The R parity violating minimal supergravity model", *Phys. Rev.* **D69** (2004) 115002, `hep-ph/0309196`.

[41] **ALEPH**, S. Schael *et al.*, "Search for neutral MSSM Higgs bosons at LEP", *Eur. Phys. J.* **C47** (2006) 547–587, `hep-ex/0602042`.

[42] **LEP Working Group for Higgs boson searches**, R. Barate *et al.*, "Search for the standard model Higgs boson at LEP", *Phys. Lett.* **B565** (2003) 61–75, `hep-ex/0306033`.

[43] B. C. Allanach, M. A. Bernhardt, H. K. Dreiner, C. H. Kom, and P. Richardson, "Mass Spectrum in R-Parity Violating mSUGRA and Benchmark Points", *Phys. Rev.* **D75** (2007) 035002, `hep-ph/0609263`.

[44] H. K. Dreiner, M. Hanussek, and S. Grab, "Bounds on R-parity Violating Couplings at the Grand Unification Scale from Neutrino Masses", *Phys. Rev.* **D82** (2010) 055027, `arXiv:1005.3309`.

[45] H. K. Dreiner, S. Grab, and M. K. Trenkel, "Stau LSP Phenomenology: Two versus Four-Body Decay Modes. Example: Resonant Single Slepton Production at the LHC", *Phys. Rev.* **D79** (2009) 016002, arXiv:0808.3079.

[46] H. K. Dreiner and S. Grab, "All Possible Lightest Supersymmetric Particles in R-Parity Violating mSUGRA", *Phys. Lett.* **B679** (2009) 45–50, arXiv:0811.0200.

[47] M. Fairbairn *et al.*, "Stable massive particles at colliders", *Phys. Rept.* **438** (2007) 1–63, hep-ph/0611040.

[48] E. J. Chun, J. E. Kim, and H. P. Nilles, "Axino mass", *Phys. Lett.* **B287** (1992) 123–127, hep-ph/9205229.

[49] E. J. Chun and H. B. Kim, "Nonthermal axino as cool dark matter in supersymmetric standard model without R-parity", *Phys. Rev.* **D60** (1999) 095006, hep-ph/9906392.

[50] E. J. Chun and H. B. Kim, "Axino Light Dark Matter and Neutrino Masses with R-parity Violation", *JHEP* **10** (2006) 082, hep-ph/0607076.

[51] H.-S. Lee, K. T. Matchev, and T. T. Wang, "A U(1)-prime solution to the mu-problem and the proton decay problem in supersymmetry without R-parity", *Phys. Rev.* **D77** (2008) 015016, arXiv:0709.0763.

[52] H.-S. Lee, C. Luhn, and K. T. Matchev, "Discrete gauge symmetries and proton stability in the U(1)'-extended MSSM", *JHEP* **07** (2008) 065, arXiv:0712.3505.

[53] F. Takayama and M. Yamaguchi, "Gravitino dark matter without R-parity", *Phys. Lett.* **B485** (2000) 388–392, hep-ph/0005214.

[54] W. Buchmuller, L. Covi, K. Hamaguchi, A. Ibarra, and T. Yanagida, "Gravitino dark matter in R-parity breaking vacua", *JHEP* **03** (2007) 037, hep-ph/0702184.

[55] S. Bobrovskyi, W. Buchmuller, J. Hajer, and J. Schmidt, "Broken R-Parity in the Sky and at the LHC", *JHEP* **10** (2010) 061, arXiv:1007.5007.

[56] H. K. Dreiner, S. Grab, and T. Stefaniak, "Discovery Potential of Selectron or Smuon as the Lightest Supersymmetric Particle at the LHC", arXiv:1102.3189.

[57] A. F. Kord and A. Yazdanian, "The Full Two-Loop R-parity Violating Renormalization Group Equations for All Minimal Supersymmetric Standard Model Couplings", *JHEP* **03** (2011) 084, arXiv:1101.4358.

[58] F. D. Aaron *et al.*, "Search for Squarks in R-parity Violating Supersymmetry in ep Collisions at HERA", *Eur. Phys. J.* **C71** (2011) 1572, arXiv:1011.6359.

[59] K. Desch, H. K. Dreiner, S. Fleischmann, S. Grab, and P. Wienemann, "Stau as the Lightest Supersymmetric Particle in R-Parity Violating SUSY Models: Discovery Potential with Early LHC Data", *Phys. Rev. D* **83** Jan (2011) 015013,

arXiv:1008.1580.

[60] e. Evans, Lyndon and e. Bryant, Philip, "LHC Machine", *JINST* **3** (2008) S08001.

[61] **The ALICE Collaboration**, K. Aamodt *et al.*, "The ALICE experiment at the CERN LHC", *JINST* **3** (2008) S08002.

[62] **The ATLAS Collaboration**, G. Aad *et al.*, "The ATLAS Experiment at the CERN Large Hadron Collider", *JINST* **3** (2008) S08003.

[63] **The CMS Collaboration**, R. Adolphi *et al.*, "The CMS experiment at the CERN LHC", *JINST* **3** (2008) S08004.

[64] **The LHCb Collaboration**, A. Alves *et al.*, "The LHCb Detector at the LHC", *JINST* **3** (2008) S08005.

[65] **The LHCf Collaboration**, O. Adriani *et al.*, "The LHCf detector at the CERN Large Hadron Collider", *JINST* **3** (2008) S08006.

[66] **The TOTEM Collaboration**, G. Anelli *et al.*, "The TOTEM experiment at the CERN Large Hadron Collider", *JINST* **3** (2008) S08007.

[67] **The ATLAS Collaboration**, G. Aad *et al.*, "Expected Performance of the ATLAS Experiment. Detector, Trigger, Physics", arXiv:0901.0512.

[68] **The CERN machine group**, A. M. Asner *et al.*, "Large hadron collider in the LEP tunnel: a feasibility study of possible options", Tech. Rep. CERN-DIR-TECH-84-01, May 1984.

[69] CERN, "Summary of the analysis of the 19 September 2008 incident at the LHC", tech. rep., CERN, Geneva, Oct 2008.

[70] CERN, "Follow up of the incident of 19 september 2008 at the LHC", tech. rep., CERN, Geneva, Dec 2008.

[71] **The Atlas Collaboration**, G. Aad *et al.*, "Observation of a Centrality-Dependent Dijet Asymmetry in Lead-Lead Collisions at sqrt(S(NN))= 2.76 TeV with the ATLAS Detector at the LHC", arXiv:1011.6182.

[72] *ATLAS Detector and Physics Performance Technical Design Report — Volume I*, 1999. CERN/LHCC/99-14.

[73] *ATLAS Detector and Physics Performance Technical Design Report — Volume II*, 1999. CERN/LHCC/99-15.

[74] M. Capeans *et al.*, "ATLAS Insertable B-Layer Technical Design Report", ATLAS Technical Design Report ATL-COM-UPGRADE-2010-016. ATLAS TDR 19, CERN, Geneva, Sep 2010.

[75] T. Cornelissen *et al.*, "The global χ^2 track fitter in ATLAS", *J. Phys.: Conf. Ser.* **119** (2008) 032013.

[76] R. Frühwirth, "Application of Kalman filtering to track and vertex fitting", *Nuclear Instruments and Methods in Physics Research A* **262** (1987) 444–450.

[77] T. Cornelissen, S. Fleischmann, *et al.*, "Concepts, Design and Implementation of the ATLAS New Tracking (NEWT)", ATLAS Publication ATL-SOFT-PUB-2007-007, CERN, Geneva, Mar 2007.

[78] G. Barrand *et al.*, "GAUDI - The software architecture and framework for building LHCb data processing applications", 2000.

[79] **The ATLAS collaboration**, "Electron and photon reconstruction and identification in ATLAS: expected performance at high energy and results at 900 GeV", ATLAS Conference Note ATLAS-CONF-2010-005, CERN, Geneva, Jun 2010.

[80] **The ATLAS collaboration**, "Muon reconstruction performance", ATLAS Conference Note ATLAS-CONF-2010-064, CERN, Geneva, Jul 2010.

[81] W. Lampl *et al.*, "Calorimeter Clustering Algorithms: Description and Performance", ATLAS Public Note ATL-LARG-PUB-2008-002, CERN, Geneva, Apr 2008.

[82] M. Spousta, "Comparison of behavior of different jet finding algorithms in a presence of background", ATLAS Internal Note ATL-PHYS-INT-2009-096, CERN, Geneva, Oct 2009.

[83] N. Ghodbane, "Performance of Jet Algorithms for the Top Quark Physics at the ATLAS Experiment", ATLAS Internal Note ATL-PHYS-INT-2009-087, CERN, Geneva, Sep 2009.

[84] G. C. Blazey *et al.*, "Run II jet physics", `hep-ex/0005012`.

[85] S. Catani, Y. L. Dokshitzer, M. H. Seymour, and B. R. Webber, "Longitudinally invariant K_t clustering algorithms for hadron hadron collisions", *Nucl. Phys.* **B406** (1993) 187–224.

[86] S. D. Ellis and D. E. Soper, "Successive combination jet algorithm for hadron collisions", *Phys. Rev.* **D48** (1993) 3160–3166, `hep-ph/9305266`.

[87] M. Cacciari, G. P. Salam, and G. Soyez, "The anti-k_t jet clustering algorithm", *JHEP* **04** (2008) 063, `arXiv:0802.1189`.

[88] **ATLAS Collaboration**, G. Aad *et al.*, "Performance of Missing Transverse Momentum Reconstruction in Proton-Proton Collisions at 7 TeV with ATLAS", `arXiv:1108.5602`.

[89] G. Corcella *et al.*, "HERWIG 6.5: an event generator for Hadron Emission Reactions With Interfering Gluons (including supersymmetric processes)", *JHEP* **01** (2001) 010, hep-ph/0011363.

[90] T. Sjostrand, S. Mrenna, and P. Z. Skands, "PYTHIA 6.4 Physics and Manual", *JHEP* **05** (2006) 026, hep-ph/0603175.

[91] S. Agostinelli *et al.*, "G4–a simulation toolkit", *Nucl. Instrum. Meth.* **A 506** (2003), no. 3, 250 – 303.

[92] **The ATLAS Collaboration**, G. Aad *et al.*, "The ATLAS Simulation Infrastructure", *Eur. Phys. J. C* **70** (2010), no. 3, 232, arXiv:1005.4568.

[93] **The ATLAS Collaboration**, S. Fleischmann, "FATRAS – A Novel Fast Track Simulation Engine for the ATLAS Experiment", in "13th International Workshop on Advanced Computing and Analysis Techniques in Physics Research", no. (ACAT2010)063 in PoS. 2010.

[94] S. Ovyn, X. Rouby, and V. Lemaitre, "Delphes, a framework for fast simulation of a generic collider experiment", arXiv:0903.2225.

[95] J. Conway *et al.*, *PGS 4*.

[96] K. Edmonds, S. Fleischmann, T. Lenz, C. Magass, J. Mechnich, and A. Salzburger, "The Fast ATLAS Track Simulation (FATRAS)", ATLAS Public Note ATL-SOFT-PUB-2008-001, CERN, Geneva, Mar 2008.

[97] A. Salzburger, "The ATLAS Track Extrapolation Package", ATLAS Public Note ATL-SOFT-PUB-2007-005, CERN, Geneva, Jun 2007.

[98] A. Salzburger, S. Todorova, and M. Wolter, "The ATLAS Tracking Geometry Description", ATLAS Note ATL-SOFT-PUB-2007-004, CERN, Geneva, Jun 2007.

[99] **The ATLAS Collaboration**, M. Beckingham *et al.*, "The simulation principle and performance of the ATLAS fast calorimeter simulation FastCaloSim", ATLAS Public Note ATL-PHYS-PUB-2010-013, CERN, Geneva, Oct 2010.

[100] D. Schmeier, "Optimierung der Identifikation von Tau Leptonen in supersymmetrischen Prozessen mit der schnellen Detektorsimulation Delphes", 2010.

[101] S. Bethke, "The 2009 World Average of $\alpha_s(M_Z)$", *Eur. Phys. J.* **C64** (2009) 689–703, arXiv:0908.1135.

[102] T. Nattermann, K. Desch, P. Wienemann, and C. Zendler, "Measuring tau-polarisation in $\widetilde{\chi}_2^0$ decays at the LHC", *JHEP* **04** (2009) 057, arXiv:0903.0714.

[103] C. Limbach, "Leptonische Tau-Zerfälle in supersymmetrischen Prozessen im ATLAS-Detektor", Oct 2009.

[104] R. Frühwirth and A. Strandlie, "Track fitting with ambiguities and noise: a study of elastic tracking and non-linear filters", *Computer Physics Communications* **120** (1999) 197–214.

[105] A. Strandlie and R. Frühwirth, "Adaptive multitrack fitting", *Computer Physics Communications* **133** (2000) 34–42.

[106] **The ATLAS collaboration**, "The Impact of Inner Detector Misalignments on Selected Physics Processes", ATLAS Public Note ATL-PHYS-PUB-2009-080, CERN, Geneva, May 2009.

[107] J. Alison, B. Cooper, and T. Goettfert, "Production of Residual Systematically Misaligned Geometries for the ATLAS Inner Detector", ATLAS Internal Note ATL-INDET-INT-2009-003, CERN, Geneva, Oct 2009.

[108] **ALEPH**, D. Buskulic *et al.*, "Performance of the ALEPH detector at LEP", *Nucl. Instrum. Meth.* **A360** (1995) 481–506.

[109] J.-C. Brient and H. Videau, "The calorimetry at the future e^+e^- linear collider", `hep-ex/0202004`.

[110] M. A. Thomson, "Particle Flow Calorimetry and the PandoraPFA Algorithm", *Nucl. Instrum. Meth.* **A611** (2009) 25–40, `arXiv:0907.3577`.

[111] M. Hodgkinson, D. Tovey, and R. Duxfield, "Energy Flow Reconstruction with the eflowRec Combined Reconstruction Software in Athena 15.6.9.8", ATLAS Internal note ATL-PHYS-INT-2011-031, CERN, Geneva, Apr 2011.

[112] R. P. Prabhu, "Studies into tau reconstruction, missing transverse energy and photon induced processes with the ATLAS detector at the LHC", PhD thesis, Bonn, 2010.

[113] T. Barillari *et al.*, "Local hadronic calibration", ATLAS Public Note ATL-LARG-PUB-2009-001-2, CERN, Geneva, Jun 2008.

[114] M. Heldmann and D. Cavalli, "An improved tau-Identification for the ATLAS experiment", ATLAS Public Note ATL-PHYS-PUB-2006-008, CERN, Geneva, Dec 2005.

[115] D. Froidevaux, P. Nevski, and E. Richter-Was, "Energy flow studies with hadronic tau-decays using DC1 data samples", ATLAS Communication ATL-COM-PHYS-2005-024, CERN, Geneva, May 2005.

[116] A. Christov *et al.*, "Performance of the tau reconstruction algorithm with release 15.3.1.6 and mc08 data", ATLAS Communication ATL-COM-PHYS-2010-878, CERN, Geneva, Oct 2010.

[117] P. Bechtle, S. Fleischmann, *et al.*, "Identification of hadronic tau decays with ATLAS detector", ATLAS Internal Note ATL-PHYS-INT-2008-003, CERN, Geneva, Sep 2007.

[118] *Athena – The ATLAS Common Framework – Developer Guide*, 2004.

[119] A. Hocker *et al.*, "TMVA - Toolkit for Multivariate Data Analysis", `physics/0703039v4`.

[120] G. P. Salam and G. Soyez, "A practical Seedless Infrared-Safe Cone jet algorithm", *JHEP* **05** (2007) 086, `arXiv:0704.0292`.

[121] Y. L. Dokshitzer, G. D. Leder, S. Moretti, and B. R. Webber, "Better Jet Clustering Algorithms", *JHEP* **08** (1997) 001, `hep-ph/9707323`.

[122] M. Wobisch and T. Wengler, "Hadronization corrections to jet cross sections in deep- inelastic scattering", `hep-ph/9907280`.

[123] A. Hoecker, P. Speckmayer, J. Stelzer, J. Therhaag, E. von Toerne, and H. Voss, "TMVA: Toolkit for Multivariate Data Analysis", *PoS* **ACAT** (2007) 040, `physics/0703039`.

[124] C.-H. Kom and W. J. Stirling, "Charge asymmetry in W + jets production at the LHC", *Eur. Phys. J.* **C69** (2010) 67–73, `arXiv:1004.3404`.

[125] P. Bechtle *et al.*, "Tau identification performance with the ATLAS detector", ATLAS Communication ATL-COM-PHYS-2010-599, CERN, Geneva, Aug 2010.

[126] **The ATLAS Collaboration**, "Tau Reconstruction and Identification Performance in ATLAS", ATLAS Note ATLAS-CONF-2010-086, CERN, Geneva, Oct 2010.

[127] B. Blakeslee *et al.*, "Tau Data Quality Good Run Lists for ICHEP 2010", ATLAS Communication ATL-COM-PHYS-2010-405, CERN, Geneva, Jun 2010.

[128] **The ATLAS Collaboration**, "Data-Quality Requirements and Event Cleaning for Jets and Missing Transverse Energy Reconstruction with the ATLAS Detector in Proton-Proton Collisions at a Center-of-Mass Energy of $\sqrt{s} = 7$ TeV", ATLAS Note ATLAS-CONF-2010-038, CERN, Geneva, Jul 2010.

[129] P. Bechtle *et al.*, "Commissioning of the ATLAS Tau-Lepton Reconstruction Using 7 TeV data", ATLAS Communication ATL-COM-PHYS-2010-392, CERN, Geneva, Jun 2010.

[130] **The ATLAS Collaboration**, "ATLAS Monte Carlo tunes for MC09", ATLAS Public Note ATL-PHYS-PUB-2010-002, CERN, Geneva, Mar 2010.

[131] **TeV4LHC QCD Working Group**, M. G. Albrow *et al.*, "Tevatron-for-LHC Report of the QCD Working Group", `hep-ph/0610012`.

[132] P. Bechtle *et al.*, "Studying Tau Reconstruction and Identification Performance in Di-Jet, Three-Jet and Photon-Jet Events with the ATLAS Experiment", ATLAS Communication ATL-COM-PHYS-2011-194, CERN, Geneva, Feb 2011.

[133] A. W. Phillips, "Studies of R-parity violating supersymmetry with the ATLAS detector", PhD thesis, Univ. Cambridge, Cambridge, 2008.

[134] E. Torro, V. A. Mitsou, and C. Garca, "Probing Bilinear R-Parity Violating Supersymmetry in the Muon plus Jets Channel", ATLAS Internal Note ATL-PHYS-INT-2010-042, CERN, Geneva, Apr 2010.

[135] S. French, "R-parity violation with jet signatures at the ATLAS detector", ATLAS Conference Proceedings ATL-PHYS-PROC-2009-089, CERN, Geneva, Sep 2009.

[136] **The ATLAS collaboration**, "Early searches for prompt R-Parity violating Supersymmetry decays with the ATLAS detector", ATLAS Note, CERN, Geneva. in preparation.

[137] **The ATLAS Collaboration**, G. Aad *et al.*, "Search for a heavy particle decaying into an electron and a muon with the ATLAS detector in $\sqrt{s} = 7$TeV pp collisions at the LHC", `arXiv:1103.5559`.

[138] T. Binoth, G. Ossola, C. G. Papadopoulos, and R. Pittau, "NLO QCD corrections to tri-boson production", *JHEP* **06** (2008) 082, `arXiv:0804.0350`.

[139] S. Allwood-Spires *et al.*, "Monte Carlo samples used for top physics", ATLAS Internal Note ATL-PHYS-INT-2010-132, CERN, Geneva, Dec 2010.

[140] P. Richardson, private communication, unpublished.

[141] P. Bechtle, K. Desch, M. Uhlenbrock, and P. Wienemann, "Extracting SUSY parameters from LHC measurements using Fittino", *AIP Conf. Proc.* **1200** (2010) 486–489, `arXiv:0909.1820`.

[142] N. Metropolis, A. W. Rosenbluth, M. N. Rosenbluth, A. H. Teller, and E. Teller, "Equation of state calculations by fast computing machines", *J. Chem. Phys.* **21** (1953) 1087–1092.

[143] S. Moch and P. Uwer, "Theoretical status and prospects for top-quark pair production at hadron colliders", *Phys.Rev.* **D78** (2008) 034003, `arXiv:0804.1476`.

[144] ATLAS egamma group, "egamma efficiency measurements". ATLAS WIKI: EfficiencyMeasurements, 2011.

[145] N. Benekos *et al.*, "Lepton trigger and identification for the first top quark observation", ATLAS Internal Note ATL-PHYS-INT-2010-131, CERN, Geneva, Dec 2010.

[146] ATLAS egamma group, "recommendations for the electron energy scale". ATLAS WIKI: EnergyScaleResolutionRecommendations, 2011.

[147] **The ATLAS collaboration**, "Jet energy scale and its systematic uncertainty for jets produced in proton-proton collisions at $\sqrt{s} = 7$TeV and measured with the ATLAS detector", ATLAS Conference Note ATLAS-CONF-2010-056, CERN, Geneva, Jul 2010.

[148] **The ATLAS collaboration**, "Update on the jet energy scale systematic uncertainty for jets produced in proton-proton collisions at $\sqrt{s} = 7$ TeV measured with the ATLAS detector", ATLAS Conference Note ATLAS-CONF-2011-007, CERN, Geneva, Feb 2011.

[149] C. Miranda *et al.*, "Determination of the muon reconstruction efficiency in ATLAS at the Z resonance in proton-proton collisons at $\sqrt{s} = 7$TeV", ATLAS Communication ATLAS-COM-CONF-2011-001, CERN, Geneva, Jan 2011.

[150] F. Cerutti *et al.*, "Muon momentum resolution in first pass reconstruction of pp collision data recorded by atlas in 2010", ATLAS Communication ATLAS-COM-CONF-2011-003, CERN, Geneva, Jan 2011.

[151] ATLAS Muon Combined Performance group, "Muon recommendations for rel15". ATLAS WIKI: MCPAnalysisGuidelinesRel15, 2011.

[152] **The ATLAS Collaboration**, "Muon momentum resolution in first pass reconstruction of pp collision data recorded by atlas in 2010", ATLAS Note ATLAS-CONF-2011-046, CERN, Geneva, Mar 2011.

[153] P. Bechtle *et al.*, "SUSY searches with dileptons and high missing transverse momentum", ATLAS Internal Note ATL-PHYS-INT-2011-030, CERN, Geneva, Apr 2011.

[154] R. D. Cousins, J. T. Linnemann, and J. Tucker, "Evaluation of three methods for calculating statistical significance when incorporating a systematic uncertainty into a test of the background-only hypothesis for a poisson process", *Nucl. Instrum. Meth.* **A 595** (2008), no. 2, 480 – 501, `arXiv:0702156`.

[155] G. Cowan, *Discovery significance with statistical uncertainty in the background estimate*, 2008.

[156] **The ATLAS collaboration**, "Performance of the Electron and Photon Trigger in p-p Collisions at a centre of mass energy of 900 GeV", ATLAS Conference Note ATLAS-CONF-2010-022, CERN, Geneva, Jul 2010.

[157] **The ATLAS collaboration**, "Performance of the ATLAS Jet Trigger in the Early $\sqrt{s} = 7$ TeV Data", ATLAS Conference Note ATLAS-CONF-2010-094, CERN, Geneva, Oct 2010.

[158] **The ATLAS collaboration**, "Performance of the ATLAS Muon Trigger in p-p collisions at $\sqrt{s} = 7TeV$", ATLAS Conference Note ATLAS-CONF-2010-095, CERN, Geneva, Oct 2010.

[159] B. C. Allanach, "SOFTSUSY: a program for calculating supersymmetric spectra", *Comput. Phys. Commun.* **143** (2002) 305–331, `hep-ph/0104145`.

[160] B. C. Allanach and M. A. Bernhardt, "Including R-parity violation in the numerical computation of the spectrum of the minimal supersymmetric standard model: SOFTSUSY3.0", *Comput. Phys. Commun.* **181** (2010) 232–245, `arXiv:0903.1805`.

[161] F. E. Paige, S. D. Protopopescu, H. Baer, and X. Tata, "ISAJET 7.69: A Monte Carlo event generator for p p, anti-p p, and e+ e- reactions", `hep-ph/0312045`.

[162] C. M. Bishop, "Pattern recognition and machine learning", Springer, August 2006.

List of Figures

List of Tables